UNIVERSITÀ
DEGLI STUDI
DI PADOVA

TÉCNICO
LISBOA

U LISBOA | UNIVERSIDADE
DE LISBOA

Università degli Studi di Padova
Centro Ricerche Fusione (CRF)

Universidade de Lisboa
Instituto Superior Técnico (IST)

JOINT RESEARCH DOCTORATE IN FUSION SCIENCE AND ENGINEERING
Cycle XXIX

Numerical and experimental characterization of beams of negative ions and investigation on strategies for beam efficiency improvement

Coordinator:
Prof. Paolo Bettini

Supervisors:
Prof. Piergiorgio Sonato
Prof. Horacio João Matos Fernandes
Dr. Gianluigi Serianni

Ph.D. student: Carlo Baltador

Padova, January 2017

JOINT Doctorate and NETWORK in Fusion Science and Engineering

Network Partners:

- Instituto Superior Técnico (IST) Lisboa, *Portugal*
- Universitá degli studi di Padova, *Italy*
- Ludwig Maximilians University Munich, *Germany*

In collaboration with:

- Consorzio RFX, *Italy*
- IPP Garching, *Germany*

Contents

Abstract

The research activity done during the three years Joint Doctorate in Fusion Science and Engineering was focused on negative ion sources and dedicated to numerical investigations of beam optics, experimental measurements and development of improvements for experimental devices. In particular, I carried out investigations on plasma source behavior and beam extraction under different operational conditions, paying special attention to beam optics improvement and co-extracted electron suppression efficiency, as well as analysing and developing solutions by means of numerical codes such as SLACCAD and OPERA, supported by dedicated post-processing by MATLAB scripts.

I investigated the beam properties for three negative ion beam sources: SPIDER and NIO1 at Consorzio RFX (Padova, Italy) and NITS at National Institute for Quantum and Radiological Science and Technology (QST, Naka, Japan). SPIDER is the full-scale prototype of the negative ion source for ITER negative ion beam injectors (NBIs) and is in the advanced construction and assembly phase, so no further design improvements could have been done. SPIDER is provided with several peculiar design solutions: I have numerically assessed the efficiency of such solutions related to beam optics with 40 beamlets (half SPIDER beamlet group). I participated in the joint experiments of Consorzio RFX and QST in the NITS facility. The aim of this collaboration was to prove experimentally, for the first time, the effectiveness of a specific magnetic field configuration adopted for ITER NBIs requiring the use of the so-called ADCM magnets to correct the residual magnetic deflection of the beamlets induced by the (CESM) magnets devoted to deflect the co-extracted electrons. In particular my contribution was to design the new extraction grid and the new magnets (both CESM and ADCM) to be installed on the source. I also cooperated to the data analysis. Lastly, for the NIO1 source, I participated in the experimental sessions since the beginning, and I gave my contribution to the spectroscopic characterization of the source and to beam optics characterization. These experimental observations suggested some upgrades needed for optics improvement. Hence, I moved in this direction designing a new extraction grid and new magnet configurations. Furthermore, the successful experimental evidences at NITS have made us confident to introduce ADCM also in NIO1. This design work was

performed in strict collaboration with Laboratori Nazionali di Legnaro (LNL, Legnaro, Italy). Unfortunately, these upgrades will be not installed on the source before spring 2017 and thus no experimental evidences of beam optics improvements are available yet.

Concerning the thesis manuscript, it is constituted by five chapters, followed by an additional summary. Here is a brief summary of the chapter contents.

In the first chapter I give an introduction on Fusion and ITER, highlighting the need for the use of NBIs in future fusion devices and the general issues related to MITICA, which is the full size prototype of ITER NBI.

In the second chapter there is a general description of the theoretical considerations related to the physics of plasma in the source, beam extraction and optics, and main components constituting the ion sources. The final part of the chapter is dedicated to the presentation of the numerical tools available at Consorzio RFX: SLACCAD, EAMCC, COMSOL and OPERA. Concerning the latter, since it is the most important numerical tool I used during my PhD, I dwell more on the possibilities it can offer and I provide also a sensitivity study in order to increase the calculation precision.

While the first two chapters have essentially introductory purposes, the last three present the actual activities I performed on the three ion sources, SPIDER, NITS and NIO1, as briefly described so far. In particular each of the three chapters is focused on the activity done on just one machine.

Lastly, two appendixes supplement this thesis concerning further activities, which are loosely related to the rest. These are the development of an Excel GUI, in Visual Basic language, to simplify the interaction with NIO1 database (Appendix A) and investigations on the energy recovery system efficiency that NIO1 will feature in the future, an activity carried out in collaboration with CNR institute of Bari (Appendix B).

Sommario

L'attività di ricerca svolta durante i tre anni del dottorato in Fusion Science and Engineering si è concentrata sulle sorgenti di ioni negativi e in particolare sulle simulazioni numeriche dell'ottica del fascio, sulle misure sperimentali e sullo sviluppo di miglioramenti. In particolare, ho eseguito indagini sul plasma in sorgente e sull'estrazione del fascio, in diverse condizioni operative. Particolare attenzione è stata data al miglioramento dell'ottica del fascio, all'efficienza della soppressione degli elettroni co-estratti, così come all'analisi e allo sviluppo di nuove soluzioni. Ciò è stato fatto per mezzo di codici numerici come SLACCAD e OPERA, supportati da appositi script MATLAB per post-processing.

Ho studiato le proprietà del fascio di tre sorgenti di ioni negativi: SPIDER e NIO1 presso il Consorzio RFX (Padova, Italia) e NITS presso il National Institute for Quantum and Radiological Science and Technology (QST, Naka, Giappone).

SPIDER è il prototipo in scala reale della sorgente di ioni negativi per l'iniettore di fasci neutri previsto per ITER, che attualmente è in fase avanzata di montaggio. Non sono, quindi, possibili ulteriori miglioramenti progettuali. SPIDER è dotato di diverse peculiari soluzioni progettuali legate all'ottica del fascio e ho provveduto alla valutazione dell'efficacia di tali soluzioni.

Ho preso parte agli esperimenti della collaborazione tra Consorzio RFX e QST sulla sorgente giapponese NITS. L'obiettivo di questa collaborazione è stato quello di dimostrare sperimentalmente, per la prima volta, l'efficacia di una configurazione di campo magnetico prevista per l'iniettore di neutri per ITER. Tale soluzione prevede l'uso dei cosiddetti magneti ADCM, per correggere la deflessione residua dei fasci indotti dai magneti dedicati a deviare gli elettroni co-estratti (CESM). In particolare, il mio contributo è stato quello di progettare la nuova griglia di estrazione e i nuovi magneti (sia CESM e ADCM) da installare nella nuova griglia. Ho anche collaborato all'analisi dei dati sperimentali.

Infine, per la sorgente NIO1, ho partecipato alle sessioni sperimentali fin dal loro inizio, dando il mio contributo alla caratterizzazione spettroscopica della sorgente e alla caratterizzazione dell'ottica del fascio. Le osservazioni sperimentali hanno suggerito alcuni aggiornamenti necessari per il miglioramento dell'ottica di NIO1: la progettazione di una nuova griglia di estrazione e il dimensionamento di

nuovi magneti. Inoltre, il successo della campagna sperimentale in NITS ha suggerito di introdurre gli ADCM anche in NIO1. Il lavoro di progettazione è stato eseguito in stretta collaborazione con i Laboratori Nazionali di Legnaro (LNL, Legnaro, Italia). Purtroppo, però, questi aggiornamenti non saranno installati su NIO1 prima della primavera del 2017 e quindi nessuna conferma sperimentale che evidenzi i miglioramenti effettivi, sono disponibili al momento.

Per quanto riguarda il presente lavoro di tesi, esso è costituito da cinque capitoli principali, seguiti da una conclusione finale. Segue ora una breve presentazione dei contenuti dei vari capitoli.

Nel primo capitolo presento un'introduzione sulla Fusione e ITER, evidenziando la necessità dell'uso d'iniettori di neutri nelle future centrali a fusione e le questioni generali relative a MITICA, che è il prototipo a dimensioni reali dell'iniettore di neutri di ITER.

Nel secondo capitolo vi è una descrizione generale delle considerazioni teoriche relative a: fisica del plasma in sorgente, estrazione del fascio e la sua ottica. La parte finale del capitolo è dedicata alla presentazione degli strumenti numerici disponibili presso il Consorzio RFX: SLACCAD, EAMCC, COMSOL e OPERA. Per quanto riguarda quest'ultimo, essendo lo strumento numerico più adoperato durante il mio dottorato, presento più in dettaglio le sue potenzialità, sostenute anche uno studio di sensibilità, al fine di aumentare la precisione di calcolo.

Mentre i primi due capitoli hanno scopi essenzialmente introduttivi, gli ultimi tre presentano le attività da me effettivamente svolte sulle tre sorgenti di SPIDER, NITS e NIO1, come brevemente descritto finora. In particolare ciascuno dei tre capitoli è focalizzato sull'attività fatta su una delle macchine.

Infine, due appendici relative a ulteriori attività, che sono connesse al resto solo in parte, completano questa tesi. Tali appendici trattano: lo sviluppo, in linguaggio Visual Basic, di un'interfaccia grafica per Excel per semplificare l'interazione con il database di NIO1 (Appendice A); lo studio dell'efficienza del sistema di recupero di energia degli ioni non neutralizzati, che sarà utilizzato su NIO1 in futuro, attività svolta in collaborazione con l'Istituto CNR di Bari (Appendice B).

1 Introduction

In this introductive chapter the background and motivations of this PhD thesis will be presented, by starting from the global energy scenario, introducing nuclear fusion and ITER, and arriving to Neutral Beam Injectors and negative ion accelerators.

1.1 The World Energy Problem

In this section the world energy scenario will be briefly presented. Figure 1.1, taken from [1], shows the world energy consumption by fuel and gives us two important information: first, the world energy consumption is constantly increasing and is today more than the triple of fifty years ago. This is due to the increase of global population and to the rapid development of big countries like China and India.

The second information is that 85% of the consumed energy comes from fossil fuels, i.e. coal, oil and natural gas. This fact has in turn other two important consequences.

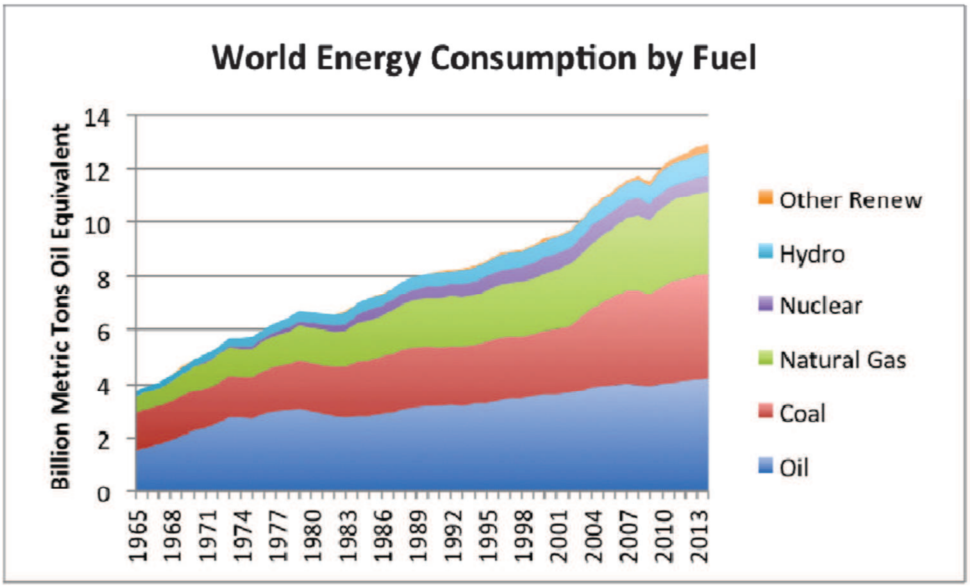

Figure 1.1: World energy consumption by fuel

The first consequence is that, since fossil fuels are practically non-renewable, their global reserve is going to deplete, soon or later. The second and more important consequence regards the greenhouse gas emission into the atmosphere and it's immediately clear if looking at **Figure 1.2**, taken from [[**2**]. This figure shows the greenhouse gas emission by fuel (averaged on twenty different studies on this subject), and shows how the consumption of fossil fuels generates high levels of greenhouse gas with respect to hydroelectric, renewable, and nuclear energy.

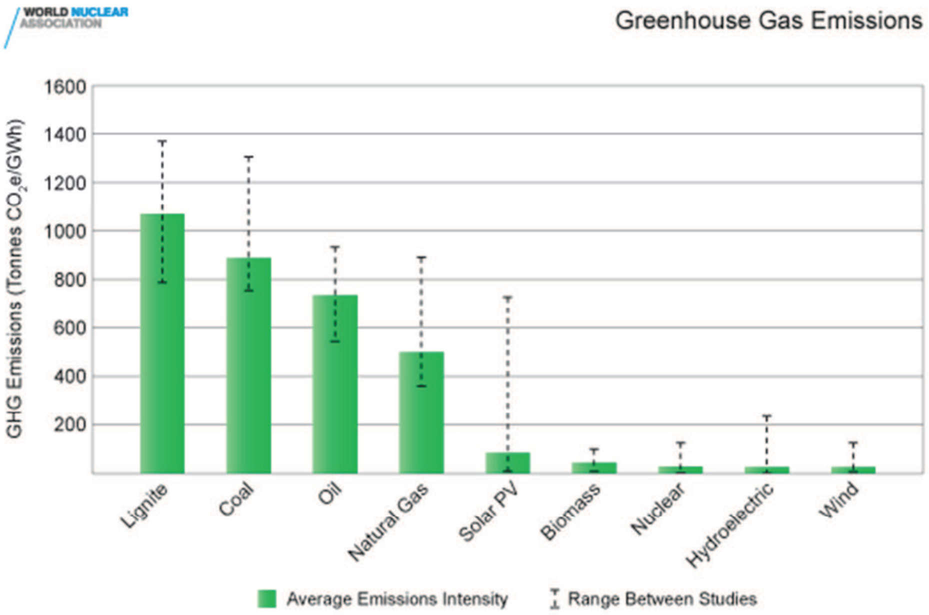

Figure 1.2: Greenhouse gas emission by fuel.

Figure 1.3, taken from [[**3**], shows the annual anthropogenic greenhouse emission by sector. The power generation sector is the one that more contributes to the total, with more than 20% of the annual word greenhouse gas emission. Strongly reducing this contribute, together with the contribution from fossil fuel retrieval, processing and distribution, and part of the transportation fuels, the global greenhouse gas emission could be reduced by approximately 40%.

Now, greenhouse gas is mostly constituted by carbon dioxide (72%, see [[**4**]), that is also more persistent in the atmosphere with respect to Methane and Nitrous oxide, the other two major contributors. A study made in [[**5**] estimates that the natural Earth carbon cycle is able to absorb about half of the anthropogenic carbon dioxide emitted per year, while the other half is accumulated in the atmosphere, where it persists for hundreds years, causing global warming with a series of adverse effects.

So, an energy scenario where consumption of fossil fuels is largely reduced could be almost compatible with the Earth natural carbon dioxide absorption, solving in turn the problem of anthropogenic global warming.

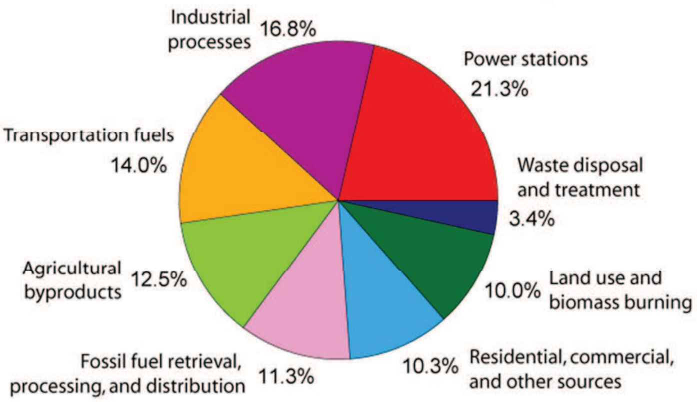

Figure 1.3: Annual anthropogenic greenhouse gas emission by sector.

Among the energies with low greenhouse gas emission there are the renewable, hydroelectric and nuclear. The first two are unfortunately unable to meet the global energy demand, due to their limited and not well space and time distributed power density, so, only nuclear power is left at present day options. Nuclear power is subdivided into nuclear fission and nuclear fusion, but at present day only the first one is available. Nuclear fission, despite being "clean" from the greenhouse gas point of view, has its non-negligible drawbacks, like the risk of serious accidents, the problem of wastes, and the limited global amount of nuclear fission fuels.

Nuclear fusion, on the other hand, has no problem of depletion of fuels (Deuterium, extremely abundant, and Tritium, which can be produced), it's intrinsically much safer than nuclear fission and the problem of waste is much easier to treat. In conclusion, nuclear fusion could be the answer to the world energy problem, being its fuel practically infinite, its power density enough to satisfy the global energy demand and its environmental impact very limited.

1.2 Thermonuclear Fusion

Nuclear fusion is a nuclear reaction in which atomic nuclei collide at a very high energy and fuse together to form a new nucleus. In this process, some matter is not conserved and is directly transformed into energy according to the Einstein relation. This process, naturally happening in stars, can be reproduced and exploited to produce energy, but there are important difficulties to overcome:

1) Very high energy is required for the reactants to fuse. **Figure 1.4** shows the cross-section of the three most relevant fusion reactions from the point of view of energy production on Earth, reported below, involving Deuterium (D or H^2), Tritium (T or H^3), Helium (He^4) and its isotope He^3.

$D - T$ reaction:

$$H^2 + H^3 \rightarrow He^4 (3.52\ \mathrm{MeV}) + n\ (14.06\ \mathrm{MeV})$$

$D - D$ reaction, which have two branches 50% probability each:

$$H^2 + H^2 \rightarrow He^3\ (0.82\ \mathrm{MeV}) + n\ (2.45\ \mathrm{MeV})$$
$$H^2 + H^2 \rightarrow He^3\ (1.01\ \mathrm{MeV}) + p\ (3.03\ \mathrm{MeV})$$

$D - He^3$ reaction:

$$H^2 + He^3 \rightarrow He^4\ (3.67\ \mathrm{MeV}\ ) + p\ (14.67\ \mathrm{MeV})$$

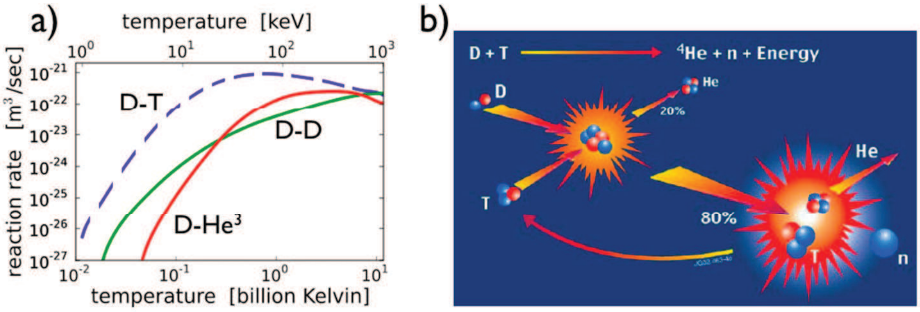

Figure 1.4: a) cross section of some fusion reaction. The reaction involving deuterium and tritium (dashed) is the most convenient. b) Schematic of the reaction 1.2.

From **Figure 1.4** it appears that the $D - T$ reaction has the highest reaction rate peak, which corresponds also to a lower energy with respect to the peaks of the $D - D$ and the $D - He^3$ reactions. Anyway, the necessary energy for achieving the highest $D - T$ reaction cross- section is still ~10 keV, corresponding to ~100 million Kelvin. At this temperature, the matter is at the state of plasma.

2) The second problem is the confinement of plasma with such a high energy. Inside the stars, the confinement is provided by the gravity, while on Earth two main methods are under research and development:

- Magnetic confinement fusion (see [[**5**]), in which the hot plasma is confined by strong magnetic fields;
- Inertial confinement fusion (see [[**6**]), in which the confinement of

a small volume of solid matter is achieved by the action of high power focused lasers that heats up the matter to critical conditions.

In this thesis, inertial confinement will not be threated.

Analysing Magnetic confinement fusion in more details, this technology exploits strong magnetic fields to confine the hot $\mathrm{D-T}$ plasma contained in the reaction chamber. This approach is more developed with respect to inertial confinement fusion, and more promising. There are two main kind of device able to achieve magnetic confinement fusion, the stellarators (see [[**7**]), and the tokamaks (see [[**8**]).

In this thesis, only the tokamaks are considered. The word tokamak comes from a Russian acronym meaning Toroidal Chamber with Magnetic Coils, in fact, a tokamak consists of a torus shaped vacuum chamber with two sets of coils, the toroidal magnetic field coils and the poloidal magnetic field coils, as shown in **Figure 1.5**.

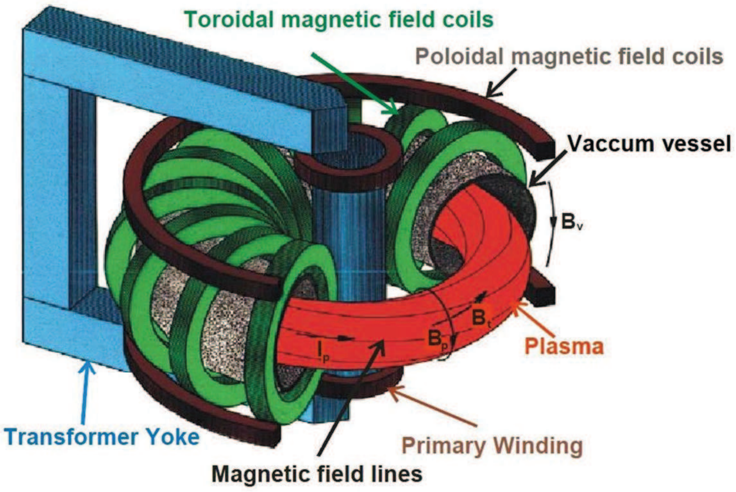

Figure 1.5: Principle scheme of a tokamack.

The combination of toroidal and poloidal magnetic field, confines the plasma inside the vacuum vessel, following helical lines. The transformers induce a current flowing into the plasma, which generates the confinement poloidal magnetic field. The poloidal magnetic field coils are used to produce additional poloidal field for plasma shaping and stabilization.

Fusion $\mathrm{D-T}$ reaction happens in the confined plasma and release energetic Helium and neutrons. The neutrons are not affected by magnetic field so the travels across the plasma and impinge on the vessel wall, releasing their energy, that can be gathered and used as hot source for producing electric energy in the traditional way. Produced Helium, on the contrary, is suddenly ionized (becoming α-particles) and releases its energy to the $D - T$ plasma.

If the plasma density, temperature and confinement time are high enough, the α-particles heating alone is enough to sustain the fusion reaction. In this case is said that the reactor has reached the ignition. The ignition condition is usually expressed using the following figure of merit, called triple product:

$$n\tau_E T \geq 3 \cdot 10^{21} [m^{-3} keV\ s]$$

where n is the plasma density, τ_E the energy confinement time and T the plasma temperature. Ignition has not been reached so far by any of the existing tokamaks and is one of the main goals on the future tokamak ITER, described in the next section.

Figure 1.6 shows the values of the triple product reached by various tokamaks since the beginning of fusion research. The next step is represented by ITER, which is designed to reach the ignition.

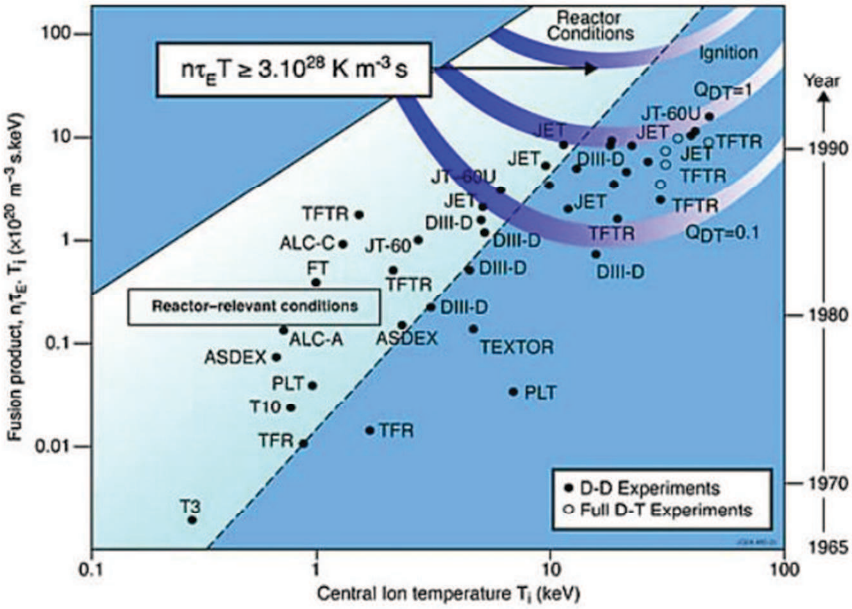

Figure 1.6: Values of triple product as a function of ion temperature for the existing tokamaks operating with D-T or D-D reactions.

In all the present tokamaks and also in a future reaction before reaching the ignition point, additional heating systems are required to maintain the fusion reactions. Another important figure of merit of a tokamak is the power amplification factor Q, defined as the ratio between the fusion power and the additional heating power.

1.2.1 ITER

ITER is an international nuclear fusion project, which will be the world's largest tokamak and nuclear fusion experiment. ITER is under construction in France, near Cadarache, and its members are European Union, United States, Russia, Japan, China, India and South Korea, for a total cost of about 15 billion dollars. The main goals of ITER are:

- To momentarily produce ten times more thermal energy from fusion heating than is supplied by auxiliary heating ($Q = 10$);
- To produce a steady-state plasma with non-inductive plasma current and ($Q > 5$);
- To maintain a fusion pulse for up to 480 seconds;
- To develop technologies and processes needed for a fusion power plant (advanced materials, superconducting magnets, remote handling,...);
- To verify tritium breeding concepts;
- To refine neutron shield/heat conversion technology.

The main ITER parameters are summarized in **Table 1.1**.

Table 1.1: Main ITER parameters overview

ITER parameters		
Fusion Power	500	[MW]
Q factor	>10	
Major radius	6.2	[m]
Minor Radius	2	[m]
Machine height	26	[m]
Machine diameter	29	[m]
Plasma volume	837	[m^{3}]
Toroidal field	5.3	[T]
Plasma current	15	[MA]
Pulse duration	480	[s]

A rendering of ITER is given in **Figure 1.7**. For more information about ITER, see [[**9**].

1.2.2 Auxiliari Heating and Current Drive

As mentioned in section 1.2, except in the case of ignition, auxiliary heating is necessary to compensate the power losses and keep the fusion plasma at the required temperature. Moreover, electric current flowing through the plasma is fundamental for plasma confinement (see again section 1.2), and must be kept at the required level as well.

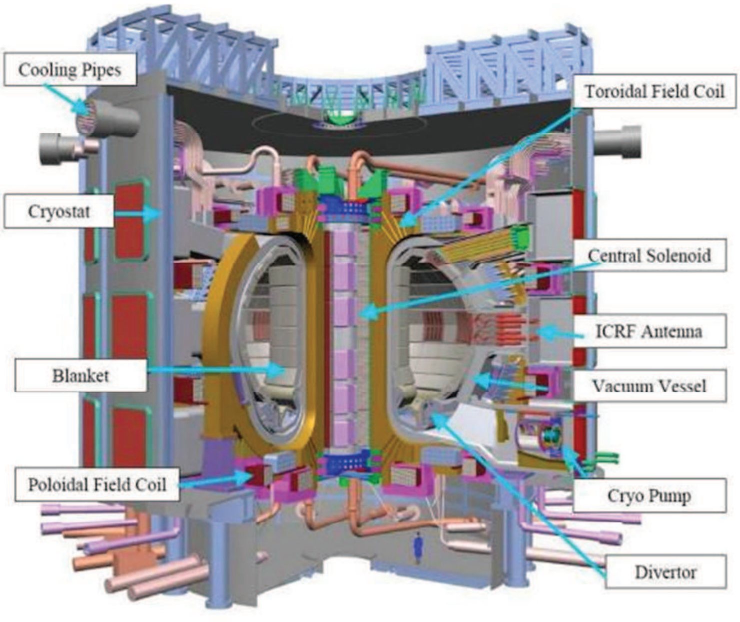

Figure 1.7: Schematic view of ITER

For this reason, several Heating and Current Drive systems have been developed and play a very important role in a tokamak. Initially, a current is induced in the plasma exploiting the principle of the transformer (see **Figure 1.5**), but this system can be adopted only in a transient phase.

Similarly, the initial plasma heating is rather simple to obtain, exploiting the ohmic heating due to the plasma current, according to $P_{ohm} \propto I_P^2 R_P$, being P_{ohm} the power produced, I_P the plasma current and $R_P$the plasma resistance. Unfortunately, above certain plasma temperature, about 2 keV, $R_P$decreases and ohmic heating is not effective anymore. To further increase the plasma temperature and to maintain and control the plasma current, two different strategies are adopted:

- Radiofrequency Heating and Current Drive;
- Neutral Beam Injection (NBI).

The first strategy exploits microwaves with a frequency equal to charged particles oscillation frequency, in order to transfer energy to ions or electrons which in turn heat up all the plasma by collisions. The second strategy consists on firing an energetic beam of neutral particles, which transfer their energy and momentum to the plasma.

With both the strategies is possible to perform both plasma heating and current drive. **Figure 1.8** shows a scheme of Heating and Current Drive systems used in tokamaks but also in stellarators.

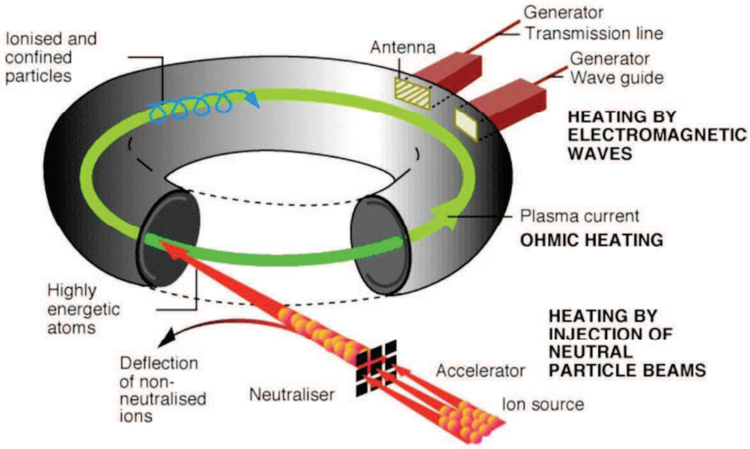

Figure 1.8: Scheme of Heating and Current Drive systems used in magnetic confinement fusion.

This thesis will focus on Neutral Beam Injection systems only, whose principles are explained in the next section.

1.3 Neutral Beam Injector

As mentioned, a Neutral Beam Injector (NBI) is a device able to produce an accelerated beam of neutral particles with the purpose of heating and driving current in fusion plasma. The beam must be neutral; otherwise it would be deflected by the strong magnetic fields produced by the tokamak coils.

Neutral particles are not subjected to electric or magnetic field, so the beam has to be initially constituted by charged particles, positive or negative, which are then electrostatically accelerated and then neutralized before entering the tokamak vessel. Once inside the hot plasma, the neutral particles are ionized and release their energy and momentum through collisions. One important fact is that the penetration distance inside the plasma is proportional to the beam energy, and so, the proper beam energy has to be chosen in order to deposit the beam power in the plasma center, without losing it in the plasma edge. This fact is very important in the case of large plasma volumes, as in ITER, because in this case the optimal beam energy can be very high, with consequent complications in NBI operation (voltage holding, heat loads on NBI components, overall efficiency).

Depending on beam energy, there is also the choice between positive or negative ions, as shown in **Figure 1.9**. Positive ions are in fact much easier to produce but their neutralization efficiency becomes very low for beam energies higher than 100 keV for Deuterium and 40 keV for Hydrogen. In ITER, for example, the plasma volume is very large, so a beam energy of 1 MeV is required and the use of negative ions is a mandatory choice.

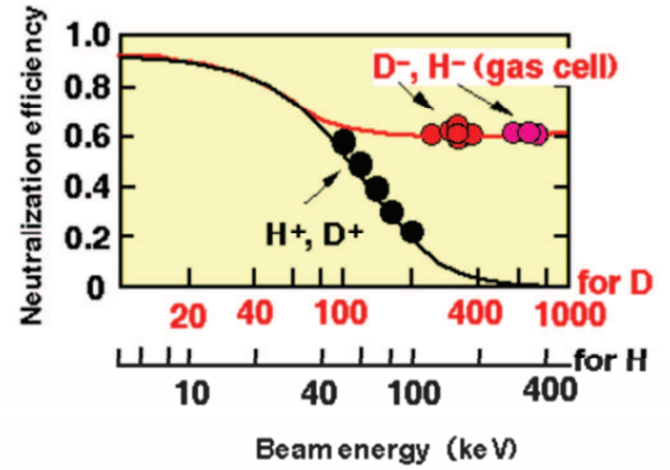

Figure 1.9: Neutralization efficiency as a function of beam energy, for positive and negative Hydrogen and Deuterium ions.

Two NBIs are foreseen in ITER, each one having beam energy of 1 MeV and beam power of 17 MW.

1.3.1 The Padua Neutral Beam Test Facility

The Padua Neutral Beam Test Facility (NBTF) is an ITER test stand in Padua, in the area of National Research Council, with the purpose of realizing the full-scale prototype of ITER NBI (see [[**10**]). The NBTF is composed by PRIMA (Padua Research on ITER Megavolt Accelerator), the facility that will host the experiments, SPIDER (Source for the Production of Ions of Deuterium Extracted from an RF plasma), an ITER full scale RF negative ions source test bed, and MITICA (Megavolt ITER Injector and Concept Advancement), the final full scale, full performance prototype of the Heating Neutral Beams (HNB) for ITER.

The facility PRIMA is now completed (see **Figure 1.10**), the experiment SPIDER is under construction, while MITICA is in the last stages of its design.

Figure 1.10: Areal view of PRIMA facility in Padova.

MITICA (see [[**11**]) is the full-scale prototype of ITER Heating Neutral Beams (HNB, see [[**12**]) and it has been designed at Consorzio RFX in the framework of NBTF project. **Figure 1.11** shows a sketch of MITICA and its components. MITICA is constituted by an RF negative ion source, an accelerator, a neutralizer, an electrostatic residual ion dump for deflecting the non-neutralized particles and a calorimeter for diagnostic purposes. The total length of the device is more than 20 meters.

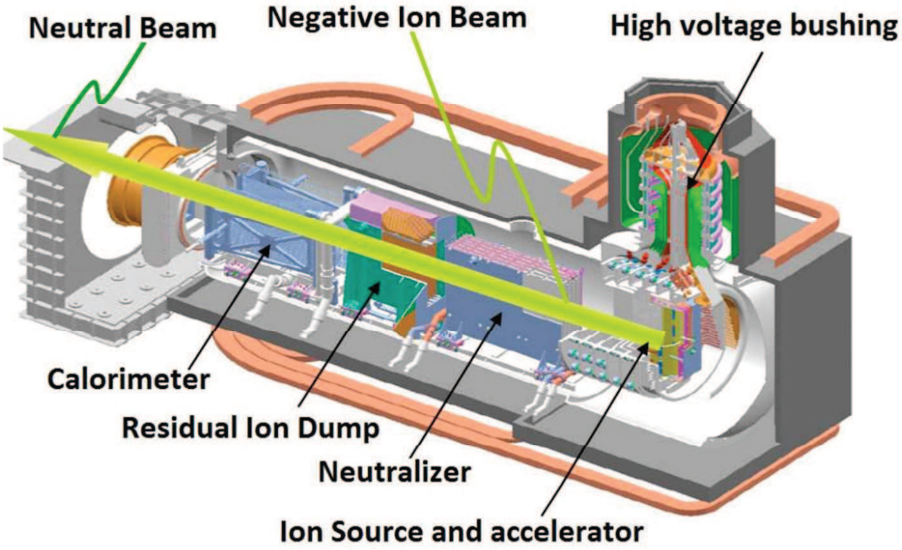

Figure 1.11: Sketch of MITICA

The main MITICA parameters are summarized in **Table 1.2**.

Table 1.2: Main MITICA parameters

MITICA parameters			
Ion species	D	H	
Beam energy	1	1	MeV
Beam power	17	17	MW
Pulse lenght	3600	3600	s
Acceleration Current	40	60	A
Extracted current density	285	355	A/m2
Extracted electron to ion ratio	1	0.5	
Source pressure	0.3	0.3	Pa

MITICA will be not a topic afforded in this thesis. Therefore, just a brief description of the device is provided.

For what concerns the ion source, it is similar to SPIDER and it will be described in detail in chapter 4. The accelerator, instead, differs on the numbers of accelerating grids, but share the same beamlet arrangement.

MITICA accelerator is constituted by seven copper grids, each one made of four parts called grid segments with 1280 apertures in total, divided in 16 beam groups 16x5. The first electrode is the Plasma Grid (PG), which is a molybdenum-coated copper plate. This grid faces the Ion source and is kept at the electric potential of -1 MV. The second grid is the Extraction Grid (EG), biased at about -991 kV, which has the purpose of shaping the electric potential so that 1280 well-focused ion beamlets are produced and extracted from the source through the PG. The EG also includes permanent magnets which produce a magnetic field for deflecting the electrons that are extracted together with the negative ions (co-extracted electrons). Downstream of the EG, there are the four Acceleration Grids (AG1 – AG4) and the Grounded Grid GG, which have a potential of -800, -600, -400, -200 and 0kV, respectively, and accelerate the negative ions at the required energy of 1 MeV.

The other components of the beam line, which are not present in SPIDER as it is not a full NBI, are: the neutraliser and electron dump (NED), divided into 4 vertical channels constituting the gas cells with the function to neutralize negative ions stopping the unwanted electrons exiting the source with steered trajectories; the electrostatic residual ion dump (ERID) divided into 4 channels in which an electric field deflects the partially positive and partially negative residual ions; the calorimeter located downstream the RID and constituted by two panels, in a V shape, of 96 tubes each parallel to the beam. The neutral power dumped onto the calorimeter can be measured, and in the ITER NBI, the V calorimeter will open and the deuterium beam of 16.5 MW power will travel the duct until the ITER plasma. Cryopumps are placed on each side of the beam path and the beamline components to reduce to the minimum the pressure of the background gas. Pressure downstream the accelerator must be low in order to minimize losses in the accelerator. The pressure downstream of the neutralizer must be also low in order to minimize re-ionization of D^0.

2 Plasma Ion Source and Beam Extraction

As the NBI foreseen for ITER [[**13**] and the other negative ions source threated in this thesis make use of plasma source, in this chapter the principles of plasma ion sources and beam extraction process will be explained. The basic theory of negative ion formation mechanism inside the plasma, plasma behaviour inside the source and beam optics related issues will be also presented. It is also appropriate to introduce the reader to plasma state of matter.

2.1 What is a plasma

In physics and chemistry, plasma is a state of matter similar to gas in which particles are ionized. By Heating a gas, it may ionize its molecules or atoms (reduce the number of electrons in the electron cloud), thus turning it into plasma, which contains charged particles: positive ions and negative electrons. Ionization can be induced also by other means, such as strong electromagnetic field applied with lasers, micro wave generator, or, as presented in the next section, arc discharges and RF coupling. Ionization is also accompanied by the dissociation of molecular bonds when dealing with molecular gasses, like hydrogen and oxygen. More generally, plasmas are generated by supplying energy to a neutral gas causing the formation of charge carriers. These charge carriers make the plasma electrically conductive so that it responds strongly to electromagnetic fields. Plasma, therefore, has properties quite unlike those of solids, liquids, or gases and is considered a distinct state of matter. Like gas, plasma does not have a definite shape or a definite volume unless enclosed in a container; unlike gas, plasma is conductive and thus, under the influence of magnetic or electric fields, it may form structures such as filaments (like the ones in our Sun) or ion beams. Plasmas are commonly found where the temperature is high enough to keep a gas ionized, as in stars and it is actually the most common state of matter in the universe. On earth, plasma can be found in lightings, fluorescent lamps and neon signs. It is also used in industries for semiconductors processing or materials modifications.

For a better understanding of plasma matter, in the next sections the most characterizing plasma features that set plasmas apart from normal fluids are presented in details.

2.2 Plasma parameters

Plasma is a gas characterized by a high ionization degree. Therefore, it is formed by ions, electrons and possibly un-ionized neutrals. For this reason, usually one refers to ions density $\mathrm{n_i}$, electron density $\mathrm{n_e}$ and neutral density $\mathrm{n_n}$. In particular, for singly ionized plasma, like hydrogen or deuterium plasma, the equality $\mathrm{n_e} \cong \mathrm{n_i}$ holds, which also suggest the fundamental plasma property of quasi-neutrality. This property will be presented in more detail in next section.

The energy of the plasma can be described by its temperature, which is commonly expressed in electron Volts ($1eV = 11600\ K$). As for density, also here one refers to electron T_e and ion T_i temperature. Unlike for the densities these two temperatures are not necessarily the same: electrons and ions react differently to external fields, due to their mass difference. Typical temperatures inside an ion source are $T_i{\sim}1\text{eV}$ and T_e several eV and usually one refers to as cold plasma. Figure 2.1 shows typical temperature and density ranges of different plasmas.

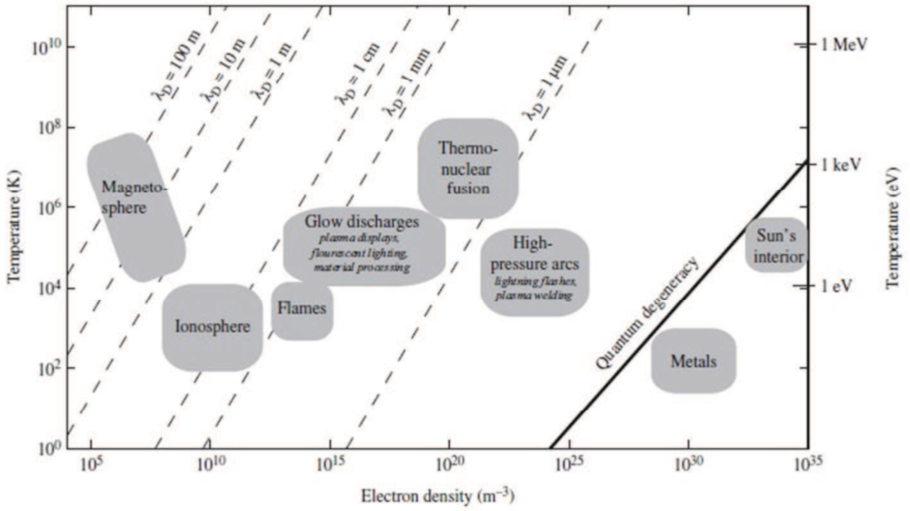

Figure 2.1: Temperature-density plasma map [[5].

When plasma is in thermal equilibrium, ions and electrons motion can be expressed in terms of Maxwellian distribution function:

$$f\left(v_x, v_y, v_z\right) = n\left(\frac{m}{2\pi k_B T}\right)^{3/2} exp^{-mv/2k_BT} \quad 2.1$$

with m mass of the particle and k_B is the Boltzman constant. This functions define the number of particles in a given velocity interval. Thus, by extending it to the entire velocity volume it is possible to obtain the total distribution function of speed:

$$F(v) = 4\pi v^2 n \left(\frac{m}{2\pi k_B T}\right)^{3/2} exp^{-mv/2k_B T} \qquad 2.2$$

and by deriving it with respect to the energy ($E = 1/2\, m\boldsymbol{v}^2$) also the distribution function of the energy can be found:

$$f(E) = n\sqrt{\frac{4E}{\pi}}(k_B T)^{-3/2} exp^{-E/k_B T} \qquad 2.3$$

From equations 2.2 and 2.3 it is possible to retrieve the mean particle speed and energy, respectively:

$$\bar{v} = \sqrt{\frac{8k_B T}{\pi m}} \qquad 2.4$$

$$\bar{E} = \frac{3}{2}k_B T \qquad 2.5$$

2.3 Plasma properties

As said before, plasma state of matter has a high degree of ionization that gives it the feature of electrical conductivity and therefore it reacts when an external field is applied. As consequence of these plasma features the following important plasma properties derive:

- Quasi-neutrality
- Debye shielding
- Particle motion under external fields

2.3.1 Quasi-neutrality

The most important feature of a plasma is the quasi-neutrality:

$$-\mathrm{q_e n_e} = \mathrm{q_i n_i} \pm \Delta \qquad 2.6$$

where q_e and, q_i are the charges of electrons and ions respectively. This plasma property means that plasmas have the capability to maintain the status of electrical neutrality. plasmas balance positive and negative charges in such a way that $n_e \sim n_i$ in any macroscopic volume element. Any local charge unbalance gives rise to an electrostatic force that tries to restore neutrality. This feature comes from the high ratio q_e/m_e.

Let's consider plasma in perfect charge neutrality and that thermal motion of its particles can be neglected (cold plasma condition). If suddenly a perturbation generates a local charge separation, creating a positive and a negative region within the plasma, this charge separation generates an electric field. This field tries to restore the neutrality by acting both on electrons and ions, but being the latter at least two thousand times more massive than electrons, it is possible to assume that ions motion can be neglected with respect to electron motion. Anyway, due to their inertia, electrons start to oscillate around the positive ion region.

In the one-dimensional case of one electron of mass m_e and charge q_e inside an electric field E_x directed along the x direction, the equation of motion of the electron is

$$m_e \frac{d^2x}{dt^2} = q_e E_x \qquad 2.7$$

while

$$E_x = -x n_e q_e \varepsilon_0 \qquad 2.8$$

being n_e the electron density. Upon substitution it becomes:

$$\frac{d^2x}{dt^2} = -\omega_p^2 x \quad 2.9$$

where ω_p is the plasma frequency defined as:

$$\boldsymbol{\omega_p = \sqrt{\frac{n_e q_e^2}{m_e \varepsilon_0}}} \qquad 2.10$$

This means that every perturbation in the plasma causes electron oscillations with frequency ω_p . Furthermore, these oscillations are localized around the charge-unbalanced region and propagate within the plasma due to collisions. Collisions are extremely important in plasmas: electron oscillations with frequency ω_p can exist only if the average time

τ_c among collisions is long enough. That means

$$\boldsymbol{\tau_c > \frac{1}{\omega_p}} \qquad 2.11$$

Plasma neutrality is then preserved on a time scale of about ω_p^{-1}.

2.3.2 Debye shielding

Being a conductor, when an external electric field is applied to a plasma, its charged particles rearrange so as to shield this field. This is the second main plasma feature: the Debye shielding. If we insert a test charge $+Q$ in a neutral plasma, this generates an electrical potential

$$\phi(r) = \frac{1}{4\pi\varepsilon_0}\frac{Q}{r} \qquad 2.12$$

Ions are repelled by this test charge while electrons are attracted. They then modify their distribution to find a new equilibrium condition taking care of the new charged particle. As $m_i \gg m_e$, ion motion can be neglected, meaning that their density n_i does not vary in time. Electron desity n_e, instead, increases around the test charge. The new electron density distribution around the test charge is (Boltzman density distribution):

$$n_e(r) = n_{e0}\exp^{-q_e\phi(r)/k_B T_e} \qquad 2.13$$

with n_{e0} the initial electron density at equilibrium, k_B the Boltzman constant and T_e the electron temperature in the plasma. This equation exhibits two important features: electron density will be higher where the potential ϕ is higher, that means close to the test charge and density variation is steeper for low T_e values, i.e. in cold plasmas.

ner=ne0exp−qeϕrkBTe **2.13** into the Poisson equation

$$\nabla^2\phi(r) = -\frac{\varrho}{\varepsilon_0} = -\frac{q_e(n_e - n_i)}{\varepsilon_0} \qquad 2.14$$

where $\varrho = q_e(n_e - n_i)$ is the exceeding free charge and solving for ϕ, the expression for the electrical potential inside a plasma is obtained:

$$\phi(r) = \left(\frac{1}{4\pi\varepsilon_0}\frac{Q}{r}\right)\exp^{-\frac{r}{\lambda_D}} \qquad 2.15$$

where λ_D is the Debeye length, defined as:

$$\lambda_D = \sqrt{\frac{\varepsilon_0 k_B T_e}{n_{e0} q_e^2}} \qquad 2.16$$

For $r \rightarrow 0$, the electrical potential returns to be the one for a free charge in space, while for $r \gg \lambda_D$, it goes to zero. This means that if in free space Coulomb force has infinite radius, in plasmas it acts only within a Debeye length λ_D. Furthermore λ_D increases with T_e due to thermal motion and decreases with n_{e0}, as there are more electrons available.

In an ion source, typically $\lambda_D \sim 10^{-4}$; as the source dimensions $L \gg \lambda_D$ the plasma bulk inside an ion source is completely shielded from the external fields. Coulomb interactions inside the plasma are then limited.

Being λ_D dependent on charged particle density, an ionized gas, in order to be considered as plasma, must to have enough charged particles inside a sphere with radius λ_D. It is possible to define the plasma parameter Λ as:

$$\Lambda = n_0 \frac{4}{3} \pi \lambda_D^3 \gg 1 \qquad 2.17$$

An ionized gas has to fulfil also this requirement to be considered plasma.

Summarizing, main conditions that define a plasma are:

$$\tau_n > \omega_p^{-1}$$
$$L \gg \lambda_D$$
$$\Lambda \gg 1$$

that is: plasma oscillations have to be more frequent than collisions, its dimensions must be much larger than the Debye length and its density must be high enough to guarantee the third requirement.

2.3.2.1 Plasma sheath

A direct consequence of the Debye shielding is the plasma sheath. When plasma interacts with the confinement boundaries, like the ion source walls, a sheath layer is formed. During this interaction, ions and electrons recombine with the walls. Assuming the case of collision-less plasma, as electrons are less massive than ions, and therefore faster, recombination process rate is higher for electrons. This means that the plasma develops a higher potential with respect to the walls.

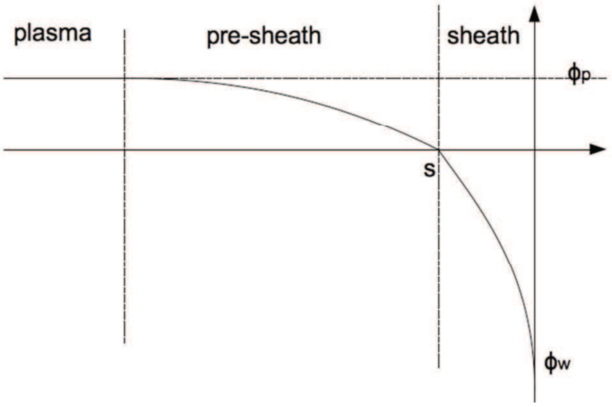

Figure 2.2: Plasma potential close to the wall of the container. The potential drop next to the wall is consequence of the sheath and the plasma bulk have an higher potential with respect to the edge. Quasi neutrality is not respected in the sheath region.

With reference to Figure 2.2, it is possible to say that the electrostatic potential of the boundary joins smoothly to the interior plasma potential. This boundary potential can be written as [[**28**]:

$$\phi_{\mathrm{sheath}}(\mathrm{x}) = \phi_{\mathrm{wall}} \mathrm{e}^{-\frac{\mathrm{x}}{\lambda_{\mathrm{D}}}} \qquad 2.18$$

where

$$\lambda_{\mathrm{D}} = \sqrt{\frac{\varepsilon_0 \mathrm{k_B T_e}}{ne^2}} \qquad 2.19$$

is again the Debye length. $\boldsymbol{\lambda_D}$ is then a measure of the shielding distance or thickness of the sheath. It depends on the inverse of the plasma density and thus as expected, since each layer of plasma contains more electrons. Indeed, it is the electron temperature which is used in the definition of the Debye length because the electrons, being more mobile than the ions, generally do the shielding by moving so as to create a surplus or deficit of negative charge.

In practice, a potential gradient is formed close to the walls. Its effect is to reflect back electrons coming from the plasma bulk, preventing them from reaching the walls, while it accelerates ions toward the boundary. Electron motion towards the walls is then slowed down and when equilibrium is reached, equal electron and ion fluxes reach the walls . As the Debye shielding prevents the potential gradient from developing deeply into the plasma, keeping it within a layer several Debye lengths thick, this layer is called plasma sheath. Inside sheath region plasma neutrality is not preserved.

In conclusion, the formation of the sheath can be seen as the tendency of the plasma to shield external static electric fields from its interior, like any good electrical conductor.

2.3.3 Particle Motion under External Fields

As said before, being a conductive medium, the plasma reacts to external electric and magnetic fields. Therefore, it is also important to know how these fields influence charged particle motion in the plasma. Mainly, the plasma acts like a fluid and collective interactions are predominant on single particle interactions. Anyway, this is not completely true because it depends on particle density. Plasmas in ion sources have a density range that sets in an intermediate range with respect to high-density fluids and very low-density systems, like particle beams in accelerators. This means that single particle motion cannot be completely neglected. Thus, now the main equations that describe single particle motion within the plasma are presented in order to give a better understanding …

Particles moving in plasma sources are subjected both to electric field $\boldsymbol{E}$ and magnetic fields $\boldsymbol{B}$ (Lorentz Force), so that the equation of motion will be:

$$\boldsymbol{m}\frac{\boldsymbol{dv}}{\boldsymbol{dt}} = \boldsymbol{F_{Lorentz}} = \boldsymbol{q}(\boldsymbol{E} + \boldsymbol{v} \times \boldsymbol{B}) \quad 2.20$$

with m, q and v mass, charge and velocity of the particle.

Now, let's consider a single a charged particle moving inside the plasma and suppose that B is directed along z-axis and investigate several cases. By considering the case of no electric field and homogenous magnetic field, i.e. $E = 0$ and $\partial_t B = 0$, the equation of motion becomes:

$$\boldsymbol{m}\frac{\boldsymbol{dv}}{\boldsymbol{dt}} = \boldsymbol{F_{Lorentz}} = \boldsymbol{q}(\boldsymbol{v} \times \boldsymbol{B}) \qquad 2.21$$

The term $v \times B$ suggest that the particle undergoes a force that is perpendicular to the plane defined by v and B. Thus, by decomposing the particle velocity in two components, one perpendicular to and one along with respect to B_z, it is possible to obtain from equation $\boldsymbol{m}\frac{\boldsymbol{dv}}{\boldsymbol{dt}} = \boldsymbol{F_{Lorentz}} = \boldsymbol{q}(\boldsymbol{v} \times \boldsymbol{B})$ **2.21** in this case:

$$\boldsymbol{v_x} = \boldsymbol{v_\perp}\, \boldsymbol{cos}(\boldsymbol{\omega_c t} + \boldsymbol{\varphi}) \quad 2.22$$

$$\boldsymbol{v_y} = \boldsymbol{v_\perp}\, \boldsymbol{sin}(\boldsymbol{\omega_c t} + \boldsymbol{\varphi}) \quad 2.23$$

$$\boldsymbol{v_z = v_\parallel} \qquad 2.24$$

where φ is an arbitrary phase, $v_\perp = \sqrt{v_x^2 + v_y^2}$ is the constant velocity in the plane perpendicular to B and ω_c is the so called cyclotron frequency defined as:

$$\omega_c = \frac{|q|B_z}{m} \qquad 2.25$$

These equations suggest that charged particle motion under homogeneous B_z field is characterized by the combination of a constant motion along field direction and a circular motion, with frequency ω_c, in the direction perpendicular to B_z. Considering that the perpendicular force is balanced by the centrifugal force:

$$\boldsymbol{m\frac{v_\perp^2}{r_L} = qv_\perp B_z} \qquad \mathbf{2.26}$$

it is also possible to calculate the radius of the circular motion, called Larmor radius, as:

$$\boldsymbol{r_L = \frac{mv_\perp}{qB_z} = \frac{v_\perp}{\omega_c}} \qquad \mathbf{2.27}$$

Obviously, Larmor radius is much bigger for ions that electrons, as it depends on the inverse of the square of the particle mass.

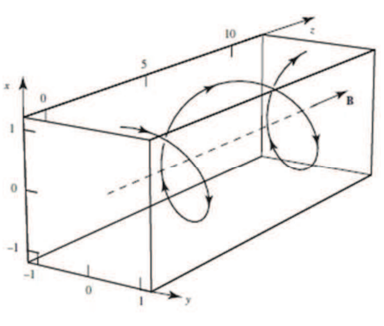

Figure 2.3 Moto di una particella in un campo magnetico uniforme diretto lungo l'asse z . E' evidente la presenza di moto girazionale nei piani perpendicolari a B e di un moto rettilineo uniforme dovuto alla componente di velocità v‖ parallela a B.

When adding also an electric field E, perpendicular to B_z charge particle motion will be characterized by a superimposition of a gyromotion perpendicular to B_z and a drift motion parallel to B_z.

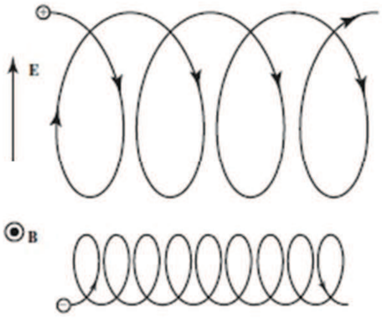

Figure 2.4: Moto complessivo di ioni ed elettroni dovuto alla presenza di un campo magnetico uniforme diretto lungo l'asse z e di un campo elettrico non nullo.

More generally, upon decomposing the electrical field with respect to B_z as $E = E_\perp + E_\parallel$, the equation of motion $\boldsymbol{m}\,\frac{\boldsymbol{dv}}{\boldsymbol{dt}} = \boldsymbol{F_{Lorentz}} = \boldsymbol{q(E + v \times B)}$ **2.20** can be split into:

$$\boldsymbol{m}\frac{\boldsymbol{dv_\parallel}}{\boldsymbol{dt}} = \boldsymbol{qE_\parallel} \quad 2.28$$

and

$$\boldsymbol{m}\frac{\boldsymbol{dv_\perp}}{\boldsymbol{dt}} = \boldsymbol{q(E_\perp + v_\perp \times B_z)} \quad 2.29$$

which show a constant acceleration along B_z direction. Particle velocity can be written as follows:

$$\boldsymbol{v(t) = v_\parallel(t) + v_\perp(t) = v_\parallel(t) + v_{const} + v_{ac}(t)} \quad 2.30$$

where transverse particle velocity was split into a constant and variable part:

$$\boldsymbol{v_\perp(t) = v_{const} + v_{ac}(t)} \qquad 2.31$$

$\boldsymbol{v\perp t=vconst+vact}$ **2.31** in the equation of motion $\boldsymbol{m}\frac{\boldsymbol{dv}}{\boldsymbol{dt}} = \boldsymbol{F_{Lorentz}} = \boldsymbol{q(E + v \times B)}$ **2.20**, one obtains:

$$\boldsymbol{m}\frac{\boldsymbol{dv_{ac}}}{\boldsymbol{dt}} = \boldsymbol{q(E_\perp + v_{cost} \times B_z + v_{ac} \times B_z)} \quad 2.32$$

where the last term is the same we've found in the previous case (with no electric field) and which is responsible for the gyromotion of the particle around the magnetic field. In fact, as it is always possible to choose $\boldsymbol{v_{cost}}$ such as $E_\perp + \boldsymbol{v_{cost}} \times B_z = 0$, the previous result is find again. Anyway it is possible to demonstrate that:

$$\boldsymbol{v_{const}} = \frac{\boldsymbol{E\times B}}{\boldsymbol{B^2}} \quad 2.33$$

It is very important to notice that this constant motion is always perpendicular both to $\boldsymbol{B}$ and $\boldsymbol{E}$ (drift motion) and that it is independent from charge and mass of the particles. For this reason, it is also called ambipolar drift motion.

Summarizing, in the presence of both $\boldsymbol{B}$ and $\boldsymbol{E}$ a charged particle motion is a superimposition of three motions: constant acceleration along **B** field, gyromotion perpendicular to **B** direction with frequency ω_c and radius r_L and a drift motion in the direction perpendicular both to $\boldsymbol{B}$ and $\boldsymbol{E}$. The first two motions are charge and mass dependent, while the last one is not.

As there aren't time varying **B** fields ($\partial_t B = 0$) in ion sources, this case will be not presented. Nevertheless, spatial non-uniformities are present ($\partial_z B_z \neq 0$), meaning that field lines can converge or diverge in different areas of the source. In this case a radial component B_r of the **B** field has to be expected. As a consequence, Lorentz force can be split in F_r and F_z. It is possible to demonstrate that:

$$\boldsymbol{F_z} = -\frac{1}{2}\boldsymbol{m}\frac{\boldsymbol{v_\perp^2}}{\boldsymbol{B}}\frac{\boldsymbol{\partial B_z}}{\boldsymbol{\partial z}} = -\boldsymbol{\mu}\frac{\boldsymbol{\partial B_z}}{\boldsymbol{\partial z}} \quad 2.34$$

12mv⊥2B the magnetic moment. Equation ***Fz=−12mv⊥2B∂Bz∂z=−μ∂Bz∂z*** **2.34** suggests that the more intense B_z, the more the $v_\parallel$ of the particles will be reduced, because energy is being transferred from the parallel to the transverse component with respect to the B field. In case B_z is intense enough, particles are possibly reflected back (magnetic mirror). In an ion source, this can happen in cusped and filter field areas, for plasma confinement (section 2.4.3) and cooling down (section 2.4.6).

This is valid only in a collisionless plasma: if collisions occur with a *ωc=qBzm* **2.25**), no gyromotion can be sustained and thus the effect of the B field will be small with respect to ion or electron transport via collisions ($\tau_c > \omega_c$).

2.4 Plasma ion sources for fusion

An ion source that has to be employed in fusion NBI must provide high negative deuterium current (40A) at low source pressure (0.3Pa). Extracted beam energy has to reach 1MeV energy. These targets will guarantee an efficient heating of the plasma inside the Tokamak and a good current drive [**8**]. Among the many types of ion sources [**14**], RF-driven plasma ion source is the one foreseen for NBI in fusion devices [**15**].

In general plasma negative ion sources are composed by the plasma source, where plasma is generated as a source of ions, and the ion extraction and accelerator system that extracts ions from the source and forms a beam.

For what concerns the ion sources on which this work is focused on and that will be presented in detail later, SPIDER and NIO1 make use of RF sources, while NITS is provided with an arc source. Thus both types will be addressed in this thesis. The following sections, up to 2.5.2.4, were inspired by [14] and [26].

The basic concept behind Arc driven ions source and RF driven ion source is very similar (**Figure 2.5**) and both can be used for extraction of positive or negative ion beams. The main difference consists in the used mechanism to initialize the ionization process (section 2.4.2):

- In arc type source, ionization of the gas is produced by an arc discharge provided by the thermo-emission of a filament (or more than one);
- In RF type source, instead, the RF electric field generated by the antenna forces the electrons to oscillate. The kinetic energy transmitted to the gas eventually strips off more and more electrons, generating the plasma [17].

The use of RF antenna provides the advantage that the source can be operated without short life components like filaments and could also be used with reactive gases, which would corrode the filaments, causing plasma poisoning. Despite its reliability, RF source needs a more complex power supply system: RF signal has to couple with the plasma and a matching box unit is necessary. This aspect will be not discussed herein.

No other type of sources will be presented in this work. For the sake of brevity and because it is also the main element that will be used in negative ion sources during their development, in the following sections of the present chapter, when referring to ions, I will refer actually only to hydrogen. Furthermore, the reader has to keep in mind that hydrogen plasma, as well as deuterium plasma, is not just a pure mixture of e^-, H^+ and H^-, but also H, H_2, H_2^+, H_3^+ are present, in concentrations even higher with respect to H^+ [[**18**]

2.4.1 Principles of arc and RF multi-cusp negative ion sources

In its simplest form a high-current arc ion source consists of a tungsten cathode filament (or more than one) biased with respect to a surrounding anode cylinder (source vessel) closed by an extraction plate opposite the cathode (left hand side of **Figure 2.5**). The extraction plate, generally referred to as the Plasma Grid (PG) as it directly faces plasma, is provided with apertures for ion extraction. The PG is also electrically insulated from the source vessel and can be biased in such a way as to help negative ions reach the extraction apertures.

The same scheme is valid also for RF ion sources by substituting the filament with the RF antenna (right hand side of **Figure 2.5**). Anyway, since neither anode nor cathode is now needed, the source vessel is not playing the anode role anymore. Again the PG can be biased with respect to the source vessel to facilitate the extraction of negative ions.

The source region in which the filaments (or the RF antenna) are located is called driver, while the space between the driver and the extraction area is called expansion region.

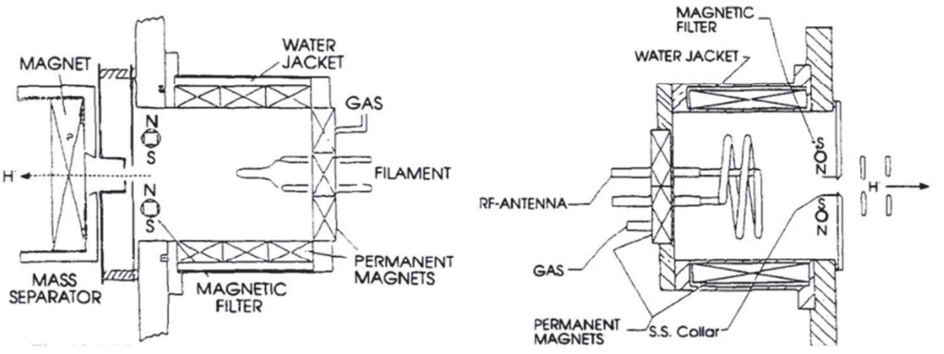

Figure 2.5: Filament plasma ion source (left) and RF plasma ion source (right) concept layout [[14].

2.4.2 Electron Impact Ionization process

Whatever the ion source type, the electron impact ionization process is always involved. The process consists in the bombardment of neutral atoms by free electrons. Neutrals eventually undergo ionization if the colliding electron energy is above the ionization energy threshold.

Therefore the ion source has to transfer enough energy to electrons so that they can ionize neutrals via collision. In turn the new free electrons can absorb energy, increasing the ionization degree of the discharge.

The energy threshold is called ionization potential and indicates the minimum energy needed to remove the outermost electron of the neutral electron cloud, which is ~ 15eV for most gasses. Considering that typical electron temperature inside a source is in the range of $1-10$eV, the ionization process inside the source is due to the high-energy tail of the energy distribution function.

Furthermore, the power transferred to the electrons (whatever technology is used: arc, RF, etc) must be coupled to the discharge inside the source at a sufficient rate to compensate for the numerous energy losses: electron loose energy during the collision process and radiation, interaction of the gas with source walls, as well as loss of charged particles due to recombination with them.

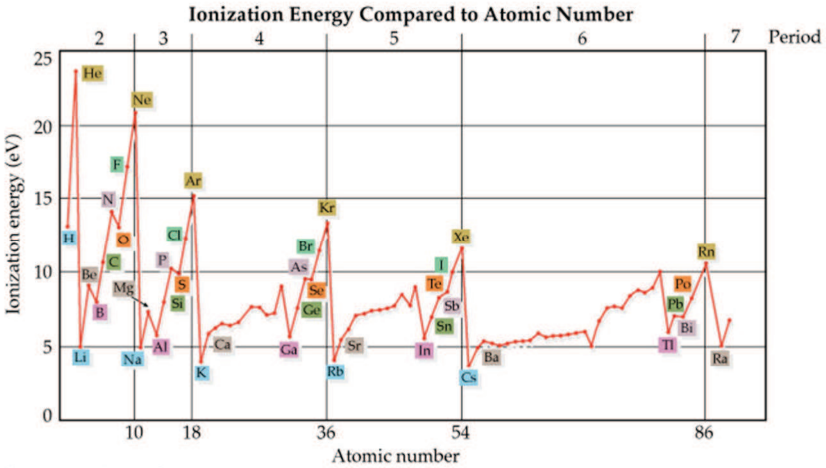

Copyright © 2000 Benjamin/Cummings, an imprint of Addison Wesley Longman, Inc.

Figure 2.6: Ionization potential

2.4.3 RF coupling

In the particular case of an RF ion source optimization of the power transferred to the electrons needs a further component: the matching box, which connects the RF power supply to the RF coil. This box, together with the transmission line and the RF coil, constitutes the primary circuit, which is coupled to the plasma, which, from an electrical point of view is the secondary circuit of a transformer. When the primary circuit transfers power to the secondary, a fraction of the injected power is reflected. Reflected power is, of course, unwanted because it reduces the overall efficiency and can damage the power supply if it is too high. Hence, it has to be minimized by finding the impedance matching condition so that the combined impedance of the circuit and the matching box equals the impedance of the power supply $Z_0 = 50\ \Omega$. This can be achieved by varying the RF frequency and the capacitance of the matching box in correspondence to the variation of plasma parameters, such as gas pressure. A full treatment can be found in [[**16**].

In some devices, like NIO1, when the matching condition is achieved, the coupling between the two circuits is said to pass from capacitive mode to inductive mode. As soon as the inductive coupling is reached, the reflected power abruptly decreases. Also plasma parameters and negative ion production benefit from this transition. I will discuss about this at the end in section 4.2.2

2.4.4 Magnetic confinement

Due to recombination processes, there is always loss of charged particles when the plasma interacts with the source walls. Thus, whatever the ion source configuration, the source vessel is surrounded by permanent magnets with alternating polarity, for plasma confinement. The magnetic confinement process is feasible, because ions and electrons in the plasma are tied during their orbital motion to the magnetic field lines provided by the magnets.

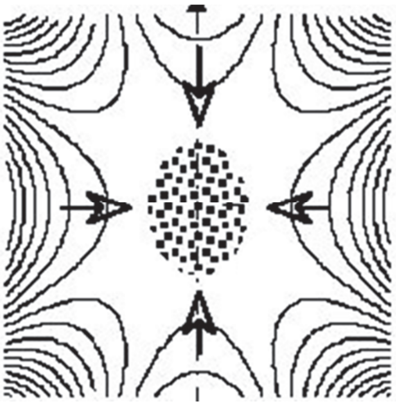

Figure 2.7: Example of the cusp fiels inside the source, generated by permanent magnets

These create a minimum-B configuration (multi-cusp, see **Figure 2.7**), which exploiting the magnetic mirroring presented in section 2.3.2, reduces the effective vessel area and yields a quiet, homogeneous plasma of large cross-sectional area.

2.4.5 Negative ion formation

As plasma formation involves the ionization of gas atoms, mostly negative electrons and positive ions compose it. Thus, negative ion formation comes as a second step. In this section, only main processes that bring to negative ion formation are described.

The processes involved in the attachment of an electron to a neutral atom are often exothermic in contrast to the endothermic processes required for positive-ion formation. The binding energy or electron affinity E_A of the negative ion is a measure of the stability and ease of negative ion formation. In general E_A must be positive for negative-ion stability. Negative E_A values refer to unstable negative-ion states. **Figure 2.8** shows the electron affinity of the elements on the periodic table.

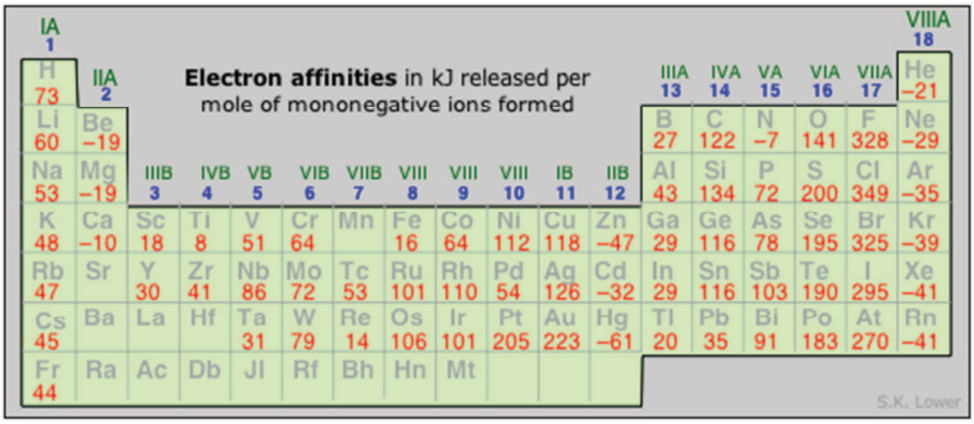

Electron affinities in kJ released per mole of mononegative ions formed

IA 1	IIA 2	IIIB 3	IVB 4	VB 5	VIB 6	VIIB 7	VIII 8	VIII 9	VIII 10	IB 11	IIB 12	IIIA 13	IVA 14	VA 15	VIA 16	VIIA 17	VIIIA 18
H 73																	He −21
Li 60	Be −19											B 27	C 122	N −7	O 141	F 328	Ne −29
Na 53	Mg −19											Al 43	Si 134	P 72	S 200	Cl 349	Ar −35
K 48	Ca −10	Sc 18	Ti 8	V 51	Cr 64	Mn	Fe 16	Co 64	Ni 112	Cu 118	Zn −47	Ga 29	Ge 116	As 78	Se 195	Br 325	Kr −39
Rb 47	Sr	Y 30	Zr 41	Nb 86	Mo 72	Tc 53	Ru 101	Rh 110	Pd 54	Ag 126	Cd −32	In 29	Sn 116	Sb 103	Te 190	I 295	Xe −41
Cs 45	Ba	La	Hf	Ta 31	W 79	Re 14	Os 106	Ir 101	Pt 205	Au 223	Hg −61	Tl 20	Pb 35	Bi 91	Po 183	At 270	Rn −41
Fr 44	Ra	Ac	Db	Jl	Rf	Bh	Hn	Mt									

S.K. Lower

Figure 2.8: electron affinities of the elements on the periodic table. Negative values refer to unstable negative-ion formation.

In addition to negative-atomic-species formation, also molecular negative ion formation may occur. There is also a class of negative ions, which are only formed in excited metastable states. Compared to positive-ion production, that are created just by ionization, negative ions can be formed by means of several physical or physico-chemical mechanisms. The ones that will be discussed here are the two most important processes for the formation of negative hydrogen ions: volume process by electron impact and charge-exchange on surfaces (surface process). As it can be deduced from the affinity value, the negative hydrogen ion is stable, although it has a low binding energy so that the additional electron can be easily removed via collisions.

- **Volume process**

  There are three types of reactions belonging to volume process:

- *Dissociative Attachment*: Slow electrons are stably attached to atoms during their interactions with neutral molecules, preferentially with excited ones, according to the following reaction

$$e^- + H_2 \rightarrow H^- + H$$

- *Polar Dissociative Attachment*: In this case the electron has an energy of at least 10eV (e^-_{hot}) and is not captured, but only excites the molecule to an unstable state. Then the excited molecule eventually capture a cold electron ($e^-_{cold} < 2$ eV) forming a negative ion by dissociating the molecule

$$e^-_{hot} + H_2 \rightarrow H_2^* + e^-_{cold} \rightarrow H^- + H$$

This reaction has a cross section five times larger than Dissociative Attachment.

- *Dissociative Recombination*: by collisions of slow electrons with positive molecular ions. Negative ions are generated with considerable cross section by the following reaction

$$e^- + H_2^+ \rightarrow H^+ + H^-$$

In any case, volume process cross sections are very small making them not very efficient and not suitable to achieve the negative hydrogen current densities required for fusion purposes: in the Japanese negative ion source NITS, for example, maximal current density achieved with volume process only has been 20 A/m^2, vary far from the 300A/m^2 foreseen for ITER NBI. This goal can be achieved by means of enhanced surface process.

- **Surface process**

Interaction between particles having sufficient energy and a low work function surface can result in the formation of a negative ion, where the work function is the energy required to extract an electron from a surface (**Figure 2.9**).

Surface process can be enhanced with alkali coatings of the surfaces exposed to particle bombardment, i.e. source walls. There are two principal processes, namely the thermodynamic-equilibrium surface ionization, where the slow atom or molecule impinging on the surface is emitted as a positive or negative ion after a mean residence time, and the most important non-thermodynamic atom-surface interaction, where negative ions are produced by material sputtering in the presence of an alkali metal coating.

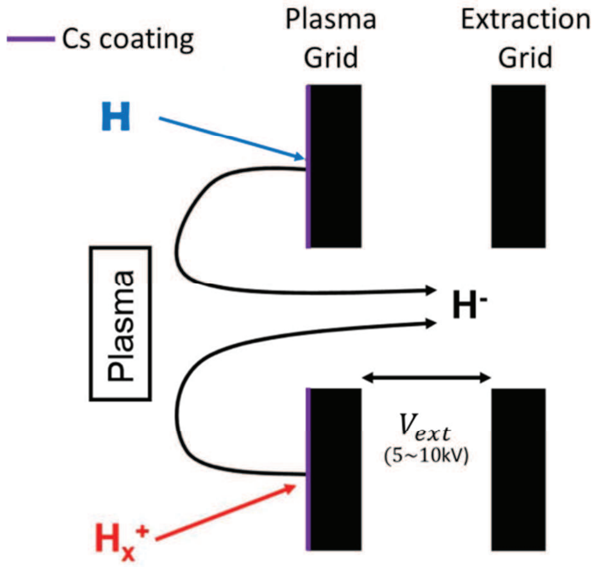

Figure 2.9: Schematic of surface production mechanism.

For what concerns the coating, the material used in negative ion sources, not only for fusion purposes, is cesium (Cs) as this is the element with the lowest work function. Cesiation of the source walls is usually performed by means of cesium ovens that make it evaporate and flow inside the source. This is essentially a random process: even if the amount of cesium injected into the source can be controlled by a wise regulation of the cesium oven temperature, its flow and thus its deposition inside the source cannot be directly controlled. In fact, cesium deposition may depend on several circumstances, among others, the plasma flow inside the source: in negative ion sources an ExB drift is generated by the magnetic filter field, presented in the next section. This drift is responsible for plasma density inhomogeneity before the PG. This results in inhomogeneous cesium deposition in the source that causes inhomogeneity in negative ion formation and, consequently, in the beam extraction. Furthermore, only ions formed very close to the extraction area can survive enough to be extracted before being neutralized again inside the source (the hydrogen electronegativity is very low), meaning that cesium deposited elsewhere but on the PG is not useful.

However, the use of cesium dramatically enhances negative ion formation and, at the moment, it is the only way to achieve the desired current density for fusion devices. Nevertheless, due to the drawbacks just described, together with its toxicity, alternatives to cesium are under investigation in several laboratories around the world.

Further references about negative production processes can be found in [19] [20] [21] [22] [26].

2.4.6 Magnetic filter field

As said before, both arc and RF ion source can be used for production of both positive and negative ions. Anyway, regardless the negative ion formation mechanism being exploited by the source, the lifetime of the generated H^- is shortened by the presence of high-energy electrons in the plasma that can easily strip the attached electron. So, in order to have good amount of negative ions to extract, the number of fast electrons has to be reduced. This can be achieved by mean of a magnetic filter field entering the ion source. **Figure 2.10** shows a schematic of the filter field effect.

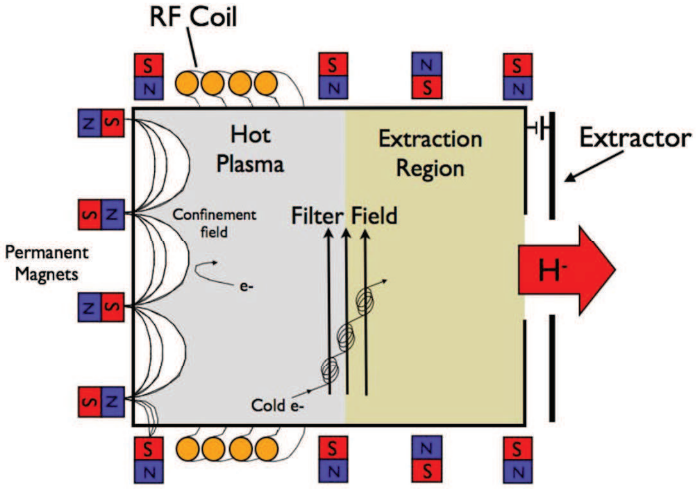

Figure 2.10: Schematic of filter field action inside the plasma source.

Both permanent magnets and dedicated loop circuits can provide this transverse magnetic field inside the expansion region, close to the extraction zone. One can imagine that this filter field ideally divides the plasma inside the source in hot region and cold region, as it prevents energetic (hot) primary electrons from the driver region from entering the extraction area (**Figure 2.11** b)). Its effect is actually to cool down electrons coming from the hot plasma by collisions: because charge particles follow field lines, filter field slow down the plasma flow toward the PG. Thus, resident time is enhanced in correspondence to the maximum of the field forming a high-density area (**Figure 2.11** a)). Being density increased, the interaction of electrons with each other by collisions is also enhanced. This process make electrons lose part of their energy.

Both positive and negative ions, together with very slow electrons, are then able to penetrate the filter and form cold plasma in which H^- ions can be produced with better efficiency. At the end of section 4.3.1 the importance of the effect of the magnetic field will be supported by measurements.

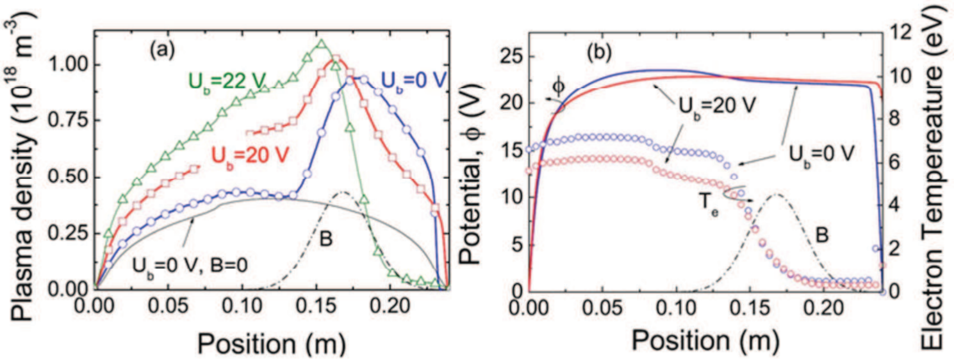

a) b)

Figure 2.11: Distribution of (a) plasma density and (b) potential (lines) and electron temperature (circles) for three values of the bias voltage, 0V, 20V, and 22V from a 1D PIC-MCC simulations [[23]. The magnetic field profile is indicated by a dashed lines (maximum of B 3 mT).

A drawback brought about by the use of the filter field is that the magnetic field combines with the electric field in the extraction region (generated by the plasma potential variation induced by the positive biasing of the PG and to the lack of negative ions due to the extraction process itself) producing an ExB drift that degrades the uniformity of the plasma density. In multi aperture sources this results in an inhomogeneity of the current density of the extracted beamlets.

2.5 Negative Ion Beams

The beams are generated by the extraction system. It determines the beam properties such as ion current and beam optics quality. For fusion applications multi-beamlet extraction systems are used, that is the grids are provided with multiple apertures. Usually these apertures are round in order to extract beamlets with a round cross section. Also beamlets with a different shaped cross section can be generated thanks to a different PG aperture geometry, but this work deals with round beamlets only.

2.5.1 Principles of multi-electrode systems for beam extraction and acceleration

The voltages applied to a multi electrode system (**Figure 2.12**) provide ion extraction from the plasma source through the circular apertures of PG and the successive ion acceleration. This system is usually composed by: the already presented plasma grid, a second electrode called the extraction grid (EG) and one (or more than one) acceleration grid (AG).

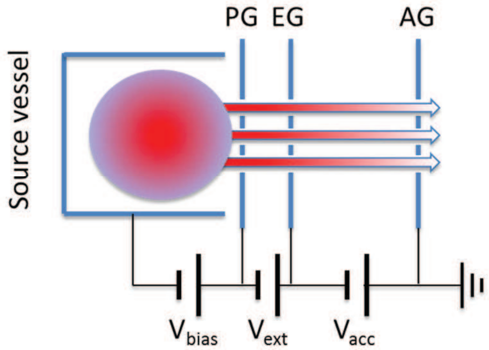

Figure 2.12: Simplest concept of multi electrode system for beam extraction.

These grids feature apertures in correspondence to the PG apertures to let the ion beam pass through the electrodes. The gap between PG and EG is usually referred to as extraction gap, while the one between EG and AG acceleration gap. The differential potential in the extraction gap is U_{ext}, the one in the acceleration gap is U_{acc}. The energy of the beam that exits the last electrode will be:

$$E = q(U_{ext} + U_{acc}) \quad 2.35$$

EG is the electrode that provides the voltage that extracts ions from the source, namely the extraction voltage V_{ext}. This voltage is not very high and typically stands within the range of $5 - 10$ kV. The extraction voltage, as we will see in section 2.5.3.3, plays a crucial role in formation of ion beams with good optics.

AG, instead, provides the voltage to accelerate the beam, extracted from the source by the extraction voltage, up to the desired energy. As in the case for ITER NBI, beams have to acquire very high energy (1MeV), meaning that the accelerating voltage (V_{acc}) can reach very high level; in such cases, a configuration that involves more than one AG, such as to provide a defined grading of the high voltage, is preferred (right hand side of Figure 2.13). In this way the accelerating voltage can be applied gradually, minimising breakdown events. The accelerating voltage plays a minor role in beam shaping.

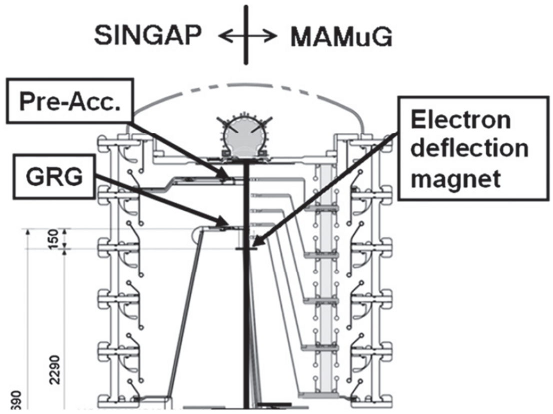

Figure 2.13: Single acceleration gap schematics (left had side) in comparison with multi acceleration gap schematics (right hand side)

From the electrical point of view, PG is usually held at the maximum voltage (negative or positive, depending if dealing with negative or positive ions beams) and the last AG is grounded (Figure 2.1). For this reason in the last electrode is usually referred to as grounded grid (GG).

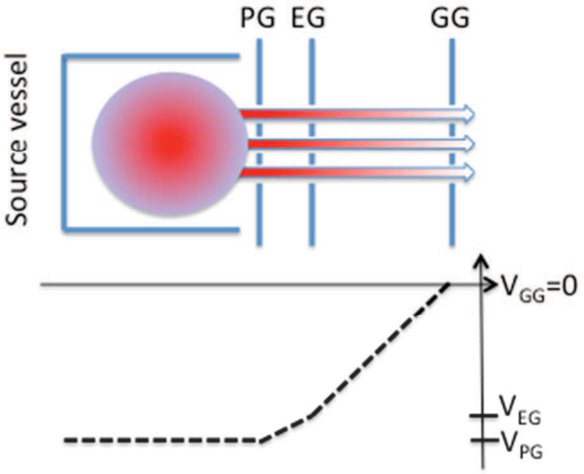

Figure 2.14: Example of the voltage drop inside the extraction system.

Possibly also a repeller grid (REP) can be

Ion sources can be operated in DC or

2.5.2 Beam extraction

We now focus on the beam extraction process. Extraction of ions from the plasma inside the source plays a crucial role while developing an ion source. Ions move randomly inside the plasma with free electrons with $v=4\pi v2nm2\pi kBT32exp-mv2kBT$ **2.2**). As already said in the previous section, the extraction systems for the different type of negative ion sources consists mainly in the triple electrode system composed by the plasma electrode PG, the extraction electrode EG and the ground electrode GG.

The trajectories of the accelerated ions, which determine the beam quality in the extraction region, are affected by several factors such as electric and magnetic field strengths, the shape of the emitting plasma surface and the space charge density of the beam itself.

2.5.2.1 Plasma meniscus

The boundary layer between the plasma and the extracted ion beam, the ion-emitting surface, is called the plasma meniscus (**Figure 2.15**). It establishes due to the balance between plasma pressure and the applied voltage in the extraction gap. Ions that reach the meniscus are able to be guided and directed by the electric field of the extraction gap. In order to help ions reach the meniscus, as already said in section 2.4.1, usually the PG is biased with respect to source walls.

Position, depth and curvature of meniscus depend on density and temperature of the plasma (electrons and ions) and on the voltage applied in the extraction gap. In particular the meniscus shape adjusts itself in order to cancel the E field of the extraction gap at the plasma meniscus. Another important role in determining the meniscus shape is played by geometrical parameters: the aspect ratio r_{PG}/d, being r_{PG} the radius of PG aperture and d the extraction gap length.

The concept of beam perveance, presented in section 2.5.3.3, will help to understand the importance of the meniscus shape.

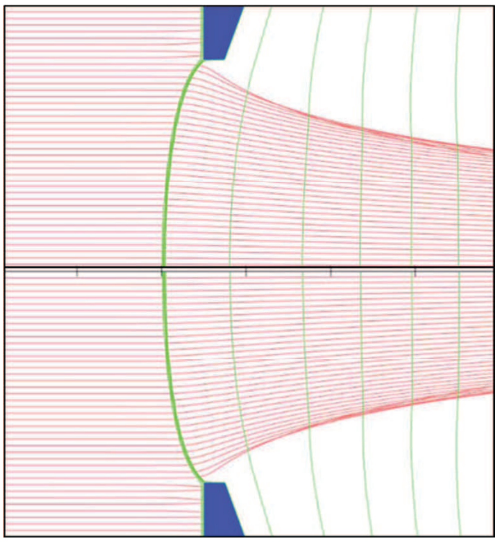

Figure 2.15: Plasma meniscus at PG aperture. It establishes due to the balance between plasma pressure and the applied voltage in the extraction gap.

2.5.2.2 Extractable ion current

The extractable ion current from the meniscus is limited by the sheath layer formation mechanism at the meniscus, which is regulated by the Bohm criterion, in the case of positive ion beams.

Bohm sheath criterion states that the ion flow must have a minimum speed (ions sound speed) at the plasma boundary in order for a sheath to form [Bacal **M and Wada** ***Negative hydrogen ion production mechanisms*** **Appl. Phys. Rev. 2 021305 (2015)**

[**27**], [[**28**]. As the meniscus is a plasma boundary, as well as the source walls, it also has its sheath layer. The sheath region begins where charge neutrality begins to break down. The electric potential gradient becomes very steep abruptly on the boundary side of the sheath edge, and because of the curvature of the potential, electrons are repelled from and ions are accelerated to the boundary. Due to the mass difference between ions and electrons, in the sheath region density gradient of electrons is higher than the ion's:

$$\frac{dn_i}{dz} < \frac{dn_e}{dz} \qquad 2.36$$

For simplicity let's imagine a flat meniscus and that the physical variables change only in the normal direction, let's say z, with respect to the boundary. Changes in ion concentration and flow are related to ion sources (S_+) and sinks (S_-) by the continuity equation:

$$\partial_t n_i + \partial_z (n_i v_i) = S_+ - S_- \qquad 2.37$$

By concentrating in a very thin region of few Debye lengths from the sheath edge $S_{+} = S_{-} = 0$ and, at the equilibrium (stationary flow of ions), $\partial_t n_i$ is also zero. The equation 2.37 can be rewritten as:

$$\frac{dn_i}{dz} = -\frac{n_i}{v_i}\frac{dv_i}{dz} \qquad 2.38$$

Each side of equation 2.38 has units of a reciprocal length that defines the characteristic length over which each quantity changes. Since ion density gradient has to be less that the electron density gradient (equation 2.36)

$$-v_i > n_i \frac{dv_i/dz}{dn_e/dz} \qquad 2.39$$

Now considering that the electrons are energetically confined by the sheath potential and thus are in electrostatic equilibrium, they are describable in terms of the Boltzmann distribution 2.8:

$$n_{e-sheath} = n_{e-bulk} exp^{q_e \phi_{plasma}(z)/k_B T_e} \qquad 2.40$$

stating that the electron density is the greatest where the potential energy is the least, and vice versa. Thus:

$$\frac{dn_e}{dz} = \frac{q_e}{k_B T_e}\frac{d\phi_{plasma}(z)}{dz} exp^{q_e \phi_{plasma}(z)/k_B T_e} \qquad 2.41$$

The spatial gradient of the velocity at the sheath edge also depends on the potential gradient because of conservation of energy. Therefore, for the ions one has:

$$\frac{d}{dz}\left(q_i \phi_{plasma}(z) + \frac{1}{2} m_i v_i^2\right) = 0 \rightarrow \frac{dv_i}{dz} = -q_i \frac{d\phi_{plasma}(z)}{dz}\frac{1}{m_i v_i} \qquad 2.42$$

Finally, by substituting equation 2.41 and 2.42 in equation 2.39, one gets:

$$v_i > \sqrt{\frac{k_B T_e}{m_i}} \qquad 2.43$$

Bohm criterion than imples that only ions which reach the minimum velocity given by equation 2.43 can reach the boundary and are available for extraction. Ion current density, j_i, also called saturated current density, at the meniscus is:

$$j_i = q_i n_i v_i = q_i n_i \sqrt{\frac{k_B T_e}{m_i}} \qquad 2.44$$

that depends on the temperature T_e of the plasma electrons.

2.5.2.3 Space Charge

It is now reasonable to introduce the important concept of space charge, as it also affects extraction current. The ion beam charge density ρ is:

$$\rho = q_i n_i = \frac{j_i}{v_i} \qquad 2.45$$

where $v_i = \sqrt{2E/m_i}$ and E is the energy the particle gained under the the effect of the potential drop. This charge density, or space charge, reduce the effective extraction voltage along the extraction direction and induces forces that tend to make the beam 'blow up' in the transverse direction. Thus space charge affects both beam extraction and beam envelope shape. These aspects are discussed in more details in section 2.5.2.4 and 2.5.3.1.

Space charge plays a major role particularly in the extraction gap, where current densities are high and velocities are low compared to other parts of accelerator systems, as V_{ext} is not very high. At higher-energy parts of the accelerator (after the EG), as particles have higher velocities, the space charge plays a minor role: particle acceleration reduces beam density, reducing space charge consequently (see equation 2.57). Furthermore, in the high energy part the magnetic force generated by the beam particles, might also contribute to compensate the blow-up, sometimes even leading to "pinching" of the beam; but it is actually an insignificant contribute for $v_i \ll c$.

2.5.2.4 Space Charge limited current

The very first consequence of the space charge is the limitation it imposes to the extractible ion current.

When the ions have reached the meniscus boundary, as soon as they are extracted by the extraction gap electric field, the space charge limitation sets in. The space charge limitation follows from Langmuir–Schottky–Child's law, which relates the extracted current density to the differential potential U_{ext} in the extraction gap. In a steady state conditions ($\partial_t j_i = 0$):

$$j_i = q_i n_i v_i = const \text{ (Continuity equation)}$$

Considering also equation of motion and Poisson equation:

$$\frac{1}{2}m_i v_i^2 = -q_i U_{ext}(z) \text{ (Equation of motion)}$$

$$\nabla^2 U_{ext}(z) = -\frac{\rho}{\varepsilon_0} = -\frac{q_i n_i}{\varepsilon_0} \text{ (Poisson equation)}$$

a three equation system is obtained. Solving for j_i one obtains:

$$j_i = \frac{4}{9}\sqrt{2} \cdot \varepsilon_0 \frac{\sqrt{q_i/m_i}}{d^2} V_{ext}^{3/2} = pV_{ext}^{3/2} \qquad 2.46$$

being $\mathrm{p} = \frac{4}{9}\sqrt{2} \cdot \varepsilon_0 \left(\sqrt{\mathrm{q_i}/\mathrm{m_i}}/\mathrm{d}^2\right)$ the so called perveance, $\mathrm{V_{ext}} = \mathrm{U_{ext}}(\mathrm{z} = \mathrm{d})$ and d the extraction gap length. Thus the maximum extractable current density depends on ion charge and mass and also on the extraction gap and the potential difference applied to the gap.

Figure 2.16 shows the Child-Langmuir limit in a typical current-voltage characteristic of plasma extraction. A more detailed discussion on the perveance is reported in section 2.5.3.3.

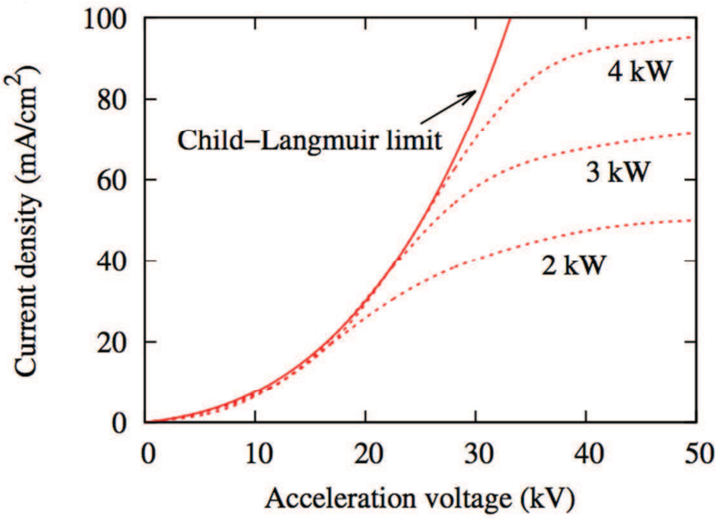

Figure 2.16: A typycal current-voltage characteristic of plasma extraction. With low extraction voltage the extraction is operating in the Child-Langmuir limit. At higher voltages the ion current saturates due to the emission limit from the plasma (given by the Bohm's criterion). This limit can be adjusted increasing the power transmitted to the plasma.

In conclusion, for positive ion beams Bohm criterion defines how many ions from the source are available for extraction, while Langmuir–Schottky–Child's law defines how many ions can actually be extracted by the extraction system. Analogously for negative ion beams a situation resembling the thermionic limited current observed in electron accelerators can be invoked to explain a limited current available at the meniscus, while the Langmuir–Schottky–Child's law rules the evolution of the beam in the extraction gap.

2.5.3 Beam optics

In any case the extraction system has two requirements to achieve: it has to be able to extract ions with the desired beam current and to provide a good beam optics at the exit.

Considering the first requirement, in principle, if plasma source is capable of providing enough ions at the emitter surface, the ion beam current depends only on the extraction voltage. Turning to the beam optics, it can be considered good when particle trajectories are parallel at the exit. This means that the extracted beam exits with a low divergence angle, provided that it does not intercept the electrodes.

The parameters that influence the extraction of a parallel ion beam are the ion temperature inside the plasma and the shape of the electrode apertures. Considering the PG, a large PG aperture r_{PG}, keeping the gap distance d constant will increase beam emittance (section 2.5.3.1), will increase the probability of negative ion destruction due to the high release of neutral gas from the source (section 2.5.3.1) and will also reduce the field strength in the gap . The decrease of the gap distance d, instead, will reduce the applicable voltage to the electrodes, as breakdown events can occur more often. Thus in general an aspect ratio $S = r/d = 0.5$ is usually preferred (especially in positive ion sources). Furthermore, PG aperture edges also are exploited: the downstream edge is always chamfered. The chamfered edge helps particle beam to converge toward the EG. In particular, in negative ion sources also the end that directly faces plasma is chamfered in order to help negative ions generated by surface production to reach the meniscus for extraction.

A good extraction of the ions from the plasma source then depends on many parameters. The concept of perveance presented in section 2.5.3.3 regulates this process.

It is interesting what happens to the beam after the extraction, following the beam envelope along its path inside the accelerator. If the extraction has been properly tuned, then the meniscus concave shape makes extracted ions converge toward the EG. As soon as ions arrive to the upstream side of the EG aperture, ions start to diverge until they reach the aperture exit, where they converge again toward the GG. As result of the potential difference of the gap, indeed, grid apertures act as electrostatic lenses on the charge particle of the beam, in the same fashion as optical lenses do for electromagnetic waves (light, laser, etc.). It is also possible to adopt classical optical lens formalism to describe the beams inside the accelerators: the focal length of the lens formed between two generic electrodes, away from each other d, is given by [[**29**]:

$$f = \frac{4\left(\sqrt{V_2/V_2}+1\right)}{V_1/V_2+V_2/V_1+2}d \quad 2.47$$

In particular, aperture entrances always act as defocusing lenses, while aperture exits as focusing lenses. It may be eventually noted that, since downstream the last electrode (GG) there is a field free region, the exit side of the GG aperture doesn't feature any electrostatic lens effect, while at the entrance the usual defocusing lens effect is still present. A more detailed description of the influence of electrode aperture geometry will be done in section 4.4.1.

From now on, I will refer to the electrode system region as the acceleration region.

2.5.3.1 Beam emittance

An important parameter that characterizes the beam quality is the emittance [[**14**]. Traditionally the emittance is defined as the six-dimensional volume limited by a contour of constant particle density in the (x, p_x, y, p_y, z, p_z) phase space (p is the momentum). This volume obeys the Liouville theorem and is constant in conservative fields.

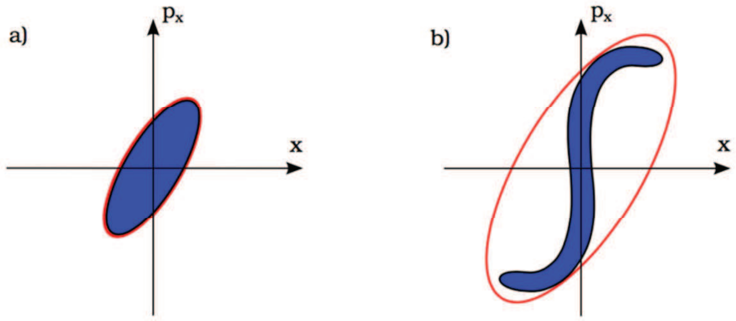

Figure 2.17: A two-dimensional projection of an ensemble of particles (a) before going through a nonlinear optical system and (b) after it. The area of the particle distribution (shown in blue) is conserved but the area of the elliptical envelope (shown in red) increases.

Typically in the case of continuous (or long pulse) beams, where the longitudinal direction of the beam is not of interest, 2D transverse distributions ($x, x' = p_x/p_z$) and ($y, y' = p_y/p_z$), i.e. dimension and divergence angle, are used instead of the full 3D phase-space distribution for simplicity. Also in this case the Liouville theorem holds and is applied to the area of the contour in the phase space, which typically has an elliptical shape: well-behaved ion beams usually have Gaussian distributions in both x and x' (or y and y') and the contour of 2D Gaussian distribution results in an elliptical shape (**Figure 2.17** a). Anyway, the envelope surrounding the distribution (the ellipse) changes when nonlinear forces act on the particles. For example, beam propagation through a periodic channel of electrostatic lenses with spherical aberrations (the particles to not meet after the lens in one focal point, this happens especially to the most externally particles), like in our ion sources, will progressively distort the ellipse (**Figure 2.17** b).

The size and shape of the transverse distribution envelope are important quality measures for beams, because most complex ion optical devices such as accelerators have an acceptance (maximum acceptable emittance) window in the phase space within which they can operate. It can also tell if the beam in a certain position of the accelerator is converging or diverging (see **Figure 2.18**).

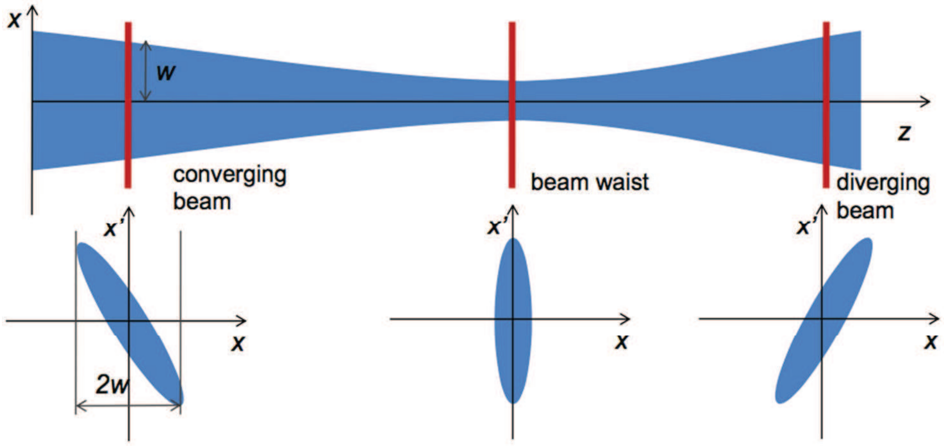

Figure 2.18: Clockwise rotation of the emittance area envelope passing from converging to diverging part of the beam.

The equation for an origin-centred ellipse is

$$\gamma x^2 + 2\alpha x x' + \beta x'^2 = \epsilon = const \qquad 2.48$$

Here ϵ, whose dimension is mm*mrad, is the two-dimensional transverse geometrical emittance, and α, β and γ are known as the Twiss parameters defining the ellipse orientation and aspect ratio. The relation between the area of the ellipse and the geometrical emittance ϵ is:

$$A = \pi R_1 R_2 = \pi\epsilon \qquad 2.49$$

if we impose

$$\beta\,\gamma - \alpha^2 = 1 \qquad 2.50$$

From equation 2.48 the dimensions of the ellipse can be calculated (**Figure 2.19**).

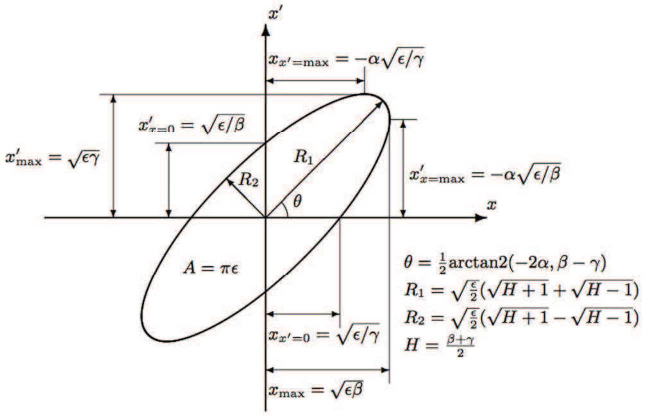

Figure 2.19: Emittance ellipse geometry with the most important dimensions

There a problem related to the geometrical emittance, it is not constant during acceleration: being $x' = p_x/p_z$, if p_z changes because of the acceleration of particle inside the acceleration region, also x' changes. The geometrical emittance ellipse will result flattened (see **Figure 2.20**).

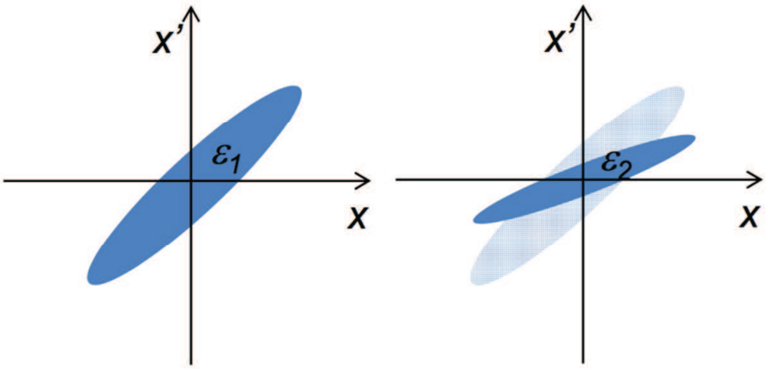

Figure 2.20: The emittance ellipse flattened by the acceleration of particles.

Thus, it is not possible to compare geometrical emittances in different parts of the acceleration region. In order to overcome this problem and so compare the emittances at different beam energies it is necessary to normalize the geometrical emittance with the relativistic parameters $\tilde{\beta} = v_i/c$ and $\tilde{\gamma} = 1/\sqrt{1-\tilde{\beta}^2}$, where c is the speed of light, obtaining:

$$\epsilon_{norm} = \tilde{\beta}\tilde{\gamma}\epsilon \quad 2.51$$

Anyway, a good figure of merit that that allows an easy comparison among emittances in various conditions or on different machines is the r.m.s. emittance:

$$\epsilon_{rms} = \sqrt{\langle x^2\rangle\langle x'^2\rangle - \langle xx'\rangle^2} \qquad 2.52$$

and the Twiss parameters can be redefined as:

$$\alpha = -\frac{\langle xx'\rangle}{\epsilon} \qquad \beta = \frac{\langle x^2\rangle}{\varepsilon} \qquad \gamma = \frac{\langle x'^2\rangle}{\epsilon}$$

Therefore, emittance can give a lot of information on the beam. Unfortunately, no ion sources on which I have worked on in this thesis are provided with an emittance measurement system. However, in substitution to emittance, information about beam quality can be given by divergence (that is the integral of the geometrical emittance on the horizontal axis), that is actually measured in these sources.

2.5.3.2 Beam divergence and electrostatic deflection

Another consequence of the space charge inside the beamlet is the beam divergence. Considering the radial direction, with respect to the beam line, assuming a cylindrical uniform-current-density beam with radius r propagating with constant velocity v_z ($\partial_t j_i = 0$), the beam-generated electric field in the transverse direction is given by Gauss's law,

$$E_r(r) = \begin{cases} \frac{I}{2\pi\varepsilon_0 v_z}\frac{r}{r_{beam}^2}, & r \le r_{beam} \\ \frac{I}{2\pi\varepsilon_0 v_z}\frac{1}{r}, & otherwise \end{cases} \qquad 2.53$$

The potential inside a drift tube with radius r_{tube} is therefore [[**29**]

$$\phi_r(r) = \begin{cases} \frac{I}{2\pi\varepsilon_0 v_z}\left[\frac{r^2}{2r_{beam}^2} + log\left(\frac{r_{beam}}{r_{tube}}\right) - \frac{1}{2}\right], & r \le r_{beam} \\ \frac{I}{2\pi\varepsilon_0 v_z} log\left(\frac{r}{r_{tube}}\right), & otherwise \end{cases} \qquad 2.54$$

Figure 2.21 gives an example of the potential distribution inside a beam in the drift tube region.

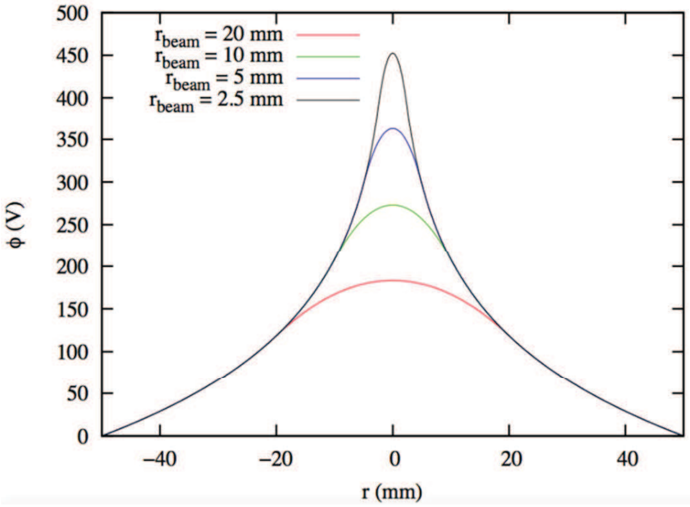

Figure 2.21: Example of the potential distribution inside a cylindrical 100 mm tube with 10 mA, 10 keV proton beam with different radius.inside a cylindrical 100 mm tube with 10 mA, 10 keV proton beam with different radius.

The electric field given by equation 2.53 is linear with radius and therefore does not cause emittance growth, but it does result in increasing divergence of the beam. A particle at the beam boundary than experiences a repulsive force:

$$F_r = m_i a_r = qE_r = \frac{qI}{2\pi\varepsilon_0 v_z}\frac{1}{r} \qquad 2.55$$

As the particle acceleration is:

$$\boldsymbol{a_r = \frac{d^2r}{dt^2} = \frac{d^2r}{dz^2}\frac{dz^2}{dt^2} = v_z^2\frac{d^2r}{dz^2}} \qquad 2.56$$

by substituting equation 2.56 into equation 2.55 one find:

$$\boldsymbol{\frac{d^2r}{dz^2} = \frac{1}{v_z^2}a_r = \frac{qI}{2\pi\varepsilon_0 m_i v_z^3}\frac{1}{r}} \qquad 2.57$$

With the change of variable $\lambda = dr/dz$, the last equation can be integrated, giving the particle trajectory:

$$\frac{dr}{dz} = \sqrt{\frac{qI}{\pi\varepsilon_0 m_i v_z^3}log\left(\frac{r}{r_{beam}}\right)} \qquad 2.58$$

assuming $dr/dz = 0$ at $z = 0$. Integrating again it becomes:

$$z = r_{beam}\sqrt{\frac{\pi\varepsilon_0 m_i v_z^3}{qI}}\int_{y=1}^{y=r/r_{beam}}\frac{1}{\sqrt{logy}}dy = r_{beam}\sqrt{\frac{\pi\varepsilon_0 m_i v_z^3}{qI}}\theta \qquad 2.59$$

where θ is the divergence of the beam boundary.

In the case of multi-beamlet sources, like the cases considered herein, each beamlet also experiences a repulsive force by the other beamlets. Using similar considerations about the electrostatic interactions among the beamlets, it will result in the increase of the distance among beamlets similar to the one among particles inside the beam. This time it is referred to an electrostatic deflection α_E rather than divergence θ.

2.5.3.3 Beam Perveance

At the end of section 2.5.2.4 the perveance was already defined as $\mathrm{p} = \frac{4}{9}\sqrt{2} \cdot \varepsilon_0\left(\sqrt{\mathrm{q_i}/\mathrm{m_i}}/\mathrm{d}^2\right)$. This parameter is a very important index of the optical beam quality.

From equation 2.46 the perveance as a function of ion current density and extraction voltage can be defined:

$$\boldsymbol{p} = \frac{j_i}{V_{ext}^{3/2}} \qquad 2.60$$

By multiplying both terms by the PG extraction aperture area πr_{PG}^2 one obtains:

$$\boldsymbol{P} = \frac{I_i}{V_{ext}^{3/2}} \qquad 2.61$$

where now

$$\mathrm{P} = \mathrm{p}\pi r_{PG}^2 = \frac{4}{9}\sqrt{2} \cdot \pi\varepsilon_0\left(\sqrt{\mathrm{q_i}/\mathrm{m_i}}\right)\left(\frac{r_{PG}}{d}\right)^2 \qquad 2.62$$

The beam perveance, then, depends on the square of the aspect ratio r_{PG}/d and on $V_{ext}^{-3/2}$. As said in section 2.5.2.1 also plasma meniscus depends on these parameters. Therefore, perveance can be intended as an index of the meniscus shape. Practically speaking, at fixed electrode system geometry, i.e. aspect ratio r_{PG}/d, it is possible to vary the perveance by an extraction voltage scan. The result of such a scan usually shows a minimum (the so called smiling curve, see **Figure 2.22**) that represent the best beam optics: the correct balancing between the extracted current density and the space charge limited current density.

When the system is at perveance match, the meniscus has a correct concave shape that makes the ions, which leave the meniscus surface almost perpendicularly, be extracted with a converging trajectory suitable to balance the repulsion force of the space charge. Then the beam enters the EG with a low divergence (the focal point is inside the EG). In this way, the defocusing electrostatic lens at the EG aperture entrance will not widen the beam too much.

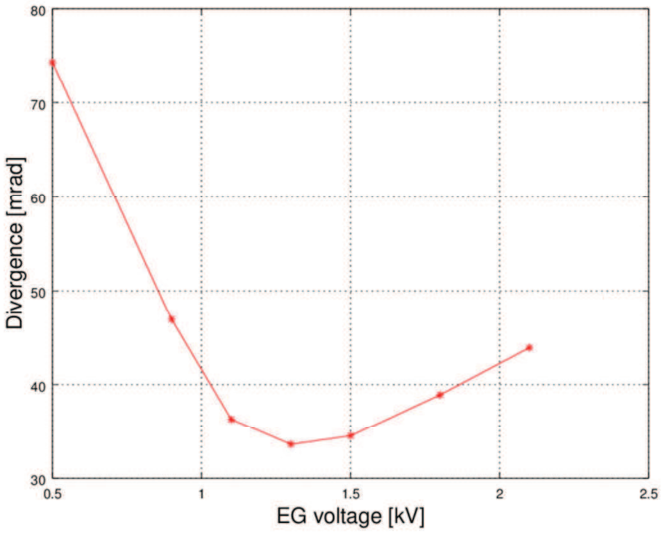

Figure 2.22: An example of perveance curve in function of the extraction voltage. As perveance is a measure of the beam optic, it is possible to plot divergence (that is usually directly measured) rather than perveance itself. The curve exhibits the typical 'smile' shape.

The focusing lens at the EG aperture exit will focus the beam again, allowing it reach the following electrode. The focusing power of the EG aperture exit, or its focal point position, can also be controlled by means of the perveance rule, using the voltage applied to the acceleration gap. This procedure can be applied to every acceleration stage in a multi electrode system. However, the perveance in the extraction gap plays the major role in determining beam optic, as, at the beginning of the acceleration, the particle velocity is still low, the space charge effects are high. Perveance tuning of the other gap can only slightly adjust the beam envelope shape.

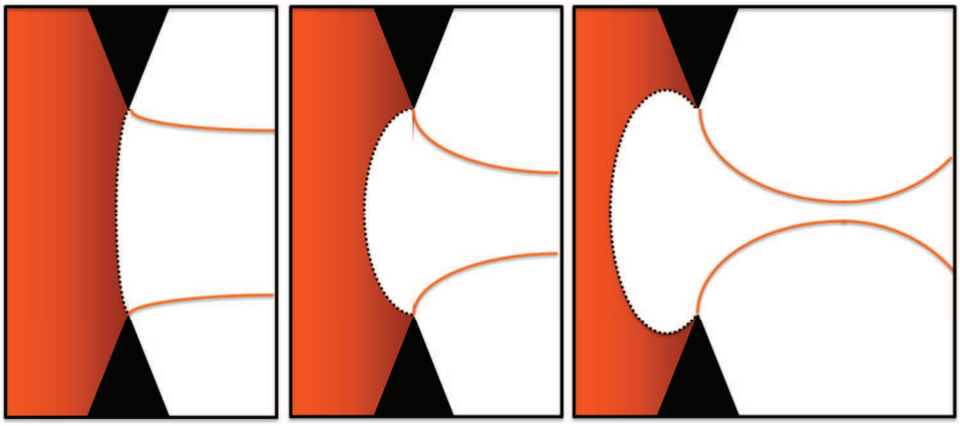

Figure 2.23: Beam profile at diferent perveance condition. Underperveance (left): meniscus is too flat and the focal point of the trajectories is after the EG. Perveance (centre): meniscus has a correct concave shape and the focal point is inside the EG. Overperveance(right): meniscus concavity is too much and the trajectory focal point is before the EG (hourglass envelope).

When the system is on the left-hand branch of the perveance curve, the extraction voltage is too low, the space charge repulsion is too high and the meniscus shape is too flat. Therefore, the particle trajectory will not converge enough (focal point after the EG). The system is said to be underperveant. It is the opposite on the right-hand branch of the curve: the applied voltage is too high and the meniscus shape will be too much concave. Therefore, the particles will also converge too much and the repulsion forces in the focal point will be very high and particles will leave the focal point with a big divergence angle, leading to the 'hourglass' beam envelope (see **Figure 2.23**).

Lastly, the Child-Langmuir law can also be used to scale the operational parameters. Keeping perveance constant, it is possible to retrieve the same optical condition (the optimal on in this case) by scaling down currents or voltages accordingly to the following relations:

$$P_{perv2} = \frac{j_{ext,2}}{V_{ext,2}^{3/2}} = \frac{j_{ext,1}}{V_{ext,1}^{3/2}} = P_{perv1} = P_{opt}$$

$$R_2 = \frac{V_{ext,2}}{V_{acc,2}} = \frac{V_{ext,1}}{V_{acc,1}} = R_1$$

where $P_{perv1} = P_{opt}$ is the perveance of the general case 1, for which the best case is considered, and P_{perv2} is the perveance of the general cases 2 that it is imposed to be equal to the case 1, in order to remain in the best optical conditions. R_1 and R_2 are the voltages ratios that must be kept equal in order to maintain the same optics. This is demonstrated by **Figure 2.24** and **Figure 2.25**, obtained with SLACCAD simulations.

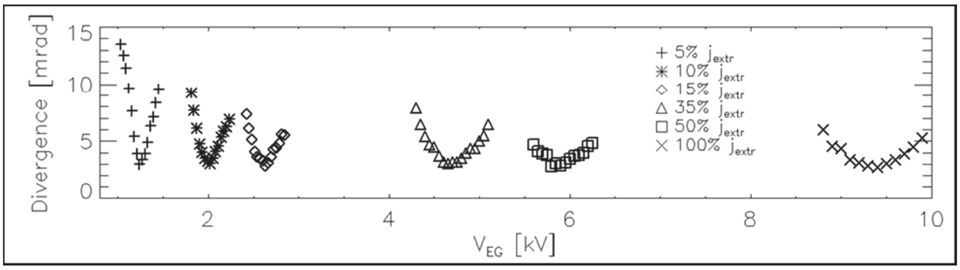

Figure 2.24: divergence is plotted as a function of V_{EG} for different j_{extr}.

In **Figure 2.24** divergence is plotted as a function of V_{EG} for different j_{extr}. The curves share the same minimum, while the shapes are different. Plotting these 'smile' shaped curves against normalized perveance, they, instead, collapse into one single curve, as shown by **Figure 2.25**. This is the proof that keeping the perveance constant provides a way to investigate beam optics conditions similar to the ones expected at nominal beam current.

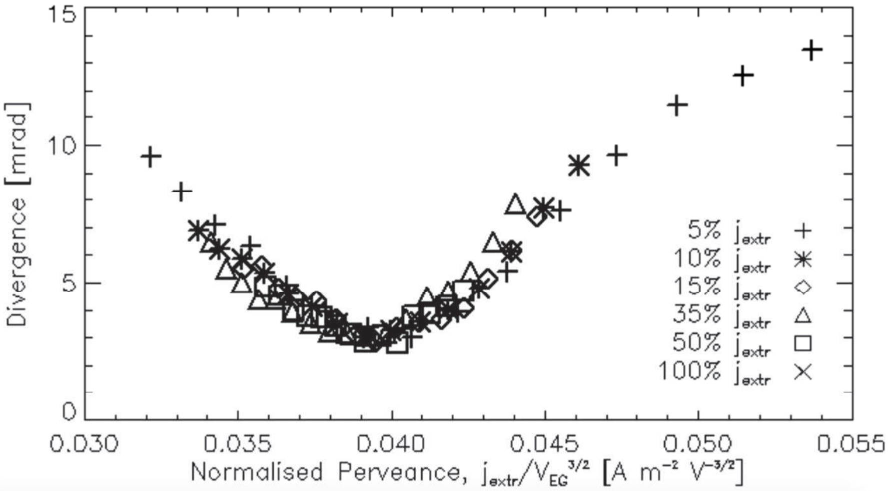

Figure 2.25: Same curves of Figure 2.24, but plotted against normalized perveance. The curves have collapsed into one single curve.

As a further confirmation on this consideration, **Figure 2.26** and **Figure 2.27** show the experimental results obtained on the ELISE (Extraction from a Large Ion Source Experiment) [[**24**] ion source, at IPP Garching, during a training activity done in 2016. Again divergence is plotted as a function of V_{ext} for two different j_{ext} values (**Figure 2.26**), sharing the same minimum value for the divergence. In the same fashion, they collapse into one single curve if plotted against normalized perveance (**Figure 2.27**).

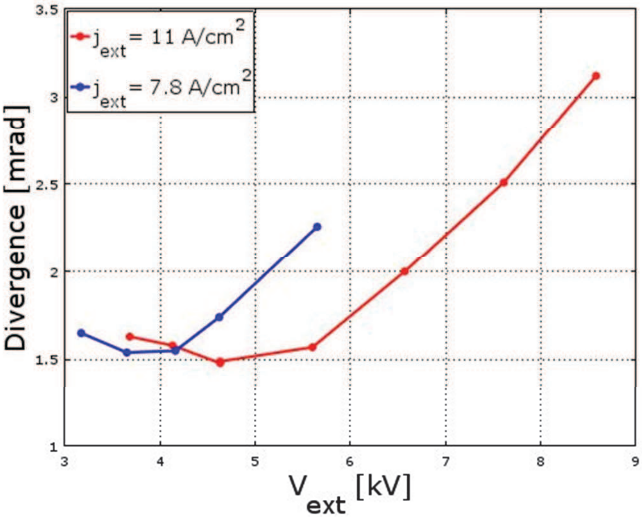

Figure 2.26: Two divergence scans at different beam current. Parameters were scaled down in such a way to keep the same optics (courtesy of IPP Garching ELISE Team) [[25].

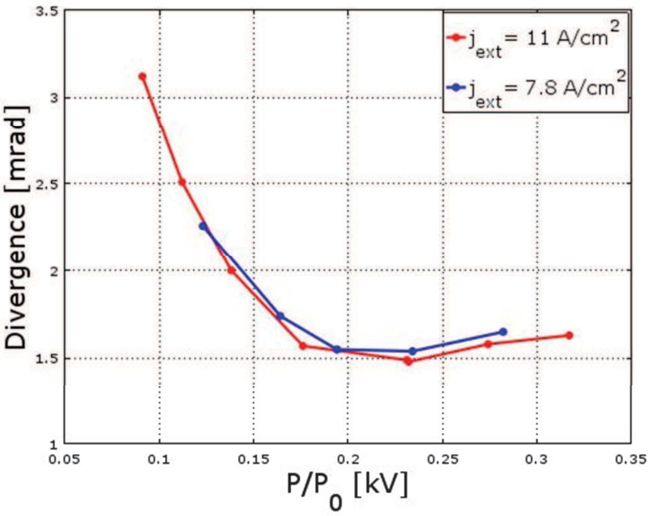

Figure 2.27: Same curves of Figure 2.26, but plotted against normalized perveance. The curves have collapsed into one single curve (courtesy of IPP Garching ELISE Team) [[25].

2.5.3.4 *Negative ion stripping and space charge compensation*

Space charge repulsion is actually less than expected inside the acceleration region and it completely disappears after few centimetres after GG: both space charge intra and inter beams is reduced due to electron stripping. Stripping reactions lead to destruction of negative ions, generating neutral atoms (H), free electrons and possibly positive ions (H^+). **Figure 2.28**, shows a schematic of the various striping processes that can happen inside the acceleration region.

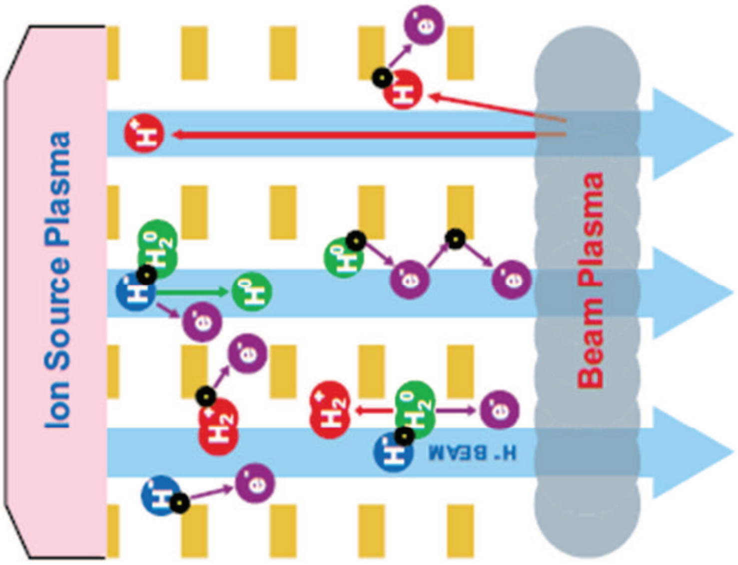

Figure 2.28: A schematic that shows secondary particles generated inside the acceleration region by interaction of the beam with the background neutral gas.

Stripping of negative ion beams occurs due to collisions with the residual background gas (H_2) in the acceleration region and in the drift tube. The main stripping reactions are:

- Single ion stripping

$$H^- + H_2 \rightarrow H + H_2 + e^-$$

- Double ion stripping

$$H^- + H_2 \rightarrow H^+ + H_2 + 2e^-$$

Secondary particles generated by stripping reactions can undergo further collision leading to these ionization reactions that also contribute to the production of positive ions:

- Ionization by negative ions

$$H^- + H_2 \rightarrow H^- + H_2^+ + e^-$$

- Ionization by neutrals

$$H + H_2 \rightarrow H + H_2^+ + e^-$$

In **Figure 2.29** cross section of these reactions are presented (ionization reactions cross section are assumed to be equal).

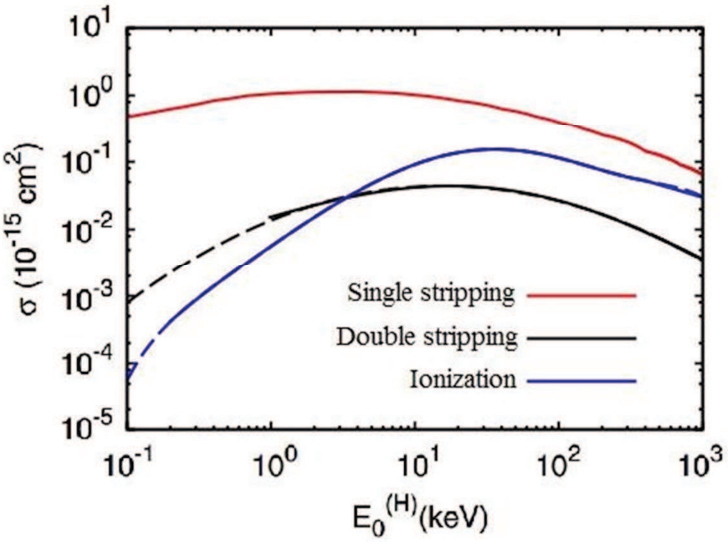

Figure 2.29: Cross section for H- single (red line) and double (black line) stripping reactions, ionization of hydrogen background gas (blue line).

Sources of background gas can be several: in a simple ion source it comes from the plasma chamber itself, thus from the upstream side. When dealing the NBI like MITICA, instead, it comes also from the gas neutralizer, from the downstream side. This is also the reason why alternatives to the gas neutralizer (like photo-neutralizers) are under development. Obviously, also the pumping capability of the system influences the amount of background gas.

Stripping of negative ions is highly undesired inside the acceleration region. As said before, this process generates secondary electrons and positive ions. When this happens inside the acceleration region, the electrodes drain both secondary species, being charge carriers as well as negative ions. Therefore electrons and positive ions gain energy that can cause high heat loads on the electrodes or to other components outside the acceleration region. In particular, positive ions, being accelerated in opposite direction with respect to negative charge carriers, may flow back inside the ion source, causing damage to source walls. Furthermore, because primary electrons from the ion source are suppressed, electrons generated by stripping reactions with the background gas are the main cause of high-energy electron production in the acceleration region (typically of the order of 20-30%). Another source of secondary electrons is the interaction of beamlets particles with the electrodes.

On the other hand, the stripping of ions after the GG is very welcome as it is critical for beam propagation: the beam maintains its integrity against space charge. This happens because the potential well of the beam formed by negative ions acts as a trap for positive charged particles outside the acceleration region, where there are no external electric fields to drain the created charges. The trapped particles compensate for the charge density of the beam, decreasing the depth of the potential well and therefore also decreasing the magnitude of the beam space-charge effects described above. This process is called space-charge compensation: beam divergence stops growing and repulsion among the beamlets too. Therefore beamlets remains well separated and their trajectories are parallel to the propagation direction.

2.5.4 Co-extracted electron issue and beam magnetic deflection

One of the most important issues associated to negative ion sources are the electrons co-extracted from the source together with the negative ions: electrons, being less massive that ions, acquire more velocity than ions when subjected to the same potential drop. This makes them dangerous, because they can seriously damage NBI components, depositing intense power loads. Thus co-extracted electrons need to be suppressed.

The magnetic filter field also certainly limits the flux of electrons from the driver to the extraction region and therefore the electron current on the plasma grid. This limitation is, however, not sufficient in practice and a “suppression magnetic field” applied directly on the grid apertures is used to limit the flux of co-extracted electrons.

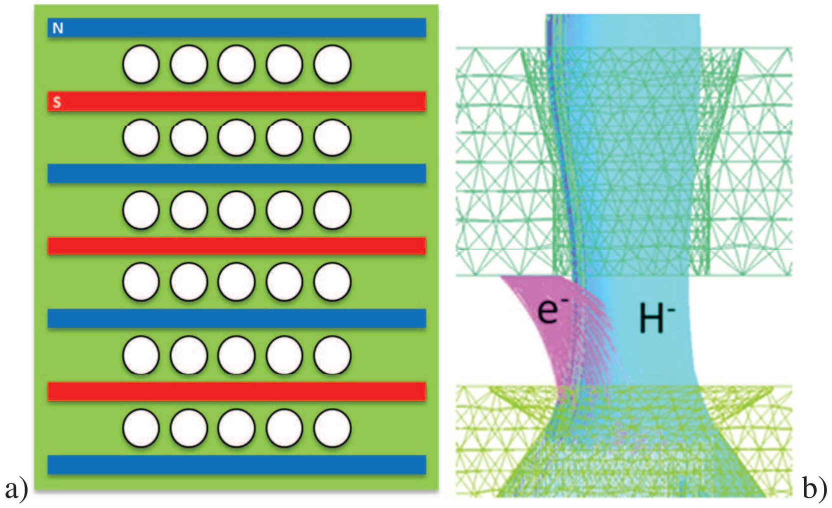

Figure 2.30: (Left) CESM position and orientation inside a generic EG. (Right) Effective co-extracted electrons suppression under the effect of CESM: electrons are deflected very much and are stopped on the EG surface. Negative ions, instead, being more massive that electrons, are only slightly deflected and are able to transmit through the EG with a residual deflection angle.

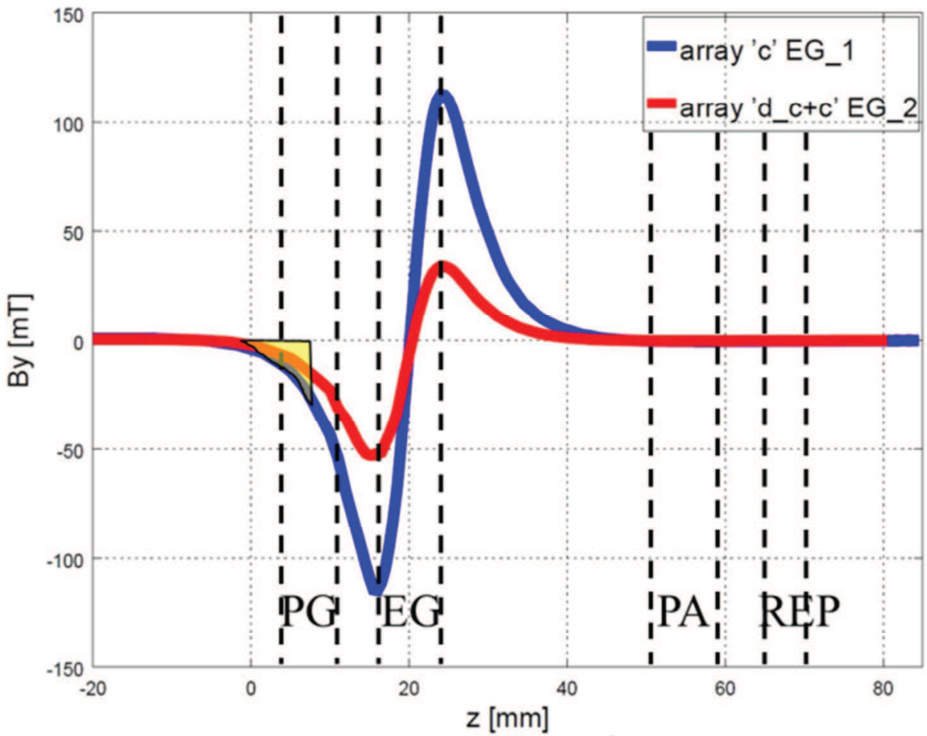

Figure 2.31: By component of the magnetic field generated by the embedded magnets inside the EG. The blue line correspond to a B_y generate only by CESM magnets. It is symmetric with respect to EG plane, but the beamlets miss the integral of the area highlighted in yellow, as it is beyond plasma meniscus. In practice the beamlets fells a non-symmetric B_y ad therefore they leave the GG with a residual deflection.

With this aim, usually the EG feature also some embedded magnets. These magnets are called Co-extracted Electron Suppression Magnets (CESM) whose B_y profile (see **Figure 2.31**) forces electrons to impact on the EG upstream face, while allows ions to pass through it, with a small residual deflection angle. These magnets are placed in between aperture rows and alternatively oriented. **Figure 2.30** gives an example of the typical CESM arrangement inside an EG and the effect of their magnetic field on extracted electrons and ions.

In multi-stage accelerators, such as MITICA, magnets having the same arrangement can be embedded in all the acceleration grids with the purpose to deflect the electrons produced by stripping reactions with the background gas.

Concerning the beamlet residual horizontal deflection at the accelerator exit, this is a non-negligible drawback of the use of CESM magnets as it can seriously compromise the overall beam optics. This deflection is related to a non-zero integral of B_y and as a first approximation, it can be estimated as the ratio of transverse velocity v_x and axial velocity v_z, according to the "paraxial approximation" formula [[**30**]:

$$\boldsymbol{\alpha_M = \frac{v_x}{v_z} = \frac{q\int_{z_0}^{z_{exit}} B_y dz}{m_i v_z} = \sqrt{\frac{q}{m_i}} \frac{\int_{z_0}^{z_{exit}} B_y dz}{\sqrt{2U_{acc}}}} \qquad 2.63$$

Looking at the CESM B_y profile in **Figure 2.31**, it can be noticed that it is symmetric with respect to the EG plane and thus its integral over z direction should be zero. However, from the point of view of extracted ions, since their trajectories start at the plasma meniscus, whose position is almost at the middle of the PG width, they lack the magnetic field contribution to the line integral along their trajectory corresponding to the yellow area of **Figure 2.31**.

Lastly the magnetic deflection α_M sums up to the electrostatic deflection α_E presented in section 2.5.3.1. As will be shown in section 3.4, it is important to distinguish the nature of the two deflections.

2.5.5 Beam residual deflection Correction

The magnetic deflection α_M is obviously an undesired effect of the use of CESM magnets. It can also be nonlinearly amplified by the electrostatic "divergent-convergent" lens effect, when the beamlet enters the lens with a non-zero angle with respect to the lens surface, like in optical lenses. This effect is stronger on the upstream side of the EG with respect to the downstream side. α_M also alternates row by row due to the fact that CESM magnet orientation changes accordingly, leading to a crisscross pattern of the beamlet footprints (see **Figure 2.32**). Hence deflection compensation of α_M is necessary in order to obtain a well-focused beam.

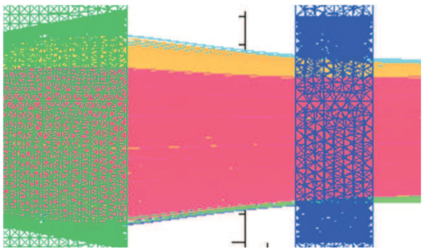

Figure 2.32: Particular of a 3D multi beamlet simulation, view from above. The picture shows two beamlets, in magenta and orange, passing through the EG (green) and GG (blue). It is possible to see the typical crisscross deflection of the beamlets caused by CESM magnets. The magenta beam is deflected rightward, since its position inside the grid aperture is not symmetric with respect to the central axis. The orange beam is also deflected, but leftward.

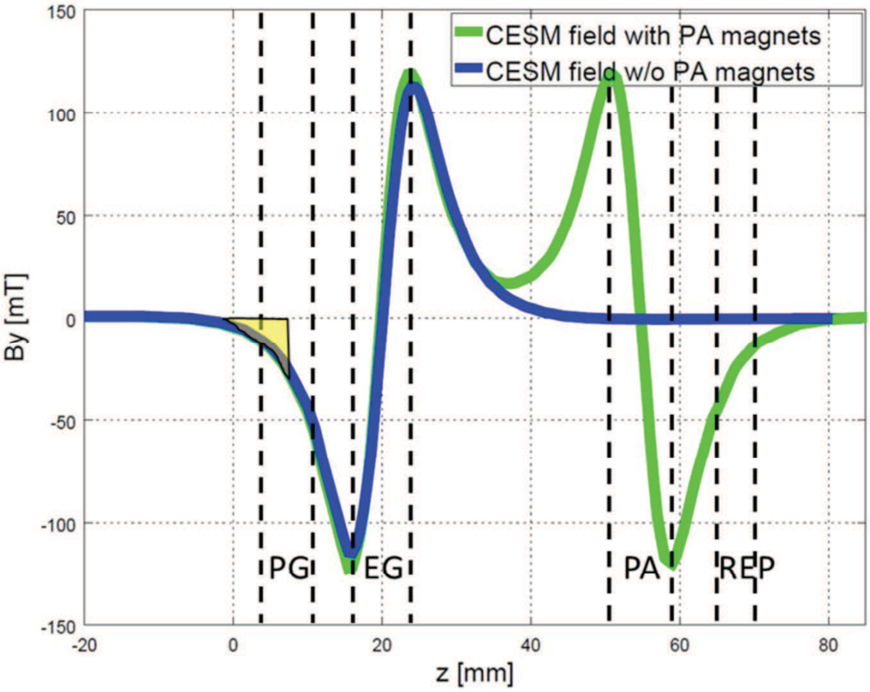

Figure 2.33: Example of magnetic compensation of α_M by means of a second set of magnets embedded in the electrode after EG, here named PA. The yellow area highlights the zone where the B_y enters the source plasma and thus it does not affect the beam, blue line shows the B_y of the CESM magnet only, while the green line shows the sum of the B_y generated by both sets of magnets: in this case the two sets are identical in size and B_r, but they are oriented oppositely. The two sets were designed considering the gap length between EG and PG: the downstream tail of the CESM magnet and the upstream tail of the PA magnet overlap in such a way the integral of the green curve is zero if integrated from the downstream border of the yellow area.

There are essentially two possibilities to correct the undesired ion deflection: by means of electrostatic offset of the grid apertures exploiting the "divergent-convergent" lens effect, that can push the beamlet in the in the same or opposite direction with respect to the offset (depending on which grid the displacement was applied), or by means of a second set of magnets embedded in the electrode that comes after the EG with opposite magnetic orientation.

Of course, magnets located inside the subsequent acceleration grids must grant an opposite contribution to the total integral of B_y with respect to the one given by CESM magnets so as to cancel it. Considering that, in magnetic configurations like CESM, the magnetic field is usually symmetric with respect to the electrode plane, the only possibility to generate a non-zero contribution to the integral of B_y is to make the tails of the B_y generated by the two sets of magnets sum up in a fashion to make ions feel a zero integral of B_y (see green curve in **Figure 2.33**). This occurrence depends on magnet size, B_r and electrode gap length and therefore it can be hard to achieve and many technical constraints may arise.

2.5.5.1 A new way to correct ion deflection: ADCM magnets

In the last years a new magnetic compensation system was developed at Consorzio RFX, which is constituted by an additional set of permanent magnets inserted vertically just in between the standard CESM configuration (see **Figure 2.35**). These magnets are alternately magnetized along the vertical direction and are called "Asymmetric Deflection Compensation Magnets" (ADCM) [30] because they cause an asymmetric B_y profile. ADCM configuration, indeed, enhance the vertical component B_y on the upstream side of the EG while reducing it on the downstream side.

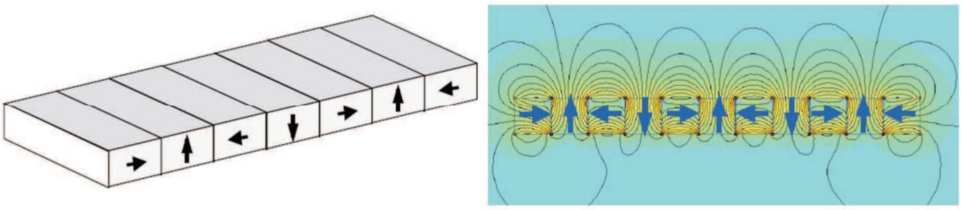

Figure 2.34: Scketch of the planar Hallbach array and of the B asymmetric B field generated.

ADCM can achieve this asymmetric profile because they are oriented, with respect to CESM, in such a way that CESM + ADCM configuration exploits the planar Hallbach array configuration, whose interesting feature is that, even if the structure is geometrically symmetric with respect to the plane where the structure lies, it produces a strong magnetic field only on one side of a plane (see **Figure 2.34**).

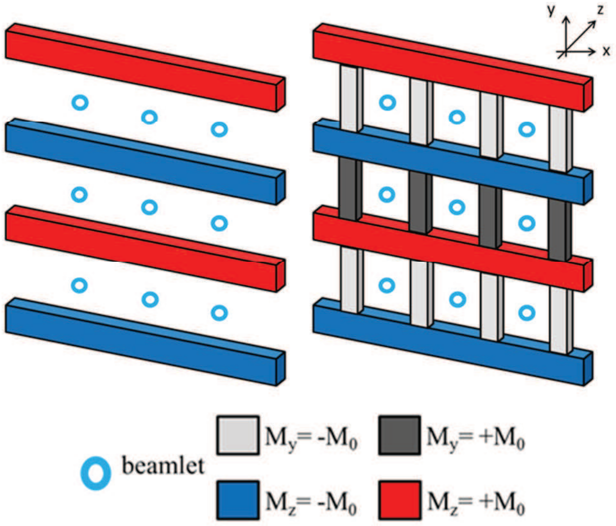

Figure 2.35: CESM only configuration in comparison with CESM+ADCM configuration in a 3x3 beamlets ion source. The orientation of each magnet is also reported.

This means that with a fine tuning of ADCM magnets size or $\mathrm{B_r}$, it is possible to achieve a $\mathrm{B_y}$ profile such that its integral is zero, cancelling α_M. Chapter 6 will be completely dedicated to the very first experimental validation of this new solution.

2.5.5.2 CESM and ADCM theory

I will try now to present a more rigorous discussion of the arguments presented in the last two sections, as it will be useful in section 4.4.2. The notation is coherent with [[**31**] to which this discussion is inspired and it is assumed to deal with a triode (three-electrodes) accelerating system: PG, EG and GG. Lastly, the quantities a_x, a_y, a_z, L_y are the geometrical dimensions of the magnets defined in **Figure 2.36**.

The line integral of H_y for a CESM array can be approximated by

$$\mathfrak{I}_y^c(z) \equiv \mu_0 \int_{-\infty}^{z} dz_1 H_y(x,y,z_1) \cong \frac{I_C}{(2\cosh k_0 z)} \qquad 2.64$$

where

$$I_C = -\frac{4B_r}{\pi k_0} \sinh(k_0 a_z) \sin\left(k_0 a_y\right) \qquad 2.65$$

k0=πLy. It can be noticed that the integral in $\mathfrak{T}ycz\equiv\mu 0-\infty zdz\,1Hyx,y,z\,1\cong Ic\,2coshk\,0z$ **2.64** vanishes for z→∞. Turning to the line integral of an ADCM array, a convenient approximation is

$$\mathfrak{T}_y^a(z) \cong I_A\,\mathrm{atan}\left(e^{k_o z}\right) + \left(\frac{1}{2}J_A - \frac{\pi}{4}I_A\right)[1 + \tanh k_o z] \qquad 2.66$$

with constants J_A and I_A (depending on ADCM a_x, a_y, a_z and B_r) given in [[**32**]; in particular $\mathfrak{T}_y^a(+\infty) = J_a$ which shows that the ADCM field line integral does not vanish, i.e. ADCM B field is not symmetric with respect to ADCM plane.

The deflection angle α_f after the GG is [[**32**]:

$$\alpha_f \cong \frac{e^{1/2}}{(2mV_t)^{1/2}} F_4[J_A - (I_A + I_C)(q_t + q_+) - (I_A - I_C)q_-] \qquad 2.67$$

with $V_t = V_a + V_b$ the total acceleration voltage, V_a the extraction voltage and an optical factor

$$F_4 = 1 - \left(\frac{2z_b}{f_2}\right)\left[1 - V_r + \sqrt{V_r + V_r^2}\right] \qquad 2.68$$

being $V_r = V_a/V_b$ and f_2 is the focal length of PA; expressions of q_t, q_+ and q_- (approximately given in eqs. (78) and (86) of [[**32**]) similarly include voltages, distances of electrodes and focal lengths.

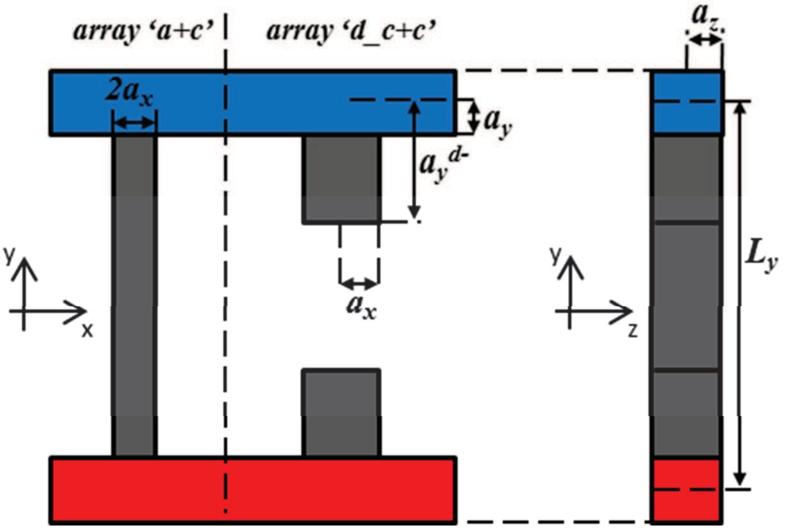

Figure 2.36: (a) xy cross section of CESM+ADCM configuration with array 'a' and 'd_c+c'

parameter definition. (b) corresponding zy section.

2.6 Simulation Tools

At Consorzio RFX a lot of effort is spent in the study of the beamlet optics in the multi electrode system of ion sources. Hence, there is a multitude of dedicated numerical tools to help these investigations. I'm providing a brief overview of the most used one.

As a premise, since the codes provide the divergence of every particle in the simulated beam, from now on, when addressing to beam divergence θ, I will refer to the θ_{rms}, defined as:

$$\theta = \theta_{rms} = \sqrt{\sum_i (\theta_i)^2} \qquad 2.1$$

where $\theta_i = \sqrt{\theta_{xi}^2 + \theta_{yi}^2}$ is the divergence of the single particle. The deflection in x direction, instead, is obtained as $\sum_i \theta_{xi}$ and a similar expression for y direction.

2.6.1 SLACCAD

SLACCAD [33],[34] is the evolution of the SLAC code that has been developed at Stanford Laboratories in the '70 to simulate electrons behaviour in linear accelerators. Negative ions in a free plasma boundary were introduced later. SLACCAD is capable to simulate negative ions behaviours inside a linear accelerator only under electric fields (**Figure 2.37**). It calculates self consistently the potential distribution generated by electrode and ion beam space charge distribution, solving Poisson equation. However SLACCAD can consider just a 2 dimensional axial symmetric geometry and neither magnetic fields nor second species, like co-extracted electrons, can be introduced in the simulation. Furthermore, it does not solve any plasma physic calculation and therefore meniscus position and shape are calculated simply by imposing a vanishing electrostatic field inside the simulation domain dedicated to the ion source area. In this way it takes into account the plasma property of self-shielding to external electric fields. Nevertheless SLACCAD is considered one of the most stable and efficient codes to calculate single beamlet optics for negative ion beams.

Due to its fast calculation capability and the easiness to change electrode geometry, SLACCAD is very useful to make rough and quick electrostatic simulations in different conditions. Thus it is possible to quickly figure out which are the best optical conditions for the beam optic (**Figure 2.38**). In this way is than possible to focus for a deeper investigation, with a more powerful and resources demanding code, like OPERA, just around the most interesting parameters found so far.

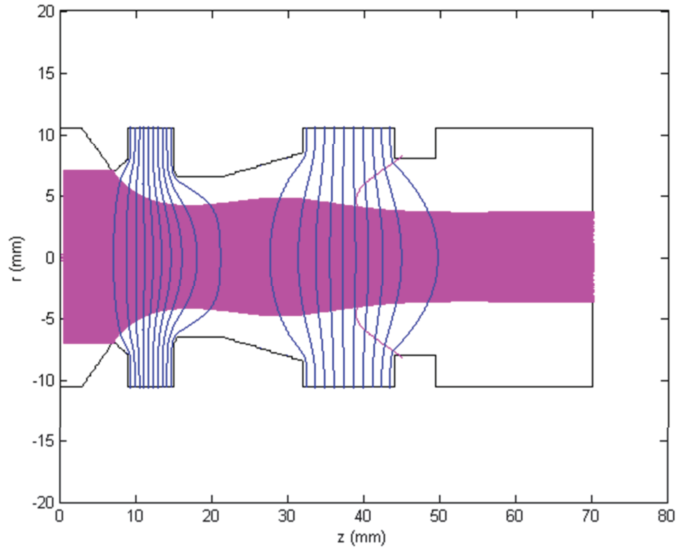

Figure 2.37: Example of graphical representation of SLACCAD simulations. It is possible to follow the particles trajectories (in magenta) through the grids. The blue vertical curves are the equipotential E field lines.

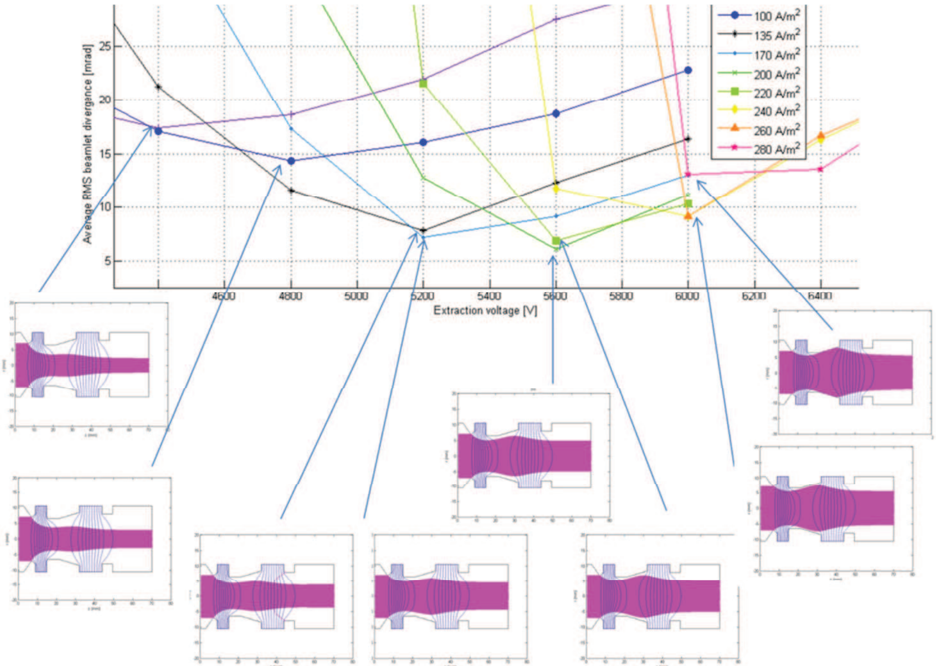

Figure 2.38: Each single point forming the curves in the divergence vs extraction voltage gap plot is the results of one single SLACCAD simulation. It is possible to appreciate the change of the shape of the beam envelope in function of the different parameters.

2.6.2 EAMCC

The code EAMCC (Electrostatic Accelerator Monte Carlo Code) was developed at CEA by G. Fubiani [35]. EAMCC can be considered the next step, with respect to SLACCAD, in simulations involving negative ions inside a linear accelerator. It also simulates just a single beamlet, but in a 3 dimensional axial symmetric geometry and even if potentials must be given a priory using potential maps generated by a third party code (like SLACCAD). EAMCC uses also a Montecarlo approach to consider the interactions with the residual gas and electrodes surfaces and the consequent production of secondary particles (see **Figure 2.39**). Moreover, it is also possible to introduce magnetic fields, by means of a magnetic field map generated by another code, in the same fashion as for the potentials.

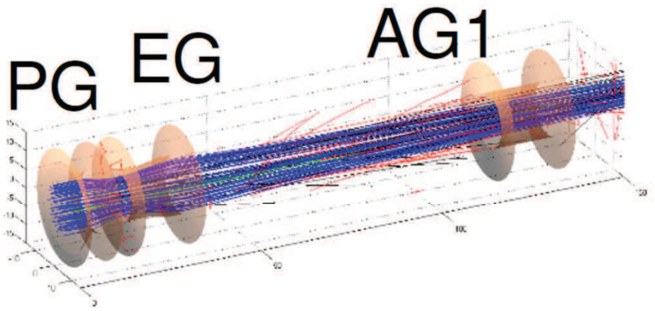

Figure 2.39: Example of EAMCC simulation result. The pink cicilders represents the grids apertures, while the blue line negative ions trajectories. The other lines represent secondary particles: electrons (red), positive ions (green) and neutral atoms (black).

EAMCC's simulations are slower that SLACCAD and it is used mainly to obtain estimations of the heat loads on the accelerator grids (**Figure 2.40**), and to acquire information on beam transmission and composition. In the past years the relativistic correction of the motion equation and the 3D geometry allowed this code to obtain reliable results on different geometry of interest [36].

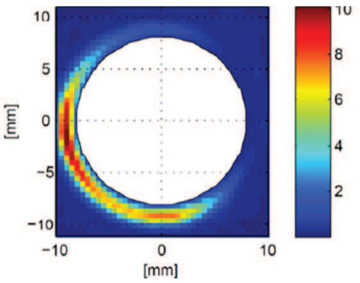

Figure 2.40: Example of power loads information obtained with a post processing of a EAMCC simulation.

2.6.3 COMSOL

COMSOL Multiphysics [[**37**] is a finite element analysis, solver and simulation software package for various physics and engineering applications, especially coupled phenomena, or multiphysics. It consists of various modules for the solution of different physics problems, Most of them can interchange information and data, often through interchange modules, in order to carry out analysis involving several physics to the solution of the specific problem.

In particular, regarding the analyses carried out for the benchmark here discussed, the Electrostatic and the Charged Particle Tracing modules were adopted, which can intercommunicate through the Electric Particle Field Interaction Multiphysics module.

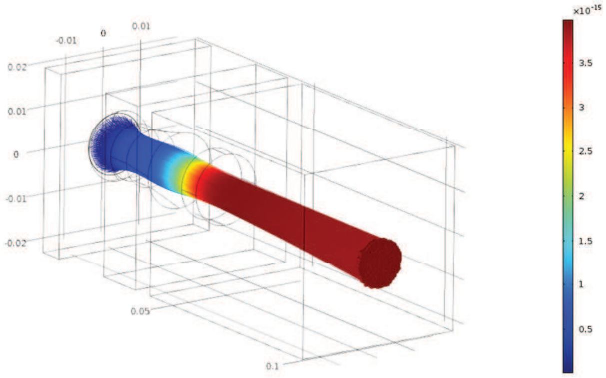

Figure 2.41: Examples of single beamlet simulation with COMSOL.

The self-consistent solution of the particle tracing problem taking into account the space charge of the accelerated particles foresees an iterative solution of the Poisson's equation for the calculation of the potential distribution due to the voltage applied to the electrodes and the updated space charge distribution. In Comsol this is done by the iterative solution of the equations implemented in the Electrostatic module for the updating of the electric potential distribution, and in the Charged Particle Tracing module for the updating of the charged particle positions.

The charged particle motion is influenced by both the electric and the magnetic field, which are introduced in the Charged Particle Tracing module through the Electric force and Magnetic force nodes. The magnetic field may be calculated through another module in Comsol for the solution of magnetic field problem, or, as in this case, can be imported from an external field map recorded in a text file. In this particular case the second option was adopted in order to use the very same magnetic field calculated in Opera, since the aim of the benchmark is only that of comparing the particle trajectory calculation method of the two codes.

Several methods can be adopted for determining how particles should enter the modeling domain and in the specific case the Release from Data File node was adopted in order to release particles in the same position and with the same velocity as it was calculated in Opera in correspondence to a beam cross section surface very close to the meniscus and corresponding to the narrowest position inside the PG apertures.

In these conditions, the benchmark between the two codes is carried out with the same geometry, same magnetic field, same initial electric field distribution and same initial particle position and velocity.

2.6.4 OPERA

OPERA is a well-known commercial code by Cobham [38], which uses the finite element method approach and is composed by several modules dedicated to different physical problems in a full 3D environment.

OPERA was the most intensively used tool to carry on the studies presented in this thesis. I had the possibility to work with the electrostatic and magnetic modules, called SCALA and TOSCA. SCALA is devoted to calculate the 3D space charge deposition of beams of particles solving the electrostatic Poisson’s equation, producing a potential map of the accelerator. Beamlet simulation is performed by launching a large number of macroparticles from an emitter surface that can be generated both manually, with an external ‘emitter file’, and, more recently, automatically with a dedicated tool called Plasma free-surface, that calculates plasma position and shape self consistently (a more detailed discussion is done later in this section). Secondary particles produced as a result of collisions with the grids can be included in the calculation, while stripping losses due to interaction with the background gas cannot be directly introduced, but can be implemented with a not dedicated tool. TOSCA, instead, focus on the magnetic field calculation generated both by permanent magnets and flowing currents.

The two modules can also be coupled to obtain the trajectories of negative ion beams in the full electromagnetic environment. However the two packages cannot be used at once: in order to perform a simulation considering both electrical and magnetic fields, a previously calculated magnetic map with a dedicated TOSCA simulations is needed, than this magnetic map has to be introduced in the SCALA model.

Moreover the flexibility in the geometry definition allows the simulations of several beamlets together (**Figure 2.42**), with the possibility to study the mutual beamlet-beamlet interaction and related effects. In this case, the plasma emitter tool cannot be used, as it encounters convergence issues.

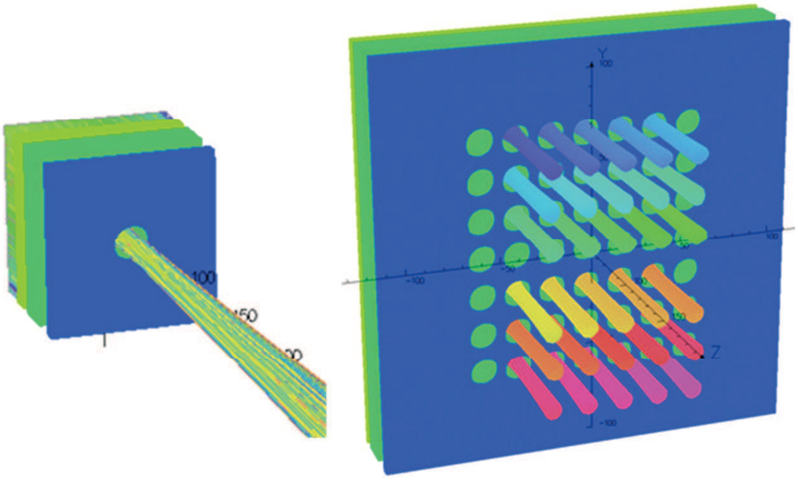

Figure 2.42: Examples of single beamlet (left) and multibeamlet (right) simulations with OPERA

The procedure to overcome this problem is to perform a single beamlet simulation first, record beamlet particles information about positions (x, y, z) and velocity (v_x, v_y, v_z) inside the PG aperture (meaning before that the beamlet-beamlet interactions due to space charge have already established) and use them to generate a proper multi-beamlet emitter file (by means of MATLAB) to use in the multi-beamlet simulation.

- OPERA plasma free-surface tool

As said in the previous paragraph, OPERA has recently included a plasma emitter tool capable to calculate meniscus shape and position in a self-consistent way. Information on current density, relative meniscus voltage and a temperature have to be specified. Space charge associated with the ion current leaving the plasma determines the meniscus position: a self-consistent space charge limited current flow forms beyond the meniscus and the program adjusts the meniscus position until the plasma's specified current density equals the self-consistent space charge limited current density. This Plasma free-surface emitter should be specified on a surface inside the plasma chamber, emitting towards the extraction aperture. The surface should have an assigned voltage equal to the expected plasma potential. The plasma meniscus will be formed in front of this surface (in the emission direction) and therefore the emitter surface must not be placed too close to the extraction aperture.

For benchmark purposes I have compared OPERA simulation results using the plasma free surface tool with the results using an the external emitter file generated from the simulation automatic meniscus simulation: it turned out that the two cases are in complete accordance, as shown in **Figure 2.43** .

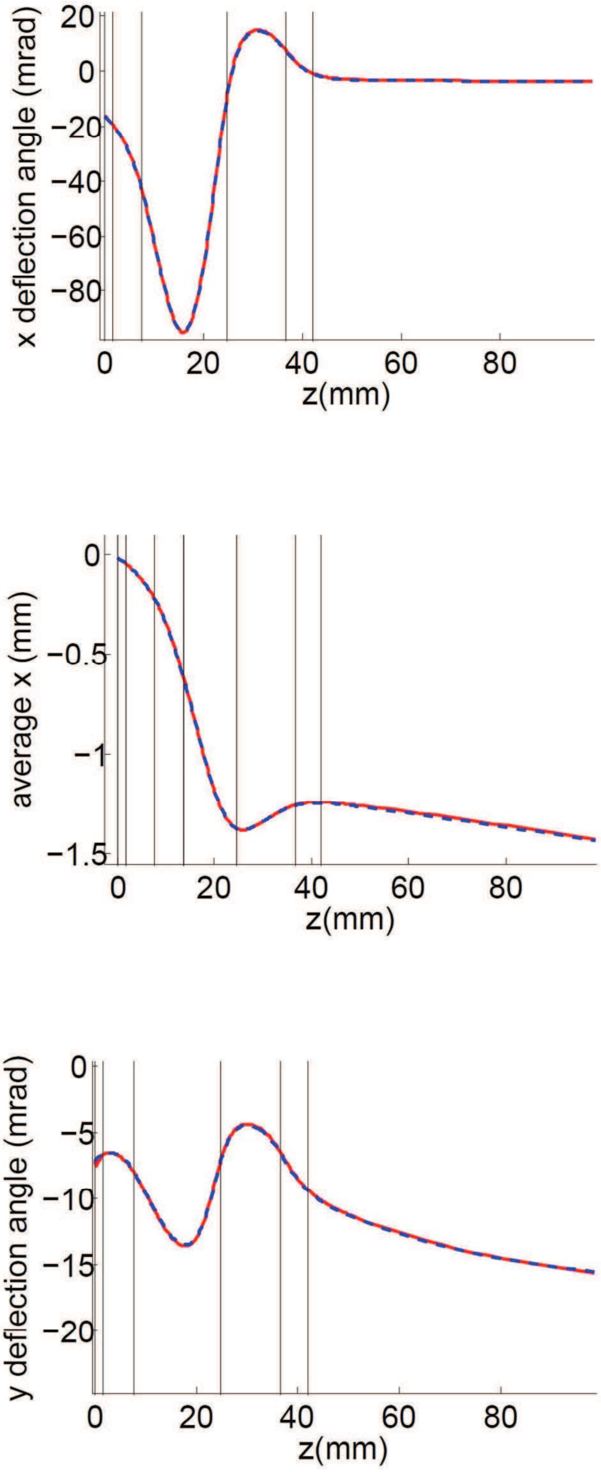

a)

b)

c)

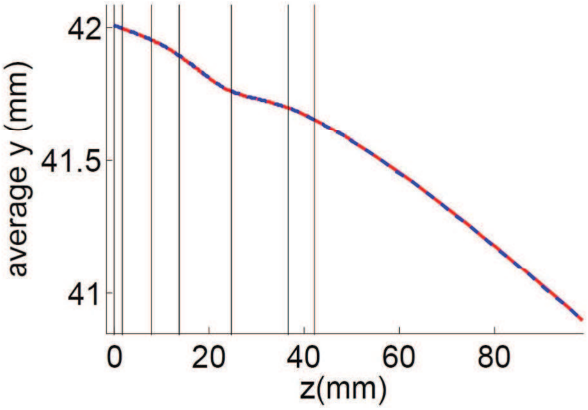

d)

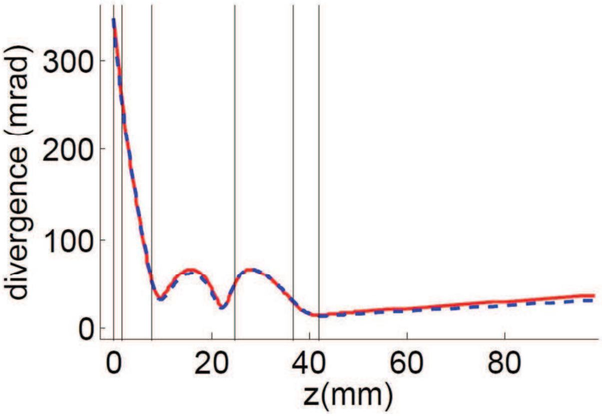

e)

Figure 2.43: Beamlet deflection average position on x and y directions and divergence along the beam path. Red curves correspond to the automatic meniscus simulation, while the blue dashed curves refer to the external emitter file simulation.

2.6.4.1 OPERA sensitivity study

OPERA is a resource demanding code and its simulation can last in tens of minutes or several hours, depending on the mesh size and how many physical aspects one wants to introduce in the simulation. Furthermore the plasma emitter tool was never used before, as it was included not long before I have started my PhD activity. Therefore, before using OPERA for beamlet optic investigation for the ion sources presented in the following chapters, I have made a sensitivity study of this tool. The purpose was to investigate the most suitable setting to use in the simulations in order to have the best accuracy with the maximum performance in evaluating rms divergence. Divergence is computed at the exit of the last electrode as usual and it is the main indicator for the quality of beam optics. This sensibility study is just a single beamlet electrostatic study, performed with the SCALA package only. Lastly, I used the three electrode system geometry of SPIDER, but this is does not really matter, as whatever geometry would have led to the same conclusions. The simulation domain ends up to 20 mm beyond the exit of the accelerator, where space charge compensation is assumed to be fully effective.

The sensitivity study is a step process. The first is the plasma emitter mesh dimension scan. The internal plasma emitter tool foresees that the number of particles used in the simulation depends on the mesh size of surface from witch the tool inject particles. In particular, each particle is emitted from the centre of the emitting surface mesh element (**Figure 2.44**). This means that increasing the number of elements (i.e. decreasing elements dimensions) the number of particles injected in the simulation increases accordingly. Considering that the more particles are used, the more accurate the simulation is, I'm now searching the best compromise between particles number and divergence accuracy.

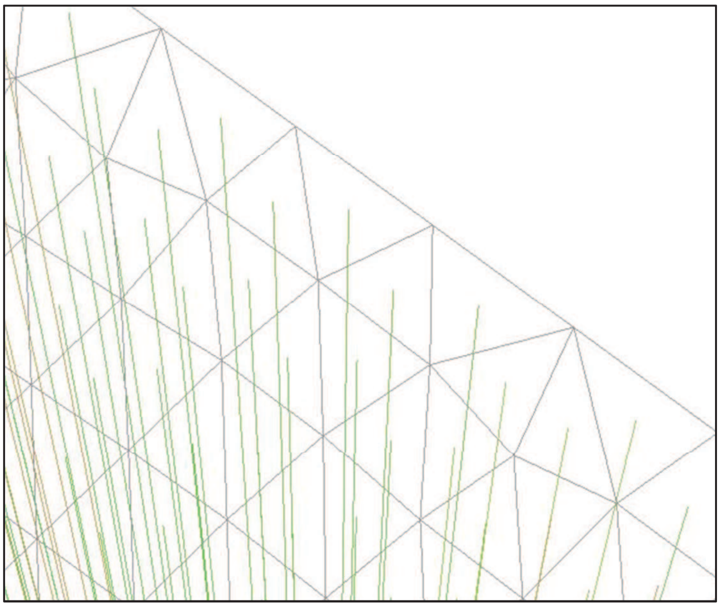

Figure 2.44: Example of the ions emitting surface. The grey tiangles are the mesh element of the surface. From the center of each element, an ion is emitted (green rays).

In **Figure 2.45** beam divergence is plotted against emitter surface mesh size in red and the number of particles resulted by the used mesh is in blue. Looking at the blue curve, one can see that the number of injected particles exhibits saturation going down with the mesh size. A possible explanation to this behaviour could be found considering that the choice of mesh dimension, is actually a choice of just its upper limit size (setting 1mm mesh size means that the surface mesh element can measure also less than 1 mm, but cannot exceed this value). Therefore, it may be that, starting from 0.6 mm maximum mesh size, the real mesh dimension associated to the emitter surface was already smaller, meaning that there is no much difference selecting smaller mesh limits.

On the other hand, one can observe that divergence decreases with decreasing mesh dimension. This trend shows a minimum plateau in correspondence to the blue curve saturation point, after which it increases again. The divergence plateau suggests that is not necessary to tight mesh dimension too much: from 1 to 0.6 mm mesh size, divergence remains the same within OPERA error (±0.5 mrad). In the end, even if the choice of 1 mm as mesh size could have improved performances, in order to be sure to stay in a safe condition, I have chosen the centre of the divergence saturation area as working point and, therefore, the mesh element size for the emitting surface will be 0.7 mm for the rest of OPERA simulations presented in this thesis.

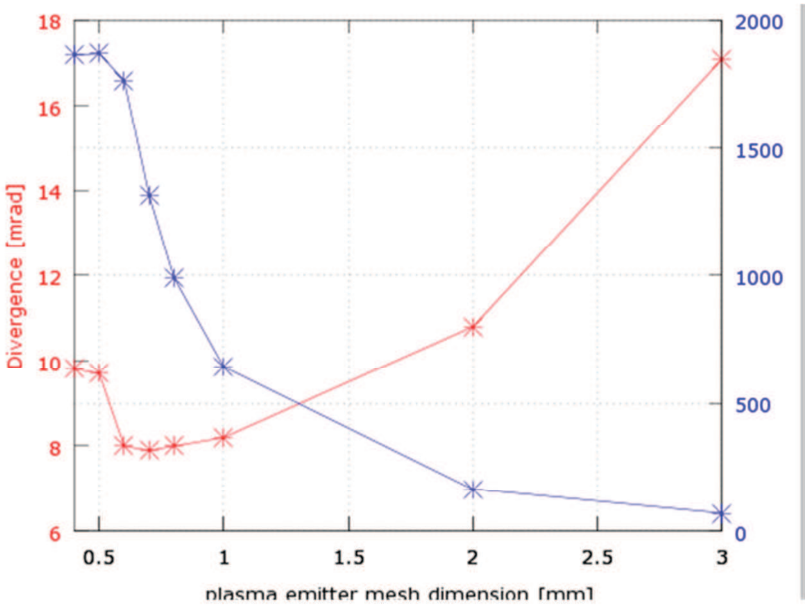

Figure 2.45: Sensibility of simulation to the emitter mesh dimension. The picture shows the divergence precision and number of particles in the simulation with respect to plasma emitter mesh dimension. When emitter mesh dimension is 0.7mm divergence precision saturates. Hence there is no need to further decrease the emitter mesh dimension.

Next step is the search for the lowest divergence (best beamlet optic) with an EG voltage scan in the range 9-10kV, as indicated in [39]. The result, shown in **Figure 2.46**, was also compared to the same scan performed with SLACCAD. It is possible to notice that the minimum of the two curves, and thus the best optical condition, does not correspond between the two numerical codes. They are far from each other about 500 V. SLACCAD curve (blue) is also more regular than OPERA one (red), meaning that SLACCAD accuracy is better for this kind of scans. Lastly, the first and the last points in OPERA curve behave a little bit differently from the other points, meaning that some external particles of the beam intercept grids walls. Anyway, even if the minimum of the SLACCAD curve should be more reliable, 500V tolerance for OPERA simulations can be considered acceptable. Therefore, in the last step of this study I have chosen −91kV as EG voltage, for the next step of the study.

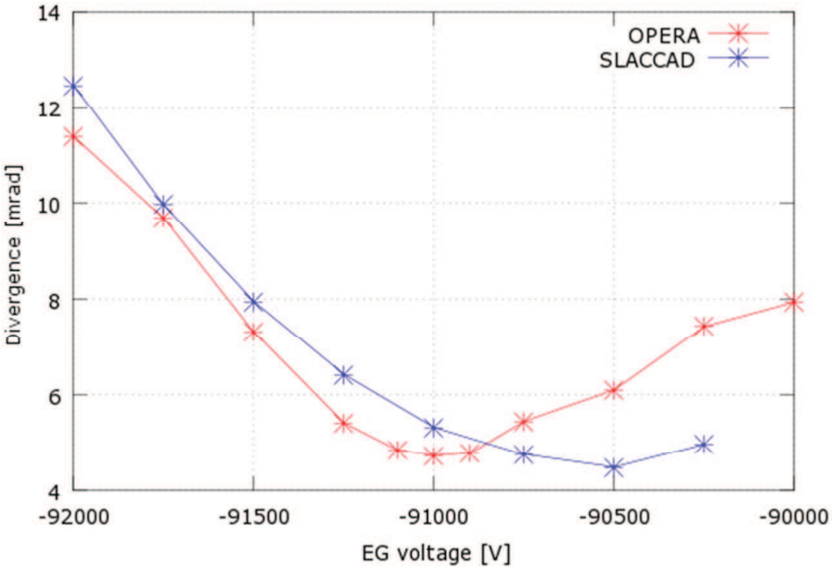

Figure 2.46: Divergence dependence with respect to the applied extraction voltage. The curve exhibits the typical 'smile' curve and the minimum represent the best optic condition for the beamlet. OPERA results (red curve) were compared with SLACCAD (blue curve): there is a 500V shift for the minimum of the two curves.

In simulations time-step integration is a usual parameter that determines the accuracy of the simulation: due to the computer calculation nature, simulation cannot follow a particle continuously, but a sampling frequency must be imposed. This means that if the time-step is too long one can lose information of what could have happened in between two time steps. For example, with a long time-step, the collision of a particle with the grid could possibly be missing and the particle will then continue to be transmitted inside the acceleration region, rather than be stopped. The drawback of a very small time-step is the performance decrease, of course.

The last step in this route is a time-step integration scan. Despite OPERA has not the possibility to change it directly, another parameter related to it, called Absolute time tolerance, can be set. For the sake of simplicity I'm referring to this parameter as integration time. The result is shown in **Figure 2.47**, where also a second scan (blue curve) with a greater emitter surface mesh dimension is juxtaposed. The need of this blue curve is explained in few lines.

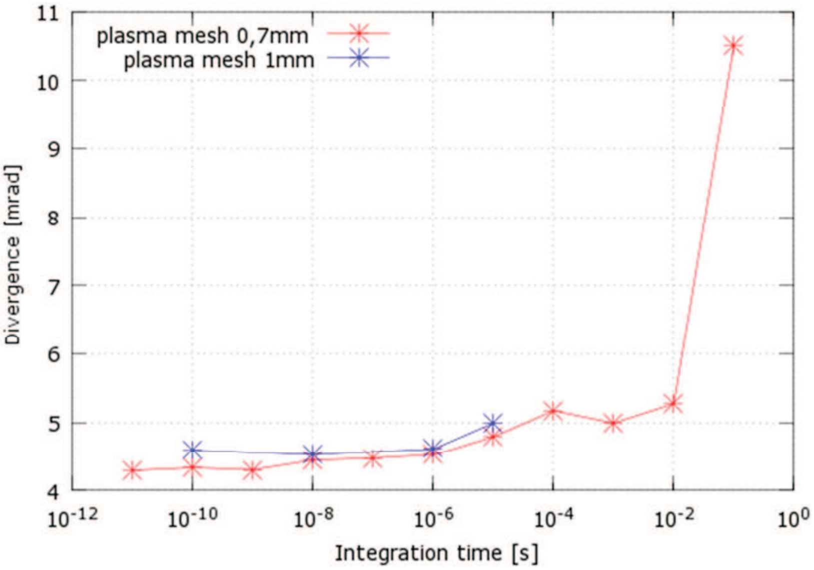

Figure 2.47: Sensibility of simulation to the integration time. The divergence precision is plotted with respect to the integration time of the simulation. Again, the precision of the divergence exhibits saturation when the integration time approaches 10^{-6} s.

The red curve shows a divergence decrease with decreasing time-step and thus increasing of the accuracy of the simulation. Anyway this trend exhibits saturation. Because divergence values in the range between 10^{-12} and 10^{-6} s are compatible within OPERA error, to make a double check from which value the trend saturates, the second scan (blue line) is added. For this scan, I chose 1 mm emitter mesh dimension as it is the value, also laying in the saturation area of **Figure 2.45**, for which simulations are much shorter. The blue scan shows that divergence trend starts to saturate at 10^{-6} s. So this was the time-step value I have selected for OPERA simulations.

3 Investigations on beamlets optic in SPIDER

This chapter presents the ion source SPIDER and the studies I have made on the solutions to improve beamlets optic. In particular the solutions foreseen in SPIDER for the compensation of electrostatic and magnetic deflections, were extensively investigated with multi beamlets simulations with OPERA. Furthermore, since SPIDER first beam is expected at the end of 2017, also an investigation for the most suitable operational parameters during its early operations was done. All the simulations are to be intended performed with the plasma emitting surface tool with the simulation parameters found in the last chapter.

3.1 SPIDER ion source

SPIDER is a full scale ITER radio-frequency plasma negative ion source design to feature an extracted negative ion current density of 355A/m2 (H^-) and 285A/m2 (D^-), particle energy of 100 keV and pulse duration of 3600s [39]. Three grids compose the extraction and acceleration system: plasma grid (PG), extraction grid (EG) and grounded grid (GG). Each grid features 1280 apertures, divided in 4 segments of 4 groups of 16x5 beamlets each (left part of Figure 3.1 shows a schematic of SPIDER grid apertures arrangement). At full extraction current density, both plasma source and PG are kept at -100kV and the EG at about -91kV.

Horizontal arrays of CESM $SmCo$ magnets ($B_r = 1.15$ T $\pm 3\%$) are embedded in between the apertures rows of the EG. As already discussed in details in section 2.5.4, the drawback effect of CESM magnets is a slight bending of the beamlets at the exit of the electrode system that has to be recovered. The principles of the recovery methods were already described in section 2.5.5 and SPIDER, or better its GG, was provided with both classical compensation methods for comparison purposes (no ADCM are foreseen). I will refer to the two systems as CESM field electrostatic (CESM-field-EC) and magnetic (CESM-field-MC) compensation systems.

In this sense, SPIDER can be considered as a test bed for the correction of the residual ions deflection.

Going deeper in the description for these two compensation systems, CESM-field-MC is constituted by horizontal arrays of $SmCo$ magnets embedded into the GG and a ferrite plate attached to the GG downstream side. The resulting magnetic field (red line in Figure 3.2) counteracts the horizontal bending effect caused by CESM-field (red line in Figure 3.2); the ferrite plate has the purpose to avoid magnetic field to continue to act on the beamlets further after GG. CESM-field-EC, instead, is based on proper GG horizontal aperture offset.

With reference to Figure 3.1, most of the SPIDER GG will be dedicated to the CESM-field-MC system (red areas), whereas the CESM-field-EC will be implemented in the green area only. Lastly, for the sake of comparison, the uppermost four beamlet groups (non highlighted area) are compensation free.

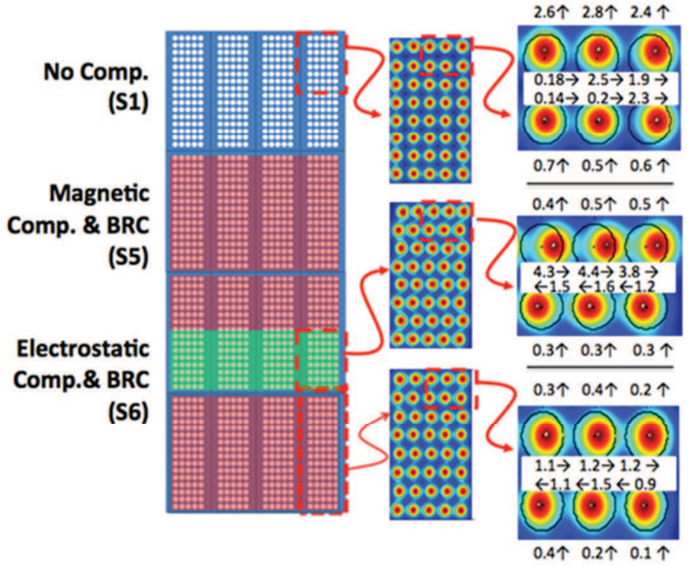

Figure 3.1: On the left hand side the SPIDER GG layout is presented. Red and Green colored areas highlight the CESM-field compensation systems arrangement. In the center, there are pictures of the results of the simulation corresponding to the various compensation zones, at nominal operational parameters. Also a zoom of the upper-right corners of the simulations are shown, with specified deflections in mrad: deflections of the uncompensated beamlet groups are higher than the compensated ones. In particular it is possible to notice that, as the compensation systems were designed in SPIDER, the magnetic compensation reduces deflections more that the electrostatic compensation.

3.2 SPIDER optical solutions design validation

The core of SPIDER optics investigation done in this thesis is focused on the residual beamlet deflection correction systems just presented.

As first step, I have repeated the OPERA simulation that in 2010 [40] brought to the design of the correction systems, using the plasma free-surface tool described at the end of section 2.6.3, that was not available previously. Doing this, only single beamlet simulations were performed, using the same geometry as in [39] and nominal operational parameters for hydrogen plasma: 355 A/m^2 current density and 100 keV beam energy. Lastly, in section 2.6.4.1 I have found that the best optical condition was provided by an EG voltage of −91 kV, with PG voltage −100 kV. Lastly, with respect to the simulations of the previous chapter, the domain of the simulations I extended to 20 cm, rather than few cm, beyond the exit of the accelerating region. The reason for this is that I wanted to be sure to get beamlet deflection information at a point where the magnetic field intensity is zero, so that beamlet deflection isn't affected anymore.

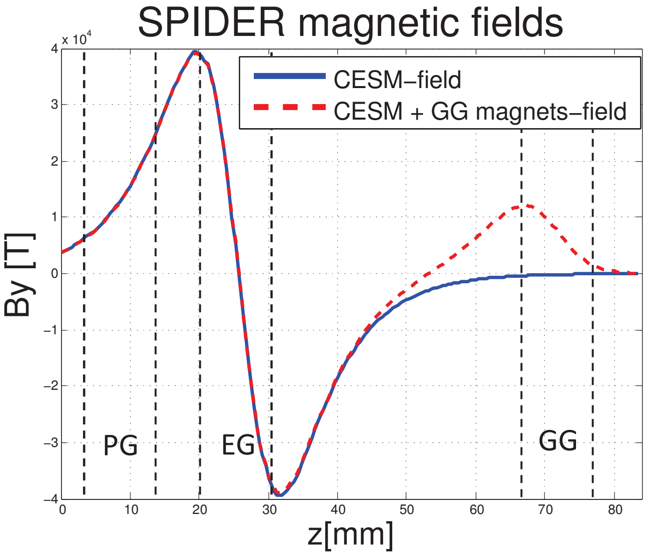

Figure 3.2: Magnetic fields in SPIDER: blue curve shows magnetic provided by EG CESM only, while red curve shows the magnetic field when the second array of $SmCo$ magnets in the GG is introduced. Grids positions are superimposed.

- Aperture's misalignment effect investigation

The relative position (misalignment or offset) between aperture and beamlet can produce a net deflection of the beamlet (section 2.5.5). This electrostatic effect is undesirable when the offset is caused by manufacturing tolerance and/or grid expansion under thermal loads.

In this paragraph simulations aimed to investigate possible effect on the beam of grids misalignment are presented. In simulations I have done scans of EG and GG aperture horizontal positions, from the theoretical on axis position up to 0.8mm offset, recording information about beam deflection in horizontal and vertical directions. Results are shown in **Figure 3.3** for EG and **Figure 3.4** for GG aperture displacement. Vertical deflection is not affected by horizontal offsets, as expected since the displacement has been applied only in the horizontal direction. Horizontal deflection, instead, exhibits a linear dependence with respect to the displacement of both EG and GG apertures. The results of this investigation are summarized in the first two rows of **Table 3.1**, where the information on slopes and intercepts were obtained with a linear fit of the mean deflection angle (α_E) of **Figure 3.3** and **Figure 3.4**. For comparison, corresponding 2010 results are also reported and a further comparison can be made looking at **Figure 3.7**: it can be observed that in 2010 deflections due to aperture offset were slightly underestimated. In particular the more remarkable difference is the angular coefficient of the GG aperture offset effect trend.

Table 3.1: Comparison between 2014 results and the 2010 results of the slopes of the red curves in figures from in **Figure 3.3** to **Figure 3.6.**

	2014		2010
aperture grid	slope	x=0	slope
EG	7,92	-0,05	7,7
GG	-7,28	-0,06	-8,06
EG $(j_n/2)$	7,73	-0,06	/
GG $(j_n/2)$	-7,17	-0,07	/

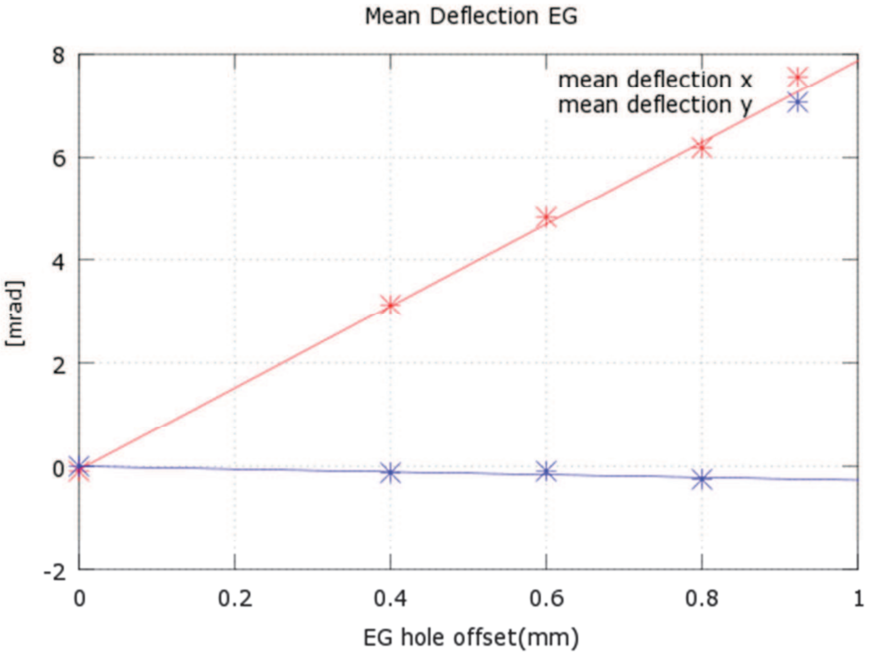

Figure 3.3: Electrostatic deflection α_E on both horizontal (redcurve) and vertical plane (blue curve) due to EG aperture horizontal offset. Nominal parameters are used.

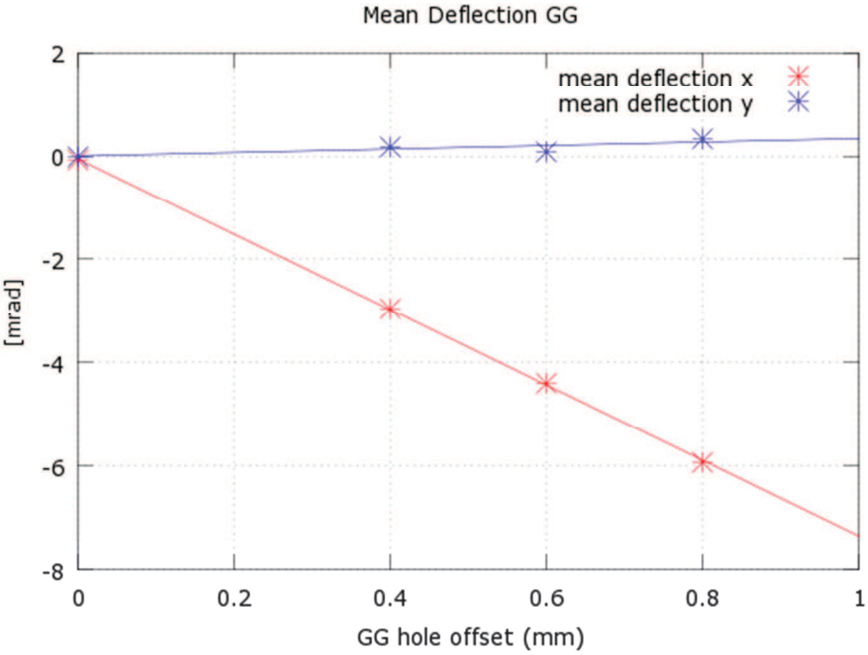

Figure 3.4: Electrostatic deflection α_E on both horizontal (redcurve) and vertical plane (blue curve) due to GG aperture horizontal offset. Nominal parameters are used.

The same simulations where repeated for half current density than the nominal one. As expected, the slope of the curve is reduced (last two rows of **Table 3.1**), because steering effect of aperture offset is an electrostatic effect a therefore it depends on the applied voltages.

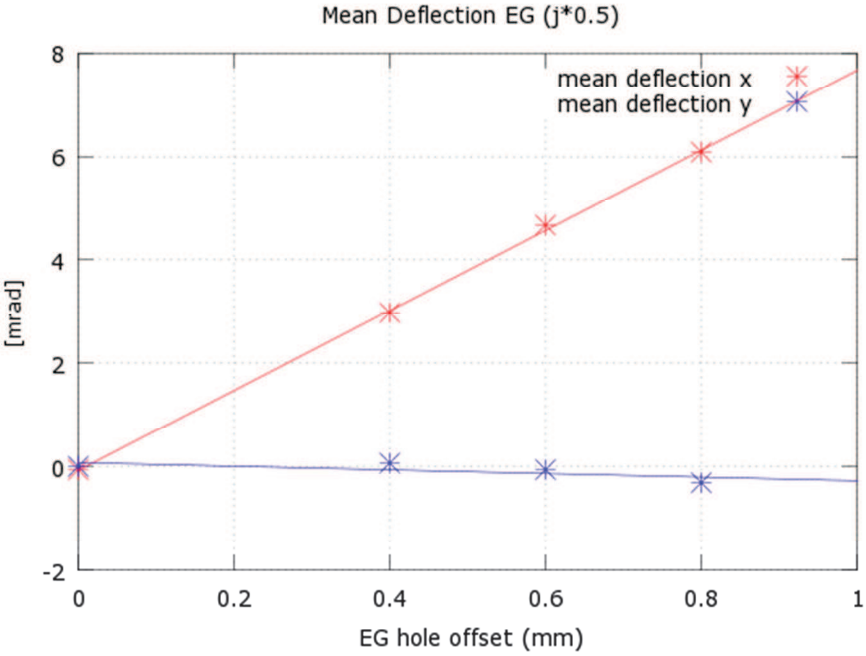

Figure 3.5: Electrostatic deflection α_E on both horizontal (redcurve) and vertical plane (blue curve) due to EG aperture horizontal offset. Half of nominal parameters are used.

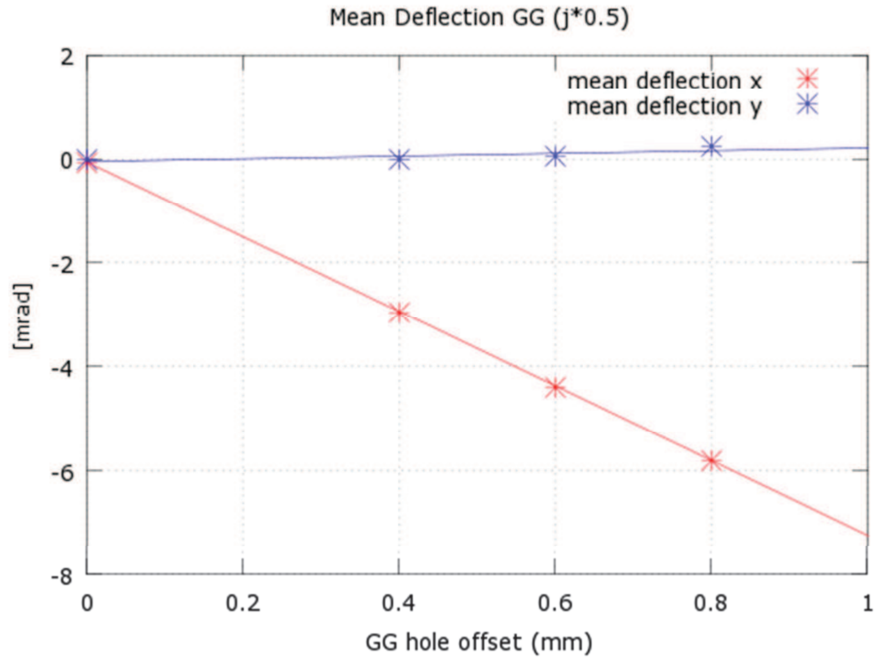

Figure 3.6: Electrostatic deflection α_E on both horizontal (red curve) and vertical plane (blue curve) due to GG aperture horizontal offset. Half of nominal parameters are used.

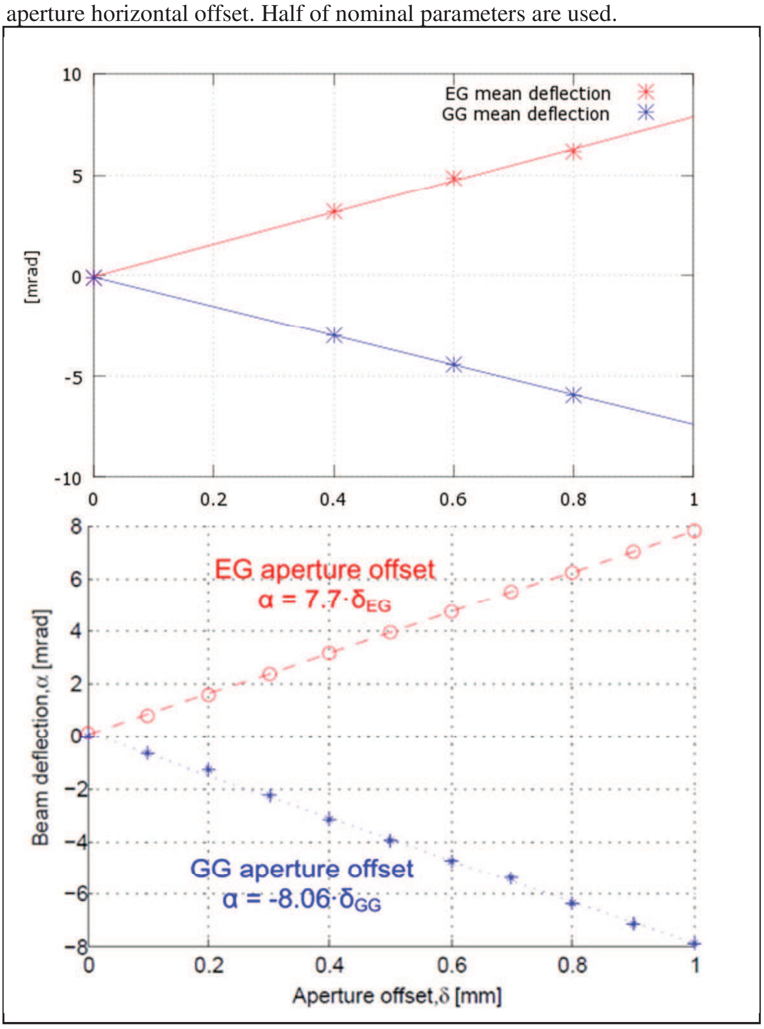

Figure 3.7: Comparison of the results of my investigation (upper part) and 2010 investigation (lower part) of the electrostatic horizontal deflection α_{Ex} due to EG (red curves) and GG (blue curves) aperture horizontal offset. More qualitative information are presented in Table 3.

- Residual deflection correction investigation

The most important aspect to investigate is the correction, with electrostatic and magnetic methods, of the residual deflection of negative ions beamlets caused by CESM magnets.

In order to do this, I had first to quantify the amount of the residual deflection. I have then modelled CESM magnets with a dedicated TOSCA simulation and retrieved a magnetic map. Introducing this map in the reference electrostatic simulation (the one in the best optic conditions and no aperture misalignment), I have figure out that this horizontal deflection is $\alpha_{Mx} = -6.55$ mrad.

As already said describing the ion source, SPIDER GG is provided with both electrostatic and magnetic compensation systems to correct the residual beam deflection. I'm now checking the design parameters of these two systems.

  - Electrostatic compensation

The electrostatic compensation part of the GG is done by aperture offsets, exploiting the effect of misalignment presented before. Using fits results in **Table 3.** for GG offset, one can find that, in order to correct the -6.55 mrad deflection due to CESM, the most suitable GG aperture horizontal offset should be -0.90 mm. Introducing this offset to the GG aperture of the reference simulation, I have found that the final beamlet residual deflection is, indeed, 0.03 mrad only. This value differs only slightly from the design values of -0.8 mm, found in 2010 [40].

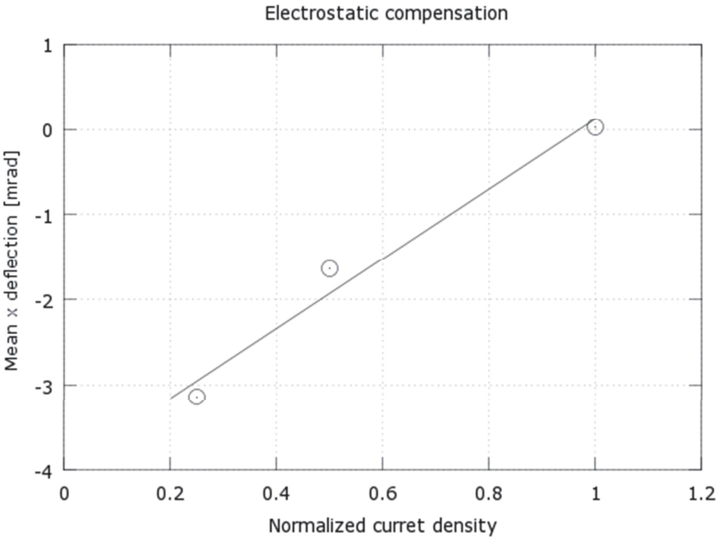

Figure 3.8: current density is normalized to the nominal value.

Furthermore, by repeating this simulation for current densities lower than the nominal one, the corrective effect of the aperture offset is again reduced (see **Figure 3.8**).

- Magnetic compensation

Magnetic compensation in SPIDER is done by mean of a new set of permanent magnets embedded in GG, in the same fashion of CESM magnets, but with opposite magnetic orientation and different B_r. Together with these magnets, also an hard ferrite grid is attached to the downstream side of the GG. Hard ferrite has the purpose to cut the downstream tail of the magnetic field generated by GG magnets, which, otherwise, would be symmetric respect to GG plane averaging away its effect: it is worth to remember that the same would occur also with magnetic field provided by CESM but its upstream tail entering the source plasma (section 2.5.4). **Figure 3.2** shows the total B_y profile generated by both CESM and GG magnets and the ferrite grid (red line), in comparison with the same profile generated by CESM only (blue line).

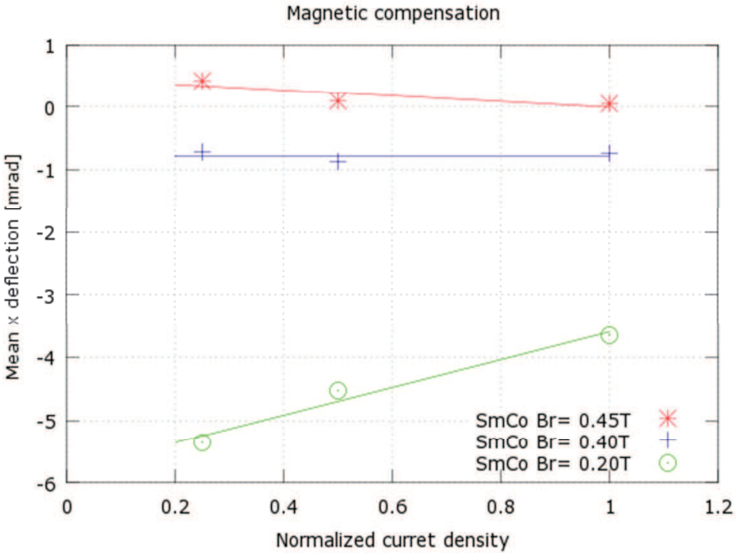

Figure 3.9: current density is normalized to the nominal value.

GG magnets are made of $SmCo$ as well as CESM magnets and their design B_r to achieve the complete compensation is 0.4 T. However, using this value the final horizontal deflection in simulation is still -0.74 mrad. Being the final deflection linear with B_r, with a simple linear extrapolation I have found that $B_r = 0.45$ T would provide a better compensation. Substituting this value to the design one in the simulation, the corresponding horizontal residual deflection is 0.04mrad only. Again, I repeated the simulation also at different current density and for three different B_r values. **Figure 3.9** shows the results. It can be seen that the recovering effect is constant despite the used current density. The $B_r = 0.2$ T case seems to suffer some numerical issues, as there is no reason it should behave differently.

Summarizing, the use of the new plasma free-surface tool provided by OPERA allowed noting that in 2010 the effect on the beam optic due to grids misalignment was slightly underestimated. This brought to the underestimation of the suitable GG offset: -0.8 mm instead of -0.9 mm. In the same fashion, also remanence field for magnetic correction through GG magnets was slightly underestimated: 0.40 T rather than 0.45 T.

Figure 3.10 shows the comparison between 2010 [40] and 2014 simulation results.

2014

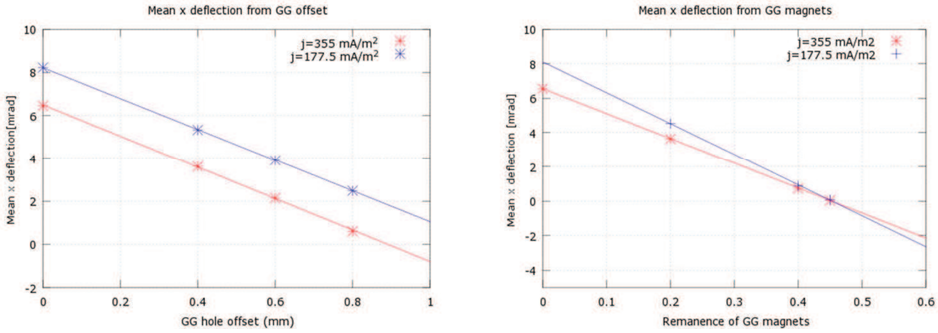

2010

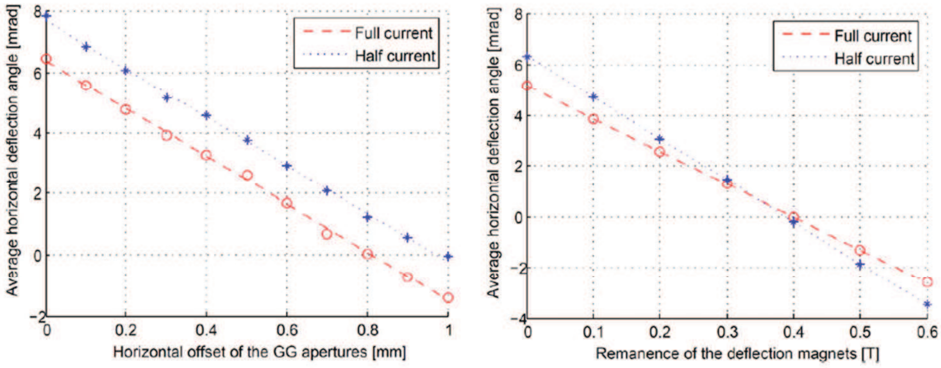

Figure 3.10: upper graphs refer to my simulations, while bottom to the one that brought to the design of the compensation systems in 2010. As results of my investigation, 2010 simulations slightly underestimate the design parameters (GG aperture offsets and GG magnets B_r) of the compensation systems for negative ion residual deflection due to CESM magnets. Anyway the residual deflection amount can still be considered acceptable.

As a matter of fact, most of SPIDER parts were already manufactured by the external companies in charge for the construction of SPIDER components. Therefore, although I have found slightly better design parameters, no further corrections to SPIDER design can be made although the magnet specifications might be changed. Anyway, from the practical point of view the underestimation of 2010 will not affect too much beamlet optics and the final deflection can still be declared acceptable.

Nevertheless an interesting conclusion can be retrieved by this investigation. Looking at **Figure 3.11**, where a comparison of the two correction approaches is shown, it is easy to realize that the magnetic compensation is a more robust solution than the electrostatic one: it can provide the right compensation also at lower current density values than the nominal one. Again, the same conclusion could already be drawn by looking at **Figure 3.10** as the electrostatic correction curves at different current densities are parallel, while the magnetic correction ones intercepts in the zero residual deflection.

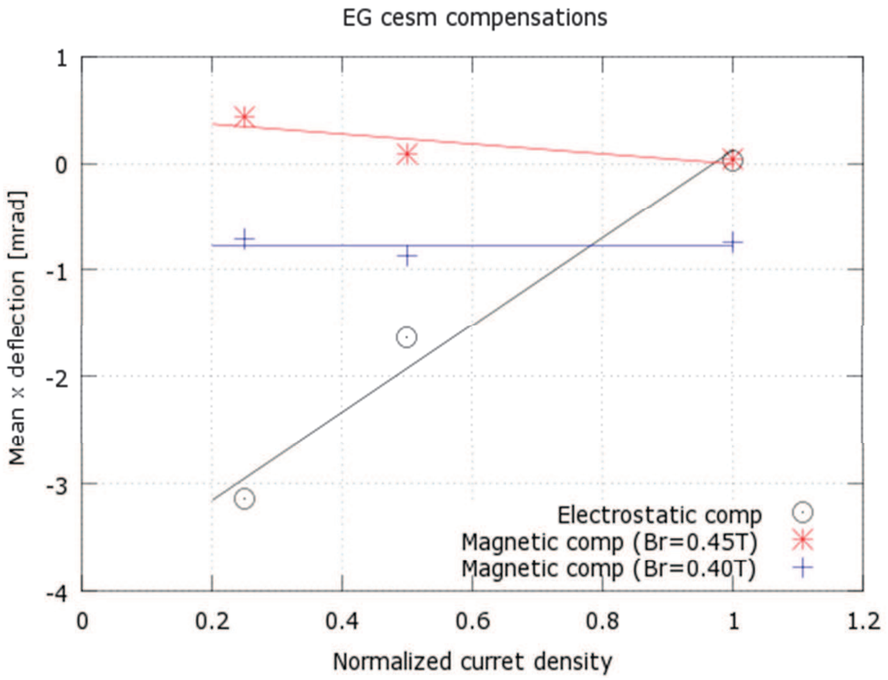

Figure 3.11: Comparison between electrostatic and magnetic compensation methods. The residual beam deflection due to CESM magnets with respect to extracted current density is reported and is possible to appreciate that the magnetic method is a more robust solution as it efficiently correct the residual deflection of the beam, at different operational parameters.

3.3 Multibeamlet simulations

In this section the multi beamlets simulations dedicated to assets the performances of the deflection compensation methods featured by SPIDER as they were designed in 2010 [40] will be presented, regardless the better design parameters found in the previous section. In this case, multi beamlet simulations are needed, because when dealing with multi beamlet ion sources, another issue has to be take into account: beamlets tend to repel each other due to the space charge that builds up also among beamlets. This happen mostly inside the acceleration region, since after the last electrode, space charge is compensated in few cm (section 2.5.3.4). In a schematic picture, if considering only two identical negative ion beamlets close enough to make them feel the space charge of each other, these repel each other, as said, and both undergo deflection. When adding a third beamlet to this system and arrange them in a row such as the distances are equally distributed, the one that is in the middle position will not be deflected because the space charge force of the two lateral beamlets is equal and opposite (see **Figure 3.12**). Hence, in an n-by-n beamlets system, only the most external beamlets will exhibit deflection due to space charge repulsion, since inner beamlets are surrounded by other beamlets that compensate for the repulsion.

For the sake of brevity, from now on I will address to this effect as beamlet repulsion (BR).

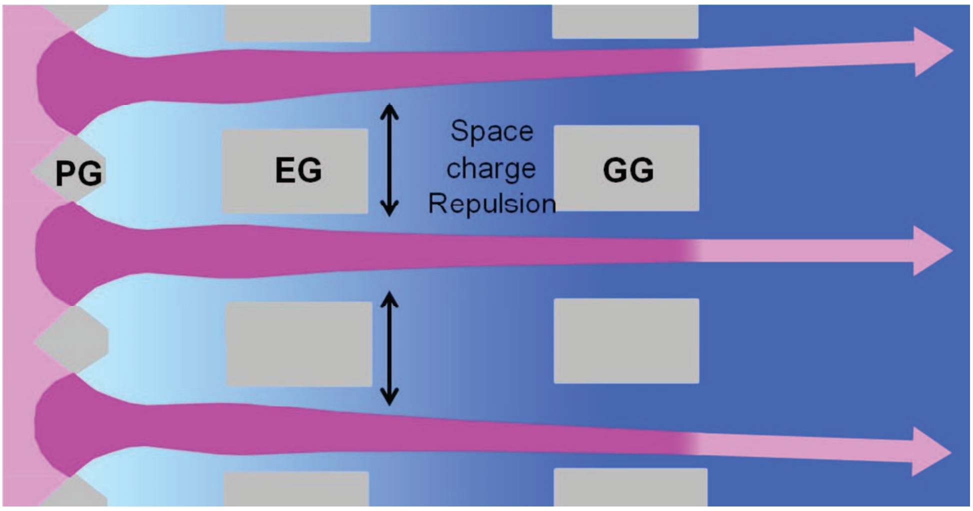

Figure 3.12: Schematic of beamlet repulsion due to space charge, in a multi beamlet ion source. The central beamlet does not exhibit any deflection because it undergoes the same amount of space charge from the lateral beamlets. Few cm after the GG the space charge is completely compensated by beamlets interaction with the background gas and deflections do not increase anymore.

In the end, BR consequence is the introduction of a further beamlet deflection that sums up to the magnetic deflection caused by CESM magnets. Being this deflection of electrostatic nature, one can think to exploit the aperture-offset mechanism, which is also of electrostatic nature, to correct it. This is the case of SPIDER, whose GG is provided with an aperture offset for beamlet repulsion compensation (BRC). Considering a single beamlet group (16x5 beamlets), these aperture offsets are provided both on the horizontal direction (in a symmetric pattern with respect to the central beamlet that has no offset, since it is not affected by deflection) and on the vertical direction. Regarding the latter, only on the two uppermost and lowermost rows are provided by vertical aperture offsets, because they are close to the edge of the beamlets group.

Turning to the deflection causes by CESM magnets, I have already said that part of GG will be provided by both electrostatic and magnetic compensation systems, referring to them as CESM-filed-EC and CESM-filed-MC respectively. CESM-filed-EC, exploits again the aperture offset to counteract the magnetic deflection. Hence, in the electrostatic compensated part of the GG, an additional aperture offsets were added to the previous BRC offsets. These new offsets are alternated from row to row in the horizontal direction, following CESM-field crisscross deflection pattern. The CESM-filed-MC, instead, makes use of a second set of magnets embedded in the GG. These deflection compensation solutions is distributed in SPIDER GG as described in section 3.1 and shown by **Figure 3.1**.

Deflection compensation systems were designed in 2010 with OPERA multi beamlet simulations [40], but just considering one row and one column. Now I want to crosscheck the effectiveness of these compensation systems by simulating for the first time a bundle of 8x5 beamlets, i.e. half a beamlet group. A complete beamlet group (16x5 beamlets) simulation would be too computational power demanding and therefore, I have preferred to exploit the up-down symmetry of the beamlet group.

3.3.1 Reliability of Multi-beamlet simulations

Before concentrating the efforts on SPIDER optic scenario, as this is the first time that a simulation concerning 40 beamlets at the same time is performed in our institute, the reliability of these simulations had to be proven. Since 1x5 and 16x1 beamlet simulations have been already considered reliable, the simplest way to crosscheck the 40 beamlets simulation reliability is to compare their results.

Being the 40 beamlet simulation in a 8x5 beamlet arrangement, the comparison is done between one of its row with the 1x5 beamlet simulation and one of its column with a 8x1 beamlet simulation, rather than a 16x1. Doing this, deflection and divergence results of corresponding beamlets are supposed to be almost identical, as the single row and single column simulation were performed taking care to reproduce the same boundary conditions of the central row and central column of the 8x5 simulation. The same comparison is done with and without taking into account CESM-field. However, as this is just reliability test, no compensation systems is considered. Lastly, OPERA plasma free-surface tool is included by means of the procedure described in 2.6.3.

Table 3.1 defines the column and row coordinates and the position in mm for beamlets in the 8x5 beamlet simulations are also shown. Yellow marked cells highlights the beamlets used for comparison with the 1x5 and 8x1 beamlets simulations. Consider the coordinates defined by this table for the rest of the chapter.

Table 3.1: reference x and y position in mm of grids apertures, looking to the apertures from upstream. Reference beamlets for the single row and single columns simulation are marked.

		Columns				
	coordinates	-2	-1	0	1	2
Rows	8	x-pos= -40 y-pos= 154	x-pos= -20 y-pos= 154	x-pos= 0 y-pos= 154	x-pos= 20 y-pos= 154	x-pos= 40 y-pos= 154
	7	x-pos= -40 y-pos= 132	x-pos= -20 y-pos= 132	x-pos= 0 y-pos= 132	x-pos= 20 y-pos= 132	x-pos= 40 y-pos= 132
	6	x-pos= -40 y-pos= 110	x-pos= -20 y-pos= 110	x-pos= 0 y-pos= 110	x-pos= 20 y-pos= 110	x-pos= 40 y-pos= 110
	5	x-pos= -40 y-pos= 88	x-pos= -20 y-pos= 88	x-pos= 0 y-pos= 88	x-pos= 20 y-pos= 88	x-pos= 40 y-pos= 88
	4	x-pos= -40 y-pos= 66	x-pos= -20 y-pos= 66	x-pos= 0 y-pos= 66	x-pos= 20 y-pos= 66	x-pos= 40 y-pos= 66
	3	x-pos= -40 y-pos= 44	x-pos= -20 y-pos= 44	x-pos= 0 y-pos= 44	x-pos= 20 y-pos= 44	x-pos= 40 y-pos= 44
	2	x-pos= -40 y-pos= 22	x-pos= -20 y-pos= 22	x-pos= 0 y-pos= 22	x-pos= 20 y-pos= 22	x-pos= 40 y-pos= 22
	1	x-pos= -40 y-pos= 0	x-pos= -20 y-pos= 0	x-pos= 0 y-pos= 0	x-pos= 20 y-pos= 0	x-pos= 40 y-pos= 0

Tables from **Table 3.2** to **Table 3.5**, instead, show data on average x (y) positions, deflection angles and divergences, comparing corresponding beamlets of the different multi beamlet simulations. Data are arranged in this way: 1x5 (8x1) simulation results on the left and corresponding 8x5 simulation results on the right.

- Simulation without CESM in EG

Table 3.2: 1x5simulation vs 8x5 simulation without CESM-field. As this beamlets row is surrounded by other beamlets rows, no vertical deflection caused by space charge repulsion is expected and thus not shown.

	1x5 simulation		8x5 simulation	
Hole position (mm)	Ave. x position	Deflection x angle (mrad)	Ave. x position	Deflection x angle (mrad)
-40	-0.07	-3	-0.06	-2.9
-20	-0.02	0.1	-0.02	-0.5
0	0	0	0	0
20	0.02	0,5	0.02	0.5
40	0.07	3	0.06	2.8

	Divergence (mrad)	
	1x5 simulation	8x5 simulation
Divergence range	5.0 – 5.1	7.4 – 8.1

Table 3.3: 8x1simulation vs 8x5 simulation without CESM-field. Vertical deflection is present only on the upper two beamlets because these are the only affected by the space charge repulsion in the vertical plane, as they are close to the border and they don't have further beamlets on top of them to compensate this repulsion. As other beamlets columns surround this beamlets column, no horizontal deflection caused by space charge repulsion is expected.

	8x1 simulation		8x5 simulation	
Hole position (mm)	Ave. x position	Deflection x angle (mrad)	Ave. x position	Deflection x angle (mrad)
154	-0.09	3	-0.08	2.6
132	-0.03	0.5	-0.03	0.7
110	-0.01	0.1	-0.01	0.1
88	-0.01	0.1	0	0
66	-0.01	0	0	0
44	-0.01	0	0	0
22	-0.05	0	-0.01	0.2
0	-0.05	0	0	0

	Divergence (mrad)	
	8x1 simulation	8x5 simulation
Divergence range	5.1 – 5.25	7.1 – 7.5

- Simulation with CESM in EG

Table 3.4: 1x5simulation vs 8x5 simulation with CESM-field As this beamlets row is surrounded by other beamlets rows, no vertical deflection caused by space charge repulsion is expected. Effect of CESM-field on the beamlets is visible, as average x positions at GG differ with respect to the case without CESM field.

	1x5 simulation		8x5 simulation	
Hole position (mm)	Ave. x position	Deflection x angle (mrad)	Ave. x position	Deflection x angle (mrad)
-40	-0.18	-11	-0.15	-11
-20	-0.12	-9	-0.1	-9
0	-0.1	-8.5	-0.1	-8.5
20	-0.08	-8	-0.1	-8
40	-0.04	-5.5	-0.05	-5.5

	Divergence (mrad)	
	1x5 simulation	8x5 simulation
Divergence range	5.5– 5.6	7.8 – 8.5

Table 3.5: 8x1simulation vs 8x5 simulation with CESM-field. Vertical deflection is present only on the upper two beamlets because these are the only affected by the space charge repulsion in the vertical plane, as they are close to the border and they don't have further beamlets on top of them to compensate this repulsion. As other beamlets columns surround this beamlets column, no horizontal deflection caused by space charge repulsion is expected, but only on by CESM-field. Horizontal deflections are anyway not reported.

	8x1 simulation		8x5 simulation	
Hole position (mm)	Ave. x position	Deflection x angle (mrad)	Ave. x position	Deflection x angle (mrad)
154	0.08	2.9	0.06	2.5
132	0.02	0.5	0.03	0.6
110	0	0.1	0	0.1
88	0	0	0	0
66	0	0	0	0
44	0	0	0	0
22	0	0	0.01	0.2
0	0	0	0	0

	Divergence (mrad)	
	8x1 simulation	8x5 simulation
Divergence range	5.6 – 5.7	7.5 – 7.9

The comparison of simulation results shows an average good accordance between the single row and column simulations with the corresponding beamlets of the half-beamlet group simulation. The largest difference can be observed for the divergence at the exit of the GG. This difference seems to be systematically ~2.5 mrad and is probably due to the different mesh used for the 8x5 simulation geometrical model, which was relaxed with respect to the 1x5 and 8x1 simulations to reduce computational time, still taking several hours.

3.3.2 Multi-beamlet investigation of the deflection compensation methods of SPIDER

The purpose of the simulations of this section is to investigate which will be beamlet optical scenario when SPIDER will operate at nominal operational parameters: current density of 355 A/m^2 (H-) and particle energy of 100 keV, at the beast optical condition found in section 2.6.4.1, i.e. EG voltage −91 kV with PG voltage −100 kV.

Briefly summarizing, in order to compensate for the two undesired causes of beamlet deflections at the exit of the acceleration region, i.e. beamlet repulsion (BR) and CESM field, SPIDER features three compensation systems: the electrostatic compensation system for beamlet repulsion (BRC) and the two compensation systems for the magnetic deflection, induced by CESM magnets, CESM-filed-MC and CESM-filed-EC.

In all simulations presented in the following paragraphs particular attention is given to the interaction of beamlets with the surrounding beamlet groups by means of suitable periodic conditions and the interaction of the beamlets with the background gas (stripping). In particular, stripping reactions have the effect of reducing BR. The used background gas profile (calculated with the AVOCADO [41][42] code) computes a reduction of beamlet current of about 14% at GG exit, while reducing deflection due to BR by about 0.3 mrad on average.

The effectiveness of the compensation system was proved with a 6-step process. These steps are presented schematically in **Figure 3.13**: each box represent a simulation, the black arrows indicate the logic of the succession of the various steps starting from the first box, while the red arrows indicate the direct comparisons allowed by the various steps. In more details, in the first simulation (S1) no magnetic fields and compensation systems are present and beamlet deflection is due to beamlets repulsion only. From the first simulation, two parallel simulations followed. In one, BRC is introduced (S2), allowing its validation making a direct comparison with the first simulation. In the other simulation, instead, CESM magnetic field only was introduced (S3). In this way, the residual deflection of the beamlets due to CESM-field only can be directly appreciated. The fourth simulation is the combination of the effects included in the previous two simulations (S4). From the fourth simulation two parallel simulations followed again, introducing the electrostatic (CESM-filed-EC) and magnetic (CESM-filed-MC) compensation systems for the residual beamlets deflection, respectively. The last two simulations eventually allowed the direct comparison of the two compensation systems for the magnetic deflection correction.

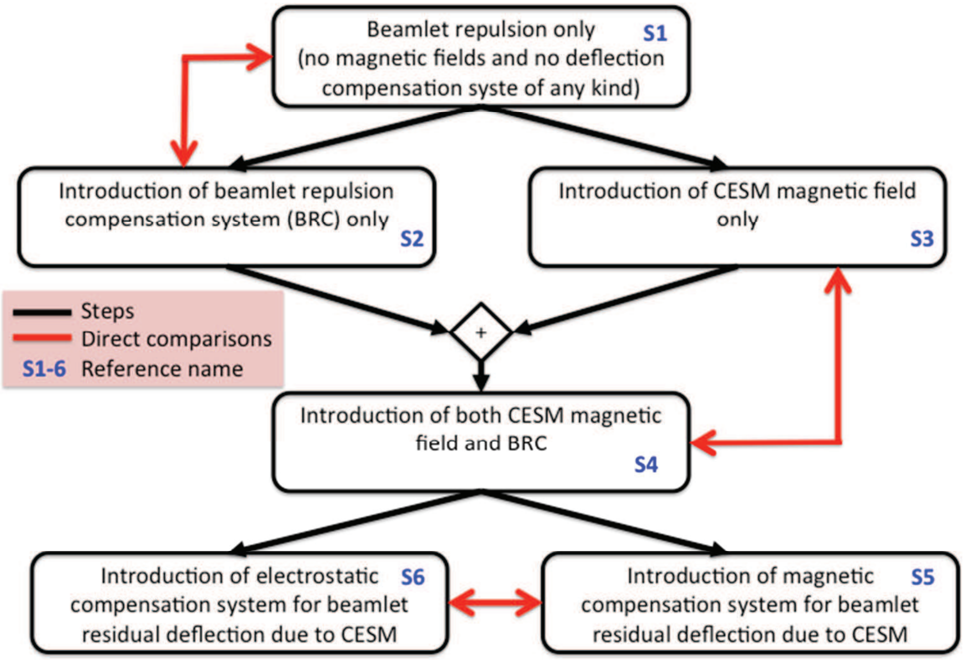

Figure 3.13: Schematic of the step process followed for investigating deflection compensation methods of SPIDER. In each box the reference name to each step is reported in blue.

The results of the comparisons indicated by the red arrows in **Figure 3.13** are summarized in **Figure 3.14**, **Figure 3.16** and **Figure 3.18**. There, the deflection angles θ are presented with respect to the rows or columns, whose coordinates respect **Table 3.1**.

Figure 3.15, **Figure 3.17** and **Figure 3.19**, instead, show the beamlet arrangement after linear prolongation of the particle trajectories to 1m from the GG, allowing a more intuitive comparison of each case. In particular, in these pictures the relative positions of each beamlets is presented with respect to the PG aperture positions. This means that the beamlets whose position in centred with the position of its respective PG aperture has exited the acceleration system with no deflection. Lastly, it has to be noticed that these are not just qualitative pictures, as they are the result of the post processing of the 40 beamlet simulations with a dedicated MATLAB script.

- Simulations results
    - Validation of BRC system

Figure 3.14 compares S1 (dashed black lines) and S2 (solid red lines) and same markers are used for corresponding beamlets in the two simulations. On the left hand side, the picture shows vertical deflection angle results only for row 7 and 8, because the effect of beam repulsion on vertical axis is seen only on the two uppermost rows. The right plot, instead, shows horizontal deflection results and for the central column 0 and the columns 1 and 2 only. Columns -1 and -2 are not reported for symmetrical reasons. In both plots, rows from 1 to 4 are not shown, since they are similar to row 5. It is possible to notice that the effect of the BRC is to push beamlets far from the centred position (the one marked in black) to a centred position (the one marked in red).

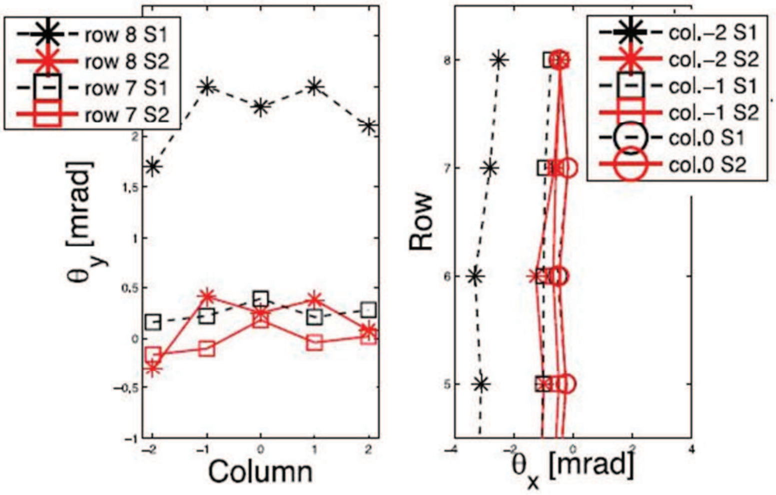

Figure 3.14: Vertical (left) and horizontal (right) deflections. Dashed black lines refers to the simulation without any compensation and beamlet repulsion is acting on beamlets only (S1) Solid red lines, instead, refers to the simulation considering only the compensation system for the beamlet repulsion (S2). Same markers are used for corresponding beamlets in the two simulations. In Both cases, beamlets far from the centered position (in black) are forced to stay centered (in red).

Figure 3.15 shows the expected beamlet arrangement after linear prolongation of the particle trajectories to 1 m from the GG, with respect to the EG aperture position, which don't have any offset like GG apertures.

This picture allows a more intuitive comparison of S1 and S2. On the left hand side (S1) beamlets on the border are not centred with respect to PG apertures due to the BR. On the right (S2), border beamlets positions are centred by the BRC system.

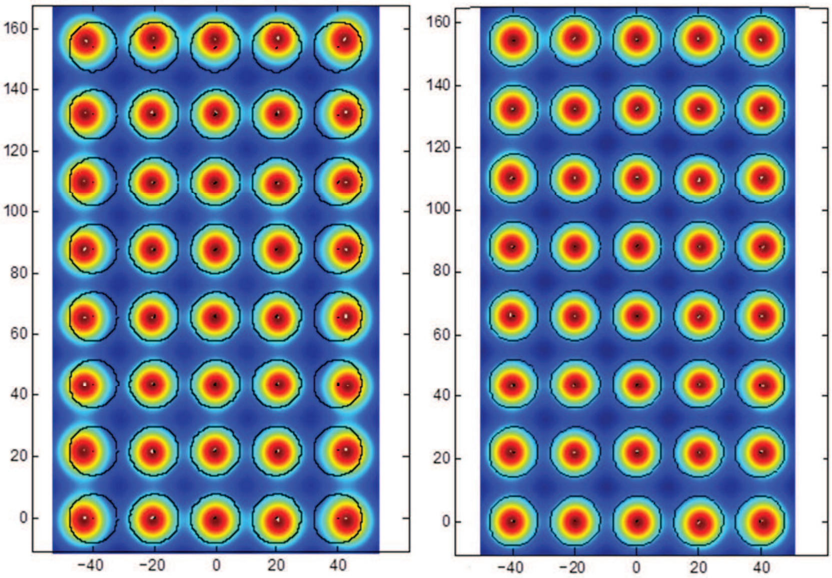

Figure 3.15: Beamlet arrangement after linear prolongation of the particle trajectories to 1m from the GG, for an intuitively comparison of S1 (left) and S2 (right). In S1 border beamlets are not centered due to the space charge interaction. In S2, instead, the corresponding beamlets are centered again thanks to the beamlet repulsion compensation system that exploits GG aperture offsets.

- Effect of the combination of electrostatic and magnetic deflection

Figure 3.16 shows results for S3 (dashed black lines) and S4 (solid red lines) horizontal deflections. Same markers are used for corresponding beamlets in the two simulations. For symmetry reasons, only the rows with positive deflection (even rows) are shown, while no results about vertical deflection are shown, since CESM-field acts only in the horizontal direction. From S3, it is possible to appreciate the breaking of the horizontal symmetry of the deflections among beamlets of different columns, caused by the combination of BR and CESM-field effects: they sum up positively on the right-hand side of the beamlet group and negatively on the left-hand side of the beamlets group. Eliminating BR thanks to BRC (S4) the symmetry is restored.

The same conclusion can be derived looking at the upper most rows of the two sides of **Figure 3.17**. On the left hand side (S3) the upper most row has a rotation around the beamlets direction (perpendicular to the picture). This rotation is almost cancelled-out in the right hand side of the picture

(S4) by the BRC system, which eliminates the beamlets repulsion effect.

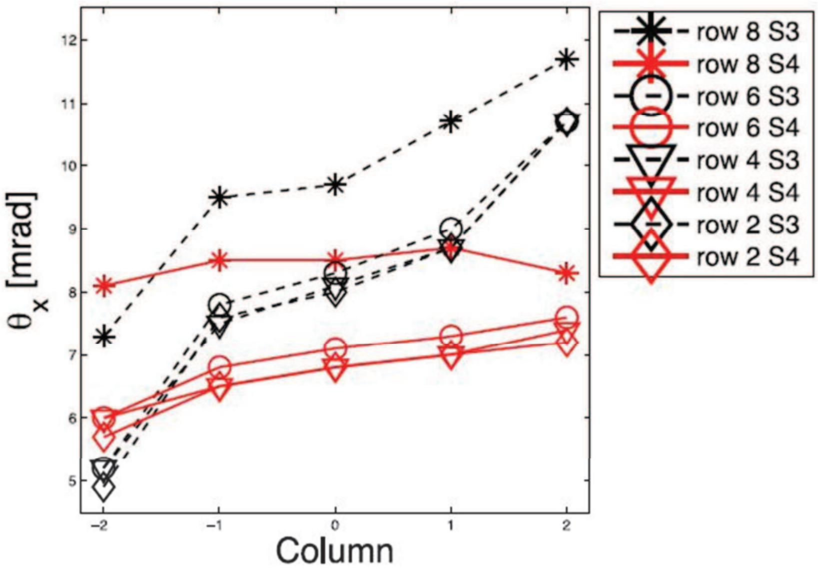

Figure 3.16: Horizontal deflections of the even rows (odd rows deflections are not reported for symmetry reasons). Both simulation feature CESM-field, but S3 (dashed black lines) has no BRC while S4 (solid red lines) has BRC. S3 rows are rotated due to the combination effect of BR and CESM deflection. The rotation is almost cancelled out by introducing the BRC, which eliminates the beamlet repulsion contribution.

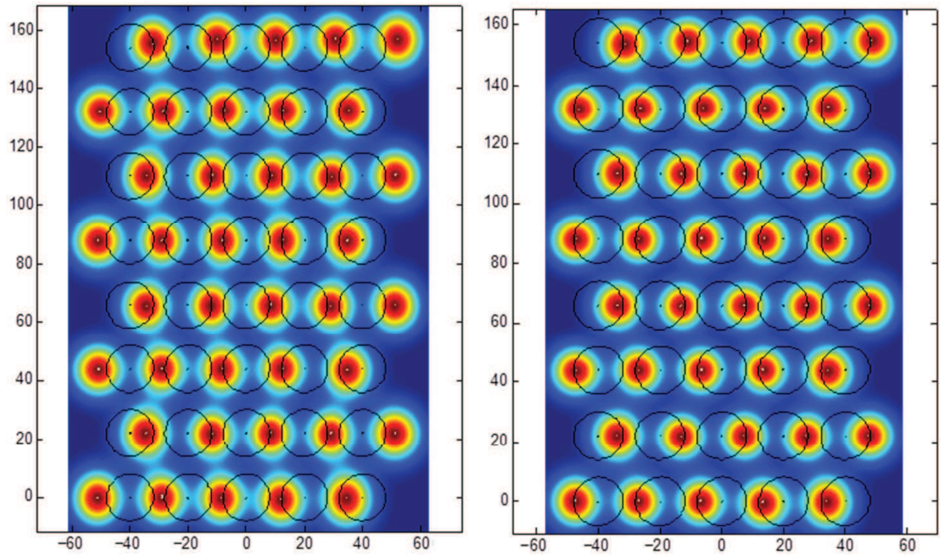

Figure 3.17: Beamlet arrangement after linear prolongation of the particle trajectories to 1 m from the GG, for an intuitively comparison of S3 (left) and S4 (right). Looking at S3 the two uppermost rows are slightly rotated with respect to the beamlet axis, as consequence of the combined effects of magnetic deflection end BC: they sum up positively on the right-hand side of the beamlet group and negatively on the left-hand side of the beamlets group. Introducing BRC, the rotation cancel out (S4).

- Comparison of CESM-field-EC and CESM-field-EC

Figure 3.18 shows results for CESM-field compensation systems. The magnetic compensation system results of S5 (solid red lines) and the electrostatic simulation system results of S6 (dotted blue lines) are reported together with the one of S4 (dashed black lines). In this way, the efficiency of the two compensation systems can be compared. As for **Figure 3.16**, only the even rows are shown and no vertical deflections are reported. Furthermore, since row 8 is the closest to the edge, beamlet deflections of this row differ from the ones belonging to the lower rows, which have, indeed, similar deflections, because they are in a symmetric configuration with respect to beamlet repulsion.

The results for S4, S5 and S6 simulations in **Figure 3.18** are well separated and it is easy to see that CESM-field-MC compensation system (S5) provides a better and almost equal corrective effect among beamlets of different rows, with respect to the CESM-field-EC one (S6). In particular, by comparing the highest deflection for row 8 at about 9 mrad, CESM-field-EC reduces this deflection to 4.7 mrad and CESM-field-MC to 1.2 mrad. This means a 48% and 87% correction effect for the two systems, respectively.

Deflection results for the most representative beamlet positions of the half beamlet group are specified in the right hand side of **Figure 3.1**, for the various part of SPIDER GG grid.

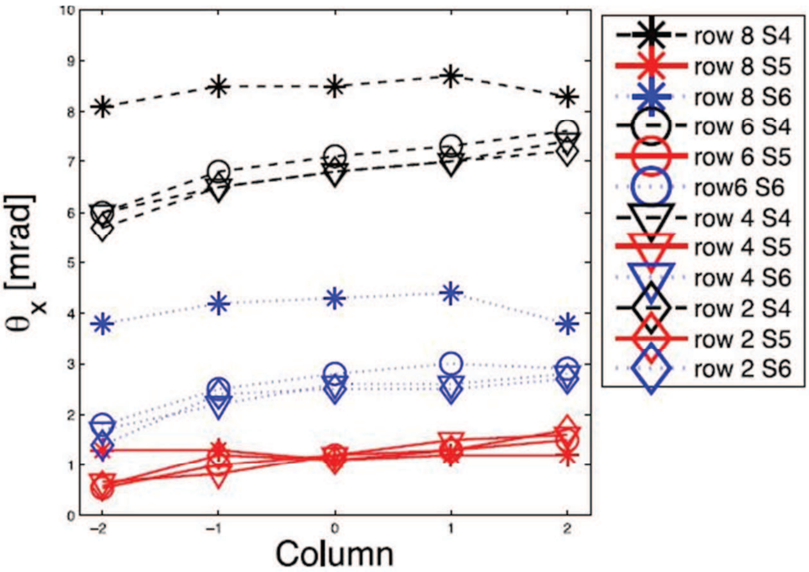

Figure 3.18: Horizontal deflections of the even rows (odd rows deflections are not reported for symmetry reasons). S4 (dashed black lines) shows the same results as red lines in **Figure 3.16**. S5 (solid red lines) and S6 (dotted blue lines) refer to the simulations with CESM-field-MC and CESM-field-EC compensation systems, respectively. It is clearly visible that CESM-field-MC cancel the deflection of the black lines quite completely. CESM-field-EC correction, instead, is only half than expected.

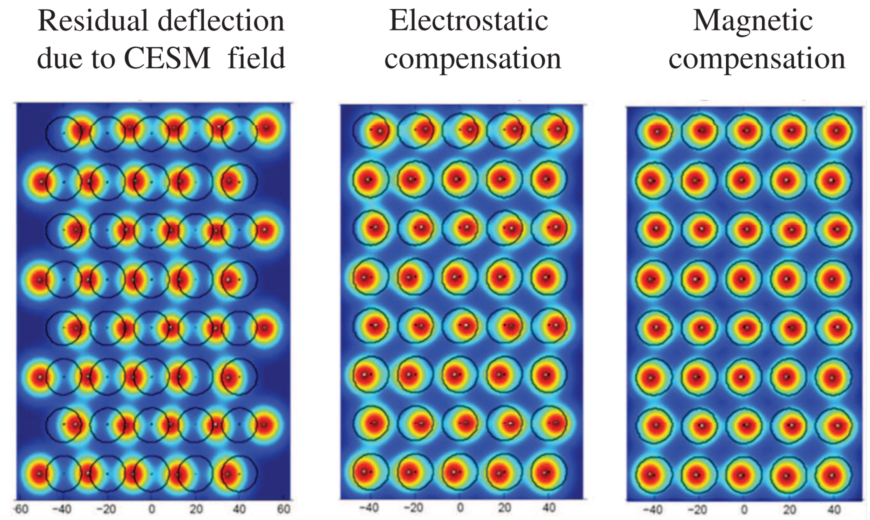

Figure 3.19: Beamlet arrangement after linear prolongation of the particle trajectories to 1 m from the GG, for an intuitively comparison of S4 (left), S5 (right) and S6 (centre). It is easy to see that as they were designed, the magnetic compensation system corrects the residual deflection more effectively.

- Results Overview and further considerations

From simulations results presented so far it is possible to assess the efficacy of beamlet deflection compensation systems in SPIDER as they were designed in 2010 [40]:

Concerning BRC, results show that even if its performance is not perfect, it is capable to apply a very good correction to the BR anyhow, since beamlet deflections remain within 1 mrad on both the horizontal and vertical directions.

The same is true also for CESM-field-MC in correcting the negative ions deflection due to the non-symmetric CESM-field: horizontal deflections of all beamlets lay around 1mrad or less (87% of correcting effect), which is considered acceptable. On the contrary, CESM-field-EC effect is not very good, applying only about half (48%) of the needed correction.

As final consideration, the underestimation of aperture offset effect on beamlet deflection highlighted in section 3.2 was high enough to reduce the effectiveness of the CESM-field-EC system to one half, while the underestimation of GG embedded magnets effect only slightly reduced CESM-field-MC system effectiveness.

3.4 Early scenarios

The present section analyses SPIDER early scenario in terms of beam optics, with the purpose to prepare for the experimental activities. When SPIDER will be ready the common procedure is to carry out a first series of beam experiments devoted to attaining a reduced set of parameters. These experiments will allow a preliminary investigation of the source parameters and of the capabilities of the diagnostic system. This will be done without evaporation of cesium into the ion source and solely volume processes create negative hydrogen. Therefore the extracted negative hydrogen current is expected to be around or below one tenth of the nominal value.

- Beamlet optics

To take into account the reduced amount of extracted current density, the voltages applied to the electrodes in the simulations presented in this section are scaled accordingly with the Child-Langmuir relationship, preserving this way the best perveance condition found at nominal parameters in section 2.6.4.1 ($V_{GG}/V_{EG} = 100/9.1$ kV), as demonstrated in at the end of section 2.5.3.3.

In **Figure 3.20** the expected divergence was computed for various extracted current densities, j_{extr}, and extraction voltages, V_{EG}, by means of SLACCAD code. The curve obtained with the nominal extracted current density, j_{extr0}, is also presented, on the rightmost part.

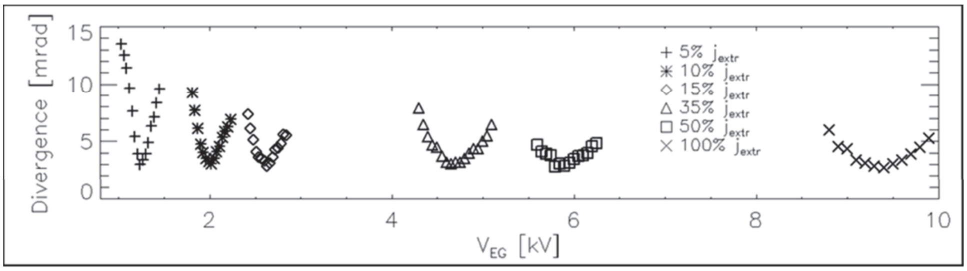

Figure 3.20: Divergence as a function of V_{EG} for different j_{extr}. The rightmost 'smile' curve correspond to the one at nominal parameters.

However, the lower the extraction voltage, the higher the deflection of ions due to the permanent magnets embedded in the EG, so that the beamlets risk intercepting the electrodes. Though this is no big problem at low extracted current, it becomes higher and higher as power increase (the power is proportional to $j_{extr}^{5/3}$).

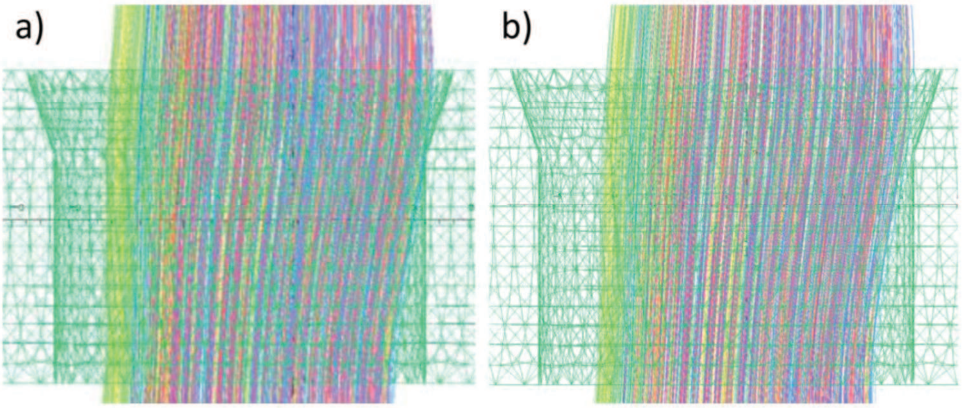

Figure 3.21: Trajectory of beam particles through EG apertures with CEMS magnets, at $\mathrm{j_{extr0}}/10$ and $\mathrm{V_{GG}} = 2.14$ kV: a) at $\mathrm{V_{EGmin}} = 2.02$ kV and b) at $\mathrm{V_{EG}} = 2.14$ kV.

Hence three-dimensional investigation is needed. The use of OPERA code, indeed, showed that, at the value of V_{EG} where the divergence is minimum, the beamlets scrape the internal surfaces of the EG apertures (Figure 3.21 b). An example is given for $V_{EG} = 2.14$ kV (larger than $V_{EGmin} = 2.02$ kV). This of course reduce beam optic quality, as the minimum perveance condition was left, and it results in an increase of the focal length, f, of the electrostatic lens at the EG aperture, becoming more defocussing. A way to counteract this effect consists in increasing accelerating gap potential difference. As already discussed in section 2.5.3.3, the divergence as a function of $\mathrm{V_{acc}}$ exhibits again the shape of a “smile”. Hence, another best optic condition is found when varying V_{GG} (Figure 3.22): in the case $V_{EG} = 2.14$ kV, the minimum divergence is found for $V_{GG} = 22.4$ kV.

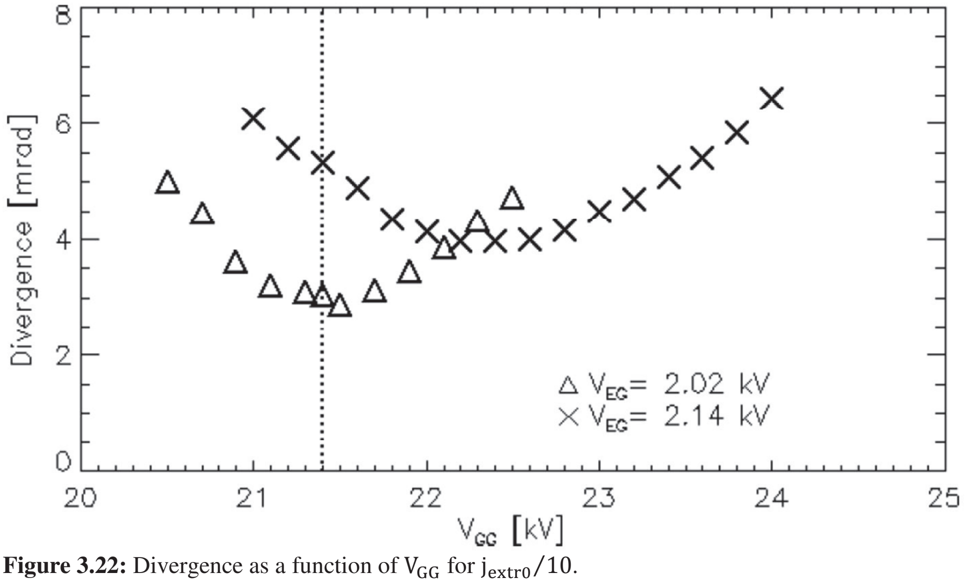

Figure 3.22: Divergence as a function of $\mathrm{V_{GG}}$ for $\mathrm{j_{extr0}}/10$.

- Compensation systems

Let's now take a look at what happen to the compensation systems in the early scenario. I have repeated the 40 beamlets simulations done in the previous section, but with the parameters scaled as described before.

In **Figure 3.23** the nominal case j_{extr0} is compared to $j_{extr0}/10$ case. The comparison confirms that the electrostatic repulsion among beamlets decreases with the extracted current and that the particle deflection is inversely proportional to the square root of V_{GG} (namely it depends on the particle velocity via the Lorentz force). Concerning the deflection compensation, the electrostatic compensation works even worse than before, while the magnetic compensation performs equally well at nominal and reduced parameters.

These results are in accordance with what I have already noticed at the end of section 3.2: the magnetic correction to the deflection due to the CESM magnetic field is a more robust solution with respect to the electrostatic one. This is due to the nature of the origin of the beamlets deflection: magnetic residual deflection remains always the same despite the operational parameters of the source, being dependent on CESM Br only. Thus being magnetic correction dependent on the GG magnets Br as well, this makes the correction independent on the operation parameters. The electrostatic correction, instead, depends on the applied voltage on the grids and beam current. Furthermore, CESM-field-MC can be further improved by replacing EG embedded magnets with a new set with a higher magnetic field, while CESM-field-EC can't be changed but replacing the entire GG, that is a very expensive solution.

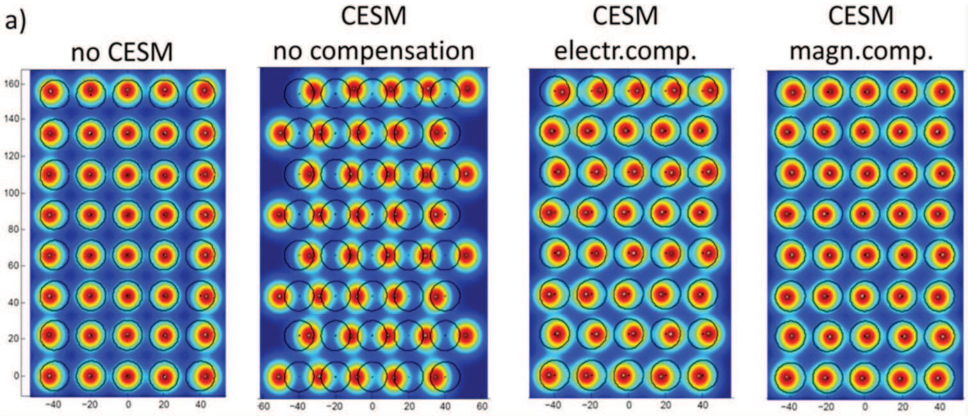

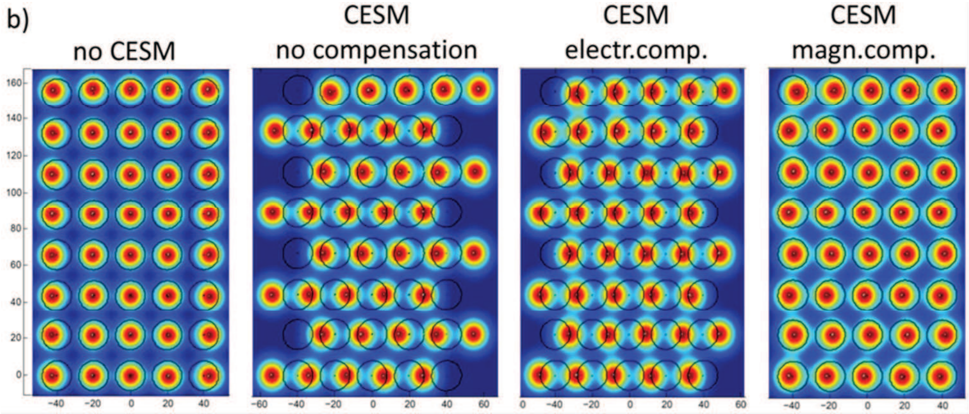

Figure 3.23: Comparison of the nominal case j_{extr0} (a) and $j_{\mathrm{extr0}}/10$ case (b). Simulations parameters of $j_{\mathrm{extr0}}/10$ case are scaled down accordingly to the Child-Langmuir law. BR exhibits reduction as well as electrostatic compensation efficacy. Magnetic compensation performance, instead, remains unchanged.

On the other hand, deflection due to BR is of electrostatic nature and depends on operational parameters (voltages and beam current) as well as BCR system, which is of electrostatic nature too. Having both the same nature, BRC can efficiently correct BR also in the early scenario.

Therefore, another interesting conclusion can be derived by investigation done in this section: it is a good approach to distinguish deflection nature and try to use a correction method of the same nature.

4 Experimental characterization of NIO1 and its improvements

In this chapter the work done on the NIO1 ion source since the start of its operations is presented. After a short presentation of the ion source, following the stages of NIO1 operations during its lifespan up to now, first the characterization of the plasma inside the source and then of the extracted beam is described, highlighting the dependence of the optics on the various operational parameters. I've dealt with the various diagnostic systems and processed the acquired data.

As a result of what observed experimentally, I've also designed some hardware upgrades, in order to improve NIO1 beamlet optics.

4.1 NIO1 negative ion source

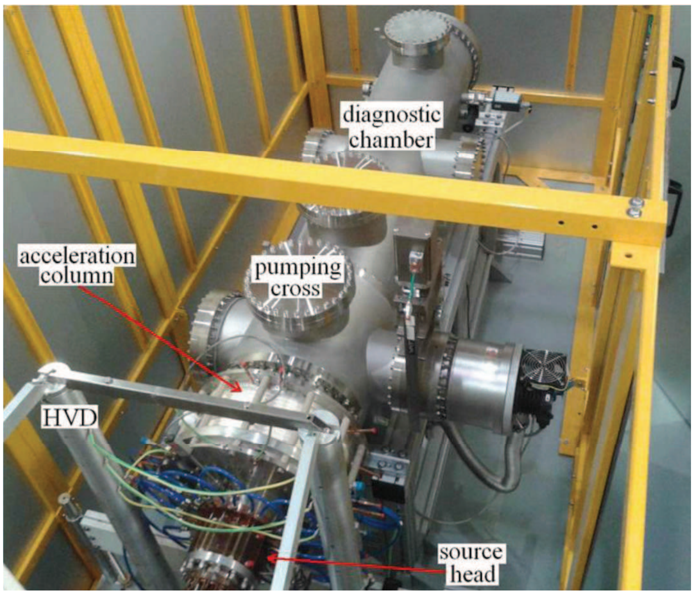

Figure 4.1: NIO1 negative ion source

NIO1 (Negative Ion Optimization 1) [43] is an RF driven negative ion source built in Consorzio RFX (Padova, Italy), which started to operate with continuity in 2015 [44], whose main purpose is to investigate general issues on ion source physics in view of the full-size ITER injector MITICA [11] as well as DEMO relevant solutions, like alternative accelerator schemes and neutralization systems, crucial for neutral beam injectors in future fusion experiments and energy recovery. Regarding the latter, more details can be found in Appendix B.

NIO1 has a modular design that makes it very flexible to hardware improvements or test of alternative solutions. **Figure 4.2** offers an exploded view of the machine modules; it is possible to highlight three main areas: source, accelerating column and drift tube.

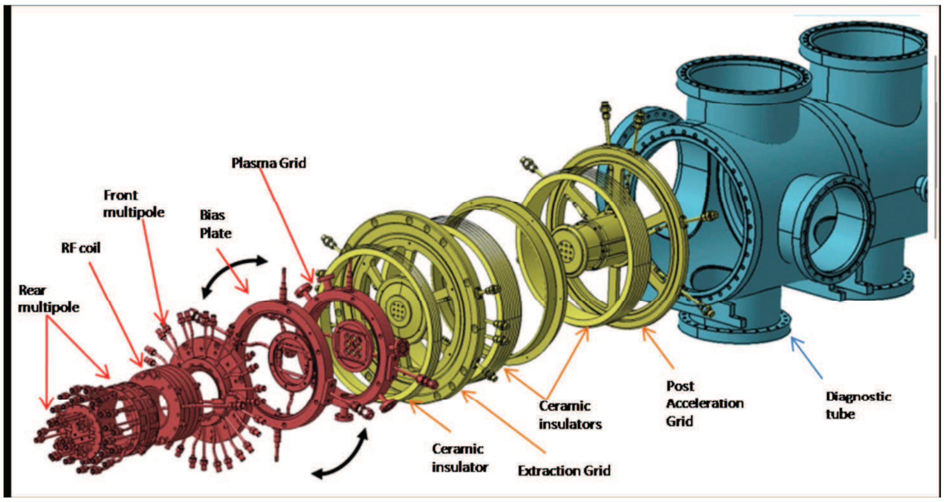

Figure 4.2: Expanded scheme of NIO1 components highlighting the source in red, the acceleration region in yellow and the diagnostic tube in light blue.

- *Plasma source*

The plasma source in NIO1 is composed by a cylindrical chamber (50mm radius, and around 200 mm length).

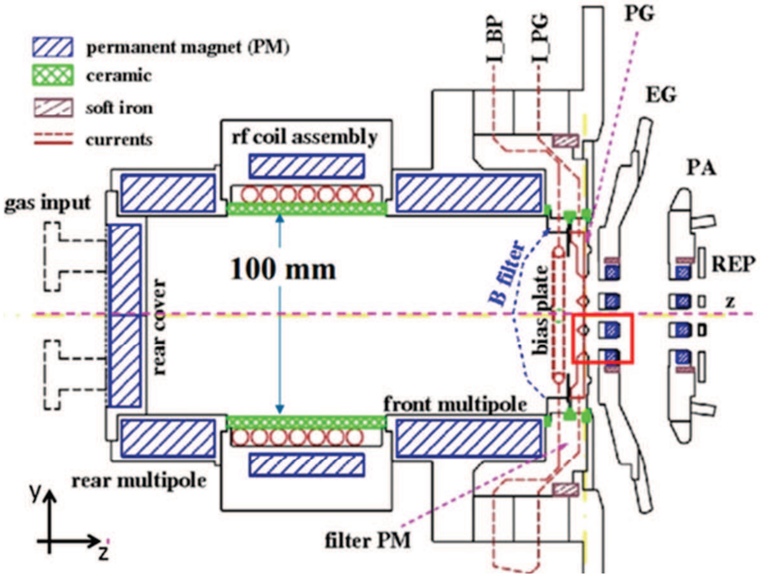

Figure 4.3: Schematic of NIO1 assembly (top view).

It is surrounded by $SmCo$ magnets forming multipoles to improve the plasma confinement: this field reduces contact between plasma and source walls that would cause charge loss. At the moment volume generation is the main process for negative ion production, while a cesium oven will be installed in the near future. **Figure 4.3** presents a schematic of the source.

The RF power is applied to the gas inside the chamber via an external antenna (see **Figure 4.3** and **Figure 4.5**) featuring a water-cooled 7 turns coil, all encased in an air-cooled polysulfone shells. From low voltage signal measurement, antenna inductance is $L_1 = 3.09$ mH and $R_1 = 0.317\ \Omega$ at 2 MHz (respectively $L_1 = 3.46$ mH and $R_1 = 83$ mΩ below 0.1 MHz), while coil capacitance C_c is about 35 pF.

NIO1 matching box uses vacuum capacitors, connected into two groups, C_a and C_b, which are adjustable (respectively from 0.1 to 2.3 nF and from 8.1 to 10.3 nF). The matching box is tuned to have an input impedance $Z_1 > 50\ \Omega$ when plasma is off. The actual impedance is not measured during plasma operation, while the digital readout of forward and reflected power is recorded. Lastly, two Rogowski coils can monitor the input and output currents.

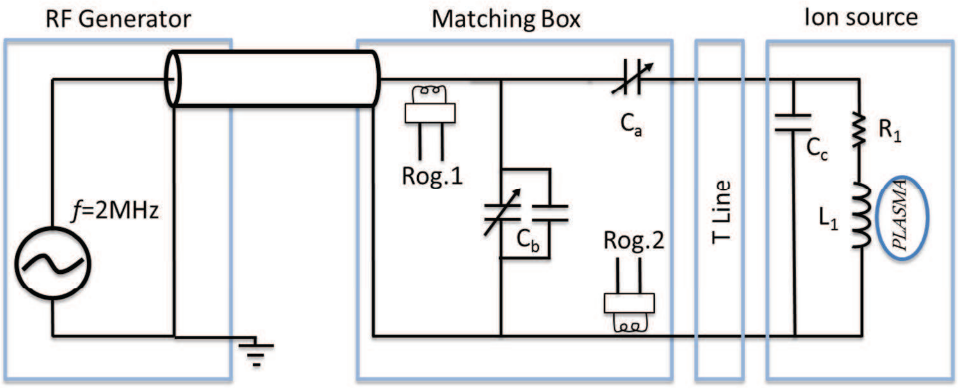

Figure 4.4: NIO1 RF circuit scheme. The RF generator can provide a signal with a power up to 2kW at 2MHz +/- 10%. The Matching box features two adjustable vacuum capacitors, C_a and C_b, and two Rogowsky coils, Rog.1 and 2, which monitor input and output currents respectively. The antenna, L_1, features a 7 turn copper coil, encased in a polysulfone shells, and is water cooled.

Inside the source chamber there are also a rectangular frame named Magnetic Bias Plate (BPm) and a round frame exposed to the plasma which is referred as Electric Bias Plate (BPe). These two frames are placed right before the first electrode of the acceleration column.

The magnetic bias plate (clearly visible in **Figure 4.5**) is electrically connected with the first electrode (the plasma grid) in such a way to make a circuit, referred to as magnetic circuit. The current that flows through the magnetic circuit generates the magnetic filter field in the region between the Plasma Grid (PG) and the BPm.

The electric bias plate (slightly visible in **Figure 4.5**), instead, is placed in between the BPm and the PG and is electrically insulated with respect to the PG and source walls. Its effect is similar to the PG polarization effect.

Thanks to the high flexibility of NIO1, the electrical connection of both BPe and BPm were changed several times, giving the possibility to study the effects of different configurations on source plasma and improve the production of negative ions as described later in this chapter.

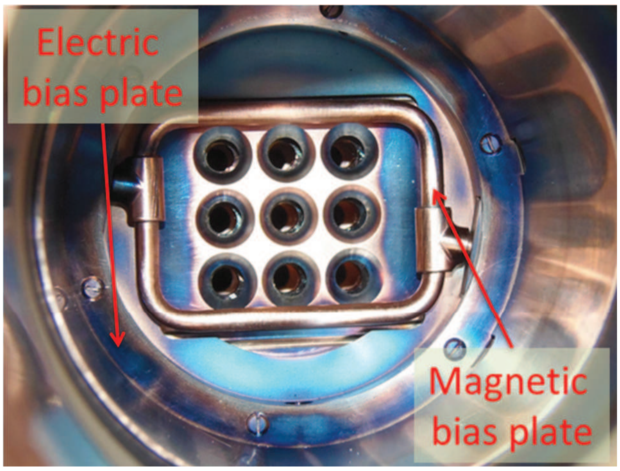

Figure 4.5: NIO1 source chamber opened. RF coil, the rectangular frame of the magnetic bias plate and plasma grid are visible.

Concerning plasma diagnostics, the source is equipped with three lines of sight (LOS), which host a photomultiplier and low and high resolution spectrometers for Optical emission spectroscopy. Measurements done with these systems will be presented in the next section.

- *Acceleration region*

Negative ions are extracted through 9 apertures (in a 3 by 3 pattern with a total extraction area of 400 mm^2) by a three-electrode system forming the accelerating column. The three electrodes are realized by electro-deposition of copper and successive milling, and include empty channels for water-cooling. In order, they are: Plasma Grid (PG), which closes the source chamber. It can be biased with respect to the rest of the chamber to help ion extraction. Extraction Grid (EG) and the Post Acceleration Grid (PA), which in NIO1 plays the role of the Grounded Grid, which extract and accelerate the ions respectively; the PA is insulated from the vessel ground, but in all experiments reported herein it was grounded. In addition to these three grids, a fourth one, the Repeller (REP) is added in order to prevent drain of positive ions from the drift region back to the source. The source can be polarized up to -60 kV giving to the beamlets a maximum energy of 60 keV, while the maximum design current is 15 mA each (assuming $\mathrm{j} = 300$ A/m^2) when EG surface is caesiated by means of a cesium oven. The right part of **Figure 4.3** shows the schematic of NIO1 accelerating column.

NIO1 EG and PA feature also some embedded magnets: EG features the usual CESM magnets for the suppression of the co-extracted electrons, while PA magnets have the double target to suppress electrons produced by the stripping process in the accelerating gap and to recover the small deflection angle induced by EG on the beamlets, retrieving their original alignment. This magnetic configuration in NIO1 is similar to the magnetic compensation system for SPIDER, presented in section 3.1. EG and PA magnets are placed in between aperture columns and alternatively oriented. Considering that the width of pockets for the permanent magnets is $2\mathrm{a_y} = 5.8$ mm and considering that the aperture pitch is $\mathrm{L_y} = 14$ mm, the magnets in EG and PA occupy 41% of space. Finally, soft iron bars are placed parallel to the EG and PA magnets to form a kind of magnetic mirror that virtually approximates an infinite periodicity for the B field. Furthermore, a dedicated copper mask holds magnets and iron bars in place, allowing an easier replacement of magnets.

- *Drift tube*

It is worth, instead, to talk about Mini-STRIKE that is the only diagnostic currently used for beam characterization during experimental sessions. Mini-STRIKE is a calorimeter made of a Composite Carbon Fiber (CFC) tile, with dimension of $120x90x12$ mm, whose thermal conductivity is anisotropic: heat flux along the direction perpendicular to the beam propagates 20 times faster than in the other directions. It is placed after the repeller electrode and it is used to measure beam divergence, beam profile and beam current. Beam profile and divergence are obtained by a thermocamera that looks at the rear side of the tile. Mini-STRIKE prototype is employed at IPP since 2012 and it was verified that it can investigate beam properties on beamlets scale [45]. This represented a test for the bigger system (STRIKE) that will be employed also in SPIDER [[**46**]. Despite I didn't made any calorimetric observation with Mini-STRIKE, the CFC tile has given a crucial contribute to the optical characterization of the beam since information of the deposited beam current was available. Information on the calorimetric observation done with Mini-STRIKE can be found in [47].

Thermocouples, which control the temperature of every sensible component of NIO1 and a dedicated water cooling system under conductivity control, complete the overview of the auxiliary systems of the machine.

4.2 Source spectroscopy characterization

As soon as NIO1 was powered on the first time, after the routine check of high voltage holding and vacuum leakage, the characterization of the plasma, without any extraction of ions by the extraction system, was the first task. This was obviously the first step to do in order to have the sensibility of NIO1 plasma production dependence on the various operational parameters, like RF power, coupling frequency, inlet gas pressure, etc. and also to check the efficiency of RF power matching box and auxiliary systems, like thermal and optical diagnostics. In particular, the plasma operation of the source was tested using both air and hydrogen, with the goal of reaching the maximum RF input power of 2 kW, reducing the source filling pressure around 1 Pa or less.

An extended characterization of the plasma properties was carried out by analysing the spectrum of the plasma light in the range $300 - 850$ nm, by means of an Optical Emission Spectroscopy (OES) diagnostic. The system includes a low resolution spectrometer and a high resolution one, receiving light from Lines Of Sight (LOSs) parallel and close to the plasma grid. Regarding the hydrogen operation of the source, from the ratios of the emissivities of specific spectral lines it was possible to measure the rotational temperature of the hydrogen molecules, the electronic temperature and density, the dissociation degree of the molecules and the ionization degree of the atoms. The interpretation of experimental data was performed with the help of YACORA [49], a Collisional-Radiative (CR) model developed at IPP Garching capable to simulate the population coefficients of the excited states of H and H_2 for low pressure and low temperature hydrogen plasmas.

4.2.1 Diagnostic setup

In NIO1, the light emitted from the plasma was observed from two viewports at 26 mm from the PG; they look exactly one into each other, so that the LOSs collect light from the same region.

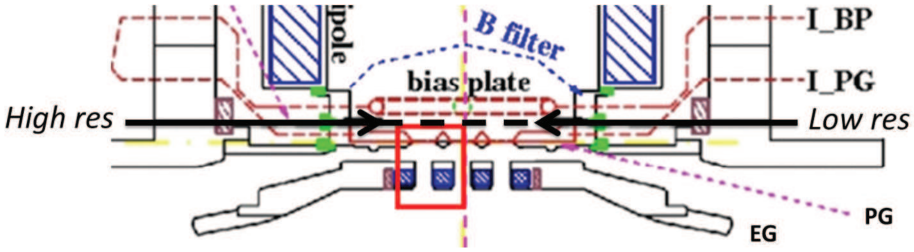

Figure 4.6: Schematic of the spectroscopic setup on NIO1. Two spectrometers (high and low resolution) look into each other in a line of sight far from the PG 26 mm (cold region).

Each of the 2 viewports hosts an optic head, consisting of a BK7 lens of 50 mm focal length and 10 mm diameter, which conveys the plasma light into a quartz optical fiber. One optic head is connected through the optical fibre to a low resolution spectrometer *Hamamatsu C10082CAH* [[**51**], mounting an integrated back thinned CCD sensor of 2048 pixels and resolution of 1 nm. This spectrometer is always used during the operation of NIO1 for a rapid survey of the plasma conditions, in particular to detect impurities sputtered from the source walls and measure Balmer lines (defined in few lines). The other optic head is connected to a high resolution spectrometer *Acton SpectraPro-750* [[**52**], with a 2D back illuminated frame transfer CCD camera of 512x512 pixel, for a spectral window 6 nm wide and a resolution of 50 pm. Both spectrometers were absolutely calibrated in order to get the radiance of spectral lines [[**54**]. The usable spectral window of the diagnostic includes the range from 300 nm to 850 nm, where hydrogen exhibits its main spectral lines in the visible range, i.e: $H_\alpha = 656$ nm, $H_\beta = 486$ nm, $H_\gamma = 434$ nm and $H_\delta = 410.17$ nm, also known as Balmer lines.

4.2.2 Source spectroscopical characterization

A typical spectrum acquired by the low-resolution system is shown in **Figure 4.7**. The spectrum refers to plasma produced in NIO1 source with an input RF power of 1575 W and a gas pressure of 2.4 Pa in hydrogen. The spectrum was collected with an exposure time of 1 s and converted in emissivity units, according to the absolute calibration, already done by means of an Ulbricht Sphere [[**54**] and assuming that the illuminated length of the LOS corresponds to the diameter of the plasma chamber, i.e.: 17.8 cm, and plasma uniformity along the LOS. The Balmer lines H_α, H_β and H_γ are clearly visible in the spectrum, as well as the molecular H_2

emission. The molecular emission is not a well-defined line, but a band comprised in the wavelength range from 565 to 640 nm, usually called Fulcher band.

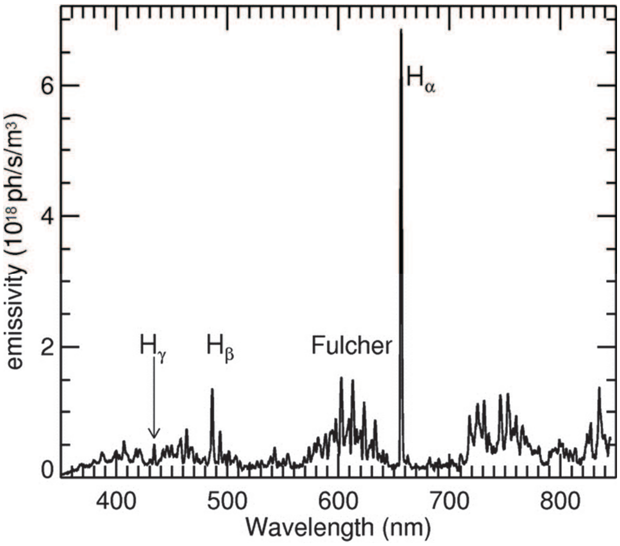

Figure 4.7: Example of a NIO1 hydrogen plasma spectrum, recorded by the low resolution spectrometer. The clearly visible H_α, H_β and H_γ lines are called Balmer lines while the band of lines called Fulcher represent the molecular H_2 emission.

The Fulcher band is acquired also by the high-resolution system to distinguish the lines composing it. These were analyzed to measure the rotational temperature T_{rot} of the H_2 molecules, which can be considered equal to the gas temperature [53]. This was possible thanks to a dedicated routine written in IDL, already available at Consorzio RFX, capable to simulate the Fulcher band shape at different gas temperatures. The best estimate of the gas temperature is then found matching the shape of the simulated Fulcher bands with the experimental one. **Figure 4.10** (a) shows the dependence of the measures of T_{rot} on the RF input power. What resulted is that the gas temperature increases with the RF power, in particular above $1100 \div 1200$ W. The plasma was sustained at various gas pressures between 1.2 Pa and 2.4 Pa while keeping the input power constant, but this did not affect the T_{rot} more than 10%.

Calling n_H , n_{H^+} and n_{H_2} the densities of atomic, ionized and molecular hydrogen, respectively, the measurements of electron temperature T_e , electron density n_e , dissociation degree n_H/n_{H_2} and ionization degree n_{H^+}/n_H was obtained with a recursive algorithm over T_e. Firstly, the electron density was calculated by comparing the experimental ratio of H_β and H_γ emissivities, ε_{H_β}, ε_{H_γ}, upon exploiting the predictions provided by the YACORA model [49], which depend on electron temperature and density: essentially the density was retrieved by a direct interpolation of the curve in **Figure 4.8** with a 4th order polynomial and setting an initial electron temperature of 2 eV (that is the usual case in negative ion source).

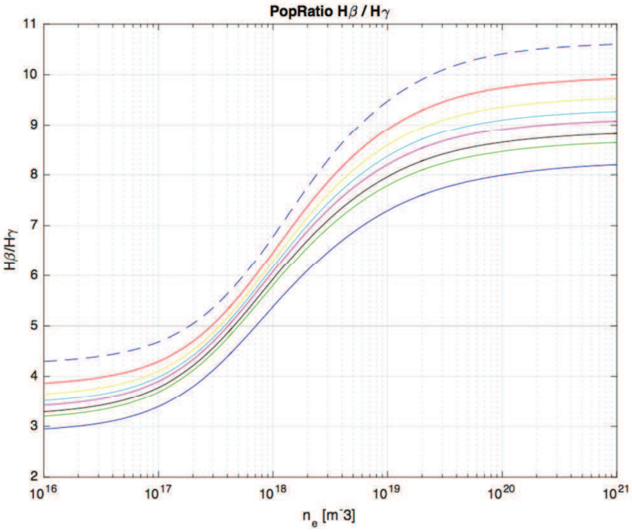

Figure 4.8: YACORA [49] prediction on H_β and H_γ emissivities in function of electron density at different temperatures. By guessing the electron temperature and thus fixing the reference curve, it is possible to obtain information about electron density, by interpolation of the chosen curve using emissivity data from experiments.

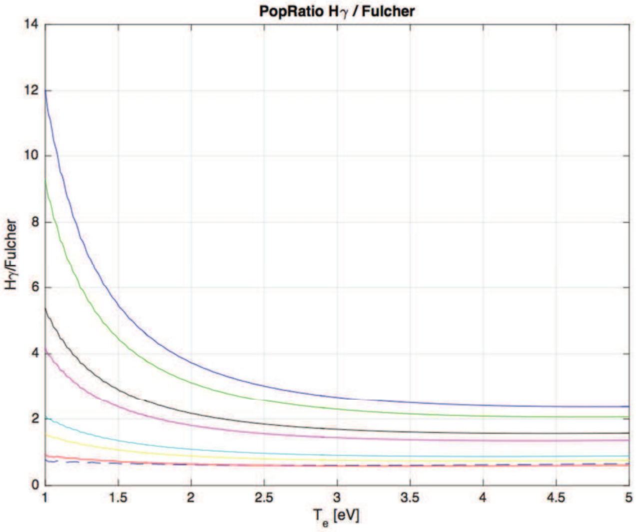

Figure 4.9: YACORA [49] prediction on H_γ/Fulcher emission rates in function of electron teperature at different densities. Using values previously found for n_e and T_e, it is possible to estimate the emission rate that can be used in 4.1 in order to compute the dissociation degree.

At this point, the dissociation degree was calculated from the emissivity of the H_γ line and the Fulcher band:

$$n_H / n_{H2} = (\varepsilon_{H\gamma} / \varepsilon_F) \cdot \left[X_F(n_e, T_e) / X_{H\gamma}(n_e, T_e) \right] \qquad 4.1$$

where $X_{H\gamma}$ and X_F are the effective emission rates of H_γ and Fulcher transition, obtained by interpolation of the curves provided by YACORA model in **Figure 4.9**, by fixing n_e and T_e to the values previously found.

The dissociation degree was then used to calculate the density n_H of the atomic hydrogen from the gas density n_{H_2}, which in turn is known from the gas pressure in the source and T_{rot}, through the ideal gas law.

Thanks to the estimates of n_e and n_H, $X_{H\gamma}$ was calculated from the measured emissivity of the H_γ line:

$$X_{H\gamma}(n_e,T_e)=\varepsilon_{H\gamma}(n_e n_H)^{-1} \quad 4.2$$

In turn, the values of $X_{H\gamma}$ and n_e were interpreted by the CR model to obtain an updated value of T_e.

At this point the whole cycle of analysis was repeated using the updated value of T_e, as many times as necessary to reach the convergence on the estimation of T_e itself. Lastly, the ionization degree n_{H^+}/n_H was calculated from the estimates of n_e and n_H, in the rough approximation that $n_{H^+} \approx n_e$.

Repeating this procedure at different RF powers or gas pressures, it is possible to check the dependence of electron temperature, density, dissociation and ionization degree on those operational parameters. This is what was done and the results are shown in **Figure 4.10**. Here, the values of n_e (plot b), T_e (plot c), n_H/n_{H_2} (plot d) and n_{H^+}/n_H (plot e) are plotted as function of the input RF power, for a constant pressure of 2.4 Pa.

In this way NIO1 source plasma was characterized by the OES spectroscopy. In more details, the electron temperature and density are respectively of the order of some eV and 10^{17} m-3; moreover, the gas is weakly dissociated ($\mathrm{n_H/n_{H_2}} \approx 10^{-2}$) and even less ionized ($\mathrm{n_{H^+}/n_H} \approx 10^{-4}$). $\mathrm{n_e}$ and $\mathrm{n_{H^+}/n_H}$ slightly increase with RF power within the experimental errors together with the electron temperature, while the dissociation degree diminishes with it. This decrease was unexpected, because both the $\mathrm{H_\gamma}$ and the molecular emissions are driven by $\mathrm{n_e}$ and $\mathrm{T_e}$, which rise with RF power. The reason for this could be some processes not included in the Yacora model, which could enhance the Fulcher band intensity, leading to an underestimation of the dissociation degree $\mathrm{n_H/n_{H_2}}$.

Above all, the most important result is that the trends of both electron temperature and dissociation degree exhibit a change of slope with the RF power at a threshold power of 1400 W. Moreover at RF powers between 1500 W and 1700 W a substantial increase of the emissivity of the Fulcher band has been clearly observed and more generally a growth of the overall plasma luminosity, measured with a plasma light detector (PLD): this behaviour highlights the transition of the plasma coupling with the RF antenna from capacitive mode to inductive mode, highlighted by the sudden reduction of the reflected power (see section 2.4.3). An example is given by **Figure 4.11**.

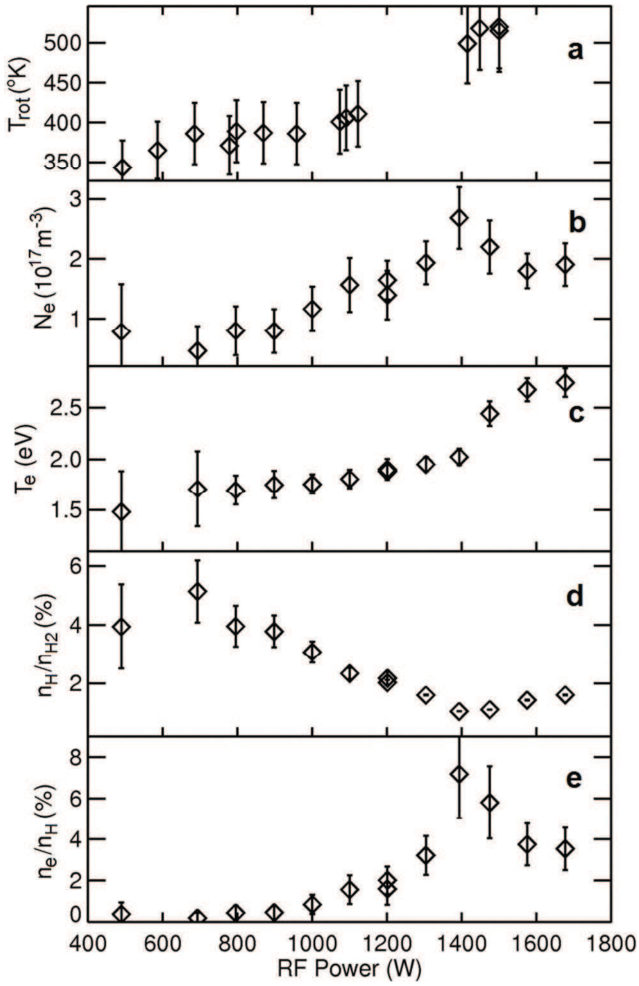

Figure 4.10: Results of the characterization of the source in hydrogen plasma according to the measurements with the OES diagnostic, using the procedure described in the text, which lead to information about: rotational temperature (a), electronic density (b), electronic temperature (c), degrees of dissociation (d) and ionization (e) of the plasma. The data of plot (a) are referred to plasmas with gas pressures between 1.2 Pa and 2.4 Pa. The data of plots (b-e) are referred to a power scan with constant source internal pressure at 2.4 Pa [[50].

During inductive mode, plasma parameters are enhanced and therefore it is the best condition to operate the source for beamlet extraction, since more hot electrons are available for H_2 excitation as well as more cold electrons for negative ion formation via Polar Dissociative Attachment (see section 2.4.5).

The transition from capacitive to inductive mode was achieved also using oxygen as inlet gas. Due to oxygen higher electronegativity with respect to hydrogen, which preserves negative ions to be destroyed by the interaction with energetic plasma electrons, the transition occurs at lower RF power (~800 W). **Figure 4.11** is an example of the new transition threshold for hydrogen plasma, shown by reduction of RF reflected power.

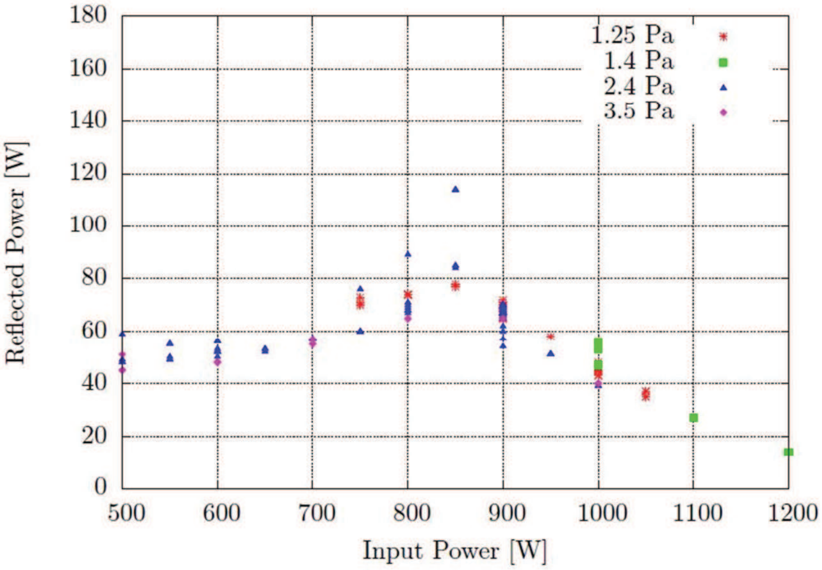

Figure 4.11: Reflected power as a function of input power with Pyrex source insulator. Transition from capacitive regime and inductive regime happens between 850 W and 900 W. The reflected power changes trend after switching to the inductive coupling.

Unfortunately, as soon as these results were found, the alumina insulator of the source cracked. Since too much time would be lost to substitute it with a new one, Pyrex was used instead. However, despite it allowed to continue operation in a reasonable amount of time, the use of Pyrex limited the usable amount of RF power to around 1 kW, since Pyrex cannot withstand too high temperatures. This limitation strongly reduced NIO1 performances and therefore a complete characterization of the device, exploiting volume process only, has not achieved yet. Operations with cesium were then delayed. A new alumina insulator is planned to be installed only during 2017. However, with the new chamber it seemed that the power level required to trigger the capacitive-inductive transition is lower (850 − 900 W) than before, but this result cannot be confirmed yet, since the limited capability and maybe only a partial transition has been observed [[**55**].

4.3 Beam characterization

The experimental measurements aimed at characterizing NIO1 beamlet extraction and the optic of the system up to now are now treated. The plan was to fully characterize the beam exploiting volume process only, before using cesium vapour to enhance surface production.

Unfortunately, the substitution of the plasma chamber made of alumina after its break with another one made of Pyrex, which cannot withstand too high temperatures, strongly limited the injected power (1 kW with respect to the available 2.5 kW). It was then decided to start measurements with oxygen, instead of hydrogen: oxygen requires less RF power for the capacitive to inductive mode transition, i.e.: 400W instead of of the corresponding one obtained in hydrogen with pyrex insulator 900W. The other reason is that oxygen is less affected by the magnetic field with respect to hydrogen, thanks to their high mass difference. This was desirable because present NIO1 CESM are strong enough to bend the hydrogen beamlets in such a way that they partially intercept the internal surface of the EG apertures. **Figure 4.31** shows a dedicated OPERA simulation that helped to realize this. However, the use of oxygen had mostly the aim to start operating NIO1 for the first time with a gas that was easier to handle with the limited available operational possibilities. Nevertheless negative hydrogen beams were also extracted and characterized.

4.3.1 Electrical measurements

As for the beamlet characterization, since the first extraction, the best optics condition was sought for, relying on the thermal observation on the CFC tile. It was soon realized that beam optics was not good enough to allow accurate beamlet divergence measurement: despite the efforts in changing the operational parameters, the thermal image on the CFC target never shown separated beamlet imprints, but only one big spot. **Figure 4.12** [56] gives an example. Hence beamlet characterization then could not rely on calorimetric observations and it was decided to exploit electrical measurements.

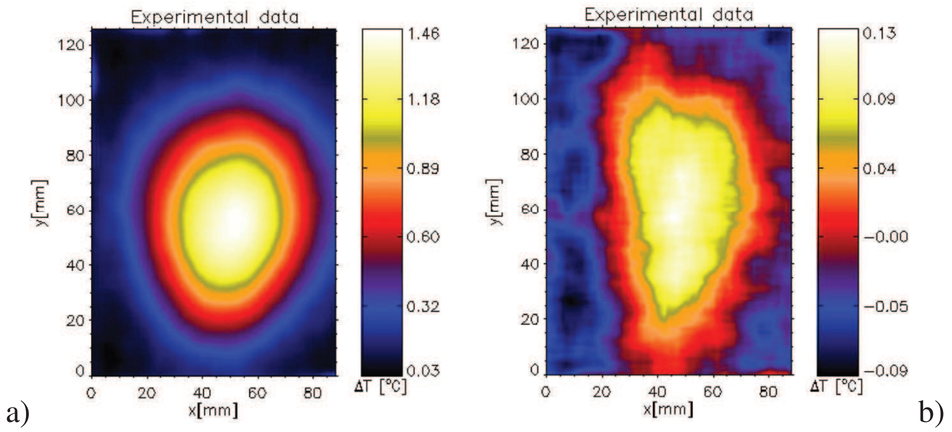

Figure 4.12: Example of thermal images done with the CFC calorimeter placed downstream the repeller grid in NIO1[56]. In both oxygen (a) and hydrogen (b) operations single beamlets footprints completely overlap don't allowing any divergence measurements [56].

Figure 4.13 gives a schematic view of the NIO1 experimental setup for beam extraction. Every electrode and the CFC tile, since they are insulated, could have their dedicated shunt resistance to measure the current flowing through them when interaction with the beamlets occurs. Furthermore, $V_{bias-PG}$ polarizes the PG with respect to the source walls and helps negative ions extraction, while reducing electron extraction, which being less massive than ions are deflected towards PG. $V_{bias-CFC}$ positively polarizes the CFC tile in order to collect secondary electrons emitted from it due to the interaction with the beam. This is necessary otherwise the loss of secondary electrons emitted by the tile would falsify CFC tile current measurement.

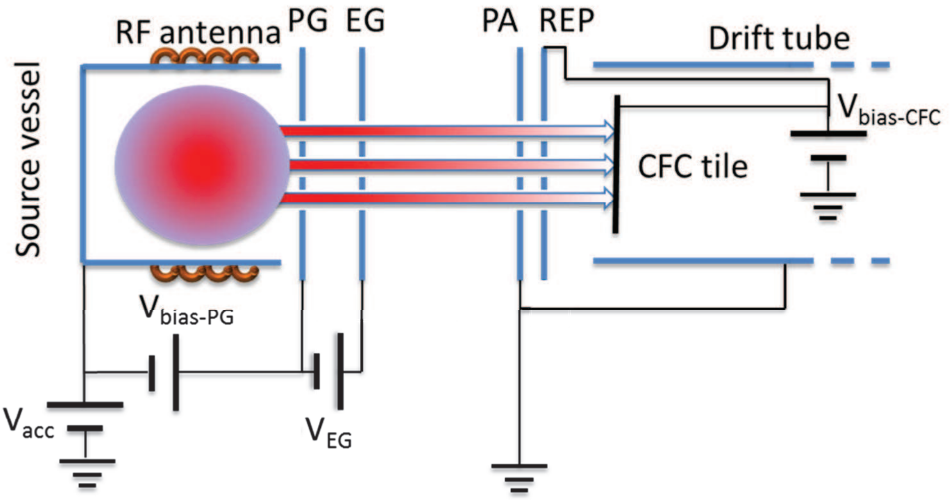

Figure 4.13: Schematic of electrical connections for NIO1.

Of course secondary electrons from ionization of background gas will be also collected by the CFC tile, however it is supposed that their contribute is negligible since the repeller grid should collect most of them (at least half for the symmetry of the system). $V_{bias-PG}$ and $V_{bias-CFC}$ are of the order of dozen volts. This setup remained unchanged during all the following measurements.

The experimental results for the beam characterization are now discussed. Since the electrical measurements described in the last section are used, some clarifications are necessary.

Supposing that all the co-extracted electrons are stopped by the CESM field before the EG, the currents collected by the PA electrode and CFC tile refer to the interaction with the negative ion beam (including also stripping electrons, which can be seen as the equivalent current of the neutralized ions). Obviously, the sum of the currents registered by PA and CFC gives the total amount of extracted negative ions. As before, this measurement is however affected by secondary electron electrons from background gas ionization. The repeller grid helps to reduce this undesired effect.

The current collected by the EG, instead, can be directly associated to the co-extracted electron current, since they are forced to intercept the EG by CESM magnets. The contribution to the EG current measurement by the possible partial interception of the ion beams with the EG, like in the hydrogen case, can be neglected, since the registered electron current is of the order of 400 mA and 80 mA for oxygen and hydrogen respectively and the corresponding ion current is of the order of few mA.

- *RF power and source pressure*

RF power and source pressure are the main parameters that can be tuned in order to change plasma properties: by increasing input power, more energy is transferred to the plasma particles, while by enhancing the pressure higher collision frequency is obtained.

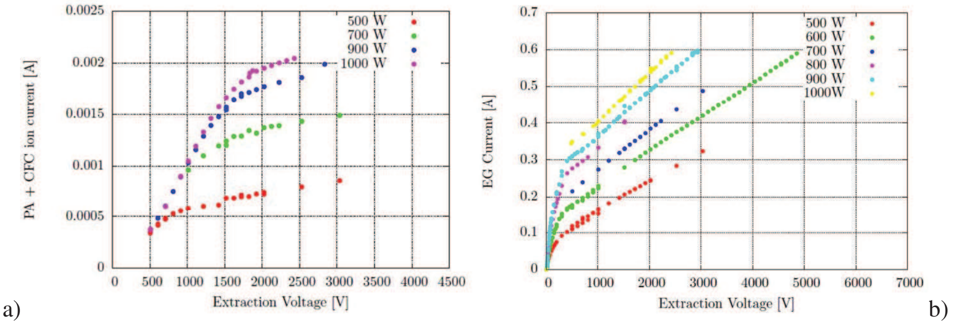

a) b)

Figure 4.14: Oxygen extraction voltage scans of ion (a) and electron current (b) at different RF powers. Other parameters are: RF power 1kV, 300 A filter current , 10V bias, Vacc=15 kV.

The first interesting results are those referred to the ion and electron current as function of the extraction voltage, at different RF injected power (see **Figure 4.14** for oxygen and **Figure 4.15** for hydrogen). A confirmation of the Child - Langmuir law was expected.

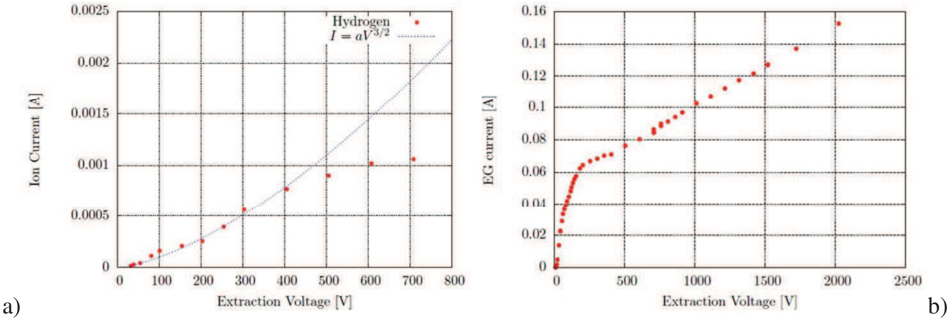

Figure 4.15: Hydrogen extraction voltage scans of ion (a) and electron current (b) at different RF powers. Other parameters are: RF power 1kV, 300 A filter current , 10V bias, Vacc=15 kV.

It resulted instead that the law is verified only at very low EG voltages, while at higher voltages a linear trend is instead found. This means that the extractible current is no longer limited by the space charge, defined by the Child-Langmuir law, but by the lack of available particles in the meniscus zone. However, the turning point of the curve slope changes with increasing RF power, which increases the number of available ions for the extraction.

The same considerations can be done varying source pressure, instead of RF power, since this can vary the amount of available particles. This can be seen in **Figure 4.16** and **Figure 4.17**. Considering **Figure 4.16** a) and **Figure 4.17** a), it can be seen that ion current characteristic curves in oxygen and hydrogen have the same trend, following the child-Langmuir law, when the source pressure is varied and the RF power is fixed, with the exception of the scan performed at 0.07 Pa, which does not follow the Child- Langmuir law also at low extraction voltages, probably because the pressure was too low.

Turning to the electron current (**Figure 4.16** b) and **Figure 4.17** b)), above 0.2 Pa EG current for oxygen stays constant and does not depend on source pressure, while this is not the case for hydrogen.

In the considered pressure and RF power range, it can be concluded that pressure and input power act in different ways on gas ionization process, depending also on the gas species.

These considerations need to be confirmed in future operations, when the maximum input power limit will be reached.

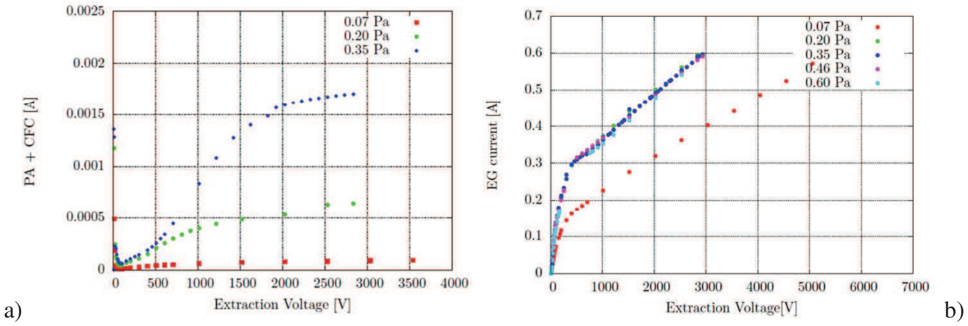

Figure 4.16: Oxygen extraction voltage scans of ion (a) and electron current (b) at different pressures. Other parameters are: RF power 1kV, 300 A filter current , 10V bias, Vacc=15 kV.

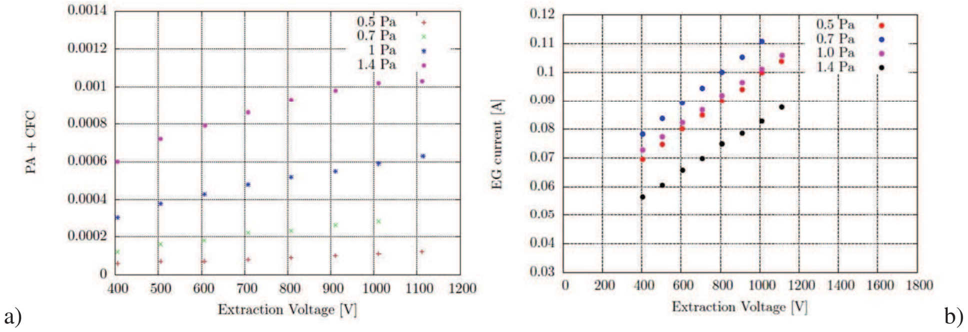

Figure 4.17: Hydrogen extraction voltage scans of ion (a) and electron current (b) at different pressures. Other parameters are: RF power 1kV, 300 A filter current , 10V bias, Vacc=15 kV.

- *Beam optics*

Since it has been decided to rely on electrical measurements because detailed thermal measurements were proved to be difficult so far [[**56**], for the beam optics characterization a good figure of merit is the PA/CFC current ratio: in principle, a beamlet with acceptable optics would have a divergence low enough that it exits the acceleration region without intercepting any electrode and is completely collected by the CFC tile. In this case no current would be detected on the PA and the ratio PA/CFC current would be zero. However the PA/CFC ration is always modified by the secondary emission electrons, which came from stripping processes with the background gas, that give a non-zero contribute to this ratio.

In NIO actual beam divergence inside the accelerator region is so high that beamlets partially intercept the PA. As a consequence, the PA/CFC current ratio is not zero. However, it is possible to assume a less divergent condition to a lower current reaching the PA and thus a lower value of the PA/CFC ratio. Therefore, trying to minimize the PA/CFC currents ratio is a good way to find the best possible optics condition with the present NIO1 limitations.

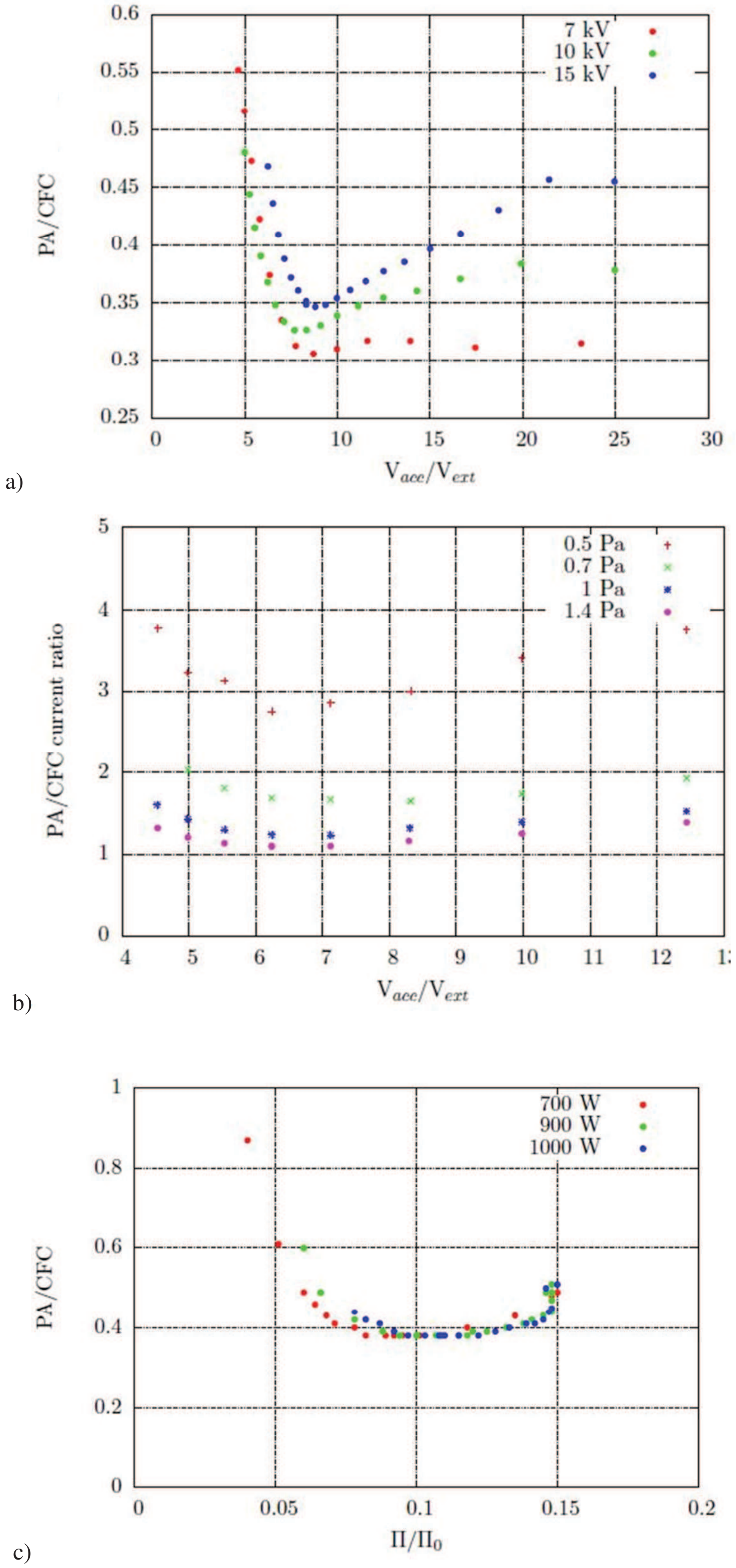

Figure 4.18: PA/CFC currents ratio in function of the extraction voltage at different acceleration voltages (a), pressures (b), RF power (c). The minimum of each curve can be associated to the best optics condition.

In **Figure 4.18** the optics figures of merit PA/CFC, for oxygen, as a function of the extraction voltage at different acceleration voltages (a), source pressure (b) and RF powers (c) are shown. It is possible to see that the minimum of the curves, i.e. the best optical condition, changes in function of the operational parameters.

- *Filter and bias*

In order to increase negative ion availability in the extraction zone, since RF power was limited, the effect of the magnetic filter field and PG bias were also considered. These parameters can improve the negative ion density because their effect is to limit the electronic density and temperature in the extraction zone.

The PG can be polarized up to 20 V with respect to the source body, thus modifying the electrostatic field in the meniscus zone and attracting electrons which are partially absorbed on the grid itself instead of being extracted. This is useful since extracted electronic current influences the extraction of negative ions, due to the space charge [[**48**].

The current that generates the magnetic filter can be raised up to 400A, increasing the filter field accordingly. The more intense the magnetic filter, the lower the electronic temperature and density in the extraction zone. This increases the extracted ion current, since hot electrons can easily destroy negative ions. This is clearly shown by the oxygen measurements presented in **Figure 4.19**.

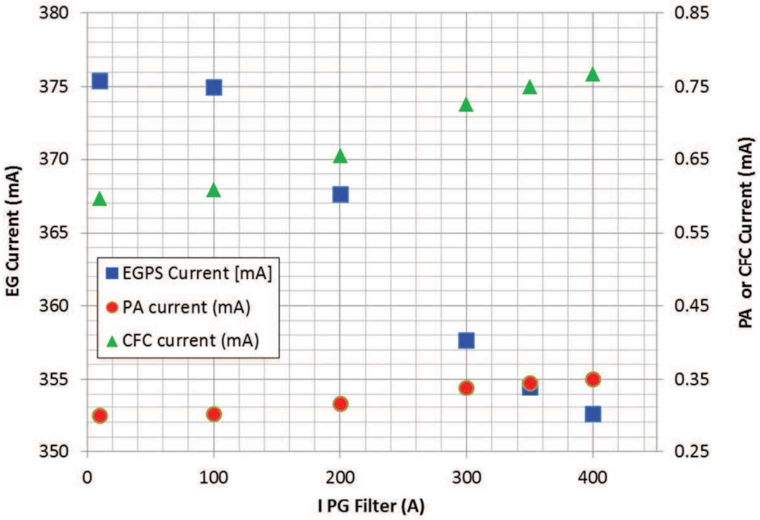

Figure 4.19: Example of filter field effect on the extracted species: increasing the filter field intensity (here reported as the current intensity that generate the field) the co-extracted electrons current (EG current) is reduced, while negative ion current (PA and CFC current) is increased. This happens independently by the other operational parameters. The source gas is oxygen.

In particular, looking at **Figure 4.20** it can be seen that the co-extracted electron current is mainly reduced by acting on the source bias, while the effect of source bias and filter field on the ion current is almost the same (**Figure 4.21**).

It is also interesting to note that in the bias scan **Figure 4.20** b) the electronic current collected on the EG decreases faster between 0 and 10V than between 10 and 20 V. The current decrease detected on the EG is related to the current collected by the PG. If this current reaches the saturation level, the bias becomes less efficient to reduce co-extracted electrons.

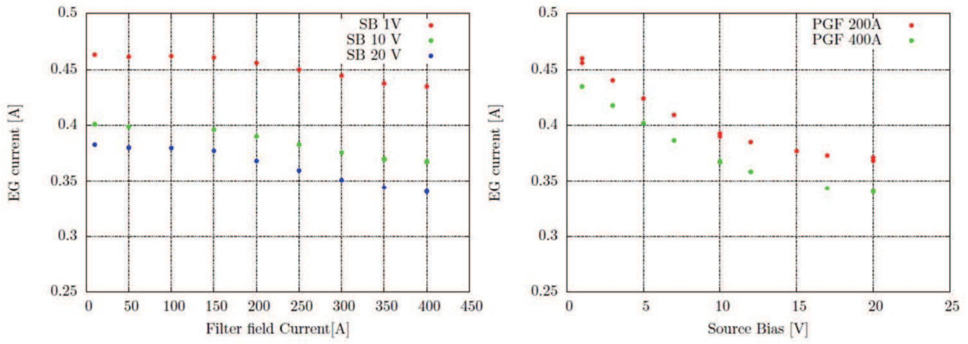

(a) (b)

Figure 4.20: a) Electron current on EG as a function of the filter field current, for different source bias values. b) Electron current on EG as a function of the source bias, for different filter currents. Each plots taken at 800 W, 0.35 Pa source pressure, EG voltage = 1500 V, acceleration voltage = 15000 V, Configuration II.

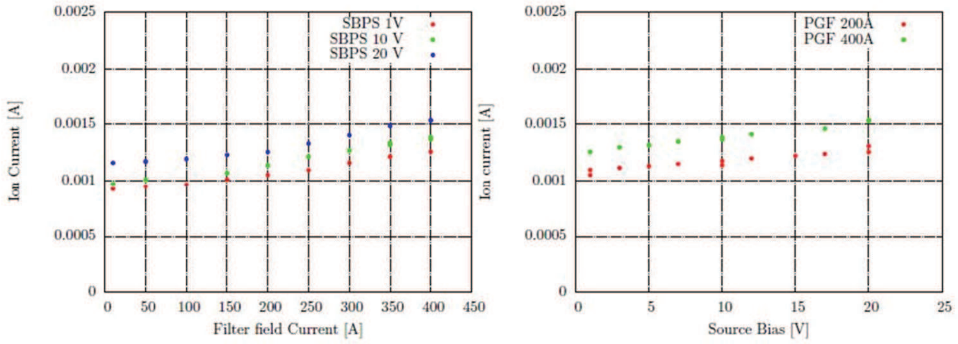

(a) (b)

Figure 4.21: a) Ion current in function of the filter field current, for different source bias values. b) Ion current in a function of the source bias, for different filter currents. Each plots taken at 800 W, 0.35 Pa source pressure, EG voltage = 1500 V, acceleration voltage = 15000 V, Configuration II.

In order to exploit these methods more efficiently, several BPe and BPm configurations (not reported in **Figure 4.13**) were tested. **Figure 4.22** shows a summary of the various configurations used during measurements.

Scans reported up to now were performed using configuration II, since configuration I has been early rejected because it was not very useful, because it generates two opposite electric fields in the extraction region.

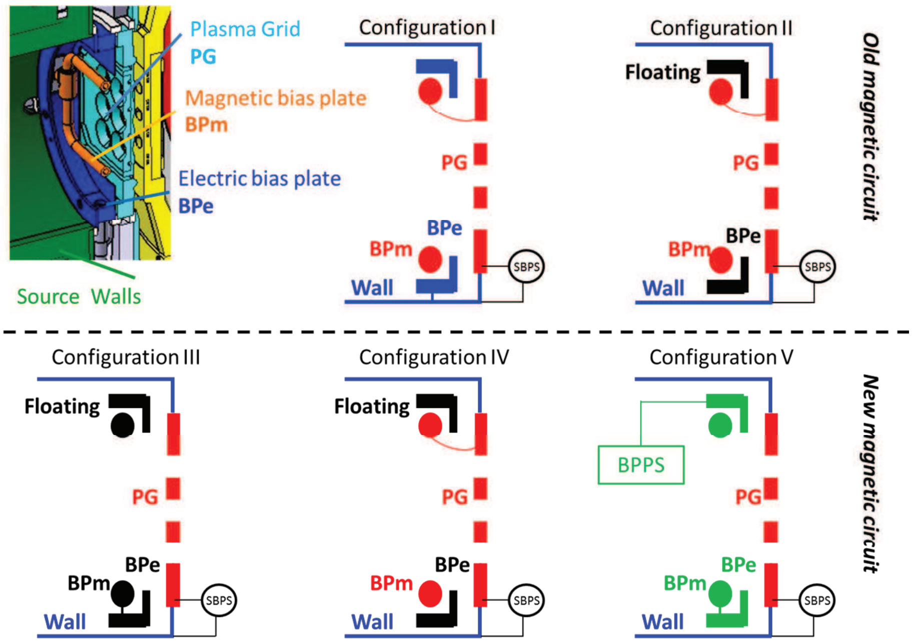

Figure 4.22: BPe and BPm configurations. The first picture shows the positions of the two plates with respect to the PG, while the others show the different electrical connections. In particular configuration from III to V make use of the new external 'double c' coil. More details in the text.

Concerning the other three configurations the main difference consists in the introduction of a new part for the magnetic circuit: a coil was added externally to the source chamber at a distance of 60 mm upstream the PG, passing from the original configuration (**Figure 4.23**(a)) to the 'double c' configuration (**Figure 4.23** (b)).

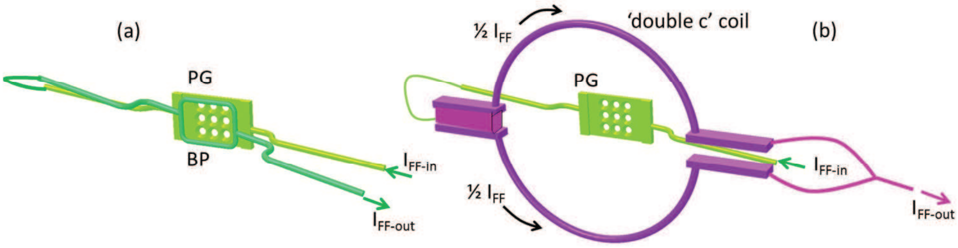

Figure 4.23: (a) Original magnetic circuit configuration. (b) New magnetic circuit configuration.

The new magnetic circuit was designed in such a way to broaden the B_y profile the filter field inside the source (see red line in Figure 4.24). With dedicated 3D simulations performed with OPERA it was realized that the original position of the filter field peak was too close to the PG aperture (few mm). Since the filter field aims at cooling electrons down inside the extraction region, where otherwise they would destroy negative ions, it is possible to say that the peak of the filter field ideally divides the source in hot and cool parts, where the latter is the one where negative ions can survive.

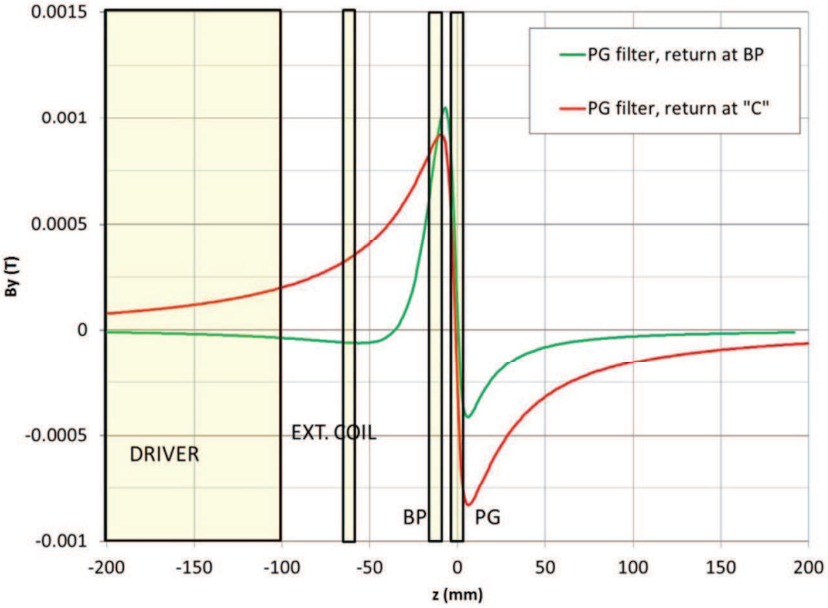

Figure 4.24: Magnetic filter field in NIO1, generated by the original configuration (green line) and by the new configuration that uses the external 'double c' coil (red line). The position of the driver region, external coil, electrical bias plate and PG are superimposed. The new configuration allows increasing the cool region of the source, since the position of the B_y profile of the filter field penetrates more inside the source. In this way the production of negative ions is enhanced.

If the cool zone is too close to the PG, negative ions have just a small portion of the source where they can survive. Therefore it is possible to influence the amount of extractable negative ions by changing the position of the peak, which changes the dimension of the cool zones accordingly (see **Figure 4.25**).

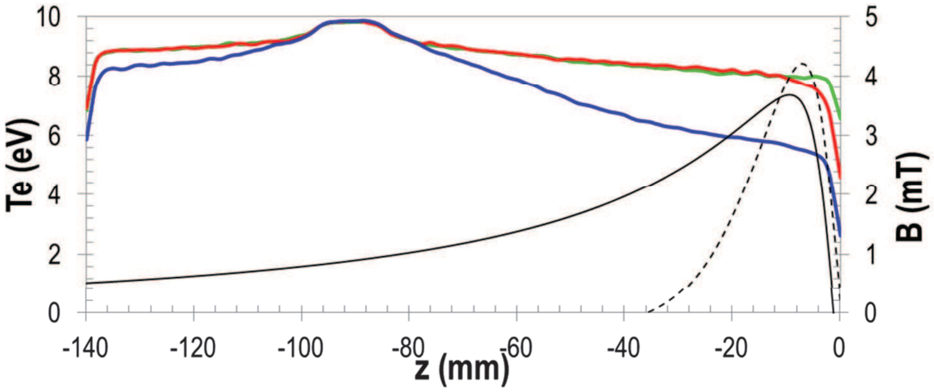

Figure 4.25: Results of a PIC simulation of the electron temperature inside NIO1 source with the filter field generated by the configuration II (dashed black line) and IV (solid black line) [[57]. The simulation explores electron temperature throughout the whole source and in particular the extraction region corresponds to the zero position and flat zone where the electron temperature is higher and all the curves overlap completely is area where the RF antenna acts. It is easy to notice that the electron temperature in configuration IV (blu line) near to the extraction region is considerably lower than in configuration II (red line). For comparison reason, also the zero filter

field case (green line) is shown.

From preliminary tests, configuration IV, which is equal to configuration II, seemed to be the most promising with respect to configuration III, hence I'm not presenting results from this configuration. Configuration V, instead, started to be studied after the completion of this thesis.

Figure 4.26 shows the comparison between configuration II and IV performances. Being the two configurations equals from the electrical connection point of view, this comparison reduces actually in the comparison between the old and new magnetic circuit configurations.

It is possible to conclude that the magnetic filter field produced with Configuration IV, which acts upon a wider region with respect to that produced by Configuration II, is more efficient to prevent high energy electrons from diffusing into the extraction zone.

Electron current decreases more and more rapidly, meaning that fewer electrons are available in the extraction zone because they are more confined in the extraction region. As a consequence less negative ions are destroyed and thus ion current increases.

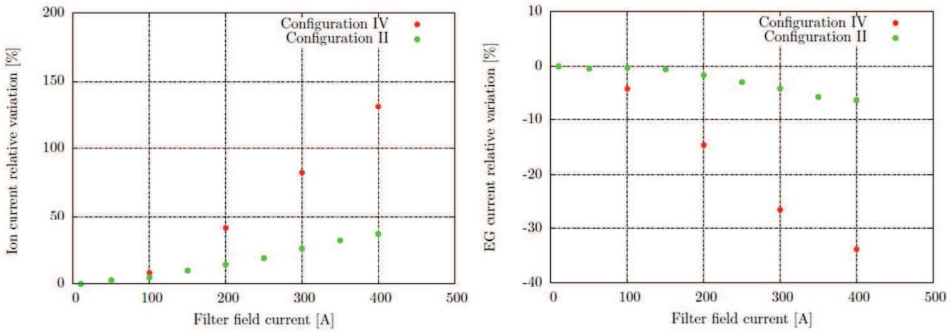

a) b)

Figure 4.26: Comparison of the configuration II and IV performances. The new magnetic circuit of the configuration IV is more efficient in preventing electrons from diffusing from the driver region to the extraction zone. Oxygen is the reference gas.

4.4 NIO1 improvements

As noticed during experimental sessions, the extraction system does not match to the beamlets divergence requirements for a suitable calorimetric observation (to high divergence, which does not allow to clearly distinguish beamlets imprints on the CFC tile). The extraction system of NIO1 needs some improvements in order to achieve a good beamlet optic, allow also better observations with the diagnostics systems.

Therefore the replacement of the present EG with a new one whose geometry can provide electrostatic lenses capable of achieving a good beamlet optics is mandatory. Also new magnets for the suppression of co-extracted electrons are highly desirable in order to reduce the Penning effect (which will be described in section 4.4.2) and avoid the interception of the hydrogen beam with the internal surface of the EG aperture due to an excessive bending.

This is the starting point for the next sections, where the simulation work related to the design of the new EG and the new magnets for NIO1 will be presented. In particular, this design was also a chance to change the magnetic configuration with the new CESM+ADCM configuration presented in section 2.5.4, allowing for a future experimental validation of this new configuration, in addition to the one presented in chapter 5. Unfortunately, despite the arrangement of NIO1 accelerator columns as a tower of alternate electrode rings and insulators allows a fast replacement of the EG by directly substituting the relative flange, a series of delays didn't allow the installation of the components I have designed. Therefore no experimental evidence of the improvements can be presented.

4.4.1 New EG design

The EG profile was optimized starting from the present configuration, reported in **Figure 4.27** (a).

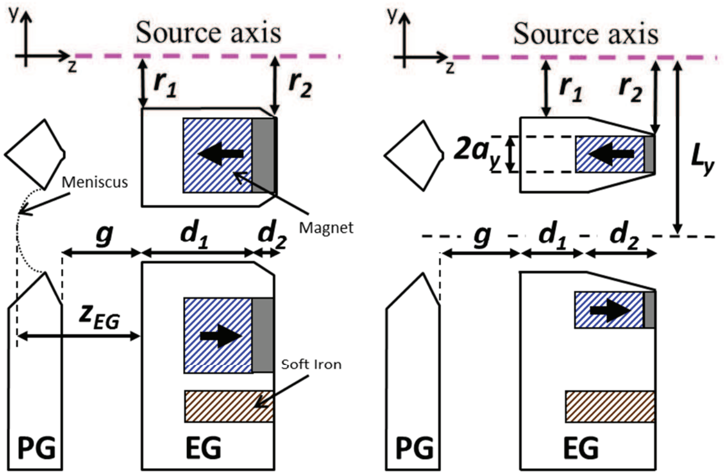

(a) (b)

Figure 4.27: Detailed top view on ½ of the ion extraction region. (a) Old EG layout. (b) New EG layout. The geometrical parameters of the extraction system g, r_1, r_2, d_1 and d_2 are shown. The dimensions of these parameters in the two configurations are listed in **Table 4.1**.

In particular, the final goal was to increase the clearance between the EG aperture and the beamlet envelope, while maintaining a low beam divergence. This can be achieved by increasing the penetration of the acceleration potential into the EG aperture, inducing a beam focusing at the EG exit, that compensates for the successive defocusing effect due to the diverging lens at the PA aperture entrance. As said in section 2.5.3, the electrostatic lenses depend on the geometrical parameters of the extraction system. With reference to **Figure 4.27**, these geometrical parameters are: g is the extraction gap distance; r_1 and r_2 are the entrance and exit radii of the EG aperture, respectively; d_1 and d_2 are the length of the cylindrical and conical parts of the EG aperture. In **Table 4.1** the dimension of these parameters are listed.

Table 4.1: Summary of the geometrical parameters of the old and new extraction sytem for NIO1.

Geometrical parameters (mm)	Old Extraction System	New Extraction system
r_1	3.2	3.5
r_2	4.1	5
d_1	8.8	4.8
d_2	1.5	5.5
g	5	5

SLACCAD code was extensively used to find the best compromise of the geometrical parameters g, r_1, r_2, d_1 and d_2 to maintain a low divergence at the accelerator exit, which means it was a five dimensional investigation. Obviously some constraints exist on these parameters, to avoid overlapping of the aperture with the cooling channels or magnet housings, and to keep the grid robust and well cooled. The total grid thickness was kept constant in any case, with the same value as the present grid: 10.3 mm. I performed a scan on the EG voltage in the range $4 - 8$ kV in order to get the usual 'smile' curve, for each variation of the geometrical parameters of the EG, while keeping the acceleration voltage $V_{PA} = V_{rep} = 60$ kV. The extracted current density, instead, was varied around the nominal value of 300 A/m^2.

The EG voltage scan allowed me to compare all configurations at perveance match condition, i.e. in the best optics condition that is the minimum of the 'smile' curve. Examples of the results obtained are shown in **Figure 4.28**, reporting the divergence and clearance for different geometries at perveance match condition.

Some considerations can be then derived: the cleareance benefits from the entrance radius r_1 increase, as well as of the exit radius r_2, but only up to a certain level when the beneficial effect saturates: upon increasing r_2 from 4.1 to 5 mm the cleareance increases too, while beyond 5 mm there are no more benefits; reducing d_1 (therefore increasing d_2) almost has no effect on the beamlet divergence, provided that the gap distance is sufficiently high ($g > 4$), but strongly increases the clearance of the beam. The optimal value is found when the connection point of the cylindrical and conical parts of the internal surface of the grid aperture, almost matches the point where the beam starts to expand under the effect of the divergent lens at the EG entrance.

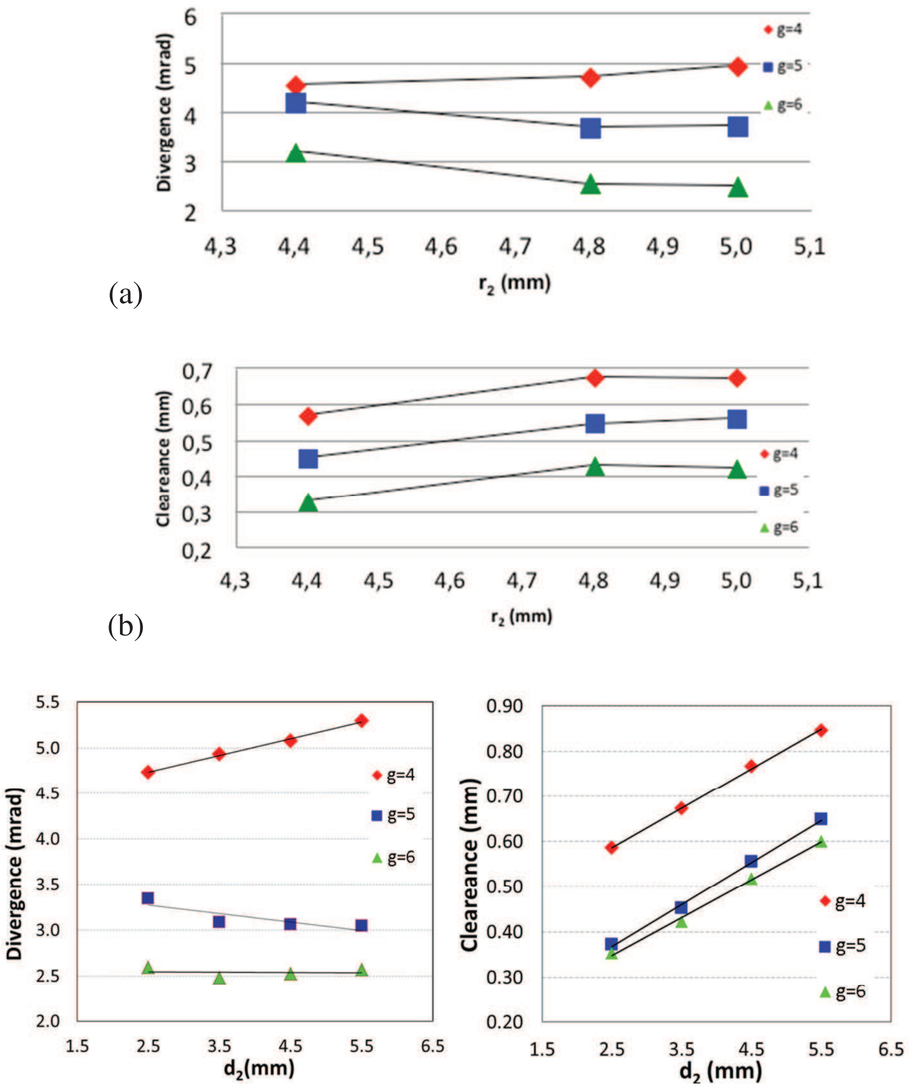

(a)

(b)

(c) (d)

Figure 4.28: SLACCAD results when the parameters r_2 and d_2 is changed, for three values of the extraction gap g. In (a) and (c) the beam divergence at the exit of the accelerator is reported, in (b) and (d) the minimum clearance between the beamlet and the EG edge. In these cases the entrance radius is $r_1 = 3.5$ mm, but similar trend were found also with other radial sizes.

Based on the previous considerations a fine scan was performed on a subset of geometries upon respecting the previous findings, to test the effect of the various geometrical parameters at different extracted current densities. **Figure 4.29** reports the results of this scan for the geometry finally adopted in the new EG design thanks to its reliability: the divergence remained low in a wide range of extracted current density, and the clearance corresponding to the optimal focusing was acceptable in most cases.

In the end, SLACCAD simulations lead to the design of the new extraction system, shown in **Figure 4.27** (b) and table **Table 4.1** in comparison with the old design. Summarizing, in the present configuration, EG_1 aperture has an entrance radius $r_1 = 3.2$ mm, exit radius $r_2 = 4.1$ mm, length of the cylindrical and conical part inside the aperture of $d_1 = 8.8$ mm and $d_2 = 1.5$ mm respectively, for a total thickness of 10.3 mm. The gap distance g between the PG and EG is g=5 mm. The new design, EG_2, instead, has an entrance radius $r_1 = 3.5$ mm, exit radius $r_2 = 5$ mm, length of the cylindrical and conical parts inside the aperture of $d_1 = 4.8$ mm and $d_2 = 5.5$ mm. The twe configurations share the total thickness of 10.3 mm and the extraction gap length $g = 5$ mm. This new design ensures a lower beam divergence in a wide range of current density as well as a better cleareance with respect to EG apertures.

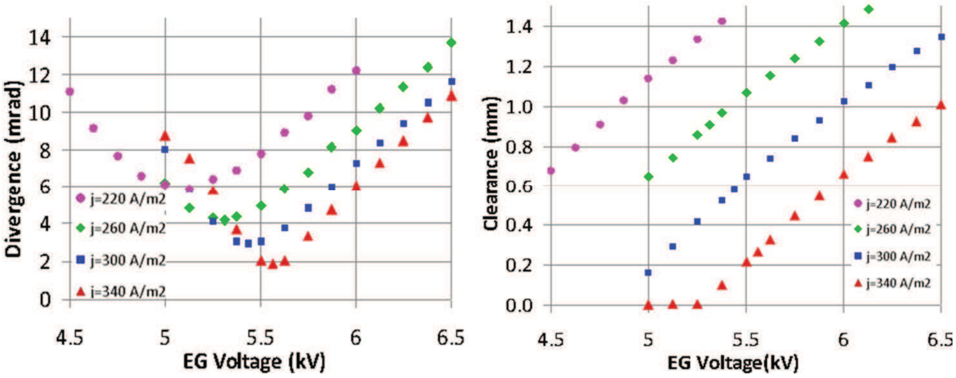

Figure 4.29: Divergence and cleareance in fuction of the extraction voltage, at different current densities, for the new extraction grid EG2, having $r_1 = 3.5$ mm, $r_2 = 5$ mm, $d_1 = 4.8$ mm ($d_2 = 5.5$ mm) and $g = 5$mm.

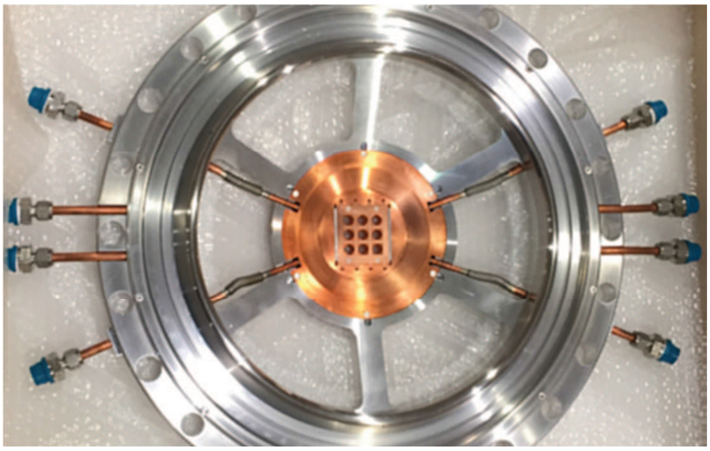

Figure 4.30: The new EG for NIO1, together to its supporting structure, ready to be installed.

4.4.2 New magnetic configuration for the new EG

The magnetic configuration of EG_1 features the usual 4 vertical arrays of CESM magnets (5.2mm x 5.8mm x 64mm, array 'c' in **Figure 4.35**) with alternated magnetization along beam direction. The residual beamlets deflection after EG_1 is cancelled by a second set of equivalent magnets, embedded in the PA, with opposite orientation with respect to EG_1 CESM, similarly to the SPIDER magnetic compensation system (see section 3.1). The B_y component of NIO1 CESM magnets is presented in **Figure 4.32** (a) with and without PA magnets. Anyway the present EG_1 array ‘c’ features $SmCo\ B_r\ = 1.02$ T magnets, which proved to generate a B_y component too strong for a hydrogen beam: ions are bent so much that they intercept the internal surface of EG aperture (see **Figure 4.31**).

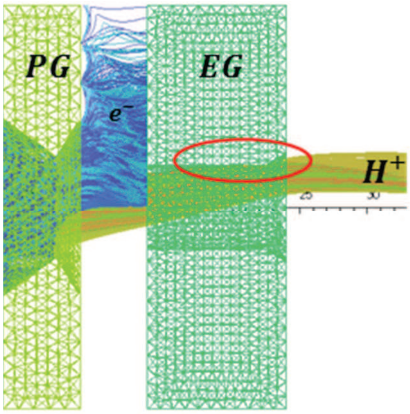

Figure 4.31: The simulation here presented is an example of the effect of the too strong EG_1 magnets, which bend the beam so much to make it intercept the inner surface of the EG aperture. The simulation was carried out with OPERA.

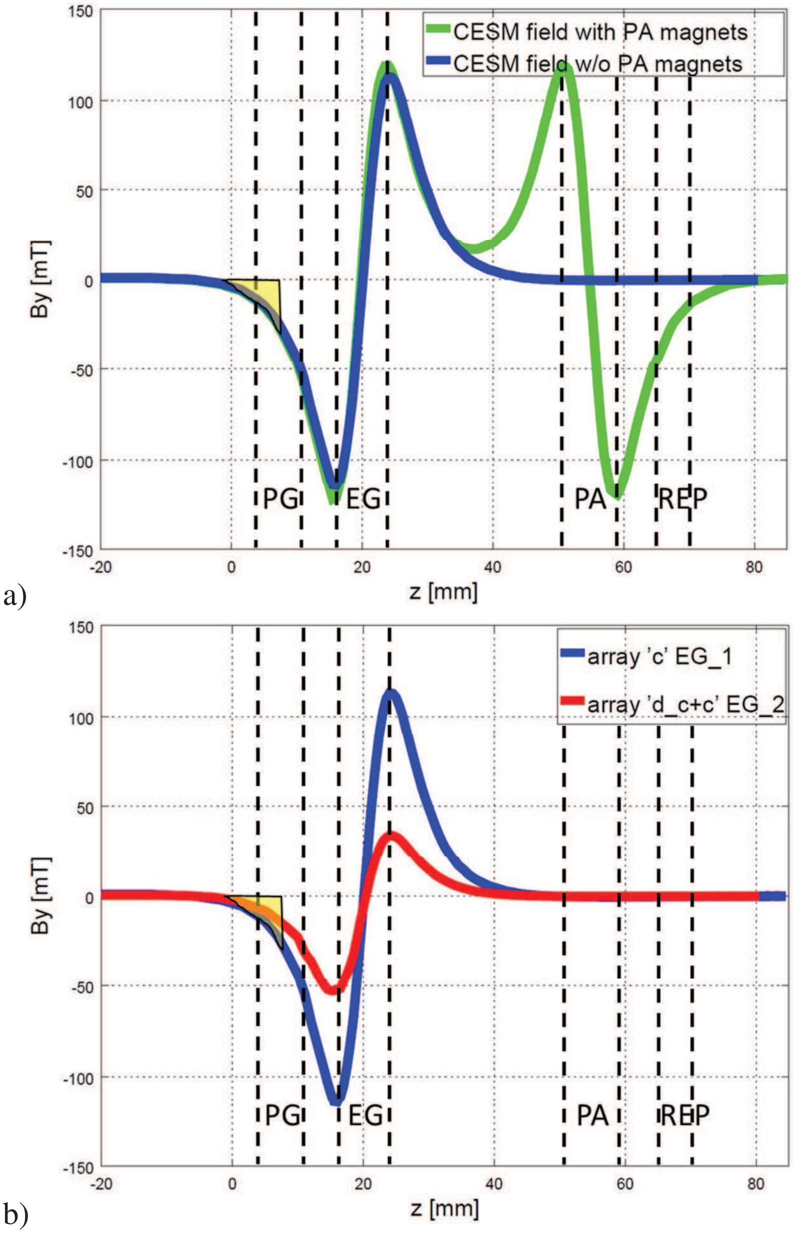

Figure 4.32: (a) By component of the magnetic field generated by B_r = 1.1 T SmCo CESM magnets with (green line) and without (blu line) magnets embedded in the PA. (b) The symmetric By field generated only by CESM (blue line) in comparison with the non-symmetric one generated by the CESM + ADCM configuration (red line). Yellow area highlights the fraction of the By component inside the plasma chamber.

Therefore, even if there is enough space in the EG_2 to insert EG_1 magnets, there is the need of a better tuning of the B_y component of the magnetic field inside NIO1, by acting on the B_r or on the size of the permanent magnets. Furthermore this opportunity was taken to completely change NIO1 magnetic configuration by introducing the new CESM+ADCM configuration (see 'array a+c' of **Figure 4.35**), that is now available and already presented in details in section 2.5.5.1. In particular, I've carried on this work in a strict collaboration with LNL colleagues in Legnaro.

Proper design of the new magnet configuration for NIO1 has to fulfil some conditions. As the main CESM target is to stop co-extracted electrons from the source, the first condition to meet is that upstream B_y peak must be large enough to dump electrons on EG face (**Figure 4.34** (a)) while avoiding interception of the EG aperture edge (see **Figure 4.34** (b)), since this occurrence can cause highly localized thermal loads that can damage the aperture and produce secondary electrons that are accelerated. The other condition is the zero ion deflection after EG.

Even if the first condition seems easy to fulfil, a fine tuning of the B_y profile is highly desirable, since the unconditional increase of the B_y upstream peak can have some drawbacks, such as too high a deflection for ions like in the actual case. But these drawbacks extend also to electrons: if electrons are deflected too much, they can reach the field lines of the CESM of the next row, which have opposite orientation since CESM magnetic orientation alternates from row to row. When this happens, electrons start to spin around the extraction gap back and forth (see **Figure 4.34** (c)),. This behaviour, known as Penning effect, may cause breakdowns in the PG-EG gap as in the case of NIO1 [[**55**].

During some experimental sessions in oxygen, indeed, a strange phenomenon was recorded, as shown by **Figure 4.33**: while increasing the EG voltage from zero to a certain value, V_{ext-A}, no breakdown events occurred. From V_{ext-A} to another voltage value, $V_{ext-B} > V_{ext-A}$ the voltage cannot be held anymore. Further increasing the voltage beyond V_{ext-B}, it could be hold again. Hence, a forbidden EG voltage range appeared, whose extremes V_{ext-A} and V_{ext-B} depend on the gas pressure.

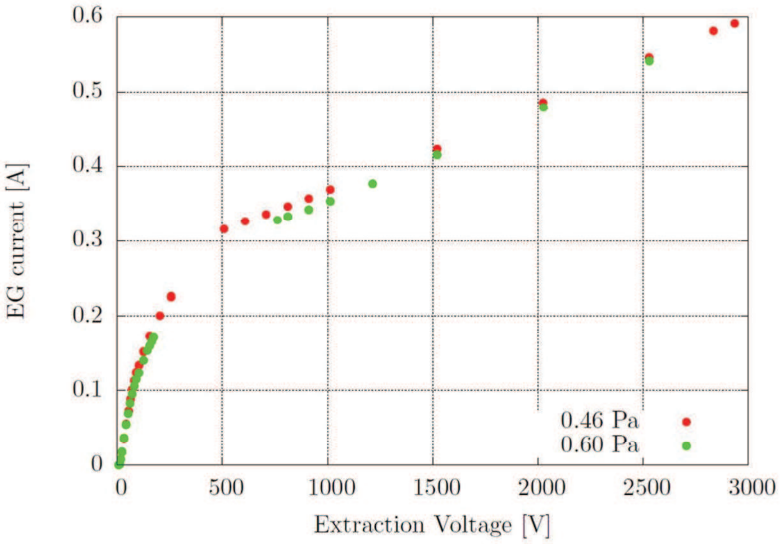

Figure 4.33: Forbidden extraction voltage range observed during experiments in oxygen. Range limits changes with the pressure.

With a dedicated OPERA simulation (see Figure 4.34 (c)) I could verify that co-extracted electrons undergo this Penning effect due to the too strong magnetic field provided by EG1 CESM magnets.

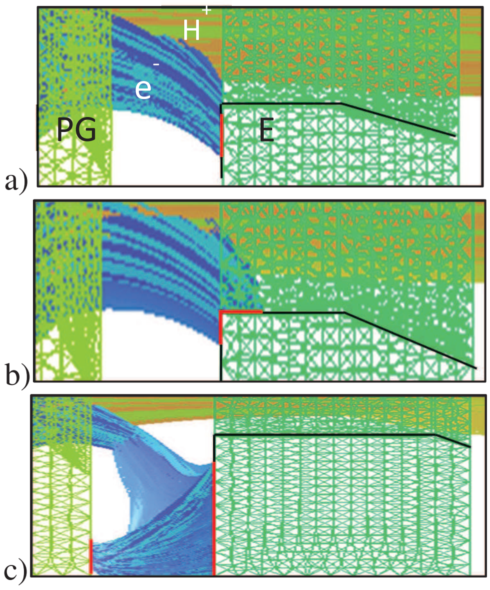

Figure 4.34: Co-extracted electrons trajectories (in blue) in the PG-EG gap under different B_y suppression fields. Red areas highlight impact position on EG. (a) Too weak field causes electron to impact on EG aperture edge. This is not desirable as the heat load on the edge could damage EG. (b) A properly tuned B_y filed component makes electrons impact on EG in the right way. (c) When the By field is too high part of the electrons are not stopped on the EG but are deflected enough to reach By field lines with opposite orientation, making them go back and forth in the extraction gap (in this picture an example with EG$_1$ is shown). This is also not desirable, because in certain conditions it can cause breakdown.

Since Penning effect is of magnetic nature, it can seem strange that the applied voltage could influence it in such a way to cause a forbidden voltage range rather than causing breakdown events at all times. Nevertheless, the process can be described as follows: as soon as the extraction voltage is applied, the co-extracted electrons start to be bent under the effect of CESM field and undergo Penning effect; however, until the applied voltage is low, co-extracted electron are too few to cause breakdown. The increase of the voltage increases also the extraction of the electrons and when they are enough, breakdown occurs. Anyway, when the voltage is very high, electron trajectories are stiff enough to reduce the amount of electrons that undergoes Penning effect, allowing again extraction operations without breakdown events. This, of course, has nothing to do with the high voltage holding limit of the extraction gap that is supposed to still hold.

Concerning the second condition, as already said, in the present NIO1 configuration the PA grid also features some embedded magnets, thus adopting the same strategy used for the magnetic compensation system of SPIDER.

However it was chosen to introduce also in NIO1 the CESM+ADCM, or array ‘a+c’ (see **Figure 4.35**), configuration proposed by Consorzio RFX for MITICA. Briefly summarizing, the effect of this configuration is to unbalance the B_y component of the magnetic field with respect to the EG plane, by increasing it on the upstream side and decreasing it on the downstream side (red line in **Figure 4.32** (b)). In this way it is possible to shape the B_y profile so that the integral of equation 2.63 is zero, thus cancelling the residual deflection of the ions. Since the array ‘a+c’ typically requests very thin magnets, I have also considered the alternative configuration, array ‘d_c+c’. In any case both configurations have advantages and drawbacks, which I will present later.

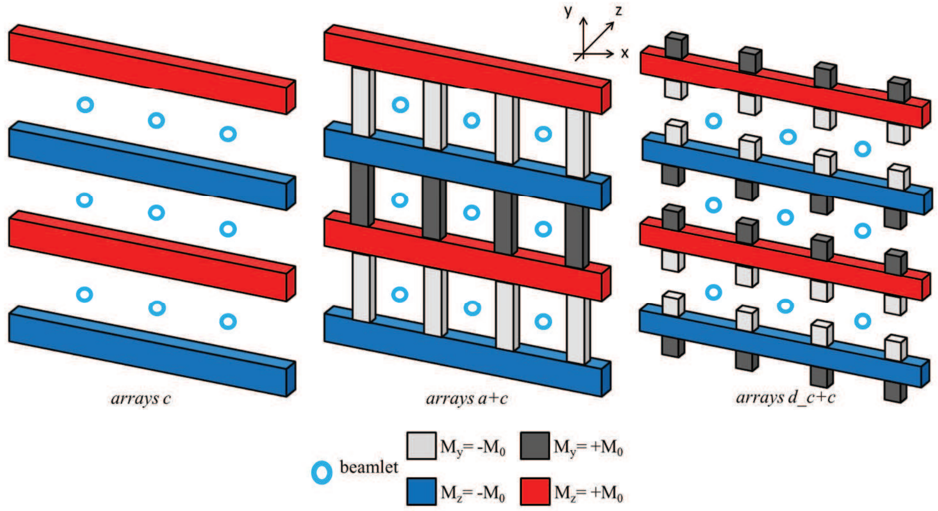

Figure 4.35: Embedded EG magnets configurations. Array c features just CESM magnets and is used with EG1. Array a+c feature CESM and ADCM in the classical grid configuration. Array d_c+c is a modified version of array a+c that will be used in EG2 for manufactory constrains.

Whatever CESM + ADCM solution (a+c or d_c+c) will be adopted for the EG_2, PA magnets will remain in their place, as their removal would increase a lot the cost and the shutdown time of NIO1 and they allow the suppression of electrons coming from the stripping process in the accelerating gap. Thus during the design of the CESM+ADCM configuration I had to take into account also PA magnet contribution.

I have designed the new magnetic configuration of the EG_2 magnets by means of the 3D simulation provided by OPERA. As I don’t want to investigate any interaction among the beamlets, but just their interaction with the magnetic fields, I concentrated on single beamlet simulations. The first step in the design procedure was to perform electrostatic simulations to find the most suitable voltage for EG_2, in order to achieve the best divergence, i.e.: the best beamlet optics, at the nominal beamlet energy of 60 keV, by keeping -60 kV as PG voltage. It turned out that EG_2 voltage should be -53.5 kV ($V_{ext} = 6.5$ kV) to have a divergence less than 7 mrad.

Once found the best optical condition from the electrostatic point of view, it is time for magnet design. The procedure I've followed was a synergic work between theory and simulation, as proposed by LNL colleagues. With reference to in **Figure 4.36** (a), I've determined the geometrical dimensions along x and y direction of the CESM and ADCM magnets by means of the equations presented in section 2.5.5.2, which depend on these parameters and on remanence of the magnets. For mechanical reasons, I've instead considered fixed the geometrical dimensions of ADCM and CESM length a_z along z direction and CESM pitch L_y (see in **Figure 4.36** (b)), as well as CESM length along x direction.

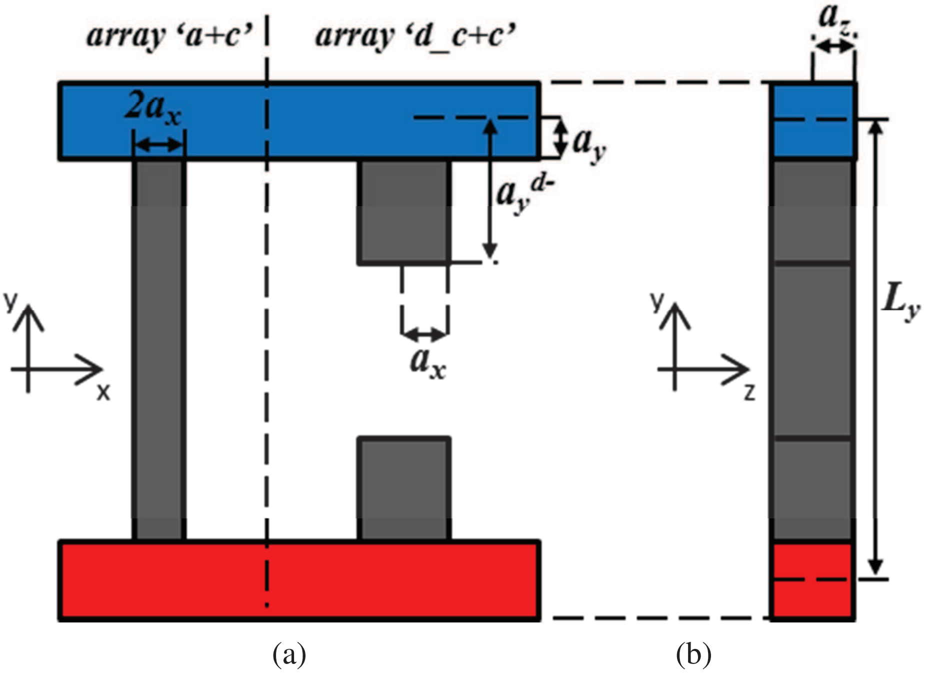

(a) (b)

Figure 4.36: (a) xy cross section of CESM+ADCM configuration with array 'a' and 'd_c+c' parameter definition. (b) corresponding zy section.

I've started the design procedure without considering PA magnets. Hence, I've tuned the intensities of the upstream and downstream peaks of the B_y profile by changing magnet dimensions and B_r in the equations, until reducing to zero residual ions deflection after PA ($\alpha_f = 0$). I've then crosschecked the theoretical predictions by inserting the corresponding magnetic field in the previous OPERA simulation. Afterwards, I've also included PA magnets in the simulation, which led to a final deflection angle, α_f^{PA}, that is about the theoretical $\alpha_f = 0$ plus 0.8 mrad. Lastly, I've repeated the procedure by setting $\alpha_f = -0.8$ mrad as ion deflection criteria, rather than zero.

Nevertheless, there is also the other criterion to fulfil: the suppression of co-extracted electrons. In principle this criteria can be defined in this way: let x_e and y_e be the electron position at EG front face; electron deflection has then to fulfil the $min\{x_e^2 + y_e^2\} \geq r_1^2$ condition, being r_1 the radius of the EG entrance aperture. Anyway, electron deflection cannot be indefinitely high since Penning effect has to be avoided, too. Unfortunately, there are no theoretical considerations to match both conditions. Hence, electrons behaviour check by means of simulations is the only help to achieve the correct amount of electron deflection.

Summarizing, the design procedure was carried out by checking the results of the theoretical considerations described before, with 3D simulations performed by OPERA and from which electron impact on EG and residual ion deflection information were registered. This was done by simulating the magnetic field that the magnets would generate and whose dimensions were indicated by the theory. When both design constrains were achieved, the configuration can be considered approved. As last notes, the entire procedure was done to design both an array 'a+c' and an array 'd_c+c' configurations, while the calculation of magnet size taking into account also some rounding for convenient manufacturing, completed the boundary conditions frame.

The set of magnets listed in Table 4.2 is the result of this procedure. For each set in the list, the following quantities are shown: geometrical dimensions, magnetic remanence, final ion beam deflection (theoretical and simulated with and without considering PA magnets) and information on operational parameters at which they were designed for. Set 34d presents a 'd_c+c' configuration at nominal parameter, while sets 36 and 37 present the same magnetic configuration, but designed for lower operation parameters, as well as set 39 who has the 'a+c' configuration.

Table 4.2: List of approved set of magnets for the new EG. α_f is the theoretical residual deflection after PA grid without considering PA embedded magnets; α_f^{sim} and α_f^{PA} are simulation results for deflections with and without PA magnets, respectively; $a_z = 5.2$ mm for all cases; ion beam current $I_b = I_0(V_{ext}/V_{ext0})^{3/2}$ where $I_0 = -13.61$ mA and $V_{ext0} = 6.5$ kV as reference value.

Set #	type	V_{tot}	V_{ext}	B_r	a_x	a_y^{d-}	a_y^{a}	a_y^{c}	α_f^{theo}	α_f^{sim}	α_f^{PA}
Units		**kV**	**kV**	**T**	**mm**	**mm**	**mm**	**mm**	**mrad**	**mrad**	**mrad**
34d	$d_c c$	60	6.5	1	1.7	3.4	2.7	2.7	-0.26	-0.39	0.29
36	$d_c c$	31	3.36	1	1.7	2.87	1.9	1.9	-0.43	-0.66	0.32
37	$d_c c$	9.17	0.99	0.39	1.7	3.42	2.7	2.7	-0.46	-0.68	-0.06
39	ac	13.1	1.42	0.39	0.4	d.n.a.	3.4	3.4	-0.67	-1.49	0.22

The need of sets of magnets designed for lower operation parameters is explained soon. In any case, all listed sets have a very good electron impact on EG, like the case shown by **Figure 4.34** (a). In particular, set 34d was chosen as new reference configuration for NIO1 at nominal parameters (beam current density and energy 300A/m^2 and 60keV).

Anyway, since NIO1 has not started operations with cesium jet, when EG$_2$ will be installed the working parameters will be much lower than the nominal one. Thus I've checked the behaviour of the 34d magnets set at lower current density, by scaling the voltages according to $V_{ext} \propto j_{ext}^{2/3}$ and $V_{ext}/V_{acc} = cost$ (see section 2.5.3.3), as to keep perveance constant. It turned out that the residual deflection gets slightly worse at very low current density (blue dots in **Figure 4.37**). Thus, a scaling down of the reference 34d set was needed in order to have magnets more suitable in these conditions.

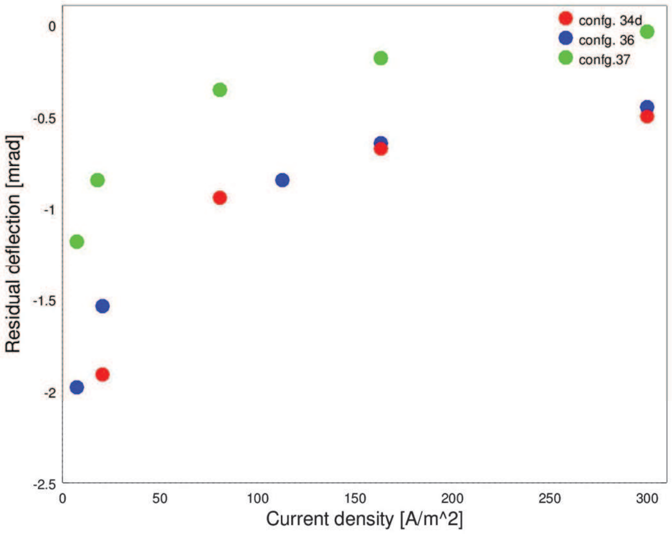

Figure 4.37: Residual deflection of the chosen magnetic configurations at different beam current density. At low current density magnets efficiency slightly decreases. Note that PA magnets effect is not taken into account in these simulations but their net effect is to increase the residual deflection of about 0.8mrad.

Note that electron deflection α_e depends on magnetic field integral in the first gap divided by the Larmor radius and is roughly proportional to $(I_A + I_C)/V_a^{1/2}$. Electron deflection criteria is satisfied if $\alpha_e z_{EG} > r_1$, r_1 being the EG$_2$ aperture radius and z_{EG} is defined in **Figure 4.27**; a reliable calculation of this margin is not complete, consequently only a tentative scaling law is given as

$$I_A + I_C \propto r_1\sqrt{V_{ext}} \qquad 4.3$$

By scaling V_{ext} it is possible to find the corresponding $I_A + I_C$ value from equation $I_A + I_C \propto r_1\sqrt{V_{ext}}$ 4.3. Scaled B$_r$ and geometrical parameters of the magnets can then be retrieved using again the theoretical consideration used before.

Sets 36, 37 and 39 in **Table 4.2** show examples of scaling from 34d to lower current densities. **Figure 4.37** shows set 36 and 37 residual deflection at different current densities, with respect to the 34d one. Note that the effect of PA magnets in **Figure 4.37** is not taken into account (they increase deflection by $+0.8$ mrad on average).

Nevertheless, all sets of magnets listed in **Table 4.2** are considered for NIO1 installation: set 34d is the reference configuration at nominal operation parameters, while cancellation of ion deflection for set 36, 37 and 39 is acceptable even when V_{ext} and V_{tot} are less than 35% of their nominal values (keeping perveance constant) and thus are suitable for operations without cesium in the source. As further considerations on the designed magnets, sets 36 and 37 have some additional convenient features: set 36 can fit both in EG$_1$ and EG$_2$; set 37 and 39 operate with lower voltage but require a lower B$_r$, suitable for more economic and/or durable material (hard ferrites).

However, even if I have designed array ‘a+c’ and ‘d_c+c’ in such a way that both would respect the two constrains for the magnetic field design (proper electron impact on EG face and low residual deflection after PA) some manufacturing consideration has to be done: since a+c configuration foresees 0.8mm thickness for ADCM magnets, manufactory tolerances can affect ADCM efficiency, as the resulting magnetic field is very susceptible to this parameter. d_c+c configuration then suffers from manufactory issues less than a+c configuration, whose thickness is larger, but the material exploitation is less effective.

5 Design and experimental validation of ADCM deflection compensation method on NITS

In 2015 I was involved in an intense collaboration activity established between Consorzio RFX, and JAEA Neutral Beam Heating and Technology Group (now part of QST, National Institutes for Quantum and Radiological Science and Technology) in Naka, Ibaraki, Japan. The main goal of this collaboration is to maximize the effectiveness of the Neutral Beam Injector for ITER (MITICA) and JT60-SA.

During 2016, the collaboration was fruitfully initiated with the joint activities:

- Experimentally test (for the first time) the ADCM configuration (section 2.5.5) for counterbalancing the undesired beam deflection in the Negative Ion Test Stand (NITS) at QST, Naka, using an extraction grid designed and built by Consorzio RFX.

- Benchmark the numerical simulation developed by QST and RFX teams, (using different codes SLACCAD, OPERA, BEAMORBT, COMSOL, EAMCC) against the experimental data obtained in the above-mentioned campaign. Especially QST colleagues carried out this part and thus it will be not reported in this thesis.

The Joint Experiment is a teamwork and my major contribution consisted in the optical design of the EG provided by Consorzio RFX and in the design of its CESM and ADCM magnets [30]. This design activity is the core of work made in Consorzio RFX in preparation for the experimental session at NITS source. Unfortunately, I couldn't join my colleagues during measurements in Japan. However, I have helped them in the data analysis activities. Therefore, I will not describe the details of the experimental sessions but I will present the main results obtained by this collaboration activity in 2016. During 2017 a new experimental campaign is also foreseen, based on the observations done during this first part of the collaboration.

5.1 NITS ion source

The Negative Ion Test Stand device (NITS) [58] is a small, flexible and easily accessible multi-beamlet negative ion accelerator, available at QST lab in Naka. NITS is constituted (see **Figure 5.1**) by a "kamaboko" arc plasma source at operational pressure of 0.25–0.3 Pa, which is equivalent to the ITER requirement, featuring also a Cs oven to exploit the surface production. Negative ions are extracted from the PG through a 7 × 7 aperture array system, with 14 mm in diameter, by the EG, which is followed by a single acceleration stage GG. A large beam line vessel, which allows the installation of multiple diagnostics, is appended to the accelerator.

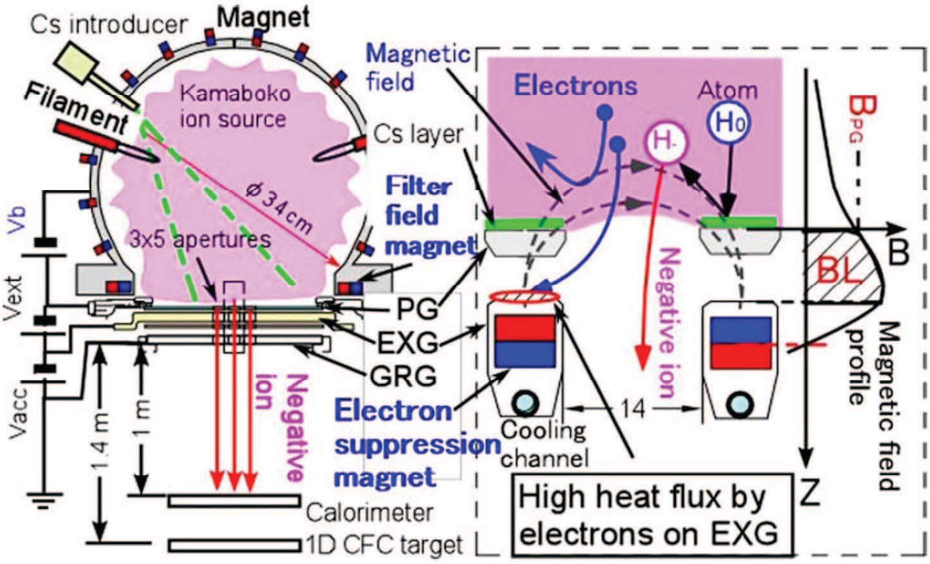

Figure 5.1: Cross sectional views of the NITS ion source and extraction mechanism [58].

Permanent magnets in the source flange produce a magnetic filter field having horizontal direction and a value of about 15 mT on the Plasma Grid. Extraction voltage is up to 10 kV, maximum acceleration voltage is 60 kV, with the limit of 30 kV for stable continuous operation, which is our case. Extracted H^- ion current density can reach ~ 170 A/m^2 when cesium is deposited on the PG in order to exploit the surface production mechanism.

5.1.1 NITS design modification and diagnostics overview

In view of the joint experiments, NITS was modified to reproduce the design solutions adopted for MITICA and ITER HNB [59],[60] and to operate it under "similarity" conditions so as to measure the beam optics characteristics of the ion extractor and accelerator, using a unidirectional carbon fibre composite (CFC) target and an IR camera.

The main modifications were:

- The original Plasma Grid was substituted with a new PG with chamfered apertures having profile very similar to that of MITICA/HNB, which in turn is based on the profile developed at IPP Garching for RF driven sources (PG part in **Figure 5.2**). The new PG was designed manufactured by QST and has 7x7 apertures with an aperture pitch of 19 mm (horizontal) and 21 mm (vertical). In addition, a mask was used in order to blind the central row of apertures, obtaining an upper and a lower group of 3x5 apertures. The need of this separation is explained in few lines, while the final aspect of the new PG is presented in **Figure 5.4** (b).

- A new Extraction Grid (EG), with aperture profile almost identical to MITICA/HNB (EG part in **Figure 5.2**), was designed and manufactured by Consorzio RFX [61] and then installed on NITS. As well as the PG, this new EG also features separated upper and lower group of 3x5 apertures, in coincidence of PG apertures. The magnetic configuration of the magnets embedded inside the EG differs in the two aperture groups: the both feature CESM magnets for co-extracted electrons suppression, but only the upper part magnetically compensates the residual ions deflection caused by CESM, by means of ADCM magnets.

- Both extraction and acceleration gap length were also modified in order to reproduce as much as possible the electrostatic field configuration of MITICA/HNB extraction and first acceleration stages [11]. This was done considering the available NITS power supply voltage ($V_{ext} \leq 10$kV, $V_{acc} \leq 30\,$kV), the achievable extracted ion current density ($j_{ext} \leq 10$ A/m^2) and the room for manoeuvring the electrodes supporting structures to change the gap length; This required also the substitution of the support for the installation of the new EG for in the required position inside the NITS accelerator, provided by QST.

More details on the last two modification are presented in the next sessions, highlighting my personal contributes.

It is also worth to make a brief presentation of the diagnostic systems that NITS was equipped with for the Joint Experiment:

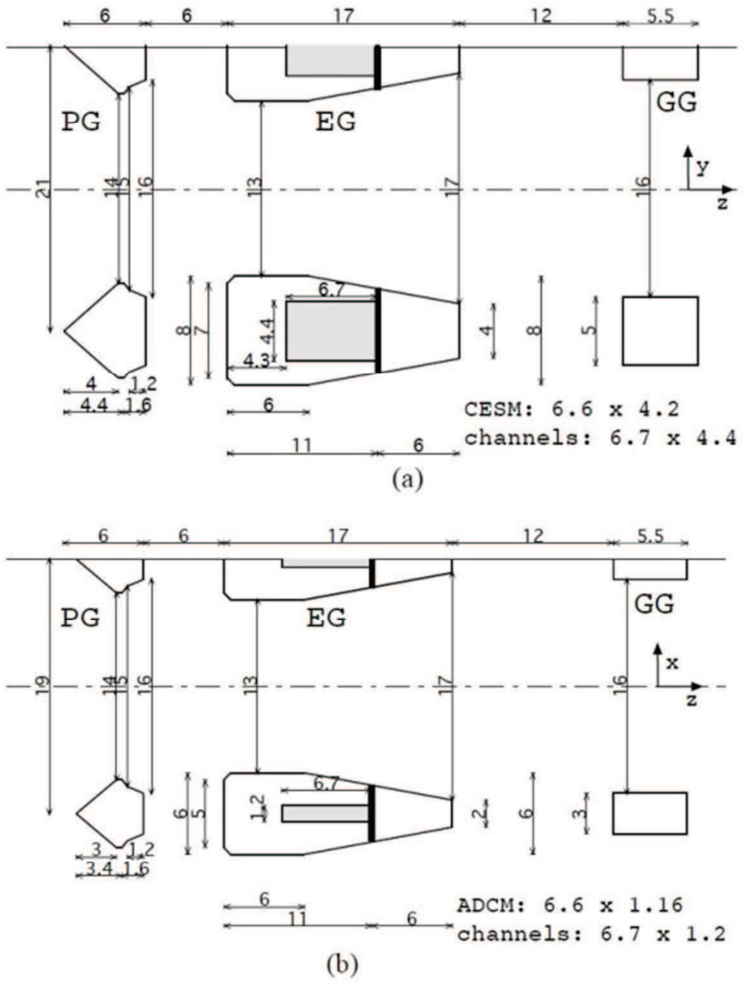

Figure 5.2: (a) vertical cross section and (b) and horizontal cross section of the NITS accelerator with the new EG (built by Consorzio RFX) and PG (built by QST). The aperture profiles and gap lengths were optimized so as to reproduce as close as possible the MITICA/HNB geometry.

- The beam target, constituted by 3 tiles of Mitsubishi MFC-1 carbon fibre composite (a single tile of this size was not available), for total target size was $155\ x\ 185$ mm^2, was positioned as close as possible (~800 mm) to the Grounded Grid (GG) on a water-cooled support (see left hand side of **Figure 5.3**). The carbon fibres in this material are aligned orthogonally to the tile surface so that the thermal conductivity along fibres is about 20 times larger than in the transverse directions. Thanks to the high longitudinal and low transverse heat diffusivity, the temperature increase on the downstream surface of the tile provides a very good measure of the power distribution deposited by the beam on the upstream surface. This allows producing a clear thermal image of each single beamlet, even in conditions of non-optimal beam optics. The CFC target vertical position is remotely controlled, and the absolute position was calibrated with respect to the accelerator axis, so that the absolute deflection of the beamlets along x and y axes could be measured.

Figure 5.3: (Left) photo of the unidirectional CFC target consisting of 3 CFC tiles with water-cooled copper support frame. (Right) optical image of entire beam passing through the beamline, the upper and the lower beamlet groups are visible in the right part, the retracted copper calorimeter is visible on the left, the CFC calorimeter (also retracted) is barely visible on the upper part of the picture.

- An infrared camera is used to detect beamlets footprints on the downstream side of CFC tiles with 640 (H) ×480 (V) pixels resolution and 30 fps frame rate. Based on the distance from the camera to the target, the effective image resolution is about 0.5 mm/pixel.

- Beyond the CFC target a retractable water-cooled copper calorimeter is used as beam dump when the CFC target is out of beam line.

Right hand side of **Figure 5.3** shows a photo of the CFC target (on top) and of the retractable copper calorimeter (in the centre) from behind. It can be also notice the separated two beamlet groups, exhibiting a pink luminescence. Lastly, a schematic of NITS during Joint experiment is presented in **Figure 5.4** (a).

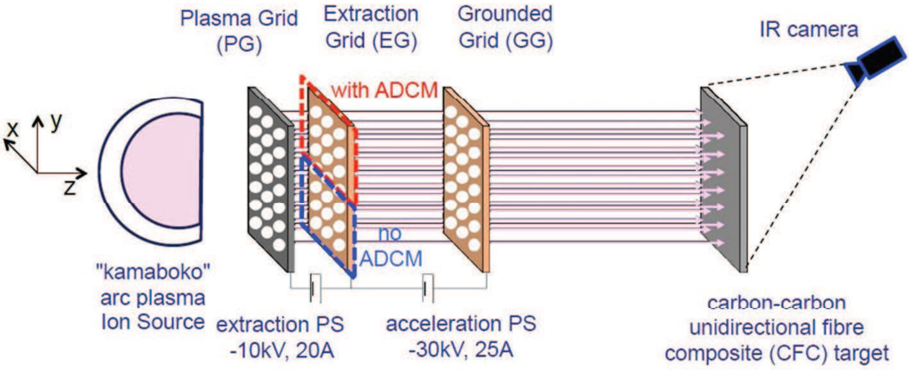

(a)


(b)

Figure 5.4: (a) conceptual scheme of NIST test facility and set-up for the joint experiments. (b) photo of the NITS molybdenum coated Plasma Grid with 3x5+3x5 beamlet apertures, the copper Extraction Grid is also visible behind.

5.2 Design of the new EG and ADCM for NITS

In this section the most important part of Consorzio RFX contribute to achieve the Joint Experiment goal is presented in details: the design of the EG to be installed at NITS and the magnets configuration design for this grid. This is also the core of my work in the collaboration.

5.2.1 Design of the new EG for NITS

While the modification of the PG and the supporting structures was performed by our Japanese colleagues, the design of the EG for NITS was carried on by Consorzio RFX.

Since the Joint Experiment aim is to test the solutions designed for MITICA, for the new EG and the gaps between the electrodes in NITS a MITICA-like geometry was chosen. This means that the r_{EG}/d ratios in both extraction and acceleration gaps were reproduced as close as possible. Nevertheless the optic provided this choice had to be tested because it is a crucial aspect: well-focused beamlets is indeed mandatory, since the beamlet deflection will be evaluated by looking at the correspondent footprint on the CFC target. This target is placed at 0.8 m downstream of the GG and therefore, in a bad optic condition, it would be impossible to measure beamlet deflections as the footprints would overlap. Hence I have done a series of electrostatic analyses using SLACCAD code, in order to evaluate final beamlet divergence (an example of these SLACCAD simulations is given in **Figure 5.5**).

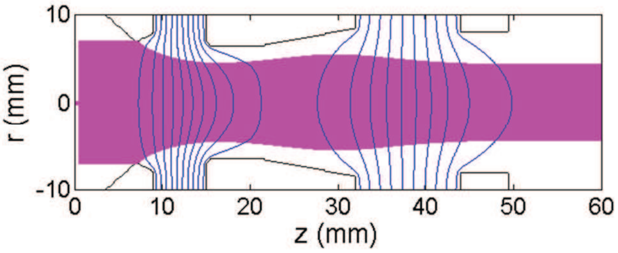

Figure 5.5: Example of a 2D electrostatic simulation of NITS accelerator with ITER-like EG geometry, using the SLACCAD code.

The used geometry is the MITICA-like geometry shown by **Figure 5.2**. The voltages considered for the simulations were the one provided by the extraction and acceleration power supplies, i.e. 10 kV and 30 kV, respectively. The typical extracted current density expected for volume process only is about 20 A/m^2 and about 150 A/m^2 when exploiting surface process by means of cesium vapour.

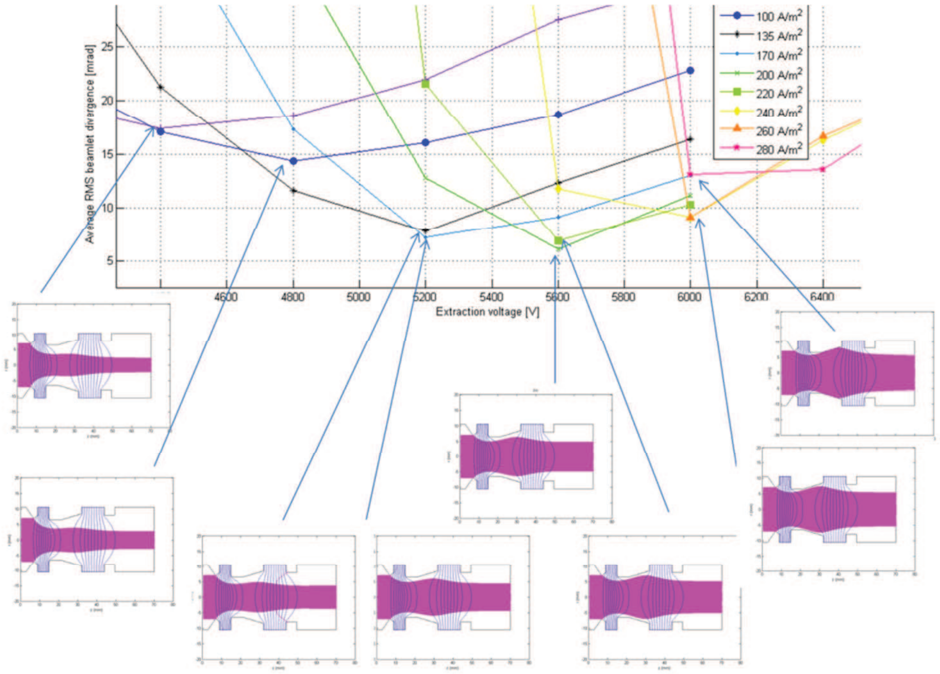

Figure 5.6: Example of the simulations done in NITS for the case of operation with Cs: the divergence of the beamlet at ~20mm from the exit of the GG (where the space charge is supposed to be fully compensated by the interaction with the background gas) is plotted in function of the extraction voltage and exhibits the usual 'smile' shape. Each curve corresponds to different current densities. The minimums represent the best optical conditions and the corresponding simulated trajectories are also shown.

The results of the SLACCAD simulation campaign (see **Figure 5.6**) show that, with the geometry reported in **Figure 5.2**, a good beam optic (divergence amount less than 10 mrad) can be achieved.

The engineering team was then responsible for the mechanical design, which had to assure a tight position of the permanent magnets, an easy and fast assembly procedure of the magnetic configuration, the interface with the NITS accelerator and the resistance to the thermal loads during the operation [61]. The final design of the new EG is actually constituted of two plates: the upstream part has cylindrical-conical beamlet apertures and also hosts the grooves (channels) for the magnet; the downstream side is a flat lid with conical beamlet apertures, hosting the anchor points to the supporting structure. Both plates present the two separated 3x5 aperture groups, plus 4 cylindrical holes for alignment pins at the corners (**Figure 5.7**).

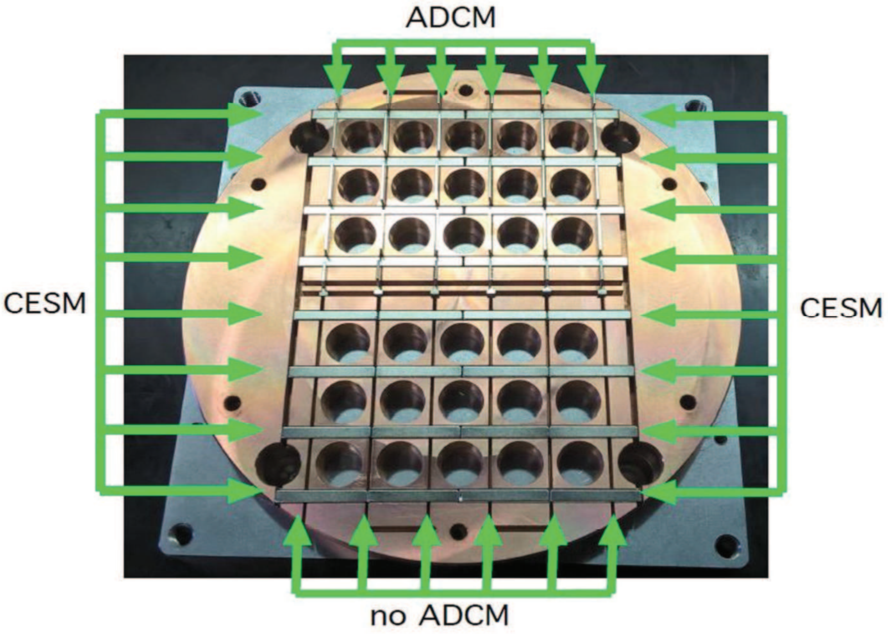

Figure 5.7: Photo of the upstreampart of the new EG for NITS during assembly. CESM and ADCM are installed in the grooves.

5.2.2 CESM and ADCM design for the new EG for NITS

Concerning the permanent magnets equipped on NITS during the Joint Experiment, filter field, CESM and ADCM [30] magnets are all made of Sm_2Co_{17}.

Filter field magnets are placed right behind PG and are embedded in the PG flange. They are arranged in a 'double C' pattern; in order make the filter field more homogenous inside the source (see **Figure 5.8**).

CESM magnets are arranged in horizontal rows embedded inside the EG between the beamlet apertures. All CESM are magnetized along the beam direction (z) and their orientation is alternate row by row, as usual. The profile of the vertical component of the magnetic field (B_y)

along the axis of each beamlet aperture is shown in **Figure 5.10** (b). It has a peak of ~ 50 mT just upstream of the EG and an opposite peak downstream of the EG.

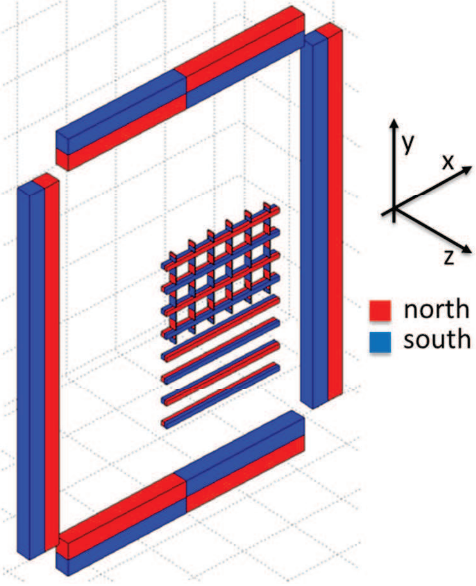

Figure 5.8: NITS permanet magnets configuration. The long magnets forming a square are the filter filed magnets. They are oriented such as to form a double c configuration.

As already said, for the Joint Experiments, the RFX EG apertures were divided in two separated groups of 3x5, in such a way it is possible to distinguish an upper and a lower part of the EG, as well as of beamlet groups. These two aperture groups feature different magnetic configuration: CESM+ADCM configuration is used only in the upper part, while leaving the bottom part to the usual CESM configuration. The left hand side of **Figure 5.10** shows the final permanent magnet configuration inside the new EG, while in the right hand side shows the different B_y profiles provided by the different magnetic configurations of the two parts of the EG, along the beamlet lines highlighted in the left hand side. In particular, these highlighted beamlets (C7 to C1) will be the reference beamlets for the rest of this section. **Figure 5.9**, instead, provides a detail of magnets installation, highlighting their magnetic orientations inside the EG.

The division of the new EG in two parts provides a way to compare directly the beamlet deflections caused by the two different magnetic configurations, and thus to proof the efficiency of ADCM compensation system for the residual deflection of the beamlets. It is worth to stress that this is the first time that this proof was done experimentally. This arrangement also allows extensive code-to experiment validations, under conditions similar to those of the HNB for ITER.

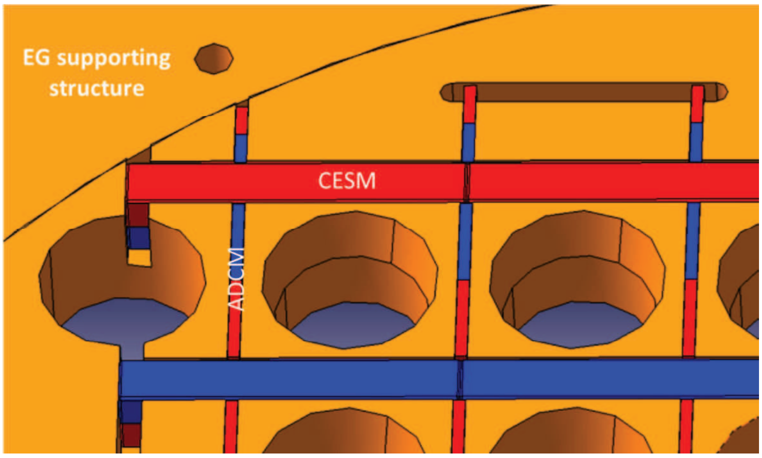

Figure 5.9: Detail of permanent magnets installation in the grooves of the upstream part of the EG. Magnetic orientations are also shown.

Anyway ADCM needs to be properly designed. The first part of the magnetic design consisted in a series of 3D single beamlet simulations, aimed at the optimization of B_y profile by tuning ADCM B_r. It would be possible to make the same optimization by keeping the maximum B_r achievable with SmCo magnets ($B_r = 1.1$ T) and changing the horizontal size of ADCM. However, in order to have operational flexibility, it was decided to realize three different sets of ADCM magnets. Therefore the three different sets must have the same size, otherwise they will not fit in the EG. In particular these three sets will be addressed as: the base set, which according to the simulation will lead to a complete compensation of ion deflection, the set with a magnetization $+20\%$ with respect to the base set (augmented set) and the reduced set, with a magnetization -20% with respect to the base set.

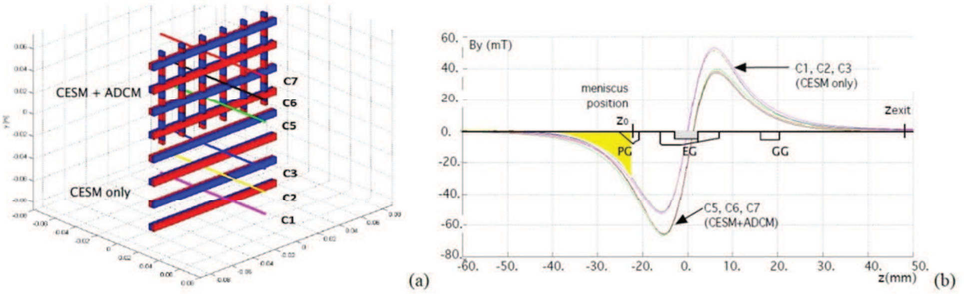

Figure 5.10: (a) layout of the permanent magnets embedded in the EG of NITS. In the lower part of the EG, only standard CESM are installed. In the upper part ADCM are also installed. (The upper and lower parts were swapped during experiments). (b) Profiles of the vertical component of the magnetic field B_y along the axis of different apertures (C1-C7). Profiles C1-C3 have zero average. The effect of the ADCM on profiles C5-C7 is clearly visible. The position of accelerator grids PG, EG and GG is also shown on the axis z.

After having fixed the size of ADCM magnets to comfortable value of 1 mm, I have performed the needed simulation to tune the magnetic remanence B_r of the ADCM. Following the usual design procedure adopted for the other two ion sources presented in the last two chapters, the first step had to be the search for the best optical condition at the desired operational parameters.

At first, I have decide to deal with a beam at the maximum achievable energy, meaning a beam of $30 - 40$ keV, since the maximum available acceleration voltage is 30 kV and the extraction voltage will be something in $1 - 10$ kV range. Hence I have made the usual divergence plot in function of the V_{ext} at different current densities, keeping V_{acc} constant at 30kV. This plot, shown in **Figure 5.11**, was done with 3D single beamlet OPERA simulations. In particular, these were simulation with CESM field only of the C6 beamlet (considering **Figure 5.10** (a) definition), that is the central beamlet of the upper part of the EG. These were not electrostatic simulations only, since interception condition of the beamlet with the EG, due to its deflection inside the EG aperture caused by CESM field, had to be avoided when searching for the best optical condition. For example, looking at the $j_{ext} = 200$ A/m^{2}curve in the left side of **Figure 5.11**, the low V_{ext} part is missing. It was not reported, because in that V_{ext} range the beamlet intercepts EG aperture internal surface, occurrence that cannot even be taken in consideration.

Figure 5.11 shows a better optical condition for the $j_{ext} = 170$ A/m^2 case, at $V_{ext} = 6.4$ kV. Anyway, since that amount of current density could be difficult to achieve, I chose a the $j_{ext} = 150$ A/m^2 case as reference, whose minimum was at $V_{ext} = 6.4$ kV too.

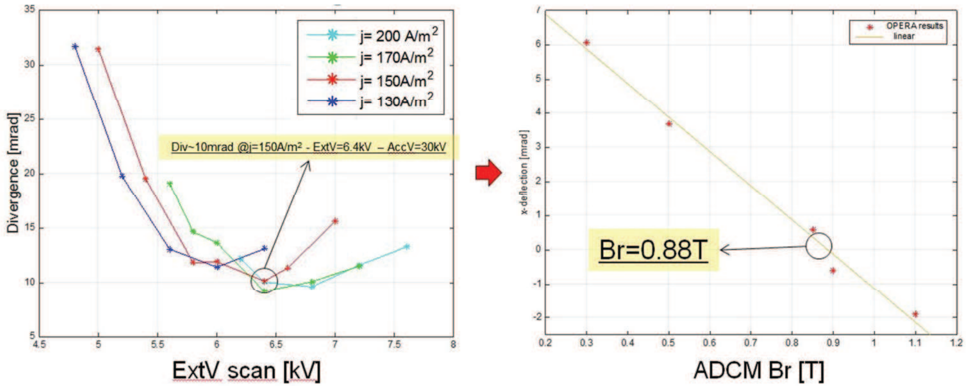

Figure 5.11: First attempt to dimension ADCM B_r. The first step was to make a Vext scan at many current densities and CESM field only. Then the best optical condition of $j_{ext} = 150$ A/m^2 case was kept. Lastly, ADCM magnetic field was added to the simulation. Changing B_r the curve on the left was obtained, which shows that the complete compensation happens with $B_r = 0.88$ T.

Having fixed the current density and voltages applied to the grids, I have started to find the most suitable ADCM B_r for deflection compensation. With respect to the complex procedure discussed in section 4.4.2, I now followed an easier approach: I have just added ADCM field with different B_r in the reference simulation. The resulting deflection in function of ADCM B_r is shown in the right hand side of **Figure 5.11**. The effect of ADCM on deflection is linear with B_r as expected and a B_r = 0.88 T is fund as provider of the best corrective effect.

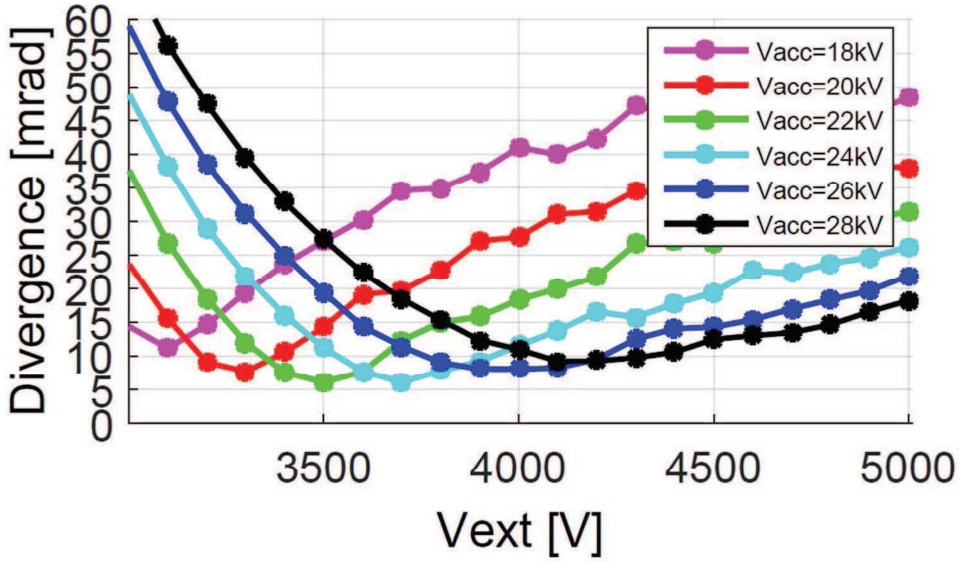

Figure 5.12: Beamlet divergence in function of V_{ext} at different V_{acc}. These are the results of SLACCAD electrostatic simulations considering j_{ext} = 100 A/m2.

However, I have realized only in second time that the divergence of j_{ext} = 150 A/m^2 case, 10 mrad, cannot be considered acceptable. That divergence amount doesn't allow the clear distinction of beamlets footprints on the CFC target placed at 0.8 m downstream the GG. Hence I have discarded the approach to deal with the beam with the highest energy in favour of a most generic one, i.e. deal with the beam with the best possible optic. Doing this, I have first performed SLACCAD simulations to find this condition, making divergence scan not only in function of V_{ext}, but also of V_{acc}. Furthermore, I choose to consider the j_{ext} = 100 A/m^2 case. These simulations are shown in **Figure 5.12**.

Before proceed to find the new B_r value for ADCM, I have reproduced with OPERA the V_{acc} = 21 and 22 kV cases of the previous SLACCAD simulations (see left hand side of **Figure 5.13**): since I have found in section 2.6.4.1 that the results of the two codes slightly differ, I wanted to be sure to find the best optical condition also with OPERA. It turned out that the best optical condition is achieved with V_{ext} = 4.3 kV and $V_{acc} = 21$ kV.

Concerning the determination of the new B_r, I have proceeded as done in the previous case, just adding ADCM field with different B_r in the simulation that returned the best optical condition. The resulting deflection in function of ADCM B_r is shown in the right hand side of **Figure 5.13**. $B_r = 1.1$ T is now the remanence value that completely corrects the residual deflection.

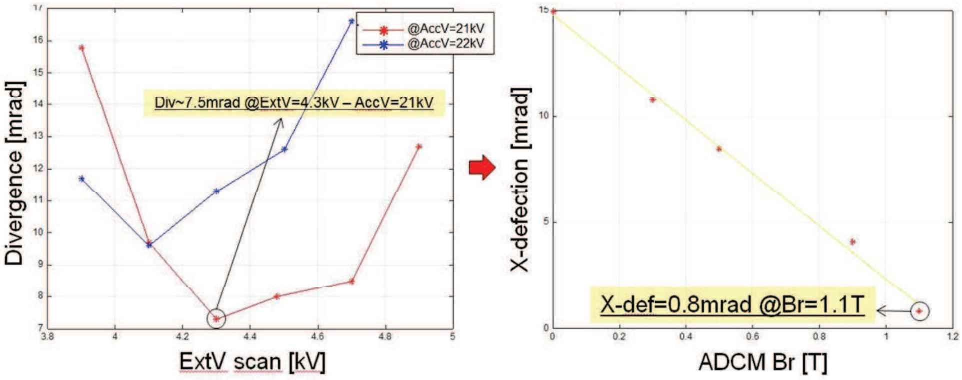

Figure 5.13: The left picture is similar with respect to **Figure 5.11**, but now j_{ext} is fixed at 100 A/m2, while V_{acc} was changed in order to reproduce the SLACCAD simulation. A better optic has achieved. Adding ADCM field at different B_r a new ADCM calibration plot is created. This time the best correction to the residual deflection is obtained with ADCM $B_r = 1.1$ T.

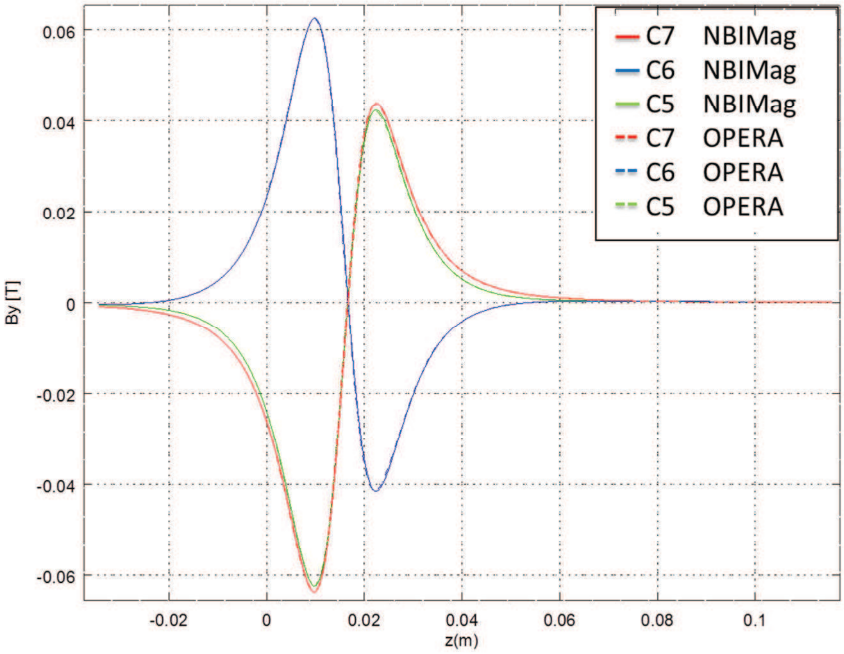

Figure 5.14: OPERA-NBIMag comparison of CESM+ADCM By profile for beamlets C7, C6 and C5. The two codes are in perfect agreement, as it is not possible to distinguish the OPERA dashed curves to their respective NBIMag solid curves.

For the sake of reliability, I have compared the magnetic By profile generated by the CESM+ADCM ($B_r = 1.1$ T, for both set of magnets) configuration calculated by OPERA with the one computed by the

Consorzio RFX internally developed code NBIMag [63]. The comparison was done considering the three central beamlets of the upper part of the new EG. **Figure 5.14** shows a very good accordance between the two codes.

It seems now appropriate to make a multi beamlet simulation using the operational parameters find so far.

Hence I run a 3x5 + 3x5 beamlet simulation and checked the results. The most important parameter to observe is, of course, beamlets deflection. In **Figure 5.15** deflection angle across the entire beamlets path in the simulation are shown. For comparison purposes the usual central beamlets, from C7 to C1, are considered. Zero final deflection is expected only for C7, C6 and C5 beamlets, since they belong to the compensated part of the new EG4.

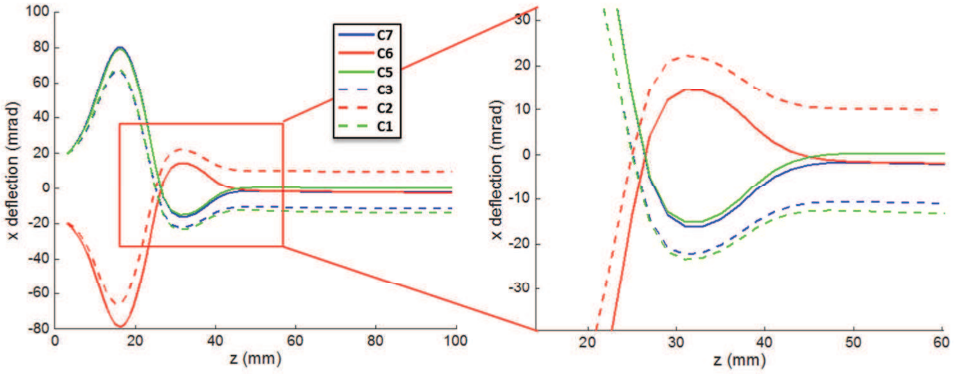

Figure 5.15: X deflection of the beamlets highlighted in **Figure 5.10** throughout the whole accelerating region with $B_r = 1.1$ T ADCM set. Solid line represents the three beamlets of the upper part of the EG and the dashed line represent the bottom ones. It is easy to see that the deflection of the upper three beamlets after the GG is quite completely recovered with respect to the bottom beamlets. Deflection of beamlets C7 and C6 are slightly under and over corrected.

Simulation results met the expectations. Therefore the designed CESM+ADCM configuration with $B_r = 1.1$ T for both set of magnets, fulfils the requirements for a good correction. Nevertheless, beamlets C7 and C6 seem to be slightly overcompensated and undercompensated respectively. Of course one cannot expect that experimental measurements will reproduce exactly simulation results, but I was expecting that simulations would give perfects results and that the correction would be equal for the three beamlets. This consideration makes me think that this imperfection would depend to some physical reason. Therefore I deeply investigate this phenomenon looking to the B_y profile of the CESM+ADCM configuration along the vertical direction (see **Figure 5.16**). It turned out that the profile is not symmetric, meaning that ADCM effect on the three upper rows is different. The phenomenon can be easily ascribed to the asymmetry of the magnetic configuration of the new EG: the symmetry of the magnetic configuration could be achieved by adding further (at least one) CESM magnets on top of the CESM+ADCM section. Unfortunately there no enough space to place any other CESM in the EG.

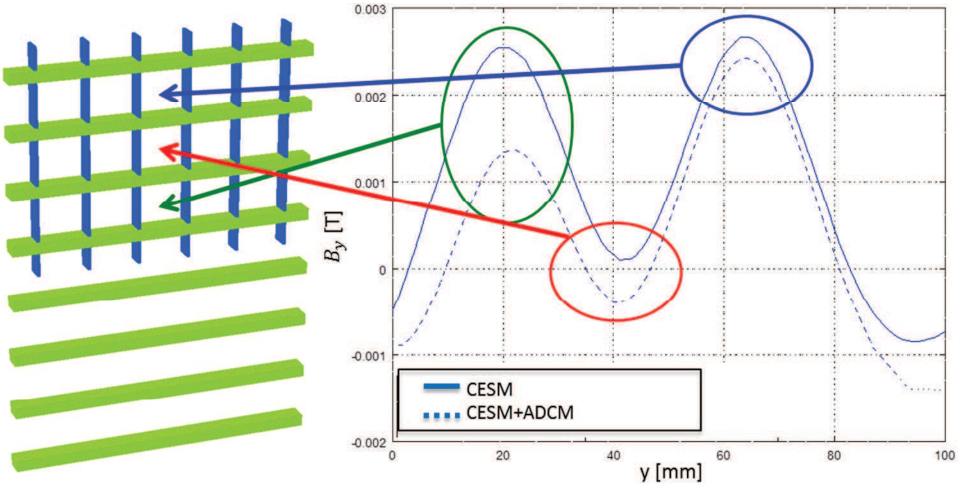

Figure 5.16: Comparison of the B_y profile along y direction with and without ADCM. The asymmetric magnetic configuration makes the B_y profile asymmetric, justifying the slight under correction of beamlet C7 and the slight overcorrection of beamlet C6 seen in in Figure 5.15.

In the right hand side of **Figure 5.17**, I show the final beamlet arrangement after linear prolongation of the particle trajectories of the simulation on the CFC target, giving the idea of what it will be possible observe on the CFC target during experiments.

It is important to notice that during the design of the new EG no measures were taken to eliminate the electrostatic deflection caused by the space charge in the extraction region. Therefore it is useful to make a comparison with a simulation without any magnetic fields, presented on the left hand side of **Figure 5.17**, in order to have an idea of the space charge effect. Anyhow the space charge is overestimated, as no interaction with the background gas was included in the simulation in order to reduce the computational time, since deflection due to permanent magnets does not depend on space charge.

Hence, looking at both pictures of **Figure 5.17** it can be notice the crisscross pattern caused by CESM magnets in the bottom part, the restoration of the original beamlet pattern in the upper part (finding again the imperfection observed in **Figure 5.15**) thanks to the ADCM contribute and lastly, the effect of the filter field that pushes all the beamlets upward. Note that the dashed red lines represent the actual CFC tile dimension (cantered with respect to acceleration region central axis) and that the EG apertures position with respect to the CFC tile borders are superimposed.

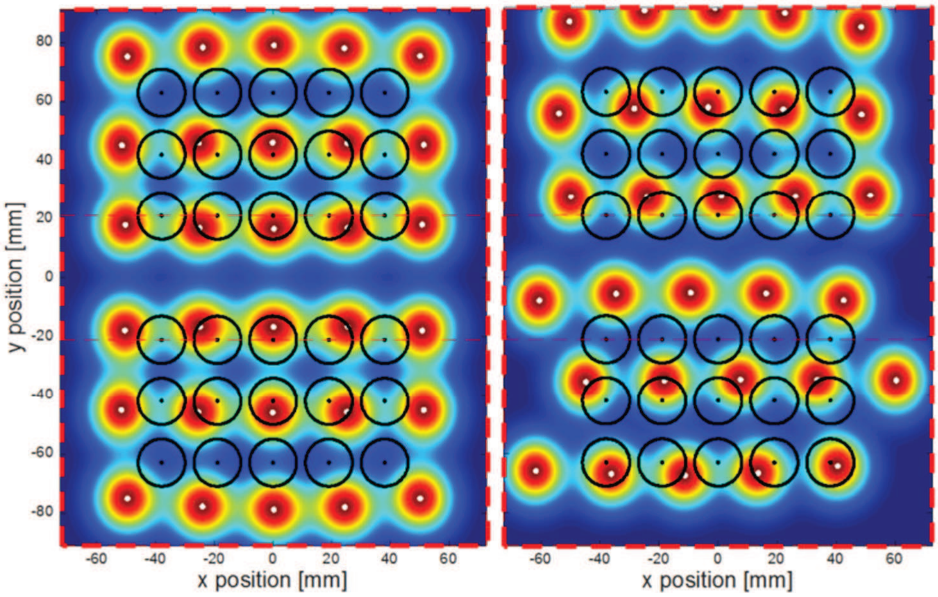

Figure 5.17: Beamlet arrangement after linear prolongation of the particle trajectories to 820 mm downstream the GG, for $j_{ext} = 100$ A/m^2 simulated current density. The positions and centers of EG apertures are superimposed and the red dashed lines represent the position of the CFC tiles. The left hand side picture represents a no B field case and the displacement of the beamlets from EG apertures is ascribed to the space charge only. On right hand side, magnetic field due to the magnets embedded in the EG and filter filed were added. Comparing the two pictures it is possible to notice the effect of CESM magnets in the bottom half (crisscross pattern), the effect of ADCM ($B_r = 1.1$ T) that cancel the crisscross pattern in the upper half and the filter filed effect that shifts all the beamlet upwards.

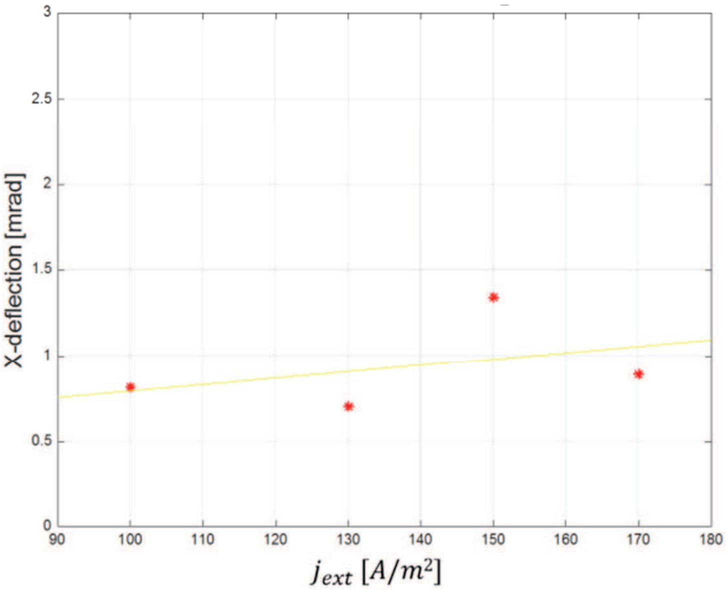

Figure 5.18: Residual deflection at different current densities.

As a further confirmation that the magnetic compensation system provided by ADCM magnets maintains its efficiency also at different operational parameters, **Figure 5.18** shows the residual deflection of the beamlets at different j_{ext}. Moreover, **Figure 5.19** compares the final beamlet arrangement on the CFC target of $j_{ext} = 100$ A/m^2 (right side) case with the $j_{ext} = 170$ A/m^2 case (left side). The two simulation results are practically identical. Again, note that the white dashed lines represent the actual CFC tile size and the black circles represent EG aperture actual positions with respect to the CFC tile borders.

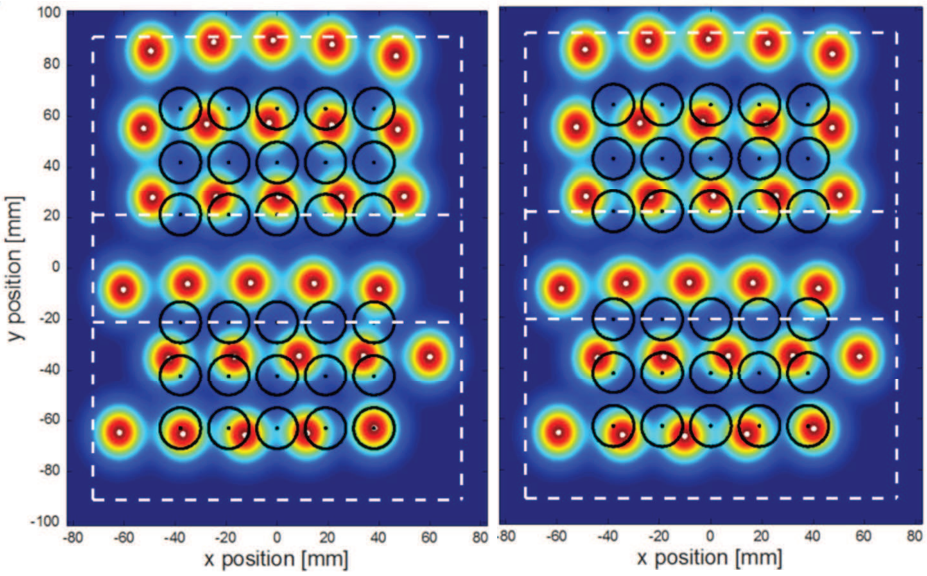

Figure 5.19: Beamlet arrangement after linear prolongation of the particle trajectories to 820 mm downstream the GG. The positions and centers of EG apertures are superimposed and the white dashed lines represent the position of the CFC tiles. On the right hand side, the picture of the right hand side of **Figure 5.17** ($j_{ext} = 100$ A/m^2 with CESM+ADCM and filter fields) is presented again, for comparison purposes. On the left hand side, instead, the $j_{ext} = 170$ A/m^2 case with the same magnetic fields is presented. Comparing the two pictures it is possible to assume that there are no differences, meaning that the ADCM correction can work efficiently also at different operational parameters.

ADCM B_r was then dimensioned. As said at the beginning of this section, in order to have operational flexibility, it was decided to realize three different sets of ADCM with the same size, but different B_r. The original idea was to find a B_r will lead to a complete compensation of ion deflection as base set, while the other two sets would have a magnetization $+20\%$ and -20% with respect to the base set, being the augmented and reduced set respectively. Unfortunately I have found that the base set must have $B_r = 1.1$ T, which is the maximum possible magnetization for $SmCo$ magnets. Anyhow it was decided to keep this three set scheme:

- -ADCM augmented set: $B_r = 1.1$ T $(+20\%)$
- -ADCM base set: $B_r = 0.8$ T
- -ADCM reduced set: $B_r = 0.7$ T (-20%)

even if the $B_r = 1.1$ T set is the one expecting to give the best correction.

These sets were eventually manufactured. After a survey on the market, the company Magneti Permanenti Industriali (MPI) in Milan (Italy) was found to be suitable for the task of magnet grading. In fact, MPI is able to produce $SmCo$ magnets with the same dimension and composition but different values of magnetic remanence, using a special machine, shown in **Figure 5.20**, able to measure and to calibrate the magnetic flux of each magnet during the magnetization process. In this way, it is possible to stop the process when the desired level of magnetization is obtained.

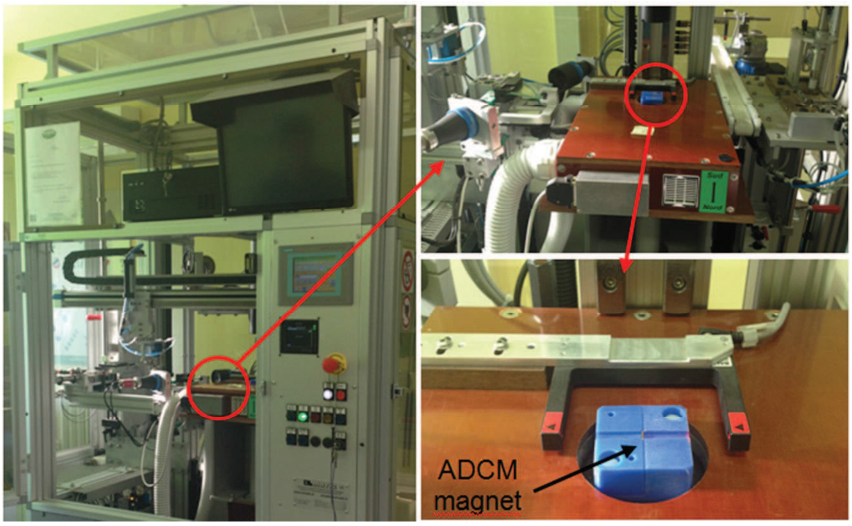

Figure 5.20: Machine for magnetization and calibration of the permanent magnets at different values of remanence.

5.3 Experimental results

Being the RFX EG realized, as well as the CESM and ADM magnets to insert into the grid, all preparation for the Joint Experiment were competed (at least by RFX side). Hence the experimental campaign started in February 2016, but as already said at the beginning of the chapter, I couldn't participate directly to the experimental session in Japan. However I helped in the data analysis once experiments were ended. Therefore, only the main results of the first Joint Experiment session are presented, referring the reader to the Consorzio RFX Technical note [[**63**],[[**64**] for more details on the experimental campaign in Japan.

- *Main results*

The experimental campaign started with operation without cesium, reaching a maximum H^- extracted current $j_{ext} \approx 40$ A/m^2. Several scans were performed in order to find the optimal beam optics conditions so as to be able to distinguish the footprints of each single beamlet on the CFC target. An example of voltage scan carried out for this purpose is shown in **Figure 5.21**.

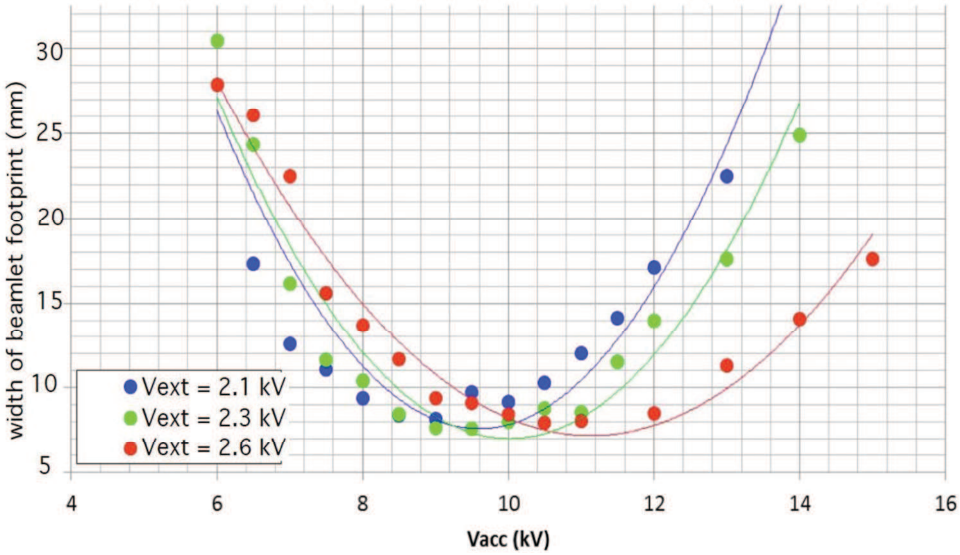

Figure 5.21: V_{acc} scan showing beamlet width obtained from thermal images, for V_{ext} = 2.1 , 2.3 and 2.56 kV;

The thermal image on the CFC target corresponding to $V_{acc} = 9.5$ kV and $V_{ext} = 2.3$ kV (best optics condition without Cs) is shown in the left side of **Figure 5.22**. The beneficial effect of the ADCM is clearly visible even if (due to the low beam power) the thermal image is not very much defined: in the three upper beamlet rows the criss-cross deflection is very much reduced with respect to the three lower rows, where no compensation is present. This is the first experimental evidence of the magnetic deflection compensation capability of the ADCM. The OPERA simulation corresponding to similar operating conditions is shown in the right side of **Figure 5.22**.

The first part of the experimental campaign, performed without cesium, has enlightened that the deflection compensation by ADCM was rather good, but also that the power deposited by the upper rows of beamlets was always lower than that of the lower rows. This behaviour was particularly evident for the uppermost row, which was much weaker than the others. In order to understand if such behaviour could be somehow related to the different magnetic field configuration produced by the ADCM, the EG was rotated by 180° along the acceleration axis (z), so that during the subsequent experiments, the ADCM were positioned on the 3 lower rows of apertures and no ADCM were installed on the 3 upper rows.

After this modification, the weak row remained the uppermost one, so the hypothesis that the weakness of the uppermost beamlets could be related to the presence of the ADCM has to be excluded. A possible cause could be a lack of plasma uniformity in the kamaboko source related to the presence of the horizontal filter field.

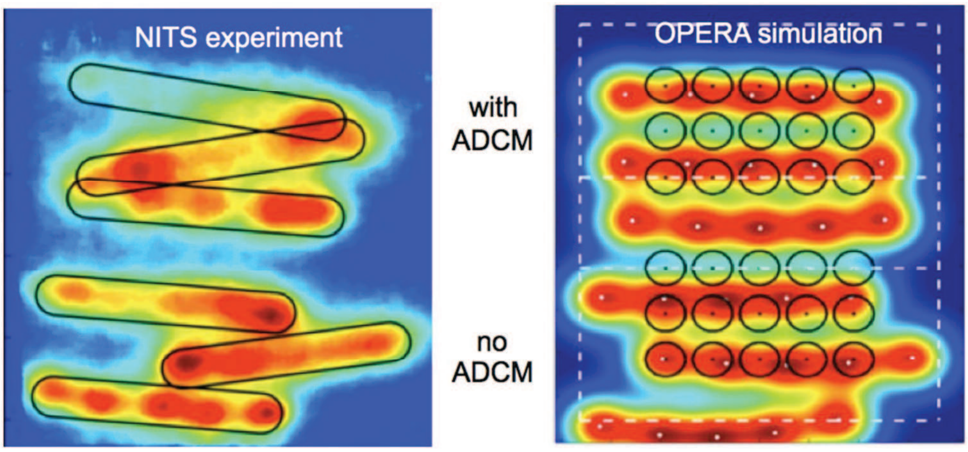

Figure 5.22: (left) thermal image of CFC target for beam pulse #8841, V_{ext} = 2.3 kV, V_{acc} = 9.5 kV no Cs, the beamlet rows are highlighted by a black contour; (right) OPERA simulation under similar conditions ($j_{ext} \approx 30$ A/m^2, $V_{ext} \approx 2$ kV, $V_{acc} \approx 9$ kV).

A large part of the experimental campaign was devoted to cesium operation, allowing reaching much higher extracted current (~ 170 A/m^2), and much more defined thermal images (the peak temperature difference measured on the back side of target was typically between 10 and 20 K at the end of the pulse). The IR images were numerically processed using numerical fitting techniques based on a Gaussian distribution fitting for each beamlet footprint, so as to obtain a precise estimation of the absolute deflection of each beamlet.

As expected the IR camera pictures gave indication that the deflection compensation obtained using the ADCM with $B_r = 0.88$ T was not sufficient. It was then substitute this set with the augmented ADCM ($B_r = 1.1$ T), which was expected to bring a full compensation.

Changing ADCM set allows more precisely determination of the dependence of the residual deflection with respect to ADCM strength. The best operating conditions were achieved with 1 s beam pulses and the image of the last frames, just before the end of the pulse. The transverse diffusion of the heat is negligible under these conditions, so that the visible beamlet footprint on the downstream side corresponds very well to the actual size of the ion beamlet impinging on the upstream side.

From the thermal images, the beamlet horizontal deflection can be evaluated as the distance δ_x of the centre of each beamlet footprint from the geometrical axis of the grid aperture ideally corresponding to the same beamlet.

Figure 5.23 shows the thermal images of the CFC tile during beam pulse #10574 (with Cs and ADCM having $B_r = 0.88$ T. Since the image has been geometrically calibrated, the absolute deflection δ_x and δ_y (in mm) can be easily determined for each beamlet. Since the CFC target is positioned ~ 900 mm downstream of the GG, a measured deflection of 1 mm corresponds to a deflection of 1.1 mrad. From this picture, the horizontal criss-cross deflection (δ_x) of the beamlets was evaluated to be 18 mm in the upper part (no ADCM) and 7 mm in the lower part (with ADCM). A vertical (downward) deflection $\delta_y = -20$ mm, caused by the horizontal magnetic filter field is also evident. Beamlet divergence can also be easily evaluated to be less than 10 mrad from the same image.

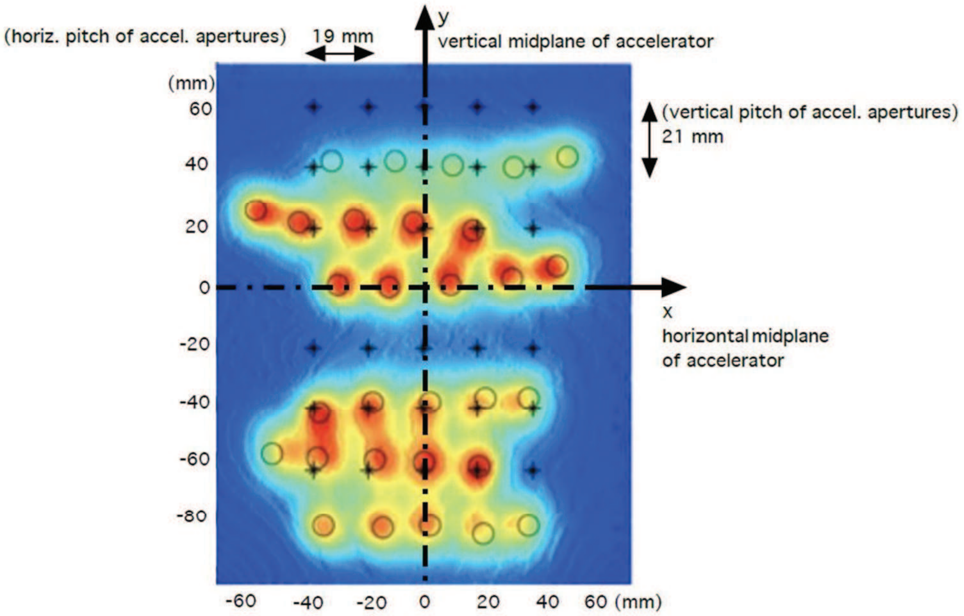

Figure 5.23: Thermal image of CFC target, for pulse # 10574, with V_{ext} = 4.5 kV, V_{acc} = 22.95 kV and I_{acc} = 0.42A, $j_{ext} \approx$ 91 A/m^2. In this pulse standard ADCM (0.88 T) are installed in the lower half of the EG, no ADCM are installed in the upper half. The image is dimensionally calibrated (in mm), black crosses correspond to the geometrical axes of the accelerator grid apertures, black circles correspond to centres of the beamlet footprints obtained by numerical fitting procedure.

From **Figure 5.23**, it can be also notice that the electrostatic beamlet-beamlet repulsion was not as strong as expected from the OPERA simulations (right side of **Figure 5.22**, for example) , indicating that the charge compensation length assumed in the simulations was probably overestimated.

Figure 5.24 shows the thermal images of six beam pulses having similar optics conditions ($I_{acc}/(V_{ext})^{3/2} \sim$ constant) but different beam current. The case of ADCM standard set and ADCM augmented set are compared, showing that the beneficial effect is not much affected by variations of the beam acceleration energy, thus confirming one of the main advantages of the compensation by ADCM.

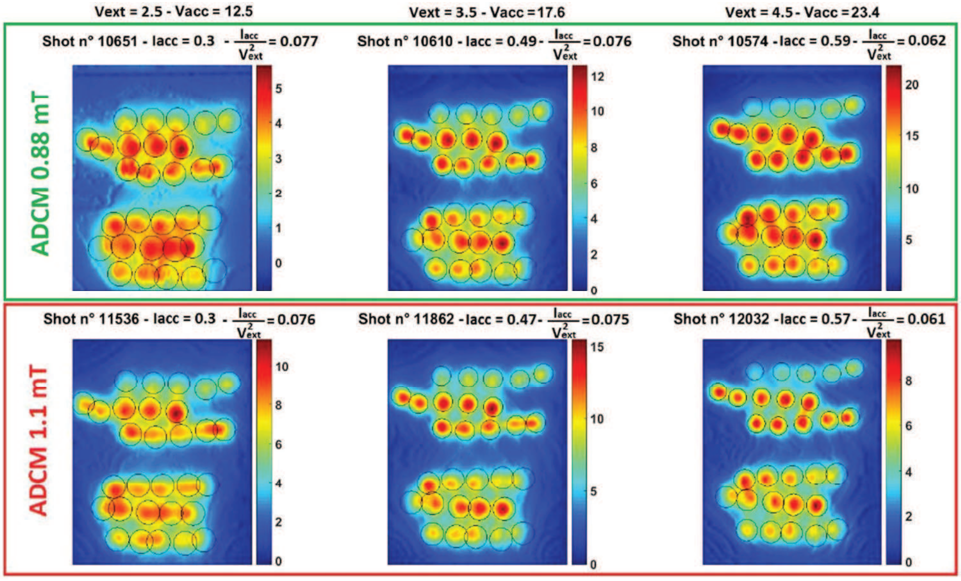

Figure 5.24: Thermal images of beam pulses with similar optics conditions, but different beam current, with the ADCM standard set (B_r = 0.88 T) and with the augmented one (B_r = 1.1 T). The scale for the target temperature increase is shown on the right.

Lastly, in **Figure 5.25**, the value of the cross-cross deflection δ_x of the beamlets with respect to the ideal axis (measured in mm on the CFC target), is plotted against the ADCM strength, expressed as magnetic remanence Br, assuming a fixed magnet size of $16.4\ x\ 6.6\ x\ 1$ mm. The deflection calculated using simple paraxial approximation formula (black) and using the OPERA 3D model (blue) is compared with the trend obtained from the experimental values (red) without ADCM, with standard ADCM ($B_r\ =\ 0.88$T) and with augmented ADCM ($B_r\ =\ 1.1$ T)

The values of the experimental deflection reported in figure are actually the average of several hundreds of beam pulses, obtained under different operating conditions. Several attempts were aimed at identifying any dependence of the beamlet deflection (both without and with ADCM compensation) on the operating parameters of the accelerator. However, it was not possible to evidence any clear trend.

However, these results obtained indicate that a complete compensation can easily be achieved by using a slightly larger magnet size ($16.4\ x\ 6.6\ x\ 1.6$ mm) maintaining $B_r\ =\ 1.1$ T.

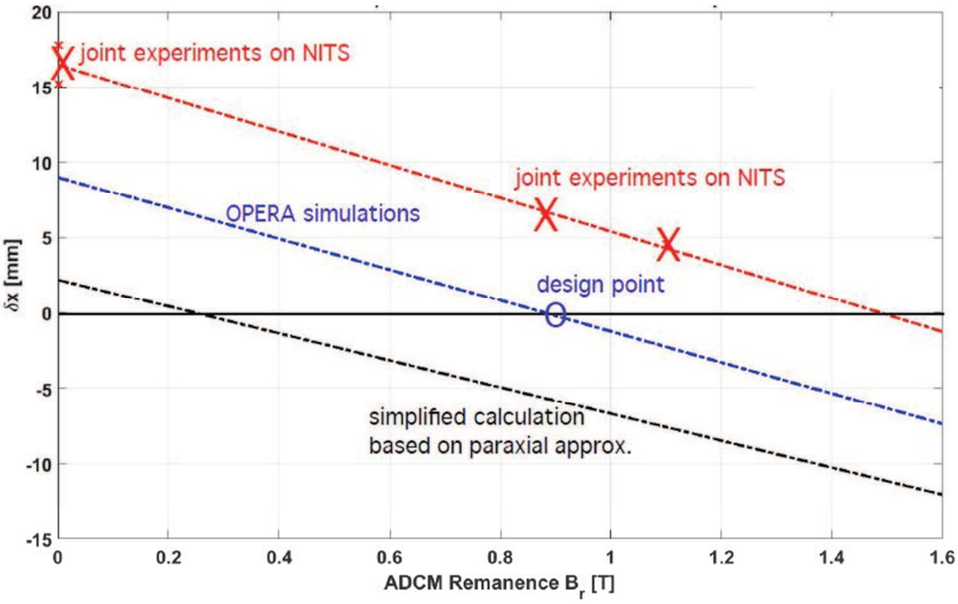

Figure 5.25: beamlet deflection on target (δ_x in mm) as a function of the ADCM strength (B_r). In all cases ADCM size is assumed to be 16.4 x 6.6 x 1.0 mm. The deflection calculated using the paraxial approximation formula (black) and using the OPERA 3D model (blue) is compared to the trend obtained from the average experimental values (red) without ADCM, with standard ADCM ($B_r = 0.88$ T) and with augmented ADCM ($B_r = 1.1$ T).

Apparently the cause of the difference between OPERA results and experiments is related to physical phenomena taking place during beam extraction, which are not included in the model and are presently under investigation. To this regard, it can be consider that the effect of transverse magnetic field on ion trajectories during acceleration is accounted by OPERA in a fairly self-consistent manner, including the modifications of the electrostatic field caused by the transverse displacement of the beamlets. On the other hand, the model of formation and extraction of negative ion current across the meniscus under transverse magnetic field seems to be inadequate, mainly because a uniform H^- extracted current density is assumed on the meniscus surface of each beamlet. This proved a good explanation for similar evidence in the analysis of data collected in the test stand at NIFS, (Toki, Japan) [65].

5.4 Benchmark OPERA-COMSOL

Since OPERA simulation results underestimate experimental results of about 50%, it has been decided to do a crosscheck with respect to COMSOL. I didn't actually use COMSOL in first person; therefore I'm not going to give many details on the program itself, but I will illustrate only the results.

For the OPERA – COMSOL benchmark firstly a single beamlet simulation was considered and in particular the beam of the position C6 in Figure 1.3. To carry out the benchmark it is important to reproduce the same simulation with both programs, meaning that not only the geometry of the simulation has to be the same, but also the initial and boundary conditions. To achieve this goal the following precautions were adopted:

- *Boundary conditions*:

- Same potential applied to the grids;
- Tangential field constrains on the lateral boundaries of the simulation domain;
- Same distance of the simulation domain boundaries to the beam axis in the x and y directions (considering z axis along the beam direction), which is larger than the aperture pitch. This is necessary because of the tangential field boundary condition;
- Consider a distance of the simulation domain boundary on the z direction downstream the Plasma Grid long enough to ensure the complete inclusion of the magnetic field tail.
- Same magnetic field. In COMSOL was inserted a magnetic field map produced by OPERA magnetic simulation with TOSCA (section 2.6.4).

- *Initial conditions*:

Since COMSOL does not have any tool to generate a self-consistent meniscus like OPERA, in order to ensure the use of the same initial conditions, the external emitter file used in COMSOL was generated from the OPERA simulation. In particular, in the file was recorded information on particle positions and velocities at PG knife of the OPERA simulation. Furthermore, another precaution was adopted: a cup surface is added upstream the PG in such a way to try to reproduce the meniscus (Figure 3.1). On this artificial meniscus a fixed voltage equal to the PG voltage is applied. This is necessary in order to reproduce the effect of the Plasma behind the meniscus that avoids the extraction electric field entering upstream the PG. Without this artificial meniscus the shape of electrostatic lens at the PG aperture would be not correct.

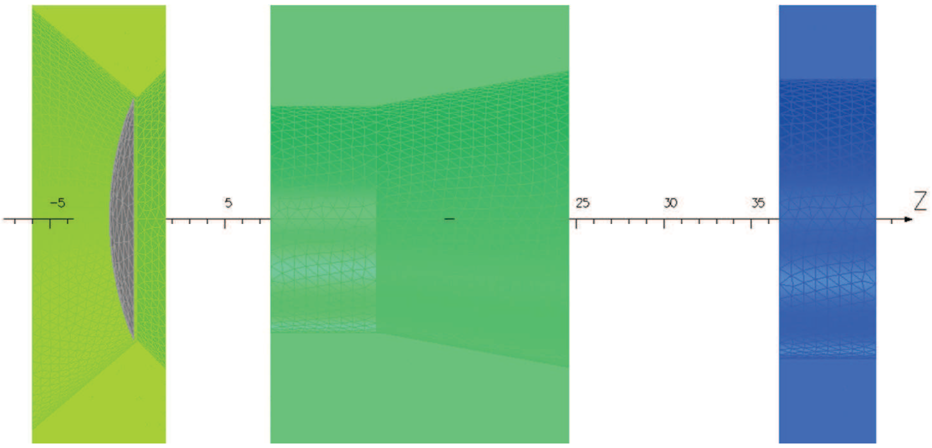

Figure 5.26: Cut view of the OPERA model of NITS grid system. It is possible to see the shapes of the apertures for PG (yellow), EG (green) and GG (blue) and the cup shaped surface acting as an artificial meniscus.

Once being sure to have taken all the precautions in order the two created models to perfectly match in geometry and boundary conditions, also the COMSOL simulation was performed.

The parameters used in both simulations are:

PG voltage:	*-25.3*	*kV*	
EG voltage:	*- 21*	*kV*	
GG voltage:		*0V*	
Current density:		*100*	*A/m^2*
ADCM remanent field:		*1.1*	*T*
Number of particles:	*1400*		

From **Figure 5.27** to **Figure 5.31** the two simulation results are compared. The comparison is encouraging in the sense that COMSOL seems to confirm the OPERA results used to design MITICA and the NITS experiment, mostly regarding the beamlet divergence. Instead, the reason of the sort of shift between the OPERA and COMSOL curves remains unclear. The only difference that can be hypothesized between the two codes is that in OPERA a current density is associated to each macroparticle defined by the emitter file, whereas COMSOL asks only for the total current associated to the emitted macroparticles and it was not possible to find detailed indications on how COMSOL algorithm distribute it to the macroparticles. This may play a non-negligible role since at the very first instant of the particle motion, when the velocity is minimum, small differences have a big impact.

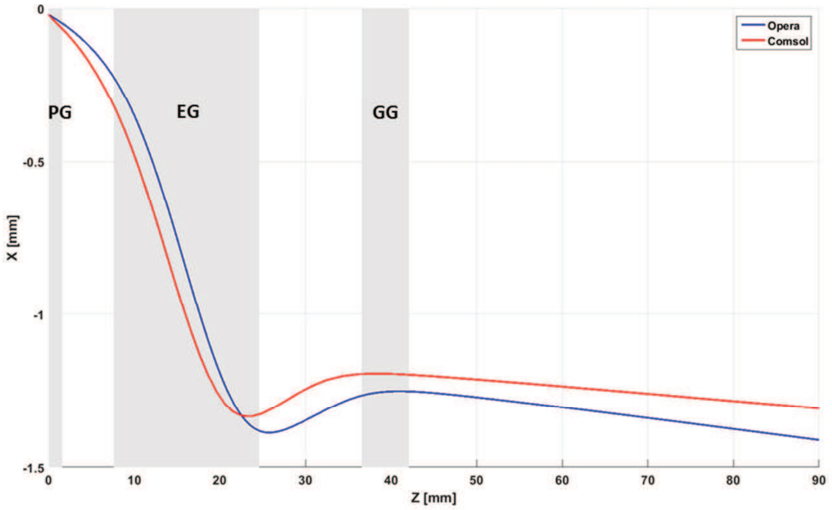

Figure 5.27: Average beamlet x coordinate along the beam path. Blue and red curves correspond to Opera and Comsol results respectively.

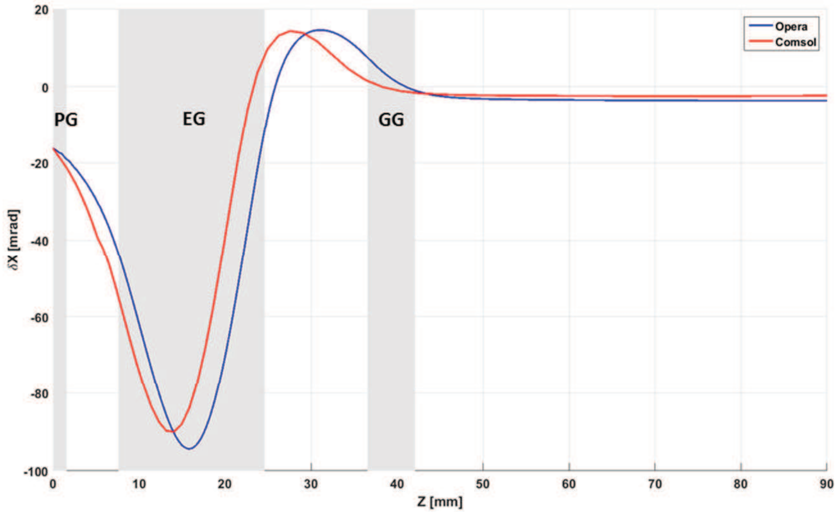

Figure 5.28: Average beamlet horizontal (x) deflection along the beam path. Blue and red curves correspond to Opera and Comsol results respectively.

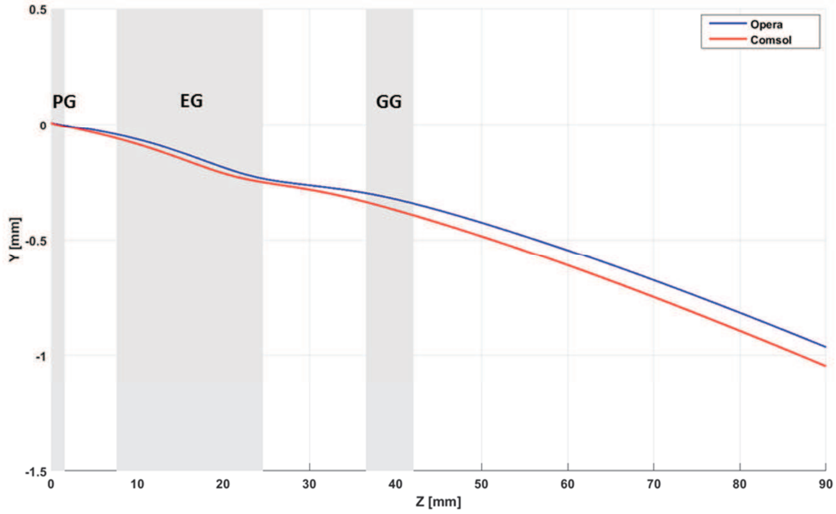

Figure 5.29: Average beamlet y coordinate along the beam path. Blue and red curves correspond to Opera and Comsol results respectively.

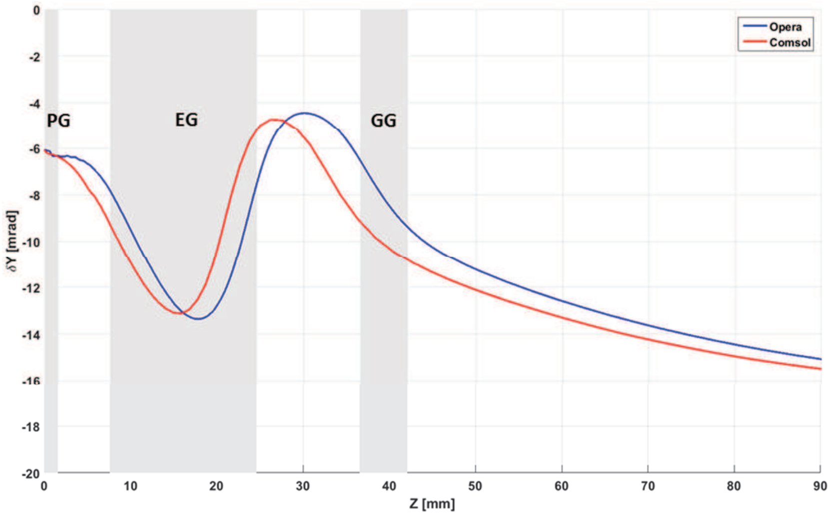

Figure 5.30: Average beamlet vertical (y) deflection along the beam path. Blue and red curves correspond to Opera and Comsol results respectively.

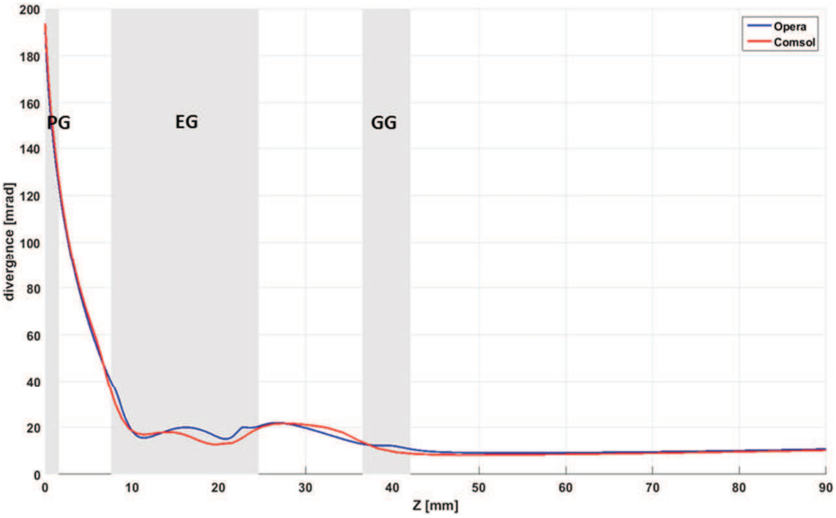

Figure 5.31: Beamlet divergence along the beam path. Blue and red curves correspond to Opera and Comsol results respectively.

Concluding, despite all the effort spent, the results of the two simulations still differ. In particular, the deflection and average position curves are shifted along z direction. The reason for this shift is not yet understood and it is under investigation. However the final results only slightly differs (less than 1mm) as regards the average beamlet position, while a more considerable difference (~2 mrad) was found regarding the beamlet deflection. Therefore, it is possible to say that even if the two programs are not in perfect agreement, both gives results far different from the experimental one. The reason for this disagreement needs further investigation.

6 Summary

In the framework of the research for ITER experiment, the development of external heating systems, in addition to ohmic heating, is fundamental. One of these additional systems involves the injection of neutral beams. The unprecedented requirements of the neutral beam injector (NBI) for ITER (a 40A current of hydrogen/deuterium particles accelerated to 1MeV, for a total of 16.7MW delivered to ITER plasma) required the construction of a prototype, MITICA that will operate at Consorzio RFX to verify all physics and engineering aspects of the NBI. In particular, special attention is paid to the production and extraction of negative ions and to beamlet optics quality. These are of crucial importance to achieve the required current density for ITER and to increase the efficiency of the neutralization system. With this purpose, Consorzio RFX is putting a lot of effort into the two smaller devices SPIDER and NIO1, whose operational parameters are scaled with respect to MITICA. SPIDER is a full size ITER ion source test bed, capable of producing 1280 beamlets of 355 A/m^2 (H$^-$) or 285 A/m^2 (D$^-$) at 100 keV, with a pulse duration of 3600 s, which is scheduled to start operation at the end of 2017. NIO1, instead, is a smaller ion source, which started operation during 2015. It is designed to produce 9 beamlets of 300 A/m^2 (H$^-$) at 60kV whose main purpose is to investigate general issues on ion source physics in view of SPIDER and MITICA as well as DEMO relevant solutions and to train personnel in view of SPIDER.

During my PhD activities I have performed many numerical simulations on these machines and I participated in the experimental sessions with NIO1. In particular, I tried to analyse the fundamental aspects which regulate beamlet formation and optics, trying to introduce new solutions to improve beamlet optics, in some cases.

As a result of the work presented in this thesis, many considerations can be done. The extraction of negative ions is regulated by the Child-Langmuir law, which relates the ion current to the extraction voltage, defining the perveance of the beam. This relation is very useful to understand whether the extracted current can be further increased just by acting on the applied voltages or it is needed to enhance negative ion production in plasma. Child-Langmuir law is also very helpful tool to scale operational parameters in such a way to keep the beamlet optics at nominal design parameters, whenever it is not possible to operate at full performances.

In general, negative ion accelerators feature at least three grids: the plasma grid (PG) bounds the plasma region where negative ions are created; the extraction grid provides the electric field that extracts negative ions from the plasma and absorbs the co-extracted electrons; the voltage drop towards the grounded grid (GG) gives the particle the final energy. Concerning the optics of a single beamlet, the divergence depends mostly on the electrostatic fields generated by the electrodes of the acceleration region and on the ratio of the geometrical parameters of electrode aperture radius and electrode gap length. These parameters determine the shape of the electrostatic lenses that form in correspondence to the grid apertures, which can focus or defocus beamlet particles in the same fashion as optical lenses for light. Furthermore, lenses can also deflect the beamlet if it enters the apertures with a non-zero angle, generating a deflection of electrostatic nature.

Deflection can be induced also by magnetic fields, which generate a deflection of magnetic nature. Negative ion sources, indeed, feature some permanent magnets embedded in the EG, called CESM, that are needed to suppress the electrons that are extracted from the plasma source together with negative ions (co-extracted electrons). Due to the mass difference between electrons and ions, the former are deflected enough to collide with the grid surface, while the latter are only slightly deflected and can be transmitted through the grid aperture with a small residual deflection. Despite the component of the magnetic field perpendicular to the beam axis, generated by CESM, is symmetric with respect to the EG plane, a small part of its profile does not affect the beamlets. Its upstream tail, indeed, enters the plasma source, where beamlets are not yet extracted. The residual deflection has to be ascribed to this missing tail and has to be anyway corrected; otherwise beamlets will be not fully transmitted across the devices after the last electrode (RID, neutralizer, etc...) necessary for future fusion injectors, resulting in a huge loss of ions and a dramatic reduction of efficiency.

In general, in order to restore the correct exit angle, electrostatic and magnetic techniques can be used. Consider a three-electrode acceleration system (PG, EG and GG) and Co-extracted Electron Suppression Magnets (CESM) embedded inside the EG. The electrostatic solution exploits the deflection power of electrostatic lenses, by means of a steering grid attached to the downstream face of the EG or with a suitable GG grid aperture offset, like in SPIDER. The magnetic solution, instead, makes use of a second set of embedded permanent magnets in the GG, with a configuration similar to CESM magnets. In principle the two solutions can achieve the same goal. However, the simulation work I have performed on SPIDER in order to verify its compensation system efficacy (since the GG features both systems, for comparison purposes), helped to confirm that the magnetic one is a more robust solution. It can indeed keep its efficiency also when dealing with operational parameters far from the nominal one.

Considering, instead, multi beamlets devices, like all ion sources presented in this thesis, there is another source of deflection: the beamlet-beamlet interaction due to the space charge that builds up as soon as the beamlets are extracted from the source. Under the effect of the space charge, beamlets tend to repel each other. The result is a deflection of electrostatic nature. Anyhow, when a beamlet is completely surrounded by other beamlets, the repulsion forces are equal in any directions and thus it is not actually deflected. Therefore, as a matter of fact, in a multi beamlet device only the beamlets close to the boundary of the beam are deflected by the space charge repulsion. This deflection is also to be corrected, but this time the electrostatic solution is the most suitable. Again, during the simulation campaign I did on SPIDER, it turned out that when the deflection is of electrostatic nature, an electrostatic correction is also robust, because when dealing with different operational parameters the intensities of both effects change together. SPIDER GG, indeed, hosts also suitable aperture offsets at the border apertures, to take into account space charge deflection. The important conclusion that can be drawn is that for beamlet optics it is important to distinguish the nature of the source of deflection and to try to counteract it by means of a solution of the same nature.

Still concerning beamlet deflection, in the last years a new solution for the CESM deflection compensation has been developed. It is a magnetic solution using a second set of magnets, but with a different configuration with respect to the previous case. This set of magnets is called ADCM and instead of being embedded into another grid, like in SPIDER, it is embedded inside EG as well, together with CESM magnets. ADCM magnets are orientated in such a way to exploit the Hallbach configuration, causing the perpendicular component of the magnetic field with respect to the beam line to be asymmetric with respect to the EG plane. In particular, in order to compensate the missing part of the upstream CESM tail entering the plasma that does not affect beamlets, one wants to increase the upstream peak intensity of the CESM+ADCM configuration. Hence, with a properly tuned asymmetric magnetic profile it is then possible to cancel the magnetic deflection induced by CESM.

This CESM+ADCM configuration seemed to be promising and it was sustained also by numerical simulations. Nevertheless, since this new configuration has been proposed as the reference one for ITER injector prototype MITICA, an experimental validation was needed. With this purpose, a collaboration between Consorzio RFX (Italy) and QST (Japan) was established to perform joint experiments: an EG featuring CESM+ADCM magnetic configuration was designed and manufactured by Consorzio RFX and then installed on the NITS ion source at QST. NITS is an arc driven ion source, which features 35 beamlets, in a pattern of 7x5, of 20 A/m^2 or 170 A/m^2 current density, depending on the exploitation of surface production by means of cesium vapours to improve the generation of negative ions, at a maximum energy of 35 keV. I designed both the EG geometrical parameters and the magnetic configuration, in such a way to reproduce MITICA configuration as close as possible. Furthermore, it was decided that the new EG for NITS had to feature two separated groups of 3x5 beamlets, one featuring CESM+ADCM configuration and the other CESM magnets only. This special configuration allowed an easy experimental evidence of CESM+ADCM configuration efficacy. Although the final deflection was not completely cancelled, the experimental evidence exhibited a clear trend towards the complete compensation that can be achieved by a linear increase of ADCM magnetic field, giving indeed the first experimental validation for the new magnetic deflection compensation system. The incomplete correction evidenced a discrepancy between numerical simulations with OPERA and experiments, regarding the beamlet deflection. Investigations on this aspect are ongoing and a preliminary benchmark between OPERA and COMSOL has shown agreement. A second Joint Experiment is then foreseen in 2017 to achieve the complete correction and for further investigations on some other doubts arisen during the first joint experiments.

Anyway the successful joint campaign supported the decision to introduce CESM+ADCM configuration also in the new EG for NIO1. NIO1 acceleration region is composed by three grids (PG, EG and Post

Accelerating PA) plus a repeller grid. A CFC tile is placed after the repeller for early calorimetric measurements. Experimental campaigns in NIO1 had shown that the optical design of its EG does not provide good beam optics (beamlets soon overlap after exiting the acceleration region and thus it was impossible to distinguish their footprints on the CFC calorimeter) and it has to be redesigned. On the other hand, CESM magnets in NIO1 had shown to be too strong for hydrogen beamlets, forcing them to partially intercept EG surface. Therefore, CESM had also to be changed. Hence I designed the NIO1 EG and the related configuration of embedded magnets introducing also ADCM. In particular, the new EG aperture geometry was designed taking care to leave enough clearance, while reducing beamlet divergence. The new magnets, instead, were designed respecting the two constrains of zero final deflection and good co-extracted electron impact on EG, including the avoidance of Penning effect occurrence, due to an excessive upstream magnetic field, which can facilitate breakdowns.

Unfortunately no experimental evidences are available yet, since these new components will be installed on the device only next year. However, dedicated simulations showed that at very low operational parameters (~3% of nominal parameters) CESM+ADCM configuration slightly loses efficiency, but it still correct 85% of the deflection without any compensation applied (10 mrad). Hence I designed more than one set of magnets, so as to have the most suitable set of magnets in every situation.

Experimental campaigns on NIO1 gave anyway some results. First of all, in its early operation, when no beam was extracted, hydrogen plasma confirmed to undergo transition from capacitive to inductive coupling with the RF antenna, at a certain RF power (1.5 kW). During inductive coupling reflected RF power back to the power supply abruptly decreased and plasma luminosity increased suddenly as well. OES spectroscopy measurements then demonstrated that plasma parameters during inductive coupling are more suitable for negative ion production.

The rupture of an alumina insulator and its substitution with Pyrex, limited the usable RF power to around 1 kW. With the new chamber it seemed that the power level required to trigger the capacitive-inductive transition is lower (850-900 W) than before, but this result cannot be confirmed yet, since the limited capability and maybe only a partial transition was observed. Therefore source gas was changed to oxygen, whose higher electronegativity allows negative ions to survive more inside the extraction region, once formed. Oxygen also exhibited a transition to inductive mode around 400 W RF power only and is less deflected by the strong EG magnets avoiding interception with the grid. Hence, oxygen allowed higher extracted current with respect to hydrogen and is also easier to handle in the NIO1 currently limited capability. Therefore it was used to lead the way to other hydrogen operations, which were performed after using oxygen. The following considerations are then valid both for oxygen and for hydrogen since they have been observed with both gases.

During experiments, since the extracted beam intensity was too low for being properly diagnosed, beam analysis could rely only on electrical measurements.

Ion current was measured as the sum of ions collected on the PA and on the CFC tile. Furthermore, since the optics of the beamlets was not good enough to allow divergence measurements, it was proved that the ratio of the current on PA and CFC could be used as an optics figure-of-merit: lower divergent conditions correspond to a lower current reaching the PA and thus a lower value of the PA/CFC ratio.

It was observed that PA/CFC current ratio can be minimized by acting on the applied extraction and acceleration voltages. This minimum condition also depends on the applied RF power. Acting on these parameters by minimising the PA/CFC current ratio, it is possible to find the best optics conditions.

The dependence of the best optics conditions on RF power is a symptom of the observation that the Child-Langmuir law holds for ion extraction only at low extraction voltages, whereas at high levels ion depletion occurs in the meniscus zone.

In order to increase negative ion availability in the extraction zone, since RF power was limited, the effect of the magnetic filter field was also considered: higher filter field allowed higher ion current extraction. The magnetic circuit was also changed and placed at 60 mm from the PG. In this way a wider region affected by the magnetic filter field is produced with respect to the original configuration, up to few cm from the PG. Since the filter effect is proportional to the cumulative effect of the magnetic field along the particle trajectory, this new circuit is more efficient in preventing high energy electrons from diffusing from the driver to the extraction region. Higher ion currents were extracted, indeed.

Biasing the PG with respect to the source wall also increases ion extraction and decreases co-extracted electrons, because in the extraction zone electrons are deflected towards the PG. The biasing effect was anyway less effective with respect to the filter field.

Better experimental characterization of the beamlets in NIO1 will be possible when the extracted current density will be more intense so as to allow optical observations (by means of BES for example) and when the optics will be improved, by means of the new EG and the new magnetic configuration, allowing better calorimetric observations.

Appendix

Appendix A – NIO1database

The MDSplus system, used in Consorzio RFX, is excellent for data archiving and manipulation, unfortunately is based on a hierarchical database. This, added to the big amount of data stored, make it difficult to perform the parametric searches among the experiments. An additional relational summary database was developed to this purpose. Users, via an appropriate websocket message, can rise an event, and the control system saves a scene of the experiment, e.g. consisting of averages of all measured data.

The free PostgreSQL is the SQL servers considered and all data are stored in a table called "summary" table. In this table data are stored in columns. Among the others, two columns are dedicated to store references to the data, which are the time-reference and Dataset number. The other comulns are dedicated to the storage of measurements and related experimental parameters. If possible, for every measure, both settings and feedback measured data are stored.

In order to easily retrieve NIO1 experimental data from the database with a widespread tool, an easy-to-read graphical user interface was created for Excel. The programme under the GUI was written in the Visual Basic language and exploits PostgreSQL queries: it imports data from the database, without modifying the database itself, and arranges them among Excel sheet columns. The GUI can be called after its association to a special button (see **Figure A-I**) that the user can self-create on the Excel ribbon.

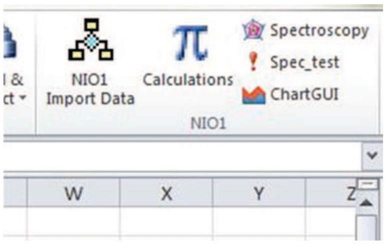

Figure A-I: Dedicated buttons on the excel ribbon

It allows any user, from any computer connected to the CNR network, to download the needed data, having the possibility to make either a date-based or a dataset-number-based search thought the database. Furthermore, it allows also the selection of specific database items so that there is no need to download the entire dataset, if not necessary. This way, consultation of data results more accessible, since the user has to deal with just few columns instead of dozens. **Figure A-II** shows the GUI.

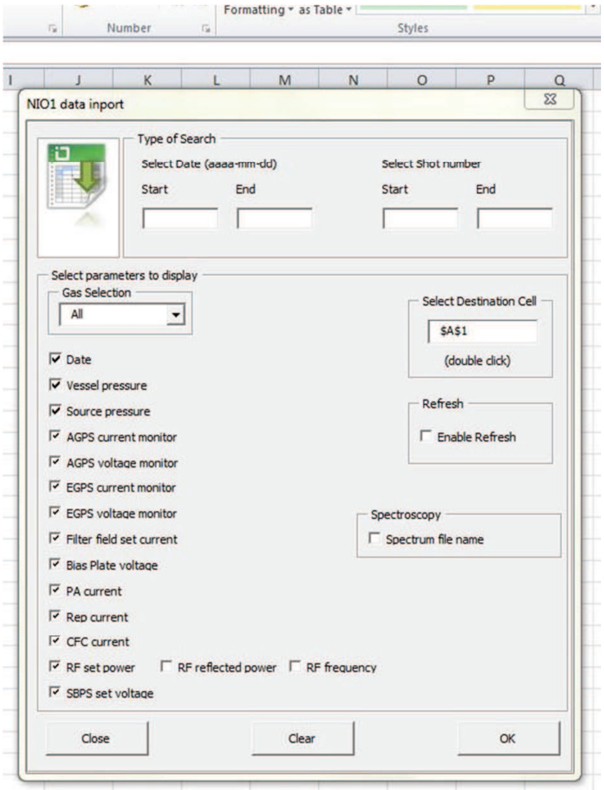

Gas Selection: All

Select Destination Cell: A1 (double click)

Refresh: ☐ Enable Refresh

Spectroscopy: ☐ Spectrum file name

☑ Date
☑ Vessel pressure
☑ Source pressure
☑ AGPS current monitor
☑ AGPS voltage monitor
☑ EGPS current monitor
☑ EGPS voltage monitor
☑ Filter field set current
☑ Bias Plate voltage
☑ PA current
☑ Rep current
☑ CFC current
☑ RF set power ☐ RF reflected power ☐ RF frequency
☑ SBPS set voltage

Figure A-II: NIO1 data import GUI made in Visual Basic language. It is possible to search among measurement data by date or Dataset Number. It also gives the possibility to import only the wanted measurements quantities by clicking on the corresponding check box.

Finally, this GUI features an automatic-refresh switch that makes the routine automatically update every minute, extending its use also during experimental sessions, i.e.: while the database is being populated with new data. Manual update is also possible when needed, thanks to a dedicated refresh button.

The consultation of data was made even faster by the creation of two tools, associated to the previous programme. These tools are written in Visual Basic language and are accessible through dedicated buttons that the user can create on the Excel ribbon: one tool can automatically makes simple routine computations among downloaded data and the other automatically generate plots among downloaded items. In particular, the automatic plot tool features a new GUI (see **Figure A-III**) and it can either generate routine plots among pre-defined data items (e.g. ion current as a function of extraction voltage) or generate plots among user-defined data items, to be selected by dedicated combo-boxes. Apart from allowing the user to easily select the desired plot parameters without manually searching for them among Excel sheet columns, the main advantage of this tool is that it can automatically detect series changes depending on a user-defined parameter. Of course these auxiliary tools can be also used during experimental sessions, calling them after every import of new data onto the Excel sheet.

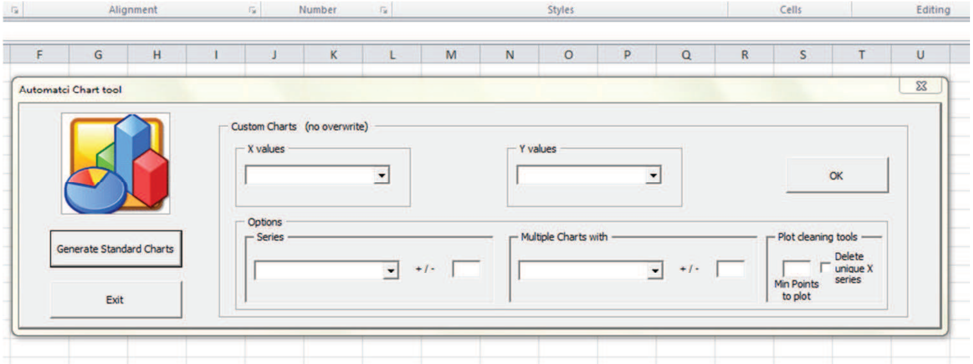

Figure A-III: Automathic chart GUI.

Appendix B – NIO1 energy recovery simulations

In the international program for the nuclear fusion energy production ITER, the plasma heating for the fusion reaction ignition will be reached through the injection of 2 Neutral Beams of Deuterium of 40 MW, each having negative ion current densities of ~300 A/m^2 at 1MeV energy.

The most efficient method for neutralization of D^- beams could be realised by applying laser detachment but it should require the development of proper lasers and mirrors [66]. Although, the method currently used to neutralize the negative ion beam is a gas cell which has an efficiency of about 55%-60% [66].

The possibility of recovering most part of the energy of the fraction of the beam not neutralized and then not used to increase the plasma heating could make the fusion energy production more efficient.

An axisymmetric system that collects beam particles which were not neutralized to recover beam energy was recently proposed. The system is mainly composed by two collectors. The first collector works by decelerating the H^- ions (into a system similar to a Faraday cup provided with an exit hole electrode), so that they are radially deflected by space charge and anode lens effects, and collected at a low kinetic energy (less than 1 keV), while neutrals and H^+ ions can pass through the exit hole electrode. The second collector can recover H^+ energy in the same fashion of the previous one. Before each collectors three electrodes are placed in order to grading the applied voltages. Figure B-I shows a sketch of the energy recovery system.

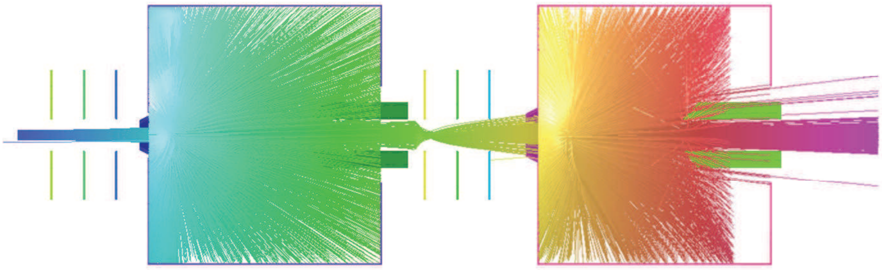

Figure B-I: Sketch of the double stage collector. In the figure, both H- and H+ ion trajectories are shown. The first collector is for the H- ions and the second for the H+. The intial energy of the beam was 20 keV.

In the case of the ion source NIO1, this energy recovery system may range from 20 to 60 kV, considering a beam with 3 mrad divergence and a composition of 25 : 50 : 25 of H^-, H^0 and H^+.

Since the space charge calculations are challenging for highly nonlinear problem and for a possible virtual cathode phenomena, different computation tools were compared for simulations. In this appendix only the comparison between COMSOL and OPERA will be presented.

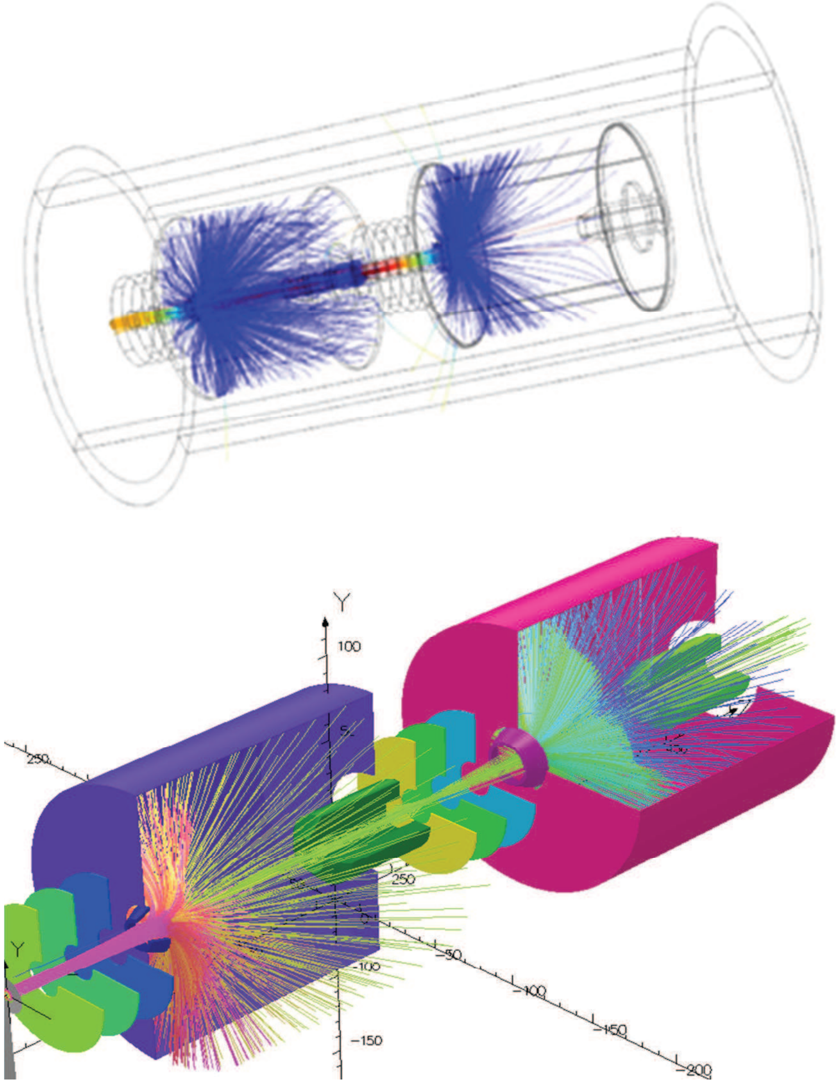

a)

b)

Figure B-II: COMSOL (a) and OPERA (b) models for the energy recovery system. The H^- and H^+ trajectories in the collectors are very similar between the two codes.

The two codes perform similar calculations to estimate the space charge. In particular the beam current (5 mA) for each species is divided among an ensemble of N particles. Their trajectory is than calculated according to the potential calculated at each iteration. At the first time step the potential is simply the solution of the Laplace equation, based on the assigned boundary conditions. In successive iteration the Poisson equation is solved, instead. The density of each specie is deposited on the nodes on the mesh depending on the time spent by the particle on each element. The charge is deposited among the 4 nodes (thetraedral mesh) using a weighting scheme

This activity was carried out in collaboration with CNR institute of Bari, which provided the COMSOL simulation, while I performed the OPERA one. Figure B-II shows the models created by the two codes.

In Figure B-III it is shown the histogram of the kinetic energy distribution of both H^+ and H^- on the electrodes as results of COMSOL simulation made by Bari colleagues. In that histogram, it can be seen a peak corresponding to an energy of $400 \div 500$ eV. Being the beam initial energy of the simulation 20 keV, the most part of the ions has lost $19.6 \div 19.5$ keV, meaning that $98\% \div 97.5\%$ of the initial energy was recovered. The histogram peak, however, has a tail up to about 1.5 keV. It can be estimated that about the 20% of the simulated particles were collected with about 1 keV, corresponding to an energy recovery of about 90%.

In the histogram are also visible few ions (about 2%) that were intercepted by electrodes out of the collectors at energies, in any case, lower than 6 keV.

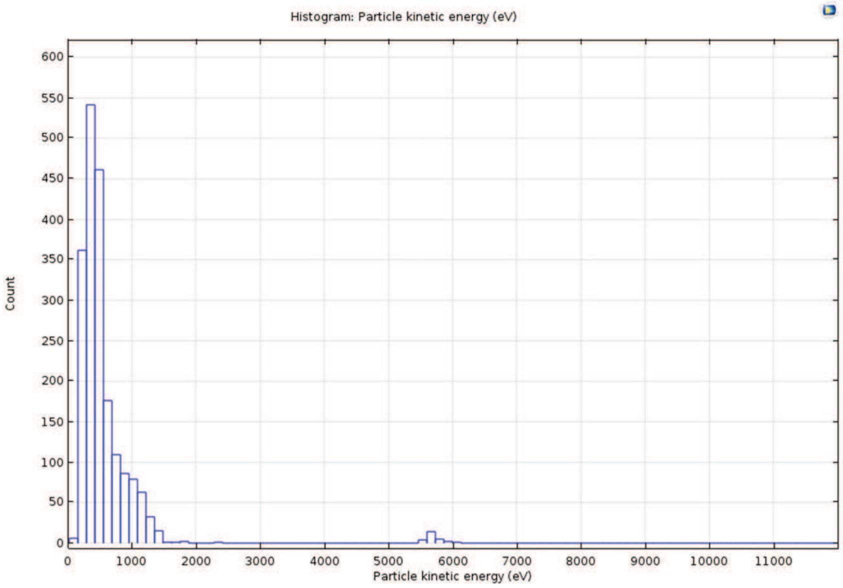

Figure B- III. Kinetic energy distribution, obtained with the OPERA simulation, for both H^+ and H^-.

In order to confirm the simulation results obtained with COMSOL the same model of two stages ion collector was simulated with OPERA. The trajectories calculated with the OPERA model are reported in Figure B-III b). It can be noticed that, practically, the trajectories of the two species are very similar to the trajectories simulated by COMSOL (Figure

B-III b)).

An histogram of the collected energies for H^{-} and H^{+} fractions is reported in Figure B-IV. According to OPERA more than 99% of H^{+} are collected and their energy stays around 300 eV that is a result very similar to COMSOL. 96% of H^{-} are also collected at around 400 eV, with few stray particles barely reaching 1 keV (not shown in the picture). A fraction of about 3.5% of the H^{-} current is not collected in the recovery system and propagates with the neutral beam with energy of around 40 keV.

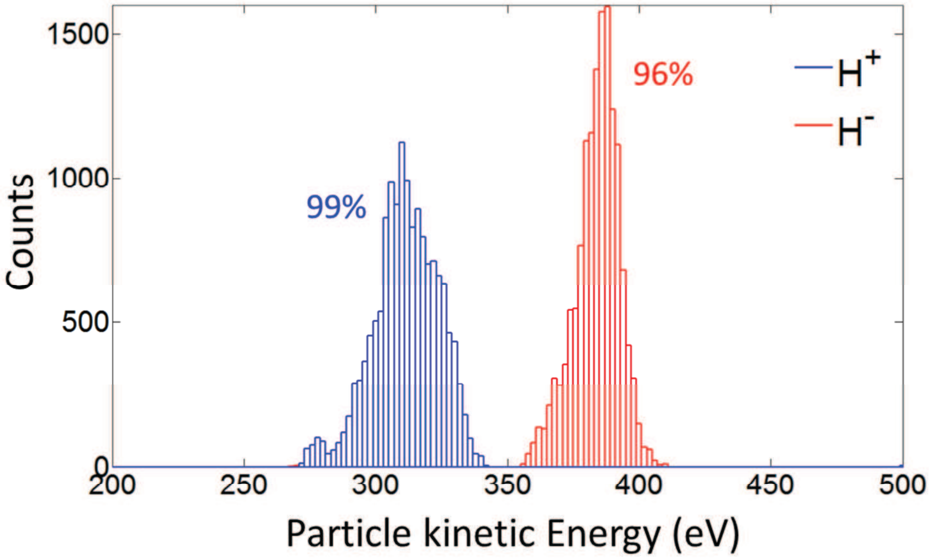

Figure B-IV. Kinetic energy distribution, obtained with the OPERA simulation, for both H^{+} and H^{-}.

Bibliography

[1]: BP Statistical Review of World Energy 2015, bp.com/statisticalreview

[2]: Emission Database for Global Atmospheric Research, http://edgar.jrc.ec.europa.eu/

[3]: World Nuclear Association, http://www.world-nuclear.org/

[4]: US Department of Energy, *What Are Greenhouse Gases?,* 2007.

[5]: K.Miyamoto, *Plasma Physics for Nuclear Fusion*, The MIT press, 1989.

[6]: W.K.Hogan. Nucl.Fusion, 44, 2004.

[7]: M. Wakatani, *Stellarator and heliotron devices,* Oxford University Press, 1998.

[8]: J. Wesson et al., *Tokamaks*, Oxford University, 2004.

[9]: ITER Organization, http://www.iter.org

[10]: V. Toigo et al, *Progress in the realization of the PRIMA neutral beam test facility*, Nuclear Fusion, 55 083025 doi:10.1088/0029-5515/55/8/083025, 2015.

[11]: P. Agostinetti, D. Aprile, V. Antoni, et al., *Detailed design optimization of the MITICA negative ion accelerator in view of the ITER NBI*, Nucl. Fusion 56 016015, doi: 10.1088/0029-5515/56/1/016015, 2015.

[12]: H.P.L. de Esch et al., *Physics design of the HNB accelerator for ITER*, Nucl. Fusion 55 096001, doi: 10.1088/0029-5515/55/9/096001, 2015.

[13]: R. S. Hemsworth et al., *Neutral beams for ITER*, Rev. Sci. Instrum. 67, 1120 (1996)

[14]: G. Brown, *The Physics and Technology of Ion sources* ISBN: 3-527-40410-4

[15]: R. S. Hemsworth et al *Status of the ITER neutral beam injection system* Rev. Scie. Instr. 79, 02C109 2008

[16]: A. Liberman, Principles of Plasma Discharges and Materials Processing, Wiley&sons, inc publication (2005).

[17]: P. Franzen et al. *Progress of the development of the IPP RF negative ion source for the ITER neutral beam system*. Nuclear Fusion, 47, 2007.

[18]: U. Fantz et al, *Spectroscopy—a powerful diagnostic tool in source development* Nucl. Fusion 46 S297 (2006)

[19]: Yu. I. Belchenko, G.I. Dimidov, and V. G. Dudnikov. Nuclear Fusion, 14, 1974.

[20]: M. Bacal, E Nicolopoulou, and H. J. Doucet. *In Proc. Symp. on the Production and Neutralization of Negative Hydrogen Ions and Beams* (Brookhaven National Laboratory Upton, NY, USA), pages 26–34, 1977.

[21]: M.Bacal and Wada, *Negative hydrogen ion production mechanisms* Appl. Phys. Rev. 2 021305 (2015)

[22]: J.N Bardsley and J.M. Wadehra. *Dissociative attachment and vibrational excitation in low-energy collisions of electrons with* H^2 *and* D^2. Phys. Rev. A, 20:1398–405, 1979

[23]: J. P. Boeuf et al. *Physics of a magnetic filter for negative ion sources. I. Collisional transport across the filter in an ideal, 1D filter*, Phys. Plasmas 19, 113509 (2012); doi: 10.1063/1.4768676

[24]: A. Masiello et al. *The European contribution to the development of the ITER NB injector*, Fusion Eng. Des. 86, 860 (2011).

[25]: private communication with D. Wünderlich.

[26]: Bacal M and Wada *Negative hydrogen ion production mechanisms* Appl. Phys. Rev. 2 021305 (2015)

[27]: G. D. Severn, *A note on the plasma sheath and the Bohm criterion* Am. J. Phys.75, 92 (2007); doi: 10.1119/1.2372469

[28]: F. Chen, Introduction to Plasma Physics and Controlled Fusion ISBN: 978-3-319-22308-7

[29]: T. Kalvas, *Beam Extraction and Transport* arXiv:1401.3951v1

[30]: G. Chitarin, et Al., *Cancellation of the ion deflection due to electron-suppression magnetic field in a negative-ion accelerato,r* Review of Scientific Instruments, Vol.85, Issue 2, 02B317 (2014)

[31]: P. Veltri, et al. *Design of the new extraction grid for the NIO1 negative ion source*, AIP Conference Proceedings, Volume 1655, Issue 1, (2015)

[32]: M. Cavenago, *Integrodifferential models of electron transport for negative ion sources*, J. Plasma Phys., vol. 81, 495810603 (2015)

[33]: W.B Hermansfeld. *Electron trajectory program*. Technical report, Stanford Linear Accelerator Center, 1979.

[34]: J. Pamela. *A model for negative ion extraction and comparison of negative ion optic calculation to experimenta result*. Review of Scientific Instruments, 62, 1991.

[35]: G. Fubiani, R.S. Hemsworth, H.P. de Esch, and A. Simonin. *Modelling of secondary emission processes in ion based electrostatic accelerator of the International Thermonuclear Experimental Reactor*. Physical review Special Topics, Accelerators and Beams, 11, 2008.

[36]: N. Fonnesu et al., *A multi-beamlet analysis of the MITICA accelerator*, Proc. Of International Symposium on Negative Ions, Beams and Sources (NIBS), IPP Garching (Germany), Oct. 6-10 2014 (to be published)

[37]: COMSOL: www.comsol.com

[38]: OPERA-3D, Vector Fields Co. Ltd. And http://www.vectorfields.com

[39]: P. Sonato et al., *The ITER full size plasma source device design*, Fusion Eng. Des. 84, 269 (2009)

[40]: P. Agostinetti et al., Nucl. Fusion 51, 063004 (2011)

[41]: E. Sartori, P. Veltri Vacuum 90 80 (2013)

[42]: E. Sartori, G. Serianni, S. Dal Bello, Vacuum 122, 275 (2015)

[43]: M.Cavenago et al. Development of a versatile multiaperture negative ion sourcen Rev Sci Instrum. 2012 Feb;83(2):02A707. doi: 10.1063/1.3670350.

[44]: M. Cavenago1, et al. *First Experiments with the Negative Ion Source NIO1* Rev. Sci. Instrum. 87, 02B320 (2016)

[45]: G. Serianni et al. *First negative ion beam measurement by the Short-Time Retractable Instrumented Kalorimeter Experiment (STRIKE)* Rev. Sci. Ins. 85, 02A736 (2014)

[46]: A. Rizzolo, M. Dalla Palma, M. De Muri, G. Serianni, *Design and analyses of a one-dimensional CFC calorimeter for SPIDER beam characterisation*, Fusion Eng. Des. 85 (2010) 2268-2273

[47]: G. Serianni, A. Pimazzoni, A. Canton, M. Dalla Palma, R. Delogu, D. Fasolo, L. Franchin, R. Pasqualotto, S. Peruzzo, M. Tollin, *Test of 1D carbon-carbon composite prototype tiles for the SPIDER diagnostic calorimeter* (presented at NIBS 2016 and currently under review)

[48]: M. Cavenago, Veltri P, Sattin F, Serianni G and Antoni V, *Negative Ion Extraction With Finite Element Solvers and Ray Maps* IEEE Trans. Plasma Sci. 36 1581 (2008)

[49]: D. Wünderlich, S. Dietrich, and U. Fantz, J. Quant. Spectrosc. Radiat. Transfer 110 (1-2), 62–71 (2009)

[50]: M. Barbisan, C. Baltador, B. Zaniol, M. Cavenago, U. Fantz, R. Pasqualotto, G. Serianni, L.Vialetto and D. Wünderlich *First hydrogen operation of NIO1: characterization of the source plasma by means of an optical emission spectroscopy diagnostic*, Rev. Sci. Instrum. 87 (2016) 02B319; doi: 10.1063/1.4936084

[51]: See www.hamamatsu.com/eu/en/4016.html for technical specifications about the low resolution spectrometer

[52]: See ridl.cfd.rit.edu/products/manuals/Acton/ld/MANUAL/Sp-750i.pdf for technical specifications about the high resolution spectrometer

[53]: S. A. Astashkevich, M. Käning, E. Käning, N. V. Kokina et al. , J. Quant. Spectrosc. Radiat. Transfer 56 (5), 725–751 (1996)

[54]: U. Fantz, *Basics of plasma spectroscopy*, Plasma Sources Sci. Technol. 15 (2006) S137–S147 doi:10.1088/0963-0252/15/4/S01

[55]: M.Cavenago et al. *Improvements of the Versatile Multiaperture Negative Ion Source NIO1* (presented at NIBS 2016 and currently under review)

[56]: A.Pimazzoni, M.Cavenago, V.Cervaro, D.Fasolo, G.Serianni, M.Tollin, P.Veltri, *A First Characterization of the NIO1 Particle Beam by Means of a Diagnostic Calorimeter* (presented at NIBS 2016 and currently under review)

[57]: P.Veltri et. al (presented at NIBS 2016 and currently under review)

[58]: M. Kashiwagi, Development of negative ion extractor in the high-power and long-pulse negative ion source for fusion applicationa REVIEW OF SCIENTIFIC INSTRUMENTS 85, 02B320 (2014)

[59]: P. Agostinetti, et Al. *Detailed design optimization of the MITICA negative ion accelerator in view of the ITER* NBI Nucl. Fusion 56 (2016) 016015; doi:10.1088/0029-5515/56/1/016015

[60]: H.P.L. de Esch et al. *Physics design of the HNB accelerator for ITER* , Nucl. Fusion 55 (2015) 096001, doi:10.1088/0029-5515/55/9/096001.

[61]: D.Aprile, P. Agostinetti, C. Baltador, G. Chitarin, N. Marconato, E. Sartori, G. Serianni, P. Veltri *Realization of a Magnetically Compensated Extraction Grid for performance improvement of next generation NBI* (presented at SOFT 2016 and currently under review)

[62]: G. Chitarin, M. Guarnieri, A. Stella: "An equivalent network approach to the electromagnetic Field diffusion in Axisymmetric configuration" (IGI report 88/03, Padova Sept. 1988)

[63]:Internal RFX technical note:RFX-MITICA-TN-351, JointExperimentsWeek 1-3_r4_2016 12_31

[64]:Internal RFX technical note:RFX-MITICA-TN-352, JointExperimentsWeek 4-6_r4_2016 12_31

[65]: P. Veltri et al 2017 Nucl. Fusion 57 016025

[66]: McGeoch, M. W., *Production and Neutralization of Negative Hydrogen Ions and Beams* (Proc. 2nd Int.Symp. BNL,1980)Rep. BNL-51304, BrookHaven National Laboratory, Upton, NY (1980) 3